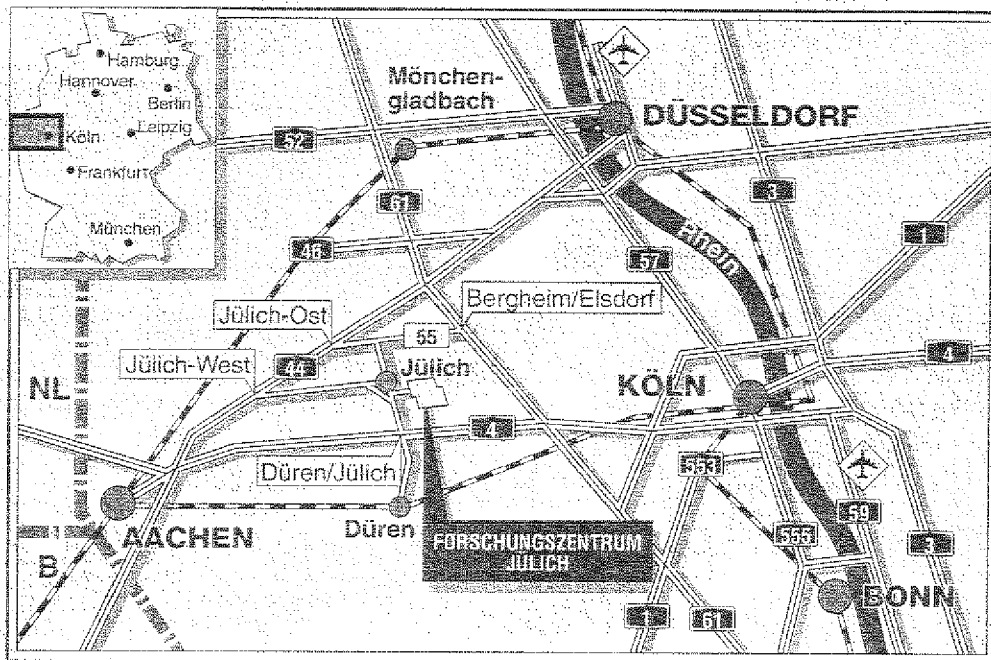


Institut für Festkörperforschung

**Structure and Spectroscopy
of Charged and Neutral Clusters
A Density Functional Study**

Stefan Hunsicker



Berichte des Forschungszentrums Jülich ; 3268

ISSN 0944-2952

Institut für Festkörperforschung Jül-3268

D 82 (Diss. RWTH Aachen)

Zu beziehen durch : Forschungszentrum Jülich GmbH · Zentralbibliothek

D-52425 Jülich · Bundesrepublik Deutschland

Telefon : 02461/61-61 02 · Telefax : 02461/61-61 03 · Telex : 833 556-70 kfa d

**Structure and Spectroscopy
of Charged and Neutral Clusters
A Density Functional Study**

Stefan Hunsicker

Zusammenfassung

Schwingungsaufgelöste Photoelektronen-Spektren massenselektierter Clusterstrahlen enthalten im Prinzip eine Fülle von Informationen über die elektronische und geometrische Struktur freier Cluster, bedürfen jedoch der Interpretation durch quantenmechanische Rechnungen. Dabei werden hohe Anforderungen an Genauigkeit und Effizienz des verwendeten Verfahrens gestellt. Durch eine systematische Untersuchung von neutralen und anionischen S_n^- , P_n^- , und $Si_nC_m^-$ -Clustern und Vergleich mit experimentellen Spektren zeigen wir, daß die lokale Spindichte-Näherung des Dichtefunktional-Formalismus in Verbindung mit der Molekulardynamik-Methode von Car und Parrinello beide Forderungen in hohem Maße erfüllt. Zum einen liefert unser Verfahren elektronische Bindungsenergien unter Berücksichtigung von Relaxationsprozessen, zum anderen kann es mit Molekulardynamik-Simulationen bei endlicher Temperatur die stabilsten Clustergeometrien effizient bestimmen. Letzteres ist entscheidend für den Erfolg unseres Vorgehens, da die Strukturen der Cluster die Bindungsenergien der Photoelektronen erheblich beeinflussen können. Das zeigen die Unterschiede der Elektronenaffinitäten ring- und kettenförmiger Schwefelcluster besonders deutlich. Experimentell beobachtete Veränderungen der Photoelektronenspektren bei verschiedenen Einstellungen der Clusterquelle lassen sich ebenfalls durch das Auftreten unterschiedlicher Isomere erklären. Auch bei P_n^- - und $Si_nC_m^-$ -Clustern entscheidet die Form der Cluster über die Gestalt der Spektren, so können zum Beispiel in einzelnen Fällen die Elektronenaffinitäten verschiedener Strukturisomere um mehrere Elektronenvolt differieren. Darüber hinaus sind elektronische Übergänge i.A. auch mit Übergängen zwischen verschiedenen Schwingungszuständen verknüpft. Diese lassen sich, falls sie im Experiment auflösbar sind, durch Vergleich mit unseren theoretisch gewonnenen Werten ebenfalls für die Strukturbestimmung nutzbar machen. Zwar ist unsere Methode auf die Bindungsenergien der niedrigsten elektronischen Zustände jeder Symmetrie eingeschränkt, jedoch hat sich dies in fast allen Fällen als ausreichend erwiesen, um die experimentellen Daten konsistent zu erklären. Damit eröffnen sich zum Teil überraschende Einblicke in die Struktur nicht nur anionischer Cluster.

Contents

1	Introduction	3
2	The Car-Parrinello Method	7
2.1	The Born-Oppenheimer Potential	7
2.1.1	The Adiabatic Approximation	7
2.1.2	The BO Potential in Density Functional Theory	9
2.1.3	Electronic Structure Optimization	17
2.2	Born-Oppenheimer Dynamics	22
2.2.1	Simulated Annealing and Molecular Dynamics	22
2.2.2	The Car-Parrinello MD	23
2.3	Practical Implementation	27
2.3.1	The CP method with a Plane Wave Expansion	27
2.3.2	Charged Systems	35
2.3.3	Vibrational Spectra	38
2.3.4	Computational Cost	42
3	Results	45
3.1	Computational Details	46
3.2	Experimental Setup	48
3.3	Sulphur Cluster Anions	50
3.3.1	Optimal Geometries, Vibration Frequencies, and Vertical Excitation Energies	51
3.3.2	Trends and Discussion	72
3.4	Phosphorus Cluster Anions	77
3.4.1	Optimal Geometries, Vibration Frequencies, and Vertical Excitation Energies	77
3.4.2	Trends and Discussion	86
3.5	Mixed Silicon-Carbon Cluster Anions	89
3.5.1	Optimal Geometries, Vibration Frequencies, and Vertical Excitation Energies	90
3.5.2	Trends and Discussion	111
4	Conclusion	117

A FFT Coefficients and Isolated Systems	118
B Excited States within the von Barth Scheme	121
C Calculated Vertical Excitation Energies	125

Chapter 1

Introduction

When Dirac discovered his famous equation that describes the dynamics of electrons, he is said to have remarked “the rest is chemistry”. Whether or not he actually said this, most physicists would agree that the quantum mechanics of electrons and nuclei contains the principles that govern most of low-energy physics, chemistry, and biology. However, the view that this is all that physics can say about the astonishing complexity of these fields was certainly too pessimistic. Powerful numerical models based on quantum mechanics are now used to explain and predict many properties of chemical compounds. It has become increasingly apparent that a key to the understanding of the behaviour of complex molecules is the geometrical arrangement of the constituent atoms. This is obvious in molecular biology, where the enzymatic function of polypeptides or the effects of drugs can be directly related to the three-dimensional arrangement of their atoms in space, and was recognized early by researchers in this field. F. Crick wrote “If you want to study function, study structure” [Cri88]. However, the structure also affects the properties of chemical compounds on a lower, more immediate level of complexity. The boiling points of alkanes C_nH_{2n-2} , for example, are correlated both with the size of the molecules (i.e., n) and the amount of branching in the structures. Conversely, we cannot expect to be able to predict the properties of a given compound correctly if we know nothing about its structure. Therefore, the determination of the correct equilibrium structures has become a major goal of computational physics.

This interest in the prediction of specific properties of individual systems might seem to contradict the search for universal laws that dominates much of theoretical physics, but is a necessary prerequisite for the understanding and prediction of more general trends and relations in this field of research. While these remarks are valid for chemical compounds in general, they are particularly important for atomic clusters, which can be expected to exhibit a large variety of different geometries as they span a larger size range than molecules.

What are clusters? There seems to be some semantic confusion about their definition, so let us consult a dictionary [Oxf93]. While a molecule is defined as “the smallest portion to which a substance can be reduced by subdivision without losing its chemical identity”, we learn that clusters are simply “compact groups of similar things”. According to this

definition, which is less restrictive (with respect to size and to chemical stability) for a cluster than for a molecule, a molecule might as well be regarded as a more or less small and especially stable cluster. In fact, since clusters are characterized by a large number of surface atoms with often strained and/or dangling bonds, most of them might be viewed by chemists as free radicals rather than molecules. On the other hand, there are some exceptional clusters that can exist in macroscopic amounts, such as small clusters of sulfur and selenium [Don74] and several carbon structures such as C_{60} [FSM⁺91]. The borderline that separates clusters from molecules is imprecise, and this is also true for the upper bound of the size range (about 10^5 atoms) that distinguishes clusters from bulk matter.

Particularly difficult to describe and predict are clusters of elements that form covalently bonded¹ molecules and solids [MRB90], such as C, Si, P and S in the first and second rows of the main groups 14 through 16 of the periodic table. These elements are the focus of the present work. The propensity to form covalent bonds has crucial implications for the complexity of the geometries of these clusters. Unlike rare gas and, from a certain size, metal clusters, these are neither simple close packed arrays nor bulk-like, but exhibit a wide variety of forms that challenge both experimentalists and theorists. These particles are also interesting from a technological viewpoint, since the uniqueness of structural features suggests that some clusters might be used as building blocks of new materials with novel properties. For example, conferences are now held on C_{60} alone, the most famous of a whole new class of "Bucky" structures. This cluster can be assembled into a molecular solid, yielding a third distinct crystal structure for bulk carbon that, doped as $Rb_3Cs_2C_{60}$ for example, can even be made into a high temperature superconductor ($T_c=33$ K [TES⁺91]). The unique features met in the mesoscopic region between atoms or small molecules and condensed matter are a serious drawback for the applicability of standard experimental and theoretical concepts and models used successfully in either region.

Despite many efforts, structural properties of most clusters are difficult to obtain from experiment, since the modest size and the comparatively high reactivity of these particles restricts the applicability of traditional solid state methods, such as nuclear magnetic resonance (NMR) or x-ray diffraction. Moreover, it is not yet possible to produce size-selected clusters of a given composition in macroscopic quantities (with the exception of Bucky-structures, see [KLFH90]). The deposition of clusters on a support or the embedding into condensed matter (matrix) could facilitate their study, but the interaction with the substrate changes the properties of the clusters and adds considerable complexity, both experimental and theoretical. These difficulties apply to all experiments where supports or matrices are used, although they can be studied by infrared, visible and ultraviolet spectroscopy or by x-ray spectroscopy (for reviews, see [CS94], [KQ94] and [DW94]). Only a few experimental results have been published for, e.g., mass-selected supported clusters (but see [EFC⁺90]) that allow for conclusions about their geometries, despite the obvious technological importance in catalysis and nanostructured devices.

¹The term "covalent bond" dates was introduced by Lewis [Lew16] (in 1916, before quantum mechanics was established fully) and refers to a directional chemical bond that results from a sharing of an electron pair (as distinct from electron transfer) between the bonding atoms (see [Pau60]). The directionality of the electron distribution is also characteristic for covalent crystals [AM76].

Experiments on clusters in the gas phase require sources that are able to produce intense cluster beams, and two of the most common designs are discussed below. Gas-aggregation sources [RMT⁺89, dHKCC87] vaporize clusters (mostly metals) continuously into a flow of cold inert gas, and the most intense sources are of this type. Pulsed sources [Sma83, SLF⁺91] use a laser or an electric discharge to produce, for a wide range of materials, a plasma of neutral and charged particles that is carried away by an inert gas, and high instantaneous cluster intensities can be reached. Among the various characteristics of clusters studied in the gas phase are the size distribution (see, e.g., [Kcd⁺84]), the polarizability [dC89], the collision-induced modes of fragmentation (see, e.g., [RJBK90]) and the fission upon charging [Sau90] and in Coulomb explosion experiments after a complete removal of all valence electrons [VFK⁺91]. The clusters can also be investigated by optical spectroscopy either by exciting the cluster with either one or two photons, where in the latter case ("two photon spectroscopy") the second is used to probe the photo-excited states by scanning their frequency (see [KM90]). The occurrence of photofragmentation has been put to advantage in depletion spectroscopy, where the photoabsorption cross section is determined indirectly from the photofragmentation cross section (see [BCC⁺95]). In infrared spectroscopy, the clusters are mixed into a rare gas carrier and the absorption spectrum probed by irradiating the mixture either in the gas phase (seeded rare gas clusters, for a review see [AGL⁺94]) or in deposited form (matrix isolation spectroscopy, see [PMGS90]). The spectra contain information about the vibrational states of the clusters.

Among the gas phase methods, electron spectroscopy has established itself in recent years as a promising source of indirect structural information about clusters with up to ~ 100 atoms. This development has been facilitated by improvements in electronic detection techniques. In electron spectroscopy, mostly negatively charged clusters that have been ionized either during or after the generation process are mass selected and focused into a beam that is irradiated by a laser. Photoelectron spectroscopy measures the kinetic energy of photo-ejected electrons, which contains information about the electronically and vibrationally excited states of the resulting neutral cluster. The energy resolution of the electron spectrometers is typically ~ 5 to 50 meV, and in chapter 3 we describe in detail a typical experimental setup and interpret the features contained in the spectra. Even higher resolution is provided by the zero kinetic energy electrons (ZEKE) spectroscopy, where the cluster beam is intersected by one or two narrow band, tunable laser beams. The laser frequency is tuned near to a threshold for electron production and only photo-ejected electrons with very low kinetic energy are detected. The energy resolution can be as high as 0.1 meV (for an application of both electron spectroscopy techniques to C and Si cluster anions, see [KN93]).

Photoelectron spectroscopy has raised particular interest among theorists, since vibrationally resolved spectra are now available for a large variety of clusters (e.g., Sb clusters [PGHL92], Au clusters [TJC⁺90], Bi clusters [PHGL91] and C/Si clusters [KCWN90], [KN93], [HGK⁺95], [NTN⁺95]) that convey a wealth of information on vibronic excitation properties and indirectly on the ground state geometries. A reliable interpretation of these spectra is a major challenge for theory in the field of clusters. Traditional "ab initio" computational methods of quantum chemistry are impracticable in the size range

covered by the spectra, and the search for more efficient algorithms (see, for instance, [ODMG95, MG94, HTP94]) is the subject of current research interest. Traditionally, the understanding of the electronic excitations of atoms and molecules relies on configuration interaction (CI) calculations, which, although highly accurate, are limited to systems with relatively few electrons (less than 100). Recently, CI calculations have provided successful interpretations of photoelectron spectra, such as in the case of anionic silver clusters [BKČ94], but the high computational cost restricts these calculations to a reduced basis set and consideration of valence s electrons only. It would be extremely expensive to perform high-level CI calculations on systems like those considered here (see [RR92] for a QCISD(T) calculation for one isomer each of Si_3^- and Si_4^-).

On the other hand, atomic and molecular clusters are fields in which density-functional theory in the local-spin density approximation, especially with the Car-Parrinello method (see, e.g. [HJCP88, JH90a, RAP94, BJ94]) has demonstrated its ability to determine ground-state structural and electronic properties both reliably and efficiently. However, while the ground-state properties can in principle be obtained exactly, the eigenvalues of the Kohn-Sham equation cannot be interpreted as electron addition or removal energies, such as those measured in photoemission. Instead, a possible calculation of the excitation spectrum might start from local density approximation results for the ground-state and then compute the quasiparticle (QP) energies of the system within many-body perturbation theory. This is often done [HL85b, SL93] using Hedin's GW approximation [Hed65]. Despite the approximations involved, this approach is computationally demanding, and is restricted to relatively simple systems, such as Na and K clusters within the spherical jellium model [SZLC89]. Application to systems such as those considered here is presently beyond the scope of this method.

This has prompted us to develop a parameter-free and manageable scheme based on the Car-Parrinello method that is able to calculate the electronic excitation energies of clusters in terms of differences of self-consistent total energies (ΔSCF). The approach, which we describe in detail in the next section, requires no approximations beyond the local spin-density approximation. Many recent publications in the area of cluster science (see, e.g., [PMG92] and [Rit92], [Rit94] and [PMG94], [GKL⁺94] and [PMGRG95]) are the result of close collaboration between theorists and experimentalists. We therefore suggested to the experimental group in our institute led by Gerd Ganteför that they check the predictions of the scheme by performing high resolution photodetachment measurements. This has been done for S_n^- , P_n^- and Si_nC_m^- microclusters and the results of the collaboration play a central role in the work described in this thesis.

Chapter 2

The Car-Parrinello Method

In this chapter, we describe a manageable theoretical scheme that leads to a successful interpretation of the photoelectron spectra of small clusters. The crucial factor to bring theory in close agreement with experiment is the accurate determination of the equilibrium atomic geometries of anionic clusters. To this end, we use the method introduced by Car and Parrinello (CP) [CP85]. The two key ingredients to the CP method are

- an accurate [Koh95] approximation to the Born-Oppenheimer (BO) potential provided by the local spin-density approximation (LSDA) of density functional theory (DFT)
- a numerically efficient approximation to the true BO dynamics, i.e., the dynamical evolution of the system of nuclei on the BO potential energy surface, provided by the CP molecular dynamics (CP-MD) scheme.

The first two sections are addressed to an outline of both aspects of the CP method. In section 2.3, the reader will be confronted with the unavoidable technicalities of the implementation of the method. In the same section we will describe our steps taken to make the method (that uses periodic boundary conditions) applicable to isolated, charged clusters, especially to calculate total energies differences.

2.1 The Born-Oppenheimer Potential

2.1.1 The Adiabatic Approximation

The Car-Parrinello (CP) method as used in this work requires the validity of the quantum adiabatic or Born-Oppenheimer (BO) approximation [BO27]. Within this approach, the kinetic energy of the nuclei is considered as a perturbation of the electronic system

$$\mathcal{H} = h(\{\mathbf{R}_I\}) + \kappa^4 \sum_I \alpha_I \frac{\mathbf{P}_I^2}{2m}, \quad (2.1)$$

where $\kappa = \sqrt[4]{m/\langle M_J \rangle}$ serves as a formal parameter of the perturbation, $\langle M_J \rangle$ being a suitable average of the nuclear masses involved. $\alpha_i = \langle M_J \rangle / M_I$ are dimensionless parameters of order one. The unperturbed (electronic) Hamiltonian reads

$$\begin{aligned} h(\{\mathbf{R}_I\}) &= \sum_i \frac{\mathbf{p}_i^2}{2m} + \frac{e^2}{2} \sum_{i \neq j} \frac{1}{|\mathbf{r}_i - \mathbf{r}_j|} + e^2 \sum_i V^{ext}(\mathbf{r}_i) \\ &\quad + \frac{e^2}{2} \sum_{I \neq J} \frac{Z_I Z_J}{|\mathbf{R}_I - \mathbf{R}_J|}, \\ V^{ext}(\mathbf{r}_i) &= \sum_I \frac{-Z_I}{|\mathbf{r}_i - \mathbf{R}_I|} \end{aligned} \quad (2.2)$$

and its eigenstates ψ_n

$$h(\{\mathbf{R}_I\})\psi_n = e_n(\{\mathbf{R}_I\})\psi_n$$

depend only parametrically on the nuclear positions. As a result of stationary perturbation theory, it turns out that close to the extremal positions¹ of the nuclei, the total wavefunctions of (2.1) factorize

$$\Psi_n(\{\mathbf{r}_i\}, \{\mathbf{R}_I\}) = \psi_n(\{\mathbf{r}_i\})|_{\{\mathbf{R}_I\}} \chi_n(\{\mathbf{R}_I\}) + \mathcal{O}(\kappa^3),$$

i.e., the electrons follow the nuclei instantaneously in their stationary states (only the ground state will be of importance here). This results from the good separation of the time scales of the motions of the particles due to their high mass ratio, allowing the (fast) electrons to follow immediately the (slow) nuclei (see the following paragraph). It is only in the higher-order terms that transitions between the electronic states due to the nuclear dynamics cause deviations from this simple form. As a consequence of the large mass difference between the electrons and the atomic cores, these terms can safely be neglected, provided that the gap between the ground and the first excited electronic state remains smaller than typical vibration energies. This holds true, for instance, for semiconductors and insulators, but is a more subtle issue for metals, where the effect of deviations on many physical properties is at least less dramatic [Che61]. The functions χ_n of the nuclei might in principle be obtained as solutions of the Schrödinger equation

$$\left(\sum_I \frac{\mathbf{P}_I^2}{2M_I} + e_n(\{\mathbf{R}_I\}) \right) \chi_n(\{\mathbf{R}_I\}) = \mathcal{E}_n \chi_n(\{\mathbf{R}_I\}) + \mathcal{O}(\kappa^4),$$

where the eigenvalues of the electrons serve as effective potentials and the \mathcal{E}_n are the exact eigenvalues of (2.1). But owing to the comparatively large ionic masses, it is possible to take the classical limit on the nuclear degrees of freedom leading to the effective Hamiltonian

$$H(\{\mathbf{R}_I, \mathbf{P}_I\}) = \sum_I \frac{\mathbf{P}_I^2}{2M_I} + e_n(\{\mathbf{R}_I\}), \quad (2.3)$$

¹defined by $\partial e_n(\{\mathbf{R}_I\}) / \partial \mathbf{R}_J = 0, \quad \forall J$

where usually only e_0 , the ground state energy of an inhomogeneous electron gas in the presence of fixed ions at positions $\{\mathbf{R}_I\}$ is considered. In its role as potential for the nuclei, it will be referred to hereafter as the BO potential and its $3N_{ion}$ -dimensional graph as the BO (potential) energy surface.

Dimensional Analysis So far, c.g.s. units have been used. However, in solid state physics, expressions and calculations are commonly simplified by the use of atomic units (a.u.), taking mass, energy and length as fundamental dimensions. One chooses the Bohr radius $a_0 = 0.529 \text{ \AA}$ as unit of length and one Hartree $\epsilon = e^2/a_0 = \hbar^2/(ma_0^2) = 27.212 \text{ eV}$ as unit of energy. In this unit system, a time-dependent Schrödinger equation with Hamiltonian (2.2) takes the form

$$i\frac{\partial}{\partial t}\psi = \left(\sum_i -\frac{\nabla_i^2}{2} + \frac{1}{2} \sum_{i \neq j} \frac{1}{|\mathbf{r}_i - \mathbf{r}_j|} + \sum_i V^{ext}(\mathbf{r}_i) + \frac{1}{2} \sum_{I \neq J} \frac{Z_I Z_J}{|\mathbf{R}_I - \mathbf{R}_J|} \right) \psi$$

Hence “ $m = \hbar = e = 1$ ” in a.u. and $\tau := \hbar/\epsilon = ma_0^2/\hbar = 2.419 \times 10^{-17} \text{ s}$ is the natural unit of time of the electronic subsystem. Writing out Newton’s equations of motion resulting from (2.3) in the same units, one finds $\tau_I := \sqrt{M_I a_0^2/\epsilon}$ as natural units of time for the subsystems of the nuclei, which is, say for Si, about 1000 times larger than τ . Therefore, at least two completely different time constants are present in the dynamics of the system. If not otherwise stated, this unit system will be used throughout the remainder of this work.

2.1.2 The BO Potential in Density Functional Theory

The calculation of e_0 would usually require the solution of a $3N_{el}$ -dimensional Schrödinger equation, which is a completely hopeless task. Hohenberg and Kohn (HK) [HK64] and Kohn and Sham [SK65] were able to recast this problem in terms of the electronic density and an universal functional E_{xc} of it. In view of the complexity of the many-body problem at hand, the task of deriving an exact expression for this density functional (DF) is altogether intractable.

This section is devoted to the most popular – and necessarily approximate – expressions for e_0 within and extensions to the DF approach [JG89] as far as they concern the present work. This means that we focus on the formulation of the theory as it applies to the description of systems with a spin-paramagnetic electronic ground state (GS), as is appropriate for the investigation of small systems like atoms and molecules. Of course, the HK theorem in its original form could also be used here, which demonstrates that all information about a system is already contained in its GS density alone. An obvious consequence would be, that the spin densities are functionals $n_\sigma[n]$ of the GS density as well and a separate description would be, at best, completely superfluous. In practice, however, the spin-density functional formalism is advantageous, because, as experience has shown, at least in the spin-polarized case a local functional $F[n_+, n_-]$ can adequately describe effects that would otherwise require a highly nonlocal functional $F[n]$.

The HK Theorem for Spin-polarized Systems

The HK theorem, as it applies to a non-degenerate spin-polarized electronic ground state [vBH72, RC73] of an N -electron system, encompasses two statements.

The first one states that it is possible to replace the all-electron wavefunction ψ_0 as basic variable by its N_{el} -particle GS spin densities²

$$n_\sigma(\mathbf{r}) = N_{el} \sum_{\sigma_2} \int d\mathbf{r}_2 \dots \sum_{\sigma_{N_{el}}} \int d\mathbf{r}_{N_{el}} |\psi_0(\mathbf{r}\sigma, \mathbf{r}_2\sigma_2, \dots, \mathbf{r}_{N_{el}}\sigma_{N_{el}})|^2, \quad \sigma = \pm.$$

Strictly speaking, it demonstrates, that the $n_\sigma(\mathbf{r})$ uniquely determine the GS wavefunction ψ_0 , i.e., there exists a bijective (fully invertible) map

$$(n_+, n_-) \rightarrow |\psi_0[n_+, n_-]\rangle.$$

Therefore, the GS expectation value of any observable of the system can in principle be obtained as a unique functional of the spin densities.

The second one, the HK variational theorem, ensures the variational accessibility of the new basic variables, without any recourse to the Schrödinger equation. It demonstrates the existence of an universal, i.e., V^{ext} -independent functional

$$F[n_+, n_-] := \langle \psi_0[n_+, n_-] | T + V_{ee} | \psi_0[n_+, n_-] \rangle,$$

where T and V_{ee} are the kinetic and electron-electron interaction operators, respectively. It is a direct consequence of the Ritz theorem that, for a given V^{ext} , the DF

$$E_{V^{ext}}[\tilde{n}_+, \tilde{n}_-] = F[\tilde{n}_+, \tilde{n}_-] + \int d\mathbf{r} V^{ext}(\mathbf{r}) \tilde{n}(\mathbf{r}), \quad (2.4)$$

being defined for all non-degenerate GS spin densities \tilde{n}_σ , attains its minimum only at the GS spin densities (n_+, n_-) belonging to V^{ext} and that

$$e_0(\{\mathbf{R}_I\}) = \min_{(\tilde{n}_+, \tilde{n}_-)} E_{V^{ext}|\{\mathbf{R}_I\}}[\tilde{n}_+, \tilde{n}_-] + \frac{1}{2} \sum_{I \neq J} \frac{Z_I Z_J}{|\mathbf{R}_I - \mathbf{R}_J|}. \quad (2.5)$$

Although the HK theorem in this formulation has little practical significance, several authors [Lev82, Lie83, EE83] have shown that the restriction to GS densities in the HK theorem is a severe one, since not all well-behaved functions $n_\sigma(\mathbf{r})$ can be realized as GS spin densities of any external potential. To bypass this so-called problem of “ V -representability”, [Lev82, Lie83] have proposed to define an extension to $F[n_+, n_-]$ by the so-called “constrained search” approach

$$F[n_+, n_-] := \min_{\psi \rightarrow (n_+, n_-)} \langle \psi | T + V_{ee} | \psi \rangle, \quad (2.6)$$

where the notation $\psi \rightarrow (n_+, n_-)$ indicates that the minimum be searched over all antisymmetric, normalized functions $\psi(\mathbf{r}_1\sigma_1, \dots, \mathbf{r}_{N_{el}}\sigma_{N_{el}})$ that yield the prescribed spin densities. This extends the domain of F to arbitrary non-negative functions $n_\sigma(\mathbf{r})$, integrating to the desired number of electrons [ZM83].

²For this review, the discussion may be restricted to the only case of practical importance, where the GS spin density matrix has only nonvanishing diagonal components n_+ and n_- .

The KS Energy Functional for Spin-polarized Systems

So far, we have assumed tacitly that $V_{ee} = \frac{1}{2} \sum_{i \neq j} |\mathbf{r}_i - \mathbf{r}_j|^{-1}$. In order to arrive at an independent-electron picture, Kohn and Sham [SK65] also considered systems with vanishing electron-electron interaction $V_{ee} \equiv 0$. Their central assumption is, that for every system of interacting electrons there exists an auxiliary system of non-interacting electrons with a suitable potential V , such that the GS spin densities of both systems are the same. For systems of independent particles, the simplest antisymmetric eigenstates (and the GS) are Slater determinants $\psi_0 = (N_e!)^{-1} \det\{\phi_j(\mathbf{r}_k)\}$ of orthonormal one-particle orbitals ϕ_n , and the GS spin densities read

$$n_\sigma(\mathbf{r}) = \sum_{n \in \mathcal{I}_\sigma} |\phi_n(\mathbf{r})|^2. \quad (2.7)$$

Here, \mathcal{I}_\pm denote the sets of indices of occupied spin up and down orbitals, respectively. It is possible to separate the restriction $F_0[n_+, n_-]$ of the universal DF $F[n_+, n_-]$ onto this class of spin densities into

$$F[n_+, n_-] =: F_0[n_+, n_-] = T_0[n_+, n_-] + \int d\mathbf{r} \frac{1}{2} V^H[n](\mathbf{r}) n(\mathbf{r}) + E_{xc}[n_+, n_-]. \quad (2.8)$$

T_0 denotes the kinetic energy DF of non-interacting electrons,

$$T_0[n_+, n_-] = \min_{\{\phi_i\} \rightarrow (n_+, n_-)} \sum_n \int d\mathbf{r} \phi_n^*(\mathbf{r}) \left(-\frac{\nabla^2}{2} \right) \phi_n(\mathbf{r}) + \text{constraints} \quad (2.9)$$

(the constraints ensure the orthonormalization of the orbitals ϕ_n during the minimization), V^H is the classical Coulomb potential for electrons, which is only defined up to a harmonic function and may be chosen as

$$V^H[n](\mathbf{r}) = \int d\mathbf{r}' \frac{n(\mathbf{r}')}{|\mathbf{r} - \mathbf{r}'|},$$

and E_{xc} may be viewed as a (admittedly somewhat indirect) definition of the exchange-correlation energy. Calculating the total electronic energy using (2.8) and (2.4), it becomes apparent that all terms apart from E_{xc} are *formally* identical to the Hartree approximation and it might be tempting to identify E_{xc} with the exact correction of the Hartree energy. However, it should be kept in mind that the spin densities that enter (2.8) must be determined under the inclusion of $E_{xc}[n_+, n_-]$ and cannot be identified any longer with Hartree densities. Instead, a more direct definition of E_{xc} that holds for spin-unpolarized systems may be found in the literature [HJ74, GL76]. The physical meaning of E_{xc} is to favor such spin densities that lower the electrostatic energy and the kinetic energy of independent electrons by two dynamical effects:

- *exchange*: due to the Pauli exclusion principle, electrons of the same spin avoid each other in \mathbf{r} -space. This interaction is essentially short-ranged and therefore prevails at high densities ($r_s \lesssim 20$). It favors alignment of the electron spins, thereby lowering their electrostatic energy at expense of their kinetic energy.

- *correlation*: due to the Coulomb repulsion, electrons avoid each other in \mathbf{r} -space, irrespective of their spin. This interaction is essentially long-ranged and prevails at low densities.

The HK variational theorem ensures now that $E_{V^{ext}}$ is stationary for small variations around the minimum spin densities (n_+, n_-) that preserve N_{el} :

$$0 = \frac{\delta E_{V^{ext}}[n_+, n_-]}{\delta n_\sigma(\mathbf{r})} = \frac{\delta T_0[n_+, n_-]}{\delta n_\sigma(\mathbf{r})} + V^H[n](\mathbf{r}) + \frac{\delta E_{xc}[n_+, n_-]}{\delta n_\sigma(\mathbf{r})} + V^{ext}(\mathbf{r}).$$

Since the corresponding variation applied to E_V of the postulated non-interacting system yields at the same spin densities

$$0 = \frac{\delta E_V[n_+, n_-]}{\delta n_\sigma(\mathbf{r})} = \frac{\delta T_0[n_+, n_-]}{\delta n_\sigma(\mathbf{r})} + V_\sigma(\mathbf{r}).$$

Therefore, if the functional derivative $\delta T_0[n_+, n_-]/\delta n_\sigma(\mathbf{r})$ exists, the postulated potential V of the auxiliary non-interacting system also exists and has the form

$$V_\sigma(\mathbf{r}) = V^H[n](\mathbf{r}) + V_\sigma^{xc}[n_+, n_-](\mathbf{r}) + V^{ext}(\mathbf{r}), \quad (2.10)$$

where $V_\sigma^{xc}[n_+, n_-](\mathbf{r}) := \delta E_{xc}[n_+, n_-]/\delta n_\sigma(\mathbf{r})$ denotes the exchange-correlation potential. The single-particle orbitals ϕ_n that enter the spin densities can be determined by solving the set of Schrödinger equations

$$h_\sigma \phi_n(\mathbf{r}) = \varepsilon_n \phi_n(\mathbf{r}), \quad h_\sigma = -\frac{\nabla^2}{2} + V_\sigma(\mathbf{r}), \quad n \in \mathcal{I}_\sigma, \quad (2.11)$$

that are connected with the independent-particle Hamiltonians h_σ with potential (2.10). For each spin $\varepsilon_n \leq \varepsilon_m$ for $n < m$. A slight amendment must be made to ensure mathematical rigor: the functional differentiability of T_0 is guaranteed only for its extension³ to a wider class of densities than those given by (2.7), allowing for fractional occupation of the orthonormal one-particle orbitals ϕ_n (see [Jan78, DG90])

$$n_\sigma(\mathbf{r}) = \sum_{n \in \mathcal{I}_\sigma} f_n |\phi_n(\mathbf{r})|^2 \quad \sum_n f_n = N_{el}. \quad (2.12)$$

The occupation numbers (apart from $f_n \in [0, 1]$, as is necessary for fermions) follow from the requirement that the GS spin densities shall minimize the Energy functional E_V of the auxiliary non-interacting system with – as inspection shows – total energy $\sum_n f_n \varepsilon_n$. Consequently, in the case of a GS, the f_n must satisfy for each spin σ separately

$$\forall n \in \mathcal{I}_\sigma : \quad f_n \in \begin{cases} \{1\} & \text{if } \varepsilon_n < \mu_\sigma \\ [0, 1] & \text{if } \varepsilon_n = \mu_\sigma \\ \{0\} & \text{if } \varepsilon_n > \mu_\sigma \end{cases} \quad \mu_\sigma = \max_{n \in \mathcal{I}_\sigma} \{\varepsilon_n | f_n \neq 0\} \quad (2.13)$$

³The only modification to the definition of T_0 as given in (2.9) is that the sum over n has to be replaced by $\sum_n f_n \dots$

As originally proposed by Kohn and Sham, the problem of determination of the BO potential is thus converted into the solution of (with regard to $V_{\sigma}^{xc}[n_+, n_-]$) self-consistent eigenvalue equations, the KS equations.

It is by no means necessary to go this byway in real calculations, since the KS equations served only as a means to establish the existence of the auxiliary non-interacting system. Having thus verified that it is permissible to use $F_0[n_+, n_-]$ as universal DF to determine the electronic GS, the BO potential may be obtained alternatively by direct minimization:

$$e_0(\{\mathbf{R}_I\}) = \min_{n_{\sigma}(\mathbf{r}) = \sum_{n \in \mathcal{I}_{\sigma}} f_n |\phi_n(\mathbf{r})|^2} \left\{ F_0[n_+, n_-] + \int d\mathbf{r} V^{ext}(\mathbf{r}) n(\mathbf{r}) \right\} + \frac{1}{2} \sum_{I \neq J} \frac{Z_I Z_J}{|\mathbf{R}_I - \mathbf{R}_J|}$$

among all non-interacting N_{el} -particle spin densities. Combining the constrained minimization $\{\phi_i\} \rightarrow (n_+, n_-)$ and the subsequent minimization with respect to the (n_+, n_-) into one minimization with respect to the electronic degrees of freedom that preserves the orthonormalization of the orbitals, we arrive at

$$e_0(\{\mathbf{R}_I\}) = \min_{\{\phi_n\}} E[\{\phi_n\}, \{\mathbf{R}_I\}] + \text{constraints},$$

$$E[\{\phi_n\}, \{\mathbf{R}_I\}] = \sum_n f_n \int d\mathbf{r} \phi_n^*(\mathbf{r}) \left(-\frac{\nabla^2}{2} \right) \phi_n(\mathbf{r}) + \frac{1}{2} \int d\mathbf{r} V^H[n](\mathbf{r}) n(\mathbf{r}) + E_{xc}[n_+, n_-] + \int d\mathbf{r} V^{ext}(\mathbf{r}) n(\mathbf{r}) + \frac{1}{2} \sum_{I \neq J} \frac{Z_I Z_J}{|\mathbf{R}_I - \mathbf{R}_J|}. \quad (2.14)$$

Hence, within this formulation, the determination of $e_0(\{\mathbf{R}_I\})$ may be viewed as an optimization problem, with a variety of mathematical and physical methods at our disposal for its solution (see section 2.1.3). This approach was originally proposed by Car and Parrinello [CP85] and is completely equivalent to the solution of the KS equations (2.11), as will be demonstrated in the following.

Convergence to KS eigenstates The electronic solutions are determined from the requirement that they make the functional (2.14) stationary. If we incorporate the constraints via Lagrange multipliers, the stationarity condition reads

$$0 = \delta \left\{ E[\{\phi_n\}, \{\mathbf{R}_I\}] - \sum_{n,m}^{occ} \Lambda_{n,m} \left(\int d\mathbf{r} \phi_n^*(\mathbf{r}) \phi_m(\mathbf{r}) - \delta_{n,m} \right) \right\},$$

or, since $\delta E / \delta \phi_n^*(\mathbf{r}) = f_n h_{\sigma} \phi_n(\mathbf{r})$ for $n \in \mathcal{I}_{\sigma}$

$$f_n h_{\sigma} \phi_n(\mathbf{r}) = \sum_m^{occ} \Lambda_{n,m} \phi_m(\mathbf{r}), \quad n, m \in \mathcal{I}_{\sigma}. \quad (2.15)$$

Note that the orbitals of different spin are not constrained to be orthogonal to each other, since they arise from different Hamiltonians h_σ and the corresponding $\Lambda_{n,m}$ are zero. Since the matrix of the Lagrange multipliers is Hermitian⁴, Eq. 2.15 is equivalent to the KS equation to within a unitary transform, if the occupation numbers are equal. In the case that $f_n \neq f_l$ for some n, l , this is not so obvious. Multiplying (2.15) by ϕ_l^* and integrating over \mathbf{r} yields

$$f_n \langle \phi_l | h_\sigma | \phi_n \rangle = \Lambda_{n,l}.$$

Subtracting the corresponding equation for l and n exchanged, we arrive at

$$(f_n - f_l) \langle \phi_l | h_\sigma | \phi_n \rangle = 0,$$

i.e., $\langle \phi_l | h_\sigma | \phi_n \rangle$ and $\Lambda_{l,n}$ must vanish if $f_l \neq f_n$. This means that the matrices are block diagonal with respect to subsets of orbitals with different occupations and the previous arguments can be applied to each of the blocks. Therefore, the minimization of (2.14) is always equivalent to the solution of the KS equations (2.11) for the lowest occupied states.

On the other hand, it is well known that numerical errors introduced during the calculations may spoil the convergence to eigenstates whenever two states of unequal occupation are separated by a small energy gap ([GHMC94]). As far as microclusters are concerned, unequal occupation numbers have to be considered only in cases of degenerate electronic states in molecules of high symmetry. If the convergence to eigenstates does fail, the symmetry of the orbitals, which can be monitored during the iterations, will be destroyed. If such a situation arises, it is sufficient to enforce the correct symmetry on the numerical orbitals to overcome this difficulty.

Excited States Although we have focused in this section on the BO potential in the GS ψ_0 of the electrons, neither the BO approximation (see section 2.1.1) nor the spin-density formalism is restricted to this case. There are basically two classes of methods for calculating excitation energies within DFT. A possible calculation of the excitation spectrum might start from local density approximation results for the ground-state and then compute the quasiparticle (QP) energies (real parts of E_i below) of the system within many-body perturbation theory. This is usually done [HL85b, SL93] within Hedin's GW approximation [Hed65] to the nonlocal energy-dependent electronic self-energy Σ , which plays in the Dyson equation for the QPs ϕ_i of the system [HL69, JG89]

$$\left(-\frac{\nabla^2}{2} + V^H(\mathbf{r}) + V^{ext}(\mathbf{r}) - E_i \right) \phi_i(\mathbf{r}) + \int d\mathbf{r}' \Sigma(\mathbf{r}, \mathbf{r}', E_i) \phi_i(\mathbf{r}') = 0$$

a similar role as the exchange-correlation potential in the Kohn-Sham equations of density-functional theory (the expressions for the remaining terms are defined in chapter 2). The

⁴For complex orbitals, the constraints take the explicit form $\sum_{n,m}^{occ} (\lambda_{n,m} \langle \phi_n | \phi_m \rangle + \lambda_{n,m}^* \langle \phi_m | \phi_n \rangle)$. Exchanging the indices in the second sum, we arrive at $\sum_{n,m}^{occ} (\lambda_{n,m} + \lambda_{m,n}^*) \langle \phi_n | \phi_m \rangle$ and the expression in brackets may be understood as the definition of $\Lambda_{n,m}$ which is obviously Hermitian.

GW approximation consists in replacing the self-energy by a convolution

$$\Sigma(\mathbf{r}, \mathbf{r}', \omega) = \lim_{\delta \rightarrow 0^+} \frac{i}{2\pi} \int d\omega' G(\mathbf{r}, \mathbf{r}', \omega + \omega') W(\mathbf{r}, \mathbf{r}', \omega') e^{\delta\omega'}$$

of the one-electron Green's function G and the dynamically screened Coulomb interaction W of the electrons. Actual self-consistent computations of QP energies can be performed in first-order perturbation theory in $\Sigma(E) - V_{xc}$ on real physical systems with the local density approximation results of density-functional theory for G and W [HL85b, GN89]. Despite the approximations involved in this procedure, the calculation of W and G requires summations over a large number of empty Kohn-Sham states [HL69, SZLC89], which has restricted the use of this scheme to relatively simple systems, as for example to Na and K clusters only within the spherical jellium model [SZLC89]. Without doubt, an application to systems as complex as these considered here would be beyond the scope of this method.

Another method for calculating excitation energies within DFT is the Δ SCF scheme that uses no approximations beyond LSDA. Δ SCF refers to a procedure, where the GS scheme is applied to both the excited state and the GS, and the energy difference is calculated. Excitation energies are then given by the total energy differences between self-consistent-field (SCF) calculations for both the excited state and the GS. This method rests on an extension of the GS formalism to the lowest excited state of a given symmetry that has been proven by Gunnarsson and Lundqvist [GL76]. In fact, all statements of the preceding section can be recovered for the corresponding $e_n(\{\mathbf{R}_I\})$, $n > 0$, with the only exception that E_{xc} and consequently V_{xc} now depend formally on the symmetry label. But since the exact form of the corresponding quantities even for the GS is unknown, we are reduced to use a single approximate functional in all cases and the symmetry dependence of a state only enters via the prescription for constructing the charge and spin densities for that state.

As von Barth [vB79] has demonstrated on multiplet energies of atoms, the naïve use of the GS functional for lowest excited states of a given symmetry leads to erroneous results if these states cannot be represented by single Slater determinants. Inverting the relation between multiplet states and their determinantal constituents, such Slater determinants may be viewed as special (i.e., noninteracting) cases of what von Barth terms "mixed-symmetry states" (MS), i.e., linear combinations of states of pure symmetry. Although MS states are in general not eigenstates of the Hamiltonian, von Barth was able to generalize the Hohenberg-Kohn theorem to the state of lowest energy (i.e., the state with the lowest energy expectation value) of a *well-defined* mixture of symmetries S_i

$$|\Psi_{MS}\rangle = \sum_{i=1}^m \alpha_i |S_i, 0\rangle, \quad (2.16)$$

where $|S_i, 0\rangle$ are (non-degenerate) eigenstates of lowest energy with symmetry S_i . If the α_i are chosen so that $|\Psi_{MS}\rangle$ reduces to a single determinant in the noninteracting case, its density and energy expectation value may be found by solution of the corresponding KS

equations. As follows from eq. 2.16, every determinantal state KS energy E_{MS} gained this way gives an estimate for a certain linear combination of term values

$$E_{MS} = \sum_{i=1}^m |\alpha_i|^2 E(S_i).$$

In general, although some of the equations might be identical, this set of linear equations will be overdetermined and so the equations should be solved, on recommendation of v. Barth, by a min-max fit. It may also happen that most or all determinants are degenerate (at least in LSDA) and we may not obtain enough different energy terms to solve the equations. Examples for both cases and a further discussion may be found in appendix B.

Local and Semi-local Approximations to E_{xc} It is established tradition in many branches of theoretical physics to study a simple (i.e., soluble) model system exhibiting the same essential features as the class of physical problems in question. Example are the harmonic oscillator in quantum mechanics and the Ising model in the theory of phase transitions. In DF theory (as in the theory of many-fermion systems) the uniform (spin polarized) electron gas plays a similar role, because it is the only many-fermion system, for which E_{xc} is known, at least to numerical accuracy. The results of extensive, high precision⁵ quantum Monte Carlo (QMC) simulations [Cep78, CA80, OB94] gave rise to analytic interpolation formulas [VWN80, PZ80, OB94] for $\epsilon_{xc}(n_+, n_-)$, the exchange-correlation energy per electron in the GS at constant spin densities n_+, n_- . The high-density limit, ($r_s \rightarrow 0$) which is known exactly [GMB57], is reproduced by these parametrizations. The famous local spin-density approximation (LSDA) consists in adopting these results to arbitrary inhomogeneous electron systems by the substitution

$$E_{xc}[n_+, n_-] =: \int d\mathbf{r} n(\mathbf{r}) \epsilon_{xc}(n_+, n_-) \Big|_{\substack{n_+(\mathbf{r}) \\ n_-(\mathbf{r})}} \quad (2.17)$$

where $\epsilon_{xc}(n_+, n_-)$ is evaluated at the local spin densities $n_+(\mathbf{r}), n_-(\mathbf{r})$. In this work, the formulas given by [VWN80] and [PZ80] have been used.

As might be expected from the somewhat uncontrolled character of this approximation, it suffers from several problems, despite its ability to describe the trends of many physical properties reliably, as documented by a large and growing body of computations. Among the problems that apply to finite systems, like molecules and clusters, are the following:

- Cohesive energies are often overestimated.
- Equilibrium bond distances are systematically overestimated and vibration frequencies are often too large.
- Negatively charged systems like H^- , O^- , F^- , Ca^- , S^- , ... are sometimes predicted to be unstable, contrary to experiment.

⁵The estimated error bars for the correlation energy per particle in the regime of valence electron densities $0.8 \leq r_s \leq 10$ are ~ 0.01 eV [OB94].

It seems to be natural to assume that the inclusion of gradients of the (spin-) densities into the DF would result in an improved description of exchange and correlation for inhomogeneous electron systems. However, early systematic attempts to develop formal gradient expansions by perturbing a uniform electron gas with slowly-varying potentials have generally been disappointing in applications to realistic systems [JG89]. Semiphenomenological gradient functionals, called “generalized gradient approximations” (GGA’s), of the form

$$E_{xc}[n_+, n_-] =: \int d\mathbf{r} n(\mathbf{r}) f_{xc}(n_+(\mathbf{r}), n_-(\mathbf{r}), |\nabla n_+(\mathbf{r})|, |\nabla n_-(\mathbf{r})|) \quad (2.18)$$

seem to be successful in a number of cases [LM83]. The fact the gradient terms enter the functional only by their modulus follows from the requirement, that E_{xc} must be invariant under rotations, for arbitrary, say spherically symmetrical $n_\sigma(\mathbf{r})$, since it is universal (independent of V^{ext}). The GGA’s of Perdew and Wang [PY86, Per86], [Per91, PCV+92] and Becke and Perdew (BP) (the exchange part is taken from [Bec88], the correlation part from [Per86]) have been studied in a range of contexts, e.g., hydrogen bonded systems [LCP92], cohesive energy and equilibrium distances in solids [PCV+92, GEZ+92], simulation of clusters [DBB92, BJ94] and molecules [Bec92, JGP92, OB91]. We have implemented and successfully tested a spin-dependent BP GGA in the formulation of [WB94], which is specially suited for the use in a CP scheme, but an intended application to clusters of carbon could not be completed during the course of this work and results are left to a future publication.

2.1.3 Electronic Structure Optimization

The direct iterative minimization of the KS energy functional (2.14) with respect to the electronic degrees of freedom would be superior to diagonalizing the KS Hamiltonian self-consistently, since

- self-consistent diagonalization can lead to instabilities during the iteration, if the density and therefore the potentials change too much from step to step
- in self-consistent diagonalization, one diagonalizes the whole Hamiltonian matrix (which has dimension $N \times N$ if the basis set has N elements) and obtains all N eigenvectors. This is in contrast to iterative minimization, where only the occupied states are calculated and stored, thus rendering feasible the treatment of larger and more complex systems.

As experience has shown, only *local* optimization methods are needed that lower the KS energy functional at every step of the iteration to reach the closest minimum nearby. This is sufficient, because, if the nuclei are kept fixed, only a single minimum for the electrons is encountered. Since a local minimization is computational less demanding than a global one, there exists a variety of traditional methods. Whereas the computation of the first derivatives $\delta E[\{\phi_n\}, \{\mathbf{R}_I\}]/\delta\phi_m$ of the KS functional is relatively straightforward, the requirement of memory and computational time to build up the Hessian matrix $(\delta^2 E/\delta\phi_n\delta\phi_m)_{nm}$

seems to be prohibitive, at least for a high-dimensional basis set such as plane waves. So we are left with methods that require the computation of the gradient alone, among which the quasi-Newton methods, as typified by the Davidson-Fletcher-Powell algorithm or the Broyden-Fletcher-Goldfarb-Shanno algorithm [PTVF92], can be ruled out here owing to their large storage requirement of order N^2 , where N is the dimension of the basis, to build up an approximation to the inverse Hessian matrix. Nevertheless, they show the desirable feature of superlinear⁶ convergence (see [Fle87]).

Here we confine ourselves to the steepest descent (SD) and the conjugate gradient (CG) methods that require storage of the gradients only. These methods may be explained using an \mathbb{R} -valued function $f(\mathbf{x})$, $\mathbf{x} \in \mathbb{R}^N$ [PTA92]. Close to a local minimum point \mathbf{x}^* , f may be approximated by its Taylor series truncated after the quadratic terms

$$f(\mathbf{x}) = c + \frac{1}{2}(\mathbf{x} - \mathbf{x}^*) \cdot A \cdot (\mathbf{x} - \mathbf{x}^*) + o((\mathbf{x} - \mathbf{x}^*)^2),$$

where

$$c = f(\mathbf{x}^*) \quad A_{ij} = \left. \frac{\partial^2 f}{\partial x_i \partial x_j} \right|_{\mathbf{x}^*}$$

with a symmetric and positive definite Hessian matrix A . Starting from a point \mathbf{x}^1 , the algorithms generate iteratively a sequence of points $(\mathbf{x}^i)_{i \in \mathbb{N}}$ that converges to \mathbf{x}^* [Fle87]. They do so by providing at every point \mathbf{x}^i a search direction \mathbf{d}^i along which the value of the function f is reduced. The next point $\mathbf{x}^{i+1} = \mathbf{x}^i + \lambda^i \mathbf{d}^i$ may be determined by line minimization

$$\begin{aligned} \frac{\partial}{\partial \lambda} f(\mathbf{x}^i + \lambda \mathbf{d}^i) \Big|_{\lambda^i} &\stackrel{!}{=} 0 = \nabla f(\mathbf{x}^i + \lambda^i \mathbf{d}^i) \cdot \mathbf{d}^i \\ &=: \mathbf{g}^{i+1} \cdot \mathbf{d}^i \end{aligned}$$

where the gradient at the point $i + 1$ has been termed \mathbf{g}^{i+1} . Resolving the last equation for λ^i , we find that

$$\lambda^i = - \frac{\mathbf{g}^i \cdot \mathbf{d}^i}{\mathbf{d}^i \cdot A \cdot \mathbf{d}^i}. \quad (2.19)$$

This means that the line minimization contains information about the Hessian matrix that can (and will) be exploited in the following. In the absence of any further information about f but its gradient at \mathbf{x}^{i+1} , the optimum search direction would be the SD direction, i.e.,

$$\mathbf{d}^{i+1} = -\mathbf{g}^{i+1},$$

because it is the direction along which f decreases most rapidly *local* to \mathbf{x}^{i+1} . SD can be shown to be globally convergent, but it exhibits only poor linear convergence [Fle87] (i.e., $|\mathbf{x}^{i+1} - \mathbf{x}^*|/|\mathbf{x}^i - \mathbf{x}^*| \leq \text{const.}$ for all i).

⁶In the terminology explained in the following, this means that $|\mathbf{x}(i+1) - \mathbf{x}^*|/|\mathbf{x}^i - \mathbf{x}^*| \rightarrow 0$, for $i \rightarrow \infty$.

But this is only the initial direction \mathbf{d}^1 of the CG method. For the following directions \mathbf{d}^{i+1} , $i \geq 1$, CG exploits the (nonlocal) information about f contained in all previous line minimizations. It does so by the further requirement that the overall decrease of f with respect to all the line searches that lead to the point $\mathbf{x}^{i+2} = \mathbf{x}^1 + \sum_{k=1}^{i+1} \lambda^k \mathbf{d}^k$, $i \geq 1$, shall be extremal, i.e.

$$\begin{aligned} \forall j \leq i+1: \quad 0 &\stackrel{!}{=} \frac{\partial}{\partial \lambda^j} f(\mathbf{x}^1 + \sum_{k=1}^{i+1} \lambda^k \mathbf{d}^k) \\ &= (\mathbf{x}^1 - \mathbf{x}^* + \sum_{k=1}^{i+1} \lambda^k \mathbf{d}^k) \cdot A \cdot \mathbf{d}^j \end{aligned}$$

Subtracting the corresponding conditions at \mathbf{x}^{i+1}

$$\forall j \leq i: \quad 0 \stackrel{!}{=} (\mathbf{x}^1 - \mathbf{x}^* + \sum_{k=1}^i \lambda^k \mathbf{d}^k) \cdot A \cdot \mathbf{d}^j,$$

we are left with the equations

$$\begin{aligned} \forall j \leq i: \quad 0 &\stackrel{!}{=} \mathbf{d}^{i+1} \cdot A \cdot \mathbf{d}^j \\ \Rightarrow \forall j \neq i: \quad 0 &\stackrel{!}{=} \mathbf{d}^i \cdot A \cdot \mathbf{d}^j, \end{aligned} \quad (2.20)$$

since A is symmetric. This is the condition that the directions \mathbf{d}^i be conjugate to each other. Since (2.20) implies that the search directions \mathbf{d}^i form a linear independent set, N of them would be sufficient to span the whole vector space and to determine the minimum, if f would be an exactly quadratic form. Because this property, known as quadratic termination, has been derived for quadratic forms only, it can not be expected to hold in the case of an arbitrary function f , where it is recommended to reset \mathbf{d}^{i+1} periodically to $-\mathbf{g}^{i+1}$. In this case, N -step superlinear convergence ($|\mathbf{x}(N+i) - \mathbf{x}^*| / |\mathbf{x}^i - \mathbf{x}^*| \rightarrow 0$, for $i \rightarrow \infty$) can be guaranteed [Fle87].

Although it might seem as if (2.20) would require the knowledge of the Hessian matrix, it is possible to eliminate A from the expressions for the \mathbf{d}^i by the assumption

$$\mathbf{d}^{i+1} = -\mathbf{g}^{i+1} + \gamma^i \mathbf{d}^i. \quad (2.21)$$

Inserting this into (2.19) and using the fact that the iterated gradients are mutually orthogonal, which may be concluded inductively from (2.20), one finds that

$$\gamma^i = \frac{\mathbf{g}^{i+1} \cdot \mathbf{g}^{i+1}}{\mathbf{g}^i \cdot \mathbf{g}^i}.$$

This is the Fletcher-Reeves formulation of the CG method, that has been implemented in the present work. The determination of the CG at any step requires the previous CG and the present SD direction. Both of these constitute an array of the same size as the vector \mathbf{x}^i itself, so that the total storage requirement is of order $3N$.

It is useful to examine (2.20) a little closer in order to understand why CG is so much better than SD in minimizing a function. The easiest way to do so is to expand any given

direction \mathbf{d}^i into the eigenvectors of the Hessian matrix A (which form in fact an orthogonal basis of the N -dimensional space):

$$\mathbf{d}^i = \sum_{k=1}^N \delta_k \mathbf{a}_k$$

If \mathbf{d}^i is multiplied by A , the directions with the largest eigenvalues α_k of A will dominate in the resulting vector. One could therefore say, that A turns \mathbf{d}^i into these directions, which

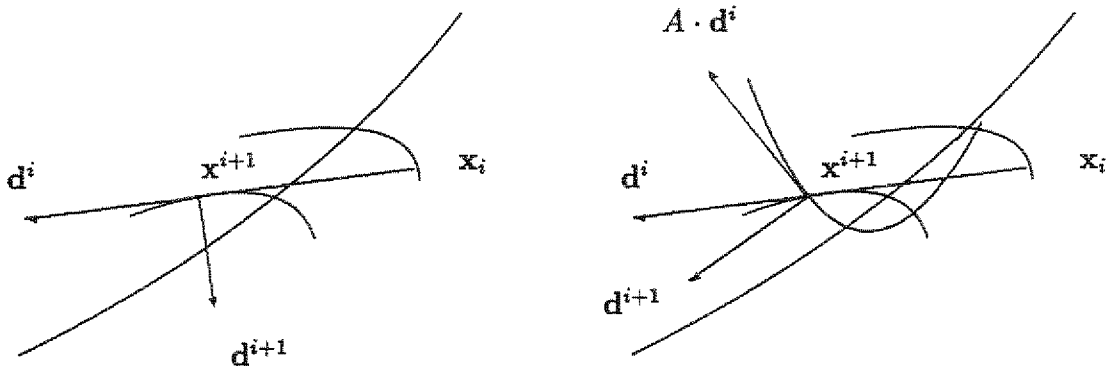


Figure 2.1: Schematic comparison between SD (left) and CG (right)

are the directions of strongest curvature of f . Choosing the new direction orthogonal onto $A \cdot \mathbf{d}^i$ means that the following step will proceed orthogonally to a direction of high curvature. Consequently, subsequent line minimizations are performed on the average along directions of successively lower curvature of f . This is particularly advantageous if the minimum \mathbf{x}^* lies in a long narrow valley such as illustrated in Fig. (2.1). If the initial SD vector does not happen to be at right angles to the axis of the valley, successive vectors will point across rather than along the valley, resulting in a large number of iterations. On the other hand, the second CG vector already points along the bottom of the valley, because this is the direction of lowest curvature, and the need for iterations will be greatly reduced.

As [ŠCPB89] have shown, the CG method can provide an efficient tool for locating the minimum of the KS energy functional with respect to electronic degrees of freedom, too. The relations derived above translate with only a few amendments. The KS energy functional E takes the place of f and the vector \mathbf{x}^i is replaced by the wavefunctions $\{\phi_n^i\}$. The occupied KS orbitals may then be updated by the prescription [ŠCPB89]

$$g_n^i(\mathbf{r}) = \left. \frac{\delta E[\{\phi_n\}, \{\mathbf{R}_I\}]}{\delta \phi_n^*(\mathbf{r})} \right|_{\phi_n^i} + \text{constraints}$$

$$\begin{aligned}\gamma^i &= \frac{\sum_n f_n \int d\mathbf{r} |g_n^{i+1}(\mathbf{r})|^2}{\sum_n f_n \int d\mathbf{r} |g_n^i(\mathbf{r})|^2} \\ d_n^{i+1}(\mathbf{r}) &= -g_n^{i+1}(\mathbf{r}) + \gamma^i d_n^i(\mathbf{r}) \\ \phi_n^{i+1}(\mathbf{r}) &= \phi_n^i(\mathbf{r}) + \lambda^i d_n^i(\mathbf{r}),\end{aligned}$$

where the constrained functional derivative preserves the orthonormality of the orbitals. The constraints may be imposed by application of the Gram-Schmidt orthogonalization at every step. The SD step can be recovered by putting $\gamma^i =: 0$ in the equations above. Furthermore, in the case of SD, the line minimization is in practice replaced by the choice of a fixed reduced "time step" $\Delta t/\mu$ instead of λ^i , that governs the convergence rate of the scheme (μ is a fictitious electron mass).

2.2 Born-Oppenheimer Dynamics

2.2.1 Simulated Annealing and Molecular Dynamics

With the advent of powerful supercomputers in recent decades, research interests have shifted towards developing efficient techniques for finding absolute minimum values of a function of very many variables. In a situation where there is a large number N of minima, e.g., the number of different isomers that is consistent with a chemical formula [HM83], none of the exact methods known require a computing effort that increases as any power of N [WV85] (“NP-hard” problems [GJ79]) for determining the optimal one. Simulated annealing has been successfully applied to this class of problems, such as the “traveling salesman problem”, as a tool to find nearly optimal solutions in which the computational effort scales as a small power of N [KGV83]. Simulated annealing adopts a statistical mechanics approach. Its original formulation is the Metropolis Monte Carlo algorithm [MRR⁺53], which generates iteratively new coordinates to lower the potential function $e(\{\mathbf{R}_I\})$, but avoids getting stuck in local minima by permitting occasional “uphill moves”. This means that $\Delta E = e(\{\mathbf{R}_I(t)\}) - e(\{\mathbf{R}_I(t - \Delta t)\}) > 0$ is also accepted with probability $p(\Delta E) = \exp(-\Delta E/k_B T)$. Initially, the “temperature” T is taken to be high compared with the energy barriers separating the competing minima. As the temperature is gradually lowered, it is highly probable that the distribution of the variables becomes progressively concentrated in the energetically favorable regions.

Because the evaluation of the BO potential for arbitrary, randomly generated $\{\mathbf{R}_I\}$ is very demanding (see section 2.1.3), a direct application of this algorithm to our problem is out of question. Instead, physically reasonable configurations are generated if one integrates numerically Newton’s equations of motion derived from the BO Hamiltonian (2.3)

$$\dot{\mathbf{P}}_I = -\frac{\partial e_0}{\partial \mathbf{R}_I}(\{\mathbf{R}_J\}), \quad (2.22)$$

by use of the Verlet algorithm (see below) or any other finite difference method, as is done by the constant-energy (the total energy corresponding to (2.3) is conserved) molecular dynamics (MD) simulations [AT87]. The instantaneous and mean temperature of the simulations may be calculated using the equipartition theorem and may be reduced from time to time by rescaling the atomic momenta. This combination of simulated annealing and MD is sometimes referred to as “dynamical simulated annealing”.

Special care must be taken when calculating the forces, since according to the Hellmann-Feynman theorem, the atomic forces can only be calculated in a straightforward way by differentiating the $\{\mathbf{R}_I\}$ -dependent potentials in (2.14), if the $\{\phi_n\}$ are *very* close to the exact eigenstates of (2.11). This requires expensive CG minimizations at every time step, as the forces will otherwise be in error and the total energy of the nuclei will not be conserved due to a steady dissipation into the electronic degrees of freedom [RM90]. On the other hand, if the atomic forces are calculated to a high precision, comparatively large time steps can be chosen for the dynamics and there are cases, especially in dealing with metallic systems, where this procedure, called “conjugate-gradient molecular dynamics”

[APJ92, PTA92] is appropriate.

Since the computation of the forces from the true BO potential is numerically demanding, most early and many current conventional MD simulations resort to approximate parameterized interaction potentials between the particles that are fitted to a given set of experimental and/or theoretically calculated data. These potentials are functions of interparticle coordinates and many include pairwise, three-body and higher-order terms,

$$e_0(\{\mathbf{R}_I\}) \approx \sum_{I<J} V_2(\mathbf{R}_I - \mathbf{R}_J) + \sum_{I<J<K} V_3(\mathbf{R}_I, \mathbf{R}_J, \mathbf{R}_K) + \dots$$

whose functional forms are related to the nature of interactions and bonding in the material under investigation (see, e.g., [SW85, BH85]). The applicability and predictive power of this approach is obviously limited in circumstances where the system evolves into regions of phase space not covered by the fitted data. For example, the strength of the covalent bond depends on the local environment, consequently potentials fitted to the bulk may be inadequate for systems such as surfaces or clusters with lower coordination. Moreover, serious difficulties are encountered in situations where electronic rearrangements occur, such as in changes in the nature of bonding (e.g., a transition from covalent to metallic behaviour as occurring in silicon upon transformation from the solid to the liquid state).

2.2.2 The Car-Parrinello MD

Car and Parrinello [CP85] have developed an alternative way to circumvent costly electronic minimizations at every time step of the MD without sacrificing the universality of the original BO formulation. In their approach, the determination of the potentials is an integral part of the simulation rather than a separate preliminary step as in conventional MD simulations. They achieved this by introducing a fictitious classical kinetic energy of the KS orbitals analogous to that of the atomic degrees of freedom and by replacing the BO potential by the KS energy functional (2.14) in the energy function corresponding to (2.3):

$$h(\{\phi_n\}, \{\dot{\phi}_n\}, \{\mathbf{R}_I\}, \{\dot{\mathbf{R}}_I\}) = \sum_n^{\infty} \int d\mathbf{r} \mu |\dot{\phi}_n(\mathbf{r})|^2 + \frac{1}{2} \sum_I M_I \dot{\mathbf{R}}_I^2 + E[\{\phi_n\}, \{\mathbf{R}_I\}]. \quad (2.23)$$

This means that the orbitals no longer evolve parametrically as in (2.22), but serve as additional degrees of freedom subjected to a classical dynamical evolution. If the electrons are initially in their GS and the fictitious electronic mass μ is small enough, the deviations from the BO Hamiltonian (2.14) and from adiabatic dynamics will be small, provided that the energy transfer between the atomic and electronic degrees of freedom is insignificant during the time scale of the simulations (see below). The advantage of this formulation is that the electronic energy need not be minimized for each atomic position, with consequent savings in time. The atomic and electronic “trajectories” are then integrated simultaneously under the (holonomic) constraints of orthonormalization, which are incorporated most easily into

the Lagrangian formulation. The Lagrangian corresponding to (2.23) reads

$$\begin{aligned} \mathcal{L}(\{\phi_n\}, \{\dot{\phi}_n\}, \{\mathbf{R}_I\}, \{\dot{\mathbf{R}}_I\}) &= \sum_n^{\text{occ}} \int d\mathbf{r} \mu |\dot{\phi}_n(\mathbf{r})|^2 + \frac{1}{2} \sum_I M_I \dot{\mathbf{R}}_I^2 - E[\{\phi_n\}, \{\mathbf{R}_I\}] \\ &\quad + \sum_{n,m}^{\text{occ}} \Lambda_{n,m} \left(\int d\mathbf{r} \phi_n^*(\mathbf{r}) \phi_m(\mathbf{r}) - \delta_{n,m} \right) \end{aligned}$$

and the Euler-Lagrange equations derived from it are

$$\begin{aligned} M_I \ddot{\mathbf{R}}_I &= - \frac{\partial E}{\partial \mathbf{R}_I} \\ \mu \ddot{\phi}_n(\mathbf{r}, t) &= - \frac{\delta E}{\delta \phi_n^*(\mathbf{r}, t)} + \sum_m^{\text{occ}} \Lambda_{n,m} \phi_m(\mathbf{r}, t), \quad \text{where} \\ \frac{\delta E}{\delta \phi_n^*(\mathbf{r}, t)} &= f_n h_\sigma \phi_n(\mathbf{r}, t), \quad n \in \mathcal{I}_\sigma, \end{aligned} \quad (2.24)$$

and h_σ is the KS Hamiltonian introduced in (2.11). The Lagrange multipliers can be determined by differentiating the constraint condition for orbitals n and m twice with respect to the time and inserting the equations of motion (2.24). The resulting equations show that Λ can be chosen to be Hermitian, so that one obtains the expression

$$\Lambda_{m,n} = \begin{cases} (f_n + f_m)/2 \langle \phi_n | h_\sigma | \phi_m \rangle - \mu \langle \dot{\phi}_n | \dot{\phi}_m \rangle & \text{if } n, m \in \mathcal{I}_\sigma, \\ 0 & \text{if } n \in \mathcal{I}_\sigma, m \in \mathcal{I}_{\sigma'}, \sigma \neq \sigma' \end{cases} \quad (2.25)$$

Note again that the ϕ_n of different spin are not constrained to be mutually orthogonal. If the equations of motion would be integrated analytically, (2.25) would yield the appropriate multipliers at any time, provided that the orbitals had been orthogonal at some initial time $t = t_0$. However, the numerical integration is performed using the Verlet algorithm

$$\begin{aligned} \phi_n(\mathbf{r}, t + \Delta t) &= -\phi_n(\mathbf{r}, t - \Delta t) + 2\phi_n(\mathbf{r}, t) - \frac{(\Delta t)^2}{\mu} f_n h_\sigma \phi_n(\mathbf{r}, t) + \sum_m^{\text{occ}} \frac{(\Delta t)^2}{\mu} \Lambda_{n,m} \phi_m(\mathbf{r}, t) \\ &=: \bar{\phi}_n(\mathbf{r}, t + \Delta t) + \sum_m^{\text{occ}} X_{n,m} \phi_m(\mathbf{r}, t), \end{aligned} \quad (2.26)$$

where n and m have the same spin ($n, m \in \mathcal{I}_\sigma$) and $X_{n,m} := \Lambda_{n,m} (\Delta t)^2 / \mu$. This introduces errors of the order $O(\Delta t^4)$ in the numerical solutions and (2.25) is no longer valid for them. But the appropriate Lagrange multipliers may be derived at each time step [RCB77] from the requirement

$$\begin{aligned} \delta_{n,m} &\stackrel{!}{=} \langle \phi_n(\mathbf{r}, t + \Delta t) | \phi_m(\mathbf{r}, t + \Delta t) \rangle \\ &= \underbrace{\langle \bar{\phi}_n(\mathbf{r}, t + \Delta t) | \bar{\phi}_m(\mathbf{r}, t + \Delta t) \rangle}_{=: A_{n,m}} + \sum_l^{\text{occ}} X_{n,l} \underbrace{\langle \phi_l(\mathbf{r}, t) | \bar{\phi}_m(\mathbf{r}, t + \Delta t) \rangle}_{=: B_{l,m}} \end{aligned}$$

$$\begin{aligned}
& + \sum_l^{\text{occ}} X_{m,l}^* \langle \bar{\phi}_n(\mathbf{r}, t + \Delta t) | \phi_l(\mathbf{r}, t) \rangle + \sum_l^{\text{occ}} X_{n,l} X_{m,l}^* \\
& = (A + XB + B^+X^+ + XX^+)_{n,m}.
\end{aligned}$$

After some rearrangement and using the fact that X is Hermitian, we obtain the following fixed point equation for X

$$X = \frac{1}{2} (1 - A - X(B - 1) - (B - 1)^+ X - XX^+) =: \Phi(X),$$

which must be solved iteratively, starting from the initial “guess” $X_0 = 1/2(1 - A)$.

Adiabatic Decoupling

The dynamical trajectories generated for $\{\mathbf{R}_I\}$ by (2.24) are generally not identical to the trajectories generated by (2.22). At equilibrium, if the forces on the orbitals vanish, $\ddot{\phi}_n = 0$, the electronic equations of motion reduce to

$$f_n h_\sigma \phi_n(\mathbf{r}, t) = \sum_m^{\text{occ}} \Lambda_{n,m} \phi_m(\mathbf{r}, t), \quad n \in \mathcal{I}_\sigma,$$

which is equivalent to the stationary condition (2.15) and the KS equations (2.11) to within a unitary transformation. Therefore, the dynamics (2.24) represent a physical system exactly only when $\ddot{\phi}_n = 0$. However, under certain conditions, it is possible to keep the deviations of the orbitals from the KS solutions small, and one can expect that the dynamics generated by \mathcal{L} are a close approximation to the KS-BO dynamics. Furthermore, the conserved energy of equations (2.24) is given by $E_{\mathcal{L}} = h(\{\phi_n\}, \{\dot{\phi}_n\}, \{\mathbf{R}_I\}, \{\dot{\mathbf{R}}_I\})$, as can be seen by computing the total time derivative of (2.23) using (2.24), the fact that Λ is Hermitian and the orthonormality constraint. However, the total energy of the atoms, i.e., the physical (if the electrons are in their GS) total energy

$$E_I = \frac{1}{2} \sum_I M_I \dot{\mathbf{R}}_I^2 + E[\{\phi_n\}, \{\mathbf{R}_I\}], \quad (2.27)$$

is conserved only approximately, due to fluctuations in the fictitious kinetic energy of the electrons. Under certain conditions, these fluctuations stay bounded and small [PSB91] during typical simulation times. To provide some rationalization for these statements, consider the following expansion of the CP orbitals with respect to the *instantaneous* eigenstates of the Hamiltonian (2.24) at time t ,

$$\phi_n(t) = \sum_k (\delta_{n,k} + \alpha_{n,k}(t)) \chi_k, \quad \text{where } h_\sigma|_t \chi_n = \epsilon_n \chi_n, \quad n \in \mathcal{I}_\sigma. \quad (2.28)$$

This is always possible, since the $\{\chi_n\}$ form an orthonormal basis of the Hilbert space. Let us assume that the ϕ_n had been initially in their GS and that we are now in a regime where

the deviations of the CP orbitals from the KS orbitals are small, resulting in small $\alpha_{n,m}$. Let us assume further that all dependencies of the KS Hamiltonian on the $\alpha_{n,m}$ can be neglected at the first order. This is reasonable, since the error in the KS energy is second order with respect to errors in the wave function. In this case, neither h_σ nor the $\{\chi_n\}$ depend explicitly on time and inserting the expansion (2.28) into the equations of motion (2.24) yields the following differential equation for the deviation functions

$$\begin{aligned} \mu \sum_m \ddot{\alpha}_{n,m} \chi_m &\approx - \sum_{m=N_{\text{occ}}+1}^{\infty} f_n \alpha_{n,m} (\epsilon_m - \epsilon_n) \chi_m \\ &+ \sum_{m=1}^{N_{\text{occ}}} \frac{f_n - f_m}{2} \alpha_{n,m} (\epsilon_n - \epsilon_m) \chi_m, \end{aligned}$$

where terms of the order α^2 and $\dot{\alpha}^2$ on the r.h.s. have been neglected. If the KS Hamiltonian were a linear operator, i.e., the dependency of the eigenvalues on the $\alpha_{n,m}$ were negligible, these equations could be integrated immediately with the result that the deviation of the orbitals from the KS solutions in this regime consists of harmonic modes with frequencies equal to

$$\begin{aligned} \omega_{m,n}^{(1)} &= \sqrt{f_n (\epsilon_m^{\text{unocc}} - \epsilon_n^{\text{occ}}) / \mu} \\ \omega_{m,n}^{(2)} &= \sqrt{(f_n - f_m) (\epsilon_m^{\text{occ}} - \epsilon_n^{\text{occ}}) / 2\mu}. \end{aligned}$$

Here the state of occupation of the eigenstates has been indicated by a superscript. We can conclude from the second equation that the system will be stable (pure real frequencies) if the occupancies of states decrease as the eigenvalues increase. If we assume that this is so and furthermore that the occupation numbers are equal for all occupied states, as is almost always the case, then the first-order forces add only the frequencies $\omega_{m,n}^{(1)}$ to the vibrational spectrum of the electronic degrees of freedom. Only if the highest atomic frequency can be separated from the lowest electronic frequency $\omega_{m,n}^{(1)}$, an effective energy transfer between the corresponding degrees of freedom by resonance can be prevented. If the energy gap is not too small or zero, this can be achieved by reducing the fictitious electron mass μ and in that case, the MD generated by (2.24) provide meaningful statistical averages in the microcanonical ensemble. But μ cannot be reduced arbitrarily, because one needs to compromise between the former requirement and the competing observation that the maximum integration time step of the Verlet algorithm and μ are proportional,

$$\Delta t_{\text{max}} \approx 2 \sqrt{\frac{\mu}{f_1 (\epsilon_\infty - \epsilon_1)}}, \quad (2.29)$$

where ϵ_∞ and ϵ_1 denote the instantaneous KS eigenvalues that belong to the highest and the lowest bound KS orbital. This can be seen by inserting (2.28) into (2.26) (see [PTA92]). If such a procedure is not possible, as in metals, where there is no energy gap in the electronic excitation spectrum, two Nosé thermostats [Nos84] can be coupled to the electronic and atomic degrees of freedom, acting as heat baths that keep each system at a different temperature so their average kinetic and potential energies are fixed [BP92]. The MD is then able to sample the canonical ensemble.

2.3 Practical Implementation

2.3.1 The CP method with a Plane Wave Expansion

The CP approach does not depend on a particular basis set and has been implemented using, e.g., floating Gaussians [SK89], augmented-plane-wave-like schemes [SW90, YSK91], the generalized valence bond method [HC92] and Wannier functions [ODMG95]. In addition, several schemes have been employed where simplified, approximative descriptions of the electronic problem are adopted such as tight-binding methods [SN89, WCH90, SJ91], Harris-functional methods [HH90] and localized orbitals [MG94]. But for several reasons, the plane wave (PW) expansion in connection with the imposition of periodic boundary conditions (PBC) is the most widely used method:

- A PW basis set is attractive from a conceptual point of view, since it offers, as the CP scheme itself, a general formulation applicable to different classes of systems. Although designed for periodic systems such as perfect crystals, the PW expansion can also be applied to disordered and finite systems by using supercells. These are unit cells that are so large that the imposed periodicity does not affect the physical properties of the configuration (for example a point defect, a cluster, ...) contained in them to within a given tolerance.
- PWs are also particularly convenient from a numerical point of view, if advantage is taken of the localized nature of nonlocal pseudopotentials and of fast Fourier transform (FFT) techniques [PTVF92] for the calculation of the energy and the forces. The evaluation of forces acting on atoms is much simpler than with Gaussian or other localized basis sets, because the PWs do not depend on atomic positions and no Pulay forces [Pul69] have to be evaluated [SVB85]. PW basis functions are orthogonal, eliminating any considerations of an overlap matrix, and they are simple; in most cases the expressions are analytic. Furthermore, the PWs form a complete basis set and accuracy can be improved in an unambiguous way by including additional PWs that correspond to larger and larger reciprocal lattice vectors.

As a consequence of the imposed periodicity, the single-particle orbitals $\{\psi_n\}$ have Bloch form

$$\psi_n \rightarrow \psi_{n\mathbf{k}}(\mathbf{r}) = e^{i\mathbf{k}\cdot\mathbf{r}} \sum_{\mathbf{G}} c_{n\mathbf{k}}(\mathbf{G}) e^{i\mathbf{G}\cdot\mathbf{r}}. \quad (2.30)$$

The computation of the corresponding spin-densities requires an integral over the Brillouin zone (BZ) of the reciprocal lattice

$$n_\sigma(\mathbf{r}) = \frac{1}{\Omega_{BZ}} \sum_{n \in \mathcal{I}_\sigma} \int_{\Omega_{BZ}} d\mathbf{k} f_{n\mathbf{k}} |\psi_{n\mathbf{k}}(\mathbf{r})|^2, \quad (2.31)$$

where Ω_{BZ} denotes the volume of the BZ. This work is devoted to the study of microclusters using supercells, where (2.31) can be approximated by

$$n_\sigma(\mathbf{r}) \approx \sum_{n \in \mathcal{I}_\sigma} f_{n(\mathbf{k}=0)} |\psi_{n(\mathbf{k}=0)}(\mathbf{r})|^2, \quad (2.32)$$

because $\Omega_{BZ} = (2\pi)^3/\Omega$ (where Ω is the volume of the supercell) is very small and the dispersion of the KS eigenvalues $\epsilon_{n\mathbf{k}}$ becomes negligible as the overlap between electronic states of different cells vanishes with increasing cell size. Therefore only the wavefunctions at the Γ -point ($\mathbf{k} = 0$) need to be considered in the following, and the index \mathbf{k} may be consequently dropped. The numerical cost can be reduced further, if we take into account that at $\mathbf{k} = 0$, the KS orbitals can always be chosen real by an appropriate choice for the global phase factor. In this case, the symmetry relation $c_n(\mathbf{G})^* = c_n(-\mathbf{G})$ for its Fourier components holds, which we exploit in the calculation to reduce the number of PWs needed by a factor of two. In principle, the sum in (2.30) extends over the whole reciprocal lattice, but is truncated in practical calculations to include only those PWs with a kinetic energy $E_{kin} = \mathbf{G}^2/2$ less than a given energy E_{cut} that determines the accuracy of the calculations. The choice of E_{cut} depends on the specific system and on the pseudopotential (PP) used. The truncated Fourier space summations will be denoted by a superscript “cut”. Of course, the errors introduced by the finite size of the supercell, the use of a single \mathbf{k} point and a finite E_{cut} have to be gauged by test calculations. It should, however, be mentioned that we cannot increase the size of the unit cell arbitrarily, since this decreases the size of the shortest reciprocal lattice vectors, which can lead to instabilities in the calculation of the Hartree potential and energy (2.43). The Hartree potential $V^H(\mathbf{G})$ is proportional to $n(\mathbf{G})/G^2$, where $n(\mathbf{G})$ is the Fourier transform of the charge density. Therefore, at small reciprocal lattice vectors, small errors in the dynamics of the wave functions and consequently the $n(\mathbf{G})$ will produce large changes in the potential and lead to instabilities in the calculation (“charge sloshing”), if the time step is too large.

Pseudopotentials

The pseudopotential (PP) approximation consists in replacing both the bare nuclear potential and the effect of the core electrons on the valence electrons by an effective PP

$$V^{ext}(\mathbf{r}) = \sum_I \frac{-Z_I}{|\mathbf{r} - \mathbf{R}_I|} \rightarrow \sum_I v_{ps}^I(\mathbf{r} - \mathbf{R}_I),$$

thereby eliminating the core states from the calculation and leaving the chemically active valence states as the only degrees of freedom, with corresponding savings in computing time. This is justified by the following observations:

- Core-electron wavefunctions change little when placed into different chemical environments.
- Their only effect on chemical bonding is to influence the shape of the valence wave functions in the bonding region via orthogonality constraints in the core region.

Further savings of the computational cost may be gained from a suitable idealization of the valence functions inside the core regions, since one is mainly interested in describing bonding properties (e.g., equilibrium structures, phase diagrams, ...) correctly, which are insensitive to details even of the valence electronic structure within the core. The first

observation above suggests that the PP may be generated in preliminary all-electron (AE) atomic calculations. Within LDA this is done by solving self-consistently the radial KS equation

$$\left(-\frac{1}{2} \frac{d^2}{dr^2} + \frac{l(l+1)}{2r^2} + V^H[n](r) + V^{xc}[n](r) - \frac{Z}{r} \right) r R_{nl}(r) = \epsilon_{nl} r R_{nl}(r). \quad (2.33)$$

A PP is then constructed to reproduce exactly the valence-electron states for all angular momenta l present in the GS and a few angular momenta present in excited states (since there is only one valence state present for each angular momentum l , the principal quantum number n may further be omitted for simplicity). This results in the following requirements [HSC79, TM91]:

Requirement 1: AE and PP eigenvalues of the valence states must be equal, $\epsilon_l^{ps} = \epsilon_l$.

Requirement 2: The eigenfunctions R_l^{ps} of the PP should contain no nodes.

Requirement 3: The normalized AE and PP radial functions must be equal beyond a chosen cutoff radius r_c

$$R_l^{ps}(r) = R_l(r), \quad r > r_c.$$

Requirement 4 (Norm Conservation): The total integrated charge inside r_c of AE and PP orbitals must be equal

$$\int_0^{r_c} dr r^2 |R_l^{ps}(r)|^2 = \int_0^{r_c} dr r^2 |R_l(r)|^2.$$

The first requirement determines the energy zero, so that total PP energies always lack a large additive constant representing the energy of the cores if compared with results of all-electron calculations, and only energy differences can be reproduced correctly, which are the experimentally observable anyway. Requirement 2 together with the elimination of the core states is motivated by numerical considerations, because the oscillations associated with the nodes of the wavefunctions would require a high E_{cut} in the PW expansion. In addition to this, r_c must be chosen to be larger than the outermost node of the AE valence orbitals, since deviations from the AE orbitals are only allowed within the core region. Requirement 3 guarantees that the AE densities and the PP densities $n^{ps}(r) = \sum_l^{val} |R_l^{ps}(r)|^2$ of the valence electrons are equal outside the core and consequently the (electrostatic) potentials generated by them as well, which may be seen by solving Poisson's equation and using Gauss's theorem. The form of the PP wavefunctions R_l^{ps} inside the core region is, however, by no means determined uniquely by the requirements (1-4) and in fact there exist many recipes for the generation of PPs that differ at this point. But, once a PP wavefunction is obtained, it defines the screened PP $v_{ps}^{l,scr}(r)$ for angular momentum l via the equation

$$\left(-\frac{1}{2} \frac{d^2}{dr^2} + \frac{l(l+1)}{2r^2} + v_{ps}^{l,scr}(r) \right) r R_l^{ps}(r) = \epsilon_l r R_l^{ps}(r). \quad (2.34)$$

With regard to the intended use of the PP in self-consistent calculations in various chemical environments, the following separation of the screened PP into an ionic PP and the PP Coulomb and exchange-correlation potentials suggests itself:

$$\left(-\frac{1}{2} \frac{d^2}{dr^2} + \frac{l(l+1)}{2r^2} + V^H[n^{\text{ps}}](r) + V^{\text{xc}}[n^{\text{ps}}](r) + v_{\text{ps}}^l(r) \right) r R_l^{\text{ps}}(r) = \varepsilon_l r R_l^{\text{ps}}(r).$$

The ionic PP may then be recovered by inversion of the radial Schrödinger equation

$$v_{\text{ps}}^l(r) = \varepsilon_l - \frac{l(l+1)}{2r^2} + \frac{1}{2r R_l^{\text{ps}}(r)} \frac{d^2}{dr^2} (r R_l^{\text{ps}}(r)) - V^H[n^{\text{ps}}](r) - V^{\text{xc}}[n^{\text{ps}}](r).$$

Two conclusions are immediate: (a) if we wish the PP to be continuous, the PP wavefunction must have continuous derivatives up to and including the second, (b) if we wish to avoid a hard-core PP with a singularity at the origin, the PP wavefunction R_l^{ps} must behave as r^l near the origin. A major consequence of the l -dependence of the PP is that each angular momentum component of a general wavefunction on which it operates must see a different potential. This is generally achieved by use of angular momentum projection operators

$$\mathcal{P}_l(\mathbf{r}, \mathbf{r}') = \delta(r - r') / r^2 \sum_{m=-l}^l Y_l^{m*}(\Omega) Y_l^m(\Omega'),$$

where the Y_l^m denote the (normalized) spherical harmonics. The ionic pseudopotential operator for arbitrary systems is then given by

$$\begin{aligned} v_{\text{ps}}(\mathbf{r}, \mathbf{r}') &= v_{\text{ps}}^{\text{loc}}(r) \delta(\mathbf{r} - \mathbf{r}') + v_{\text{ps}}^{\text{nlloc}}(\mathbf{r}, \mathbf{r}'), \quad \text{where} \\ v_{\text{ps}}^{\text{nlloc}}(\mathbf{r}, \mathbf{r}') &= \sum_l \Delta v_{\text{ps}}^l(r) \mathcal{P}_l(\mathbf{r}, \mathbf{r}'), \quad \Delta v_{\text{ps}}^l(r) = v_{\text{ps}}^l(r) - v_{\text{ps}}^{\text{loc}}(r). \end{aligned} \quad (2.35)$$

The local part $v_{\text{ps}}^{\text{loc}}(r)$ introduced here can, in principle, be chosen arbitrarily, but a rapidly decaying function of \mathbf{G} is numerically most convenient, since the contribution of $v_{\text{ps}}^{\text{loc}}$ to the potential energy is calculated in reciprocal space, whereas the nonlocal part is evaluated in \mathbf{r} space, see section 2.3.1. For simple sp-bonding elements of the first, second and third rows of the periodic table, it is then advisable to take the smooth $v_{\text{ps}}^{l_{\text{max}}}(r)$ that belongs to the finite l_{max} , where the summation over l needs to be truncated. This choice also has the advantage, that the atomic scattering for all angular momentum channels with $l > l_{\text{max}}$ is adequately reproduced. Of course, this choice is not optimal for transition series elements and rare earths, where in general the s and/or p components are much smoother than the d and/or f components. It turns out that the form (2.35) of the nonlocal part (which is in this context sometimes called semilocal since it is local in r but nonlocal in Ω) is computationally rather expensive (see section (2.3.4) for details). As a remedy, [KB82] proposed a “truly nonlocal” form for $v_{\text{ps}}^{\text{nlloc}}$

$$v_{\text{ps}}^{\text{truly nlloc}}(\mathbf{r}, \mathbf{r}') := \sum_{l,m} \frac{\langle \mathbf{r} | \Delta v_{\text{ps}}^l | R_l^{\text{ps}} Y_l^m \rangle \langle R_l^{\text{ps}} Y_l^m | \Delta v_{\text{ps}}^l | \mathbf{r}' \rangle}{\langle R_l^{\text{ps}} Y_l^m | \Delta v_{\text{ps}}^l | R_l^{\text{ps}} Y_l^m \rangle} \quad (2.36)$$

that has been used in the investigation of S and P clusters. It is easy to show that $v_{ps}^{nlloc} |R_l^{ps} Y_l^m\rangle = \Delta v_{ps}^{nlloc} |R_l^{ps} Y_l^m\rangle$, i.e., the two potentials will produce the same solutions for the atomic reference configuration (but will produce different solutions in arbitrary environments).

The modifications to the potential within the core have been dictated by "smoothness" considerations (i.e., there shall be a rapid convergence of the systems properties with respect to an increase of the cutoff E_{cut} of the PW basis set) and the requirement that it reproduce exactly the AE results in the atomic reference configuration. On the other hand, the final purpose of the PP approximation is to reproduce closely AE calculations in different environments, i.e., we require a "transferable" PP. While a large core radius r_c enhances smoothness, the opposite is true for transferability. The choice of r_c is then a compromise between the two requirements, and a perfect transferability cannot be expected. A prescription that ensures transferability at least in an approximate way has already been incorporated in the generation procedure by requirement 4 above, as we now show. The logarithmic derivative $d \ln R_l / dr$ at any r_0 specifies uniquely (apart from a constant factor) a solution of the radial Schrödinger equation for all $r > r_0$, since it is a linear second order differential equation. By considering solutions for arbitrary ε in (2.33) and (2.34) (in general no bound states), it follows from the Wronskian theorem [Mes69, §3.2.1] that

$$-\frac{\partial}{\partial \varepsilon} \frac{\partial}{\partial r} \ln R(r, \varepsilon) \Big|_{\substack{\varepsilon = \varepsilon_l \\ r = r_c}} = \frac{1}{r_c^2 R^2(r_c, \varepsilon_l)} \int_0^{r_c} dr r^2 R^2(r, \varepsilon_l). \quad (2.37)$$

Therefore, not only the logarithmic derivatives for $\varepsilon = \varepsilon_l$ match at $r = r_c$, as is required for the equality of AE and PP solutions for $r > r_c$, but the same holds also true for neighboring energies ε at the first order. This is advantageous, since the atomic eigenvalues will shift when the atom experiences different chemical environments. However, this result should not be taken as an absolute criterion for transferability, since (2.37) has been derived under the assumption that the potential is spherically symmetrical.

In the present calculations, two recipes for the generation of norm-conserving PPs have been employed. The approach of Bachelet *et al.* [HSC79, BHS82] has been applied to the investigation of charged S and P clusters. This scheme starts from a crude guess for the screened PP $v_{ps}^{l,scr}$

$$\tilde{v}_{ps}^{l,scr}(r) =: \left(V^H[n](r) + V^{sc}[n](r) - \frac{Z}{r} \right) \left(1 - f\left(\frac{r}{r_c}\right) \right) + c_l f\left(\frac{r}{r_c}\right), \quad \text{where } f(r) = e^{-r^{3.5}},$$

and c_l follows from requirement 1 for the lowest nodeless eigenfunction \tilde{R}_l^{ps} of this potential. \tilde{R}_l^{ps} is then modified to meet the remaining requirements (2-4) above in the form

$$R_l^{ps}(r) = \gamma_l \left(\tilde{R}_l^{ps}(r) + \delta_l r^l f\left(\frac{r}{r_c}\right) \right),$$

where the coefficients are adjusted numerically. The final PP obtained by inversion of the corresponding Schrödinger equation has been fitted to the analytical form

$$v_{ps}^{loc}(r) = -\frac{z}{r} \sum_{i=1}^2 c_i^{core} \operatorname{erf}(\sqrt{\alpha_i^{core}} r), \quad c_1^{core} + c_2^{core} = 1 \quad (2.38)$$

$$\Delta v_{ps}^l(r) = \sum_{i=1}^3 (A_i + r^2 A_{i+3}) e^{-\alpha_i r^2}, \quad (2.39)$$

where z denotes the valence charge and the remaining parameters have been tabulated by the authors [BHS82]. It should be noted that v_{ps}^{loc} is finite at the origin. A modification to this method [Van85] to render the PP optimally smooth has not been considered in the present work. An alternative recipe originally proposed by [Ker80] and then modified by Trouiller and Martins [TM91] to be optimally smooth, has been applied in the investigation of mixed $C_n Si_m$ clusters. It involves an analytic expression for the PP functions inside the core radius

$$R_l^{ps}(r) = \begin{cases} R_l(r) & \text{if } r > r_c \\ r^l \exp(p(r)) & \text{if } r \leq r_c \end{cases}, \quad \text{where } p(r) = \sum_{m=0}^6 c_{2m} r^{2m}.$$

The seven unknown coefficients c_m (odd powers of r have been discarded for smoothness considerations) are determined from the conditions of norm conservation (1), the continuity of $R_l^{ps}(r)$ and its first four derivatives at r_c (2-6) and zero curvature of the screened PP at the origin, $v_{ps}^{loc}''(0) = 0$ (7). We have generated PPs for C and Si within this scheme, choosing 1.17/2.24 a.u. and 1.84/1.89 a.u. as sp/d ($l=0,1/l=2$) cutoff radii for C and Si, respectively. The PPs are provided to the MD/DF program in numerical form, i.e., they are tabulated on a logarithmic radial mesh, without any further fitting procedure.

The KS Energy Functional in the PW expansion

Within the PP approximation, the KS energy functional (2.14) takes the form

$$\begin{aligned} E[\{\phi_n\}, \{\mathbf{R}_I\}] &\rightarrow E^{ps}[\{\phi_n^{ps}\}, \{\mathbf{R}_I\}] \\ E^{ps}[\{\phi_n^{ps}\}, \{\mathbf{R}_I\}] &= \sum_n^{val} f_n \int_{\Omega} d\mathbf{r} \phi_n^{ps}(\mathbf{r})^* \left(-\frac{\nabla^2}{2} \right) \phi_n^{ps}(\mathbf{r}) + \frac{1}{2} \int_{\Omega} d\mathbf{r} n^{ps}(\mathbf{r}) V^H[n^{ps}](\mathbf{r}) \\ &\quad + E_{xc}[n_+^{ps}, n_-^{ps}] + \int_{\Omega} d\mathbf{r} n^{ps}(\mathbf{r}) \sum_{\mathbf{n}, \nu} v_{ps}^{loc, \nu}(\mathbf{r} - \mathbf{R}_{\nu}^{\mathbf{n}}) \\ &\quad + \int_{\Omega} d\mathbf{r} \int d\mathbf{r}' \phi_n^{ps}(\mathbf{r})^* \sum_{\mathbf{n}, \nu} v_{ps}^{nl, \nu}(\mathbf{r} - \mathbf{R}_{\nu}^{\mathbf{n}}, \mathbf{r}' - \mathbf{R}_{\nu}^{\mathbf{n}}) \phi_n^{ps}(\mathbf{r}') \\ &\quad + \frac{1}{2} \sum'_{\mathbf{n}, \nu, \mu} \frac{z_{\nu} z_{\mu}}{|\mathbf{R}_{\nu}^{\mathbf{n}} - \mathbf{R}_{\mu}^{\mathbf{n}}|} \\ &=: E_k + E_{ee} + E_{xc} + E_{ps}^{loc} + E_{ps}^{nl, loc} + E_{II}, \end{aligned} \quad (2.40)$$

where the last line contains abbreviations of the terms given explicitly above (in order of their appearance). z_ν is now the number of valence electrons of the atom located at $\mathbf{R}_\nu^{\text{n}} := \mathbf{R}^{\text{n}} + \mathbf{R}_\nu$, where \mathbf{R}^{n} are vectors of the direct lattice and \mathbf{R}_ν denotes the position of ion ν within each supercell. The prime in the expression for the ion-ion Coulomb energy indicates that ionic self-interaction terms are excluded from the summation. In practice, some mathematical manipulations are necessary, since E_{ee} , $E_{\text{ps}}^{\text{loc}}$ and E_{II} are individually divergent quantities. Only their sum is well defined [IZC79] and may be evaluated using Ewald's summation method [MMWI71]. An elegant trick to avoid the explicit evaluation of Ewald sums has been used by Car and Parrinello (see, e.g. [GP91]). Instead of E_{ee} they consider the (finite) electrostatic self-interaction of a *neutral* system of electronic and fictitious smeared Gaussian charges centered at the ionic sites

$$\tilde{n}(\mathbf{r}) := n^{\text{ps}}(\mathbf{r}) - \sum_{\mathbf{n}, \nu} n^{\text{at}, \nu}(\mathbf{r} - \mathbf{R}_\nu^{\text{n}}), \quad n^{\text{at}, \nu}(r) = \frac{z_\nu}{(\sqrt{\pi} R_c^\nu)^3} \exp\left(-\frac{r}{R_c^\nu}\right)^2.$$

The fictitious Gaussian charges give rise to the following Coulomb potentials (apart from arbitrary constants):

$$\int d\mathbf{r}' \frac{n^{\text{at}, \nu}(\mathbf{r}')}{|\mathbf{r} - \mathbf{r}'|} = \frac{z_\nu}{r} \operatorname{erf}\left(\frac{r}{R_c^\nu}\right),$$

as may be seen by straightforward integration. This introduces spurious interaction energies of the Gaussian density with itself and with the electronic (pseudo-)density that are compensated for by fictitious contributions of equal amount and opposite sign to E_{II} and $E_{\text{ps}}^{\text{loc}}$, respectively. In all, the above terms are replaced by

$$\begin{aligned} E_{ee} &\rightarrow \tilde{E}_{ee} := \frac{1}{2} \int_{\Omega} d\mathbf{r} \tilde{n}(\mathbf{r}) V^H[\tilde{n}](\mathbf{r}), \\ E_{\text{ps}}^{\text{loc}} &\rightarrow \tilde{E}_{\text{ps}}^{\text{loc}} := \int_{\Omega} d\mathbf{r} n^{\text{ps}}(\mathbf{r}) \sum_{\mathbf{n}, \nu} \tilde{v}_{\text{ps}}^{\text{loc}, \nu}(\mathbf{r} - \mathbf{R}_\nu^{\text{n}}) \\ &\quad \text{where } \tilde{v}_{\text{ps}}^{\text{loc}, \nu}(r) := v_{\text{ps}}^{\text{loc}, \nu}(r) + \frac{z_\nu}{r} \operatorname{erf}\left(\frac{r}{R_c^\nu}\right) \quad (2.41) \\ E_{II} &\rightarrow \tilde{E}_{II} := \frac{1}{2} \sum'_{\mathbf{n}, \nu, \mu} \frac{z_\nu z_\mu}{|\mathbf{R}_\nu - \mathbf{R}_\mu^{\text{n}}|} \left(1 - \operatorname{erf}\left(\frac{|\mathbf{R}_\nu - \mathbf{R}_\mu^{\text{n}}|}{\sqrt{R_c^\nu{}^2 + R_c^\mu{}^2}}\right)\right) - \sum_{\nu} \frac{z_\nu^2}{\sqrt{2\pi} R_c^\nu} \\ &\approx \frac{1}{2} \sum_{\nu \neq \mu} \frac{z_\nu z_\mu}{|\mathbf{R}_\nu - \mathbf{R}_\mu|} \left(1 - \operatorname{erf}\left(\frac{|\mathbf{R}_\nu - \mathbf{R}_\mu|}{\sqrt{R_c^\nu{}^2 + R_c^\mu{}^2}}\right)\right) - \sum_{\nu} \frac{z_\nu^2}{\sqrt{2\pi} R_c^\nu}, \end{aligned}$$

where the last, approximate relation results from the rapid convergence of the error function to unity, i.e., for $0 \leq x$, we have $0 \leq 1 - \operatorname{erf}(x) \leq \frac{2}{\sqrt{\pi}} \frac{\exp(-x^2)}{x + \sqrt{x^2 + 4/\pi}}$ (see [AS72]). The last term

$$\sum_{\nu} \frac{z_\nu^2}{\sqrt{2\pi} R_c^\nu} = \frac{1}{2} \sum_{\nu} \int_{\Omega} d\mathbf{r} n^{\text{at}, \nu}(\mathbf{r} - \mathbf{R}_\nu) \int d\mathbf{r}' \frac{n^{\text{at}, \nu}(\mathbf{r}' - \mathbf{R}_\nu)}{|\mathbf{r} - \mathbf{r}'|}$$

represents the self-energy of the Gaussian charges, which has been omitted in the preceding sum. All the resulting energy terms are separately finite quantities and are evaluated using a dual-space method [MC88], i.e., both real- and momentum-space representations of the wave functions are used. The following terms are most easily evaluated in Fourier space:

$$E_k = \Omega \sum_n^{val} \sum_{\mathbf{G}}^{cut} f_n G^2 |c_n(\mathbf{G})|^2 \quad (2.42)$$

$$\tilde{E}_{ee} = \frac{1}{2} \Omega \sum_{\mathbf{G} \neq 0}^{dcut} |\tilde{n}(\mathbf{G})|^2 \frac{4\pi}{G^2} \quad (2.43)$$

$$\tilde{E}_{ps}^{loc} = \Omega \sum_{\mathbf{G}}^{dcut} n_{ps}^*(\mathbf{G}) \sum_{\nu} \tilde{v}_{ps}^{loc,\nu}(\mathbf{G}) e^{i\mathbf{G}\mathbf{R}_{\nu}}. \quad (2.44)$$

The superscript “*dcut*” indicates that the cutoff for the expansion of the electronic density has to be larger than the one used for the expansion of the wavefunctions. The convolution theorem would require a factor $x = 4$ between the two cutoff energies, but one usually resorts to smaller factors in practical calculations [MC88] (factors used here are $x = 2$ (S, P) and $x = 3.36$ (C, Si), see section 3 for details). The expressions for \tilde{E}_{II} and E_{xc} are evaluated in real space in a straightforward way, while the integral in eq. 2.17 or 2.18 is replaced by a sum over the FFT grid. The remaining term E_{ps}^{nloc} depends on the form of the nonlocal PP used. If (2.35) is employed, we obtain

$$E_{ps}^{nloc} = \sum_n^{val} f_n \int_0^{\infty} dr r^2 \sum_{l,\nu} \Delta v_{ps}^{l,\nu}(r) \sum_m \left| \sum_{\mathbf{G}}^{cut} 4\pi j_l(gr) Y_l^m(\Omega_{\mathbf{G}})^* c_n^{ps}(\mathbf{G}) e^{i\mathbf{G}\mathbf{R}_{\nu}} \right|^2. \quad (2.45)$$

The upper integration limits are largely arbitrary, since the Δv_{ps}^l are short-ranged (cf. eq. 2.39) and may safely be assumed to have vanished at the cell boundaries. The choice made above allows to use a Gauss-Hermite integration formula (i.e., abscissas are the roots of the Hermite polynomials, orthonormal in $(-\infty, \infty)$ with weight function e^{-x^2} [PTVF92]),

$$\int_0^{\infty} dr r^2 \Delta v_{ps}^{l,\nu}(r) j_l(gr) j_l(g'r) \approx \frac{1}{2} \sum_i w_i x_i^2 e^{x_i^2} \Delta v_{ps}^{l,\nu}(x_i) j_l(gx_i) j_l(g'x_i). \quad (2.46)$$

This is appropriate, since the $\Delta v_{ps}^{l,\nu}$ have approximately Gaussian shape (see also eq. 2.39). On the other hand, if the separable form (2.36) had been chosen to represent the nonlocal part of the PP, we find

$$E_{ps}^{nloc} = \sum_n^{val} f_n \sum_{l,m} \frac{(2l+1) \left| \int_0^{\infty} dr r^2 \sum_{\nu} \Delta v_{ps}^{l,\nu}(r) R_l^{ps,\nu}(r) \sum_{\mathbf{G}}^{cut} 4\pi j_l(gr) Y_l^m(\Omega_{\mathbf{G}})^* c_n^{ps}(\mathbf{G}) e^{i\mathbf{G}\mathbf{R}_{\nu}} \right|^2}{\int_0^{\infty} dr r^2 \sum_{\nu} \Delta v_{ps}^{l,\nu}(r) R_l^{ps,\nu}(r)^2}. \quad (2.47)$$

The forces on the expansion coefficients of the electrons may be calculated from either side of the equation

$$-\frac{1}{\Omega} \frac{\partial E^{\text{ps}}[\{c_n^{\text{ps}}(\mathbf{G})\}, \{\mathbf{R}_I\}]}{\partial c_n^{\text{ps}}(\mathbf{G})^*} = -f_n \frac{1}{\Omega} \int_{\Omega} d\mathbf{r} (h_\sigma \phi_n^{\text{ps}})(\mathbf{r}) e^{-i\mathbf{G}\mathbf{r}}.$$

The former is better suited for contributions to the forces arising from E_{kin} and E_{ps}^{nloc} that are analytic expressions in the $c_n^{\text{ps}}(\mathbf{G})$. It is not appropriate for contributions from the remaining energy terms, since they are analytic in the $n^{\text{ps}}(\mathbf{G})$, which are convolutions of the $c_n^{\text{ps}}(\mathbf{G})$. This would make their evaluation in Fourier space cumbersome. On the other hand, their contribution to the forces is a simple product in direct space,

$$-f_n \left(V^H[\tilde{n}](\mathbf{r}) + V_\sigma^{xc}[n_+^{\text{ps}}, n_-^{\text{ps}}](\mathbf{r}) + \sum_{\mathbf{n}, \nu} \tilde{v}_{ps}^{loc, \nu}(\mathbf{r} - \mathbf{R}_\nu^{\text{ps}}) \right) \phi_n(\mathbf{r}),$$

so they are more conveniently calculated there using the second expression above and FFTs to switch between the dual spaces. The forces on the atoms are calculated in a straightforward way as the analytic derivatives $-\partial \left(\tilde{E}_{ee} + \tilde{E}_{ps}^{loc} + E_{ps}^{nloc} + \tilde{E}_{II} \right) / \partial \mathbf{R}_\nu$ of the energy terms given above.

2.3.2 Charged Systems

PW calculations imply periodic boundary conditions (PBC). This is appropriate for crystal calculations, and neutral clusters can also be treated by use of the supercell method described above. However, this approach leads to serious problems if charged clusters are to be investigated. In order to avoid a divergence of the electrostatic energy, any practical calculation using PBC [YOBC90, Jon93, MPC95] must resort to an artificial compensating charge density that is spread uniformly throughout space to maintain neutrality in each unit cell. This amounts to a constant (albeit infinite) shift in the potential that rules out a direct calculation of electron addition or removal energies from energy differences between differently charged systems within the Δ SCF scheme. The application of the Δ SCF scheme requires that the constants in the potentials of differently charged systems are chosen in a consistent way. We can achieve this if we assume that the electron density is nonzero only in an isolated cell Ω_c containing the cluster, say the region of space of volume Ω defined by

$$\Omega_c := \left\{ \mathbf{r} \mid \mathbf{r} = \sum_{i=1}^3 \lambda_i \mathbf{a}_i, 0 \leq \lambda_i < 1 \right\},$$

and solve the Poisson equation

$$\Delta V^H(\mathbf{r}) = \tilde{n}_c(\mathbf{r}),$$

subject to zero boundary conditions at infinity (instead of PBC). Its solution is the Hartree potential, given by

$$V^H(\mathbf{r}) = \int_{\Omega_c} d\mathbf{r}' \frac{\tilde{n}_c(\mathbf{r}')}{|\mathbf{r} - \mathbf{r}'|}, \quad (2.48)$$

where the density \tilde{n}_c introduced here is identical to the periodic density \tilde{n} inside Ω_c and zero outside. As far as the calculation of the total energy of such an isolated system is concerned, we must recalculate only this term (the Hartree potential) and its contribution $\tilde{E}_{ee,c}$ to the total energy, because these are the only terms of long-range form, as we can see if we analyze the individual terms in the expression for the total energy. E_{zc} , E_{ps}^{loc} and \tilde{E}_{II} can be used unchanged, because they involve only contributions from real-space sums and/or integrals over a single unit cell. E_{kin} (2.42) can be calculated as before if we also assume that the wavefunctions are nonzero only in Ω_c . This is reasonable, since the exact electronic density decays exponentially to zero outside a cluster [LPS84] and both the density and the wave functions should be negligible at the cell boundary. The only terms that are affected by the abandonment of PBC are \tilde{E}_{ee} and, to lesser extent, \tilde{E}_{ps}^{loc} , for their evaluation in reciprocal space (2.43), (2.44) relies on periodicity. The computation of \tilde{E}_{ps}^{loc} is less critical, because $\tilde{v}_{ps}^{loc,\nu}$ is short-ranged in direct space, and it may be assumed that its periodic images are negligible inside Ω_c . We have verified this assumption by numerical tests (see below). Furthermore, we always have $\tilde{v}_{ps}^{loc,\nu}(\mathbf{G} = 0) = 0$ in reciprocal space (see equation 2.41), and there is no divergence for either charged or neutral unit cells.

The calculation of the modified Hartree energy of an isolated cluster, denoted by $\tilde{E}_{ee,c}$, can be done in \mathbf{r} -space, for example by calculating multipolar charges and the corresponding potentials of \tilde{n}_c , as has been proposed by [YOBC90], who included terms up to $l = 3$ in their expansion with respect to Legendre polynomials. An alternative approach proposed here proceeds in Fourier space and uses FFTs to compute both the potential and $E_{ee,c}$. The method implemented is similar to the approach presented in [BL93] and uses some ideas of the so-called ‘‘partial FFT’’ introduced in [KTMS87]. Of course, our procedure cannot offset the influence of residual interactions between images in periodically repeated cells on the charge density, e.g., in the presence of large multipolar moments, where other methods should be employed [BL93].

The evaluation of the Hartree energy is especially convenient in reciprocal space (see equation 2.43) if a compensating charge density is used to guarantee neutrality. We can maintain this convenient description to estimate the Hartree energy of an isolated cluster, if we consider a sequence of periodic arrays where the clusters are separated by increasing lattice constants la_{lat} . If we then take the limit $l \rightarrow \infty$, the corresponding densities \tilde{n}_l and Hartree energies $E_{ee,l}$ should converge to their values for the isolated system. The densities \tilde{n}_l can be obtained from the original density \tilde{n} subjected to PBC by the description

$$\tilde{n}_l(\mathbf{r}) = \begin{cases} \tilde{n}(\mathbf{r}) - z/(l^3\Omega) & \text{if } \mathbf{r} \in \Omega_l \\ -z/(l^3\Omega) & \text{otherwise,} \end{cases}$$

where the neutrality of the lattice is always maintained by adding a uniform positive background charge $-z/(l^3\Omega)$ to the density (z denotes the electronic excess charge of the cluster). Ω_l is the region of space enclosed by the separated supercells, i.e.,

$$\Omega_l = \left\{ \mathbf{r} \mid \mathbf{r} = \sum_{\mathbf{n}} l\mathbf{R}^{\mathbf{n}} + \sum_{i=1}^3 \lambda_i \mathbf{a}_i, 0 \leq \lambda_i < 1 \right\}.$$

In real applications, we use FFTs to calculate the Fourier components of the densities \tilde{n}_l . The expansion of the periodic lattice enlarges the r-space FFT mesh to

$$\{\mathbf{r}\}_l := \left\{ \sum_{i=1}^3 j_i \frac{\mathbf{a}_i}{N_i}, 0 \leq j_i < lN_i \right\} \quad (2.49)$$

and refines the conjugate FFT-mesh in reciprocal space to

$$\{\mathbf{G}\}_l := \left\{ \sum_{i=1}^3 m_i \frac{\mathbf{b}_i}{l}, -\frac{lN_i}{2} < m_i \leq \frac{lN_i}{2} \right\} \quad (2.50)$$

(where the original meshes are recovered for $l = 1$). Under the condition that \tilde{n} vanishes (or is negligibly small) at the boundaries of the original cells (which can always be satisfied by increasing the dimension of these cells and/or by translating and rotating the system inside the cells) the FFT coefficients (for $\mathbf{G} \neq 0$) can be related to both the Fourier coefficients of \tilde{n}_l and the Fourier transform \hat{n} of \tilde{n}_c (see appendix A):

$$\begin{aligned} \tilde{n}^{fft}(\mathbf{G}) &:= \sum_{\{\mathbf{r}\}_l} \tilde{n}_l(\mathbf{r}) e^{-i\mathbf{G}\cdot\mathbf{r}} = l^3 N \tilde{n}_l(\mathbf{G}), \quad \mathbf{G} \in \{\mathbf{G}\}_l \setminus \{0\} \\ &= \frac{N}{\Omega} \hat{n}(\mathbf{G}). \end{aligned}$$

Using these relations, the Hartree energy of \tilde{n}_l may be calculated from

$$\tilde{E}_{ee,l} = \frac{1}{2} \frac{\Omega}{l^3} \sum_{\{\mathbf{G}\}_l \setminus \{0\}} \left| \frac{\tilde{n}^{fft}(\mathbf{G})}{N} \right|^2 \frac{4\pi}{G^2}$$

and may alternatively be expressed by

$$\tilde{E}_{ee,l} = \frac{1}{2} \frac{(2\pi)^3}{l^3 \Omega} \sum_{\{\mathbf{G}\}_l \setminus \{0\}} \frac{1}{(2\pi)^3} |\hat{n}(\mathbf{G})|^2 \frac{4\pi}{G^2}. \quad (2.51)$$

As we show in appendix A, the Hartree energies $\tilde{E}_{ee,l}$ converge to the Hartree energy $\tilde{E}_{ee,c}$ of the isolated density, which may be expressed by a k-space integral (see, e.g. [Jac75, §3.13, (3.164)])

$$\tilde{E}_{ee,l} \xrightarrow{l \rightarrow \infty} \frac{1}{2} \int \frac{d\mathbf{k}}{(2\pi)^3} |\hat{n}(\mathbf{k})|^2 \frac{4\pi}{k^2} = \tilde{E}_{ee,c}. \quad (2.52)$$

In the practical implementation, FFT components and Hartree energies for several $l_1 \leq l_2 \leq \dots$ are calculated and are extrapolated polynomially to the limit $l \rightarrow \infty$. Choosing $l_n = 2l_{n-1}$, all the components of the previous steps can be used, since $\{\mathbf{G}\}_{l_{n-1}} \subset \{\mathbf{G}\}_{l_n}$. For all results presented in section 3, $l_{max} = 8$ has been used.

The FFTs above may be confined to the original r-space mesh since the uniform positive background charge that is alone present at the additional FFT points \mathbf{r} , $j_i \geq N_i$ contributes

only to the $\mathbf{G} = 0$ component (which is thereby eliminated). This fact may be exploited to reduce the effort for the computation of the $\tilde{n}(\mathbf{G})$ by taking into account that each vector of the finer k -space mesh can be decomposed unambiguously into a sum of a vector \mathbf{G}' of the coarser original mesh and some vector $\boldsymbol{\gamma}$:

$$\mathbf{G} = \mathbf{G}' + \boldsymbol{\gamma}, \quad \boldsymbol{\gamma} = \sum_{i=1}^3 m_i \frac{\mathbf{b}_i}{l}, \quad m_i = 0, \dots, l-1, \quad \mathbf{G} \in \{\mathbf{G}\}_l, \quad \mathbf{G}' \in \{\mathbf{G}\}_1.$$

The set $\{\boldsymbol{\gamma}\}$ contains l^3 vectors. The FFT components on this mesh can be written as

$$\begin{aligned} \tilde{n}^{fft}(\mathbf{G}) &= \tilde{n}(\mathbf{G}' + \boldsymbol{\gamma}) \\ &= \sum_{\mathbf{r}} \tilde{n}(\mathbf{r}) \exp -i(\mathbf{G}' + \boldsymbol{\gamma})\mathbf{r} \\ &= \sum_{\mathbf{r}} [\tilde{n}(\mathbf{r}) \exp -i\boldsymbol{\gamma}\mathbf{r}] \exp -i\mathbf{G}'\mathbf{r}, \quad \mathbf{G} \in \{\mathbf{G}\}_l, \quad \mathbf{G}' \in \{\mathbf{G}\}_1. \end{aligned} \quad (2.53)$$

This means that we need l^3 FFT's, each of length $N := N_1 N_2 N_3$, to compute all the $l^3 N$ FFT-components of the entire set $\{\mathbf{G}\}_l$. The number of operations for one large FFT is $\mathcal{O}(l^3 N \log_2(l^3 N))$, while the present procedure needs $\mathcal{O}(l^3 N \log_2(2N) - N)$ operations (including $\mathcal{O}((l^3 - 1)N)$ operations to compute the quantities in the brackets in (2.53). As usual in this context, only multiplications and/or divisions are considered.

Obviously the largest contribution to the error in approximating (2.52) by (2.51) stems from the omission of the $\mathbf{G} = 0$ -term. It is possible to increase accuracy and to improve convergence if a more accurate description of this contribution to the integral is used, as indicated at the end of appendix A. To assess the accuracy of the resulting method, we have applied it to analytically soluble test cases and experimented by changing the size of the original supercell and/or changing the energy cutoff of the PW expansion (see section 3). The results were both accurate and stable. The tests indicated further that an extrapolation of $\tilde{E}_{ps,l}^{loc}$ analogous to the above for $\tilde{E}_{ee,l}$ made a negligible difference (the total energy differences changed always less than 0.01 eV) if a value of E_{dcut} large enough to achieve convergence has been used. Therefore such a correction has only been included if the computational effort (of memory and CPU time) to calculate the additional FFT coefficients of the PP seemed feasible, i.e., only if analytical PPs [BHS82] have been used (S, P), whereas it has been omitted if numerical PPs were employed (C, Si), where the FFT components require demanding numerical integrations.

2.3.3 Vibrational Spectra

Within the framework of Car Parrinello MD, a natural source of information about the vibration frequencies of the eigenmodes of a given (local) minimum structure under investigation is provided by non-thermally equilibrated MD trajectories at low temperatures (≤ 300 K). In particular, the frequencies may be determined as the peak positions of the

vibrational density of states (VDOS) computed by Fourier transforming the (normalized) velocity autocorrelation function $c_{vv}(t)$ [AT87] in a harmonic regime ($\langle \mathbf{v} \rangle = 0$)

$$\hat{c}_{vv}(\omega) = \int_{-\infty}^{\infty} dt c_{vv}(t) \exp i\omega t, \quad \text{where } c_{vv}(t) = \frac{\langle \mathbf{v}(t) \cdot \mathbf{v}(0) \rangle}{\langle \mathbf{v}(0) \cdot \mathbf{v}(0) \rangle}. \quad (2.54)$$

Here, \mathbf{v} encompasses all $3N_{ion}$ components of the ionic velocities $\dot{\mathbf{R}}_I$, $I = 1, \dots, N_{ion}$ of the system and the brackets denote the microcanonical ensemble average. In MD calculations however, the ensemble average is replaced by a time average (assuming ergodicity) and the discretization of time $\{t_n = n\Delta t, n = 0, \dots, N-1\}$, introduced, e.g., by (2.26), must be taken into account. The numerator of $c_{vv}(t)$ (2.54) is therefore replaced by

$$\langle \mathbf{v}(t_m) \cdot \mathbf{v}(0) \rangle \rightarrow \lim_{N \rightarrow \infty} \frac{1}{N-m} \sum_{n=0}^{N-m-1} \mathbf{v}(t_{n+m}) \cdot \mathbf{v}(t_n) \quad (2.55)$$

and the denominator is substituted correspondingly. The resulting discrete $c_{vv}(t_n)$ is called an autocorrelation sequence (ACS). In practice, instead of extrapolating $N \rightarrow \infty$, the length of the MD run $T := N\Delta t$ is chosen to be reasonably large (for the results presented in section 3, the trajectories have been followed for 2000 – 8000 time steps, depending on the size of the cluster). A direct application of FFT to $c_{vv}(t_m)$ to obtain the VDOS

$$\hat{c}_{vv}(2\pi k/T) = \Delta t \sum_{n=0}^{N-1} c_{vv}(t_n) \exp i2\pi kn/N, \quad -\frac{N}{2} < k \leq \frac{N}{2}$$

suffers mainly from two limitations:

- Due to the discretization of frequencies, the frequency resolution is limited to $2\pi/T$, i.e., by the length of the MD run.
- The strength of the peaks is proportional to the weight of the modes in the original data set. An efficient energy transfer between the modes would then be required to ensure that all of them would be excited sufficiently to be discernible from numerical noise. This condition is seldom met during typical simulation times, since anharmonic terms in the potential that account for thermal equilibration are weak at low temperatures.

The multiple signal classification (MUSIC) analysis method [Mar87] is able to overcome these difficulties to a large extent by constructing a frequency estimator, i.e., a *continuous* function of frequency that exhibits sharp peaks at the frequencies of the eigenmodes, even if their amplitudes in the incoming trajectory are small or even comparable to the numerical noise. It should be noted, however, that a frequency estimator function, unlike power spectral density estimators (e.g., the maximum entropy estimator [PTVF92]) does not preserve the weight of the eigenmodes in the trajectory, nor can the ACS be recovered by

Fourier transforming the frequency estimator. To get the essence of the method, let us assume the following idealized form of an ACS:

$$c_{vv}(t_m) = \frac{1}{N-m} \sum_l^P \tilde{a}_l(\omega_l)^2 \exp -\omega_l m \Delta t + \rho_w \delta_{m,0}, \quad m = 0, \dots, L, \quad L < N. \quad (2.56)$$

The last term has been added to account for numerical uncertainties. It is called white noise, justified by the fact that its FFT is a constant ($\Delta t \rho_w$) for all frequencies. The remaining terms may be imagined as being produced by, e.g., a linear combination of complex sinusoidal functions

$$\mathbf{v}(t_n) = \sum_l^P \mathbf{a}(\omega_l) \exp -\omega_l n \Delta t, \quad (2.57)$$

where the case of a real \mathbf{v} would be contained by the requirement that, for every ω_l , there is a $\omega_{l'}$ with $\omega_{l'} = -\omega_l$ and $\mathbf{a}(-\omega_l) = \mathbf{a}^*(\omega_l)$. Applying (2.55) to this sequence for a large but finite N and a complex scalar product then would yield (2.56) with $\tilde{a}_l(\omega_l) = a_l(\omega_l) / \sqrt{\sum_{l'} a_{l'}(\omega_{l'})^2}$ apart from corrections of $\mathcal{O}(1/N)$. The number of independent vibrational modes would then be $P/2 = 3N_{ion} - 5$ for linear and $P/2 = 3N_{ion} - 6$ for non-linear molecules, respectively, since they occur in pairs $(\omega_l, -\omega_l)$. So far, the frequencies have not been specified, but they may be determined by diagonalizing the complex $L \times L$ autocorrelation matrix defined by

$$R_{n,m} := c_{vv}(t_{n-m}) =: S_{n,m} + \rho_w \delta_{n,m}.$$

The decomposition reflects the assumed form (2.56) of the ACS. By construction, R and S are Hermitian and consequently all eigenvalues are real and their (common) eigenvectors constitute an orthonormal basis $\{\mathbf{q}_1, \dots, \mathbf{q}_L\}$ of \mathbb{C}^L . A perfectly sinusoidal signal, such as the harmonic part of the ACS (2.56) may be represented in this space as linear combinations of complex sinusoidal vectors

$$\mathbf{e}(\omega) := (1, \exp -\omega \Delta t, \dots, \exp -\omega(L-1)\Delta t)^T$$

which may also serve to write a compact expression for the signal matrix S

$$S = \sum_{l=1}^P \mathbf{e}(\omega_l) \tilde{a}_l(\omega_l)^2 \mathbf{e}(\omega_l)^H.$$

We may safely assume that for small microclusters $P < L$ is always valid. In this case, it can be shown (see [Mar87]) that S has rank P and therefore only P nonzero eigenvalues $\lambda_1, \dots, \lambda_P$, such that the eigendecomposition of R is given by

$$R = \sum_{k=1}^P (\lambda_k + \rho_w) \mathbf{q}_k \mathbf{q}_k^H + \sum_{k=P+1}^L \rho_w \mathbf{q}_k \mathbf{q}_k^H.$$

The eigenvectors $\{\mathbf{q}_{P+1}, \dots, \mathbf{q}_L\}$ that span (part of) the noise subspace all have the same eigenvalue and should therefore easily be distinguishable from the \mathbf{q}_k of the signal subspace. In practice their eigenvalues will show dispersion due to the fact that a finite number of steps has been used to estimate c_{vv} , but their moduli are usually markedly smaller than those of the signal subspace eigenvalues, provided that L is sufficiently large. As soon as the \mathbf{q}_k of the noise subspace are known, they may be used to construct the MUSIC frequency estimator function by the definition

$$P_{MUSIC}(\omega) = \left[\sum_{k=P+1}^L |e^H(\omega)\mathbf{q}_k|^2 \right]^{-1}. \quad (2.58)$$

Whenever a signal vector $\mathbf{e}(\omega)$ happens to lie within the signal subspace, $P_{MUSIC}(\omega)$ should diverge by virtue of the orthogonality of noise and signal subspaces. In practice, estimation errors will cause the function (2.58) to be finite, but with very sharp peaks at the frequencies ω_l . On the other hand, if $\mathbf{e}(\omega)$ belongs to the noise subspace, it is desirable to choose L as large as possible, in order to maximize the overlap with the noise subspace eigenvectors, since this results in a large signal-to-noise ratio. In practice, a value $L \geq 5P$ seems to be recommendable ([Koh94]).

However, it has been observed [FAPC91], that the stability of the MUSIC algorithm is reduced in the presence of anharmonicity and/or a short run, causing frequencies to move significantly when varying the sampling interval Δt and/or L . In order to improve the stability of the MUSIC algorithm in such situations, Kohanoff [Koh94] proposed a combination of MUSIC with a projection technique that singles out the normal mode components of the trajectories. For this purpose, a first MUSIC estimate of the frequencies ω_l is used to perform a least-squares fit of the MD velocity sequence (2.57) to a linear combination of sinusoidal functions at these frequencies

$$\bar{\mathbf{v}}(t_n) = \sum_{l=1}^P b_l \boldsymbol{\xi}_l \sin(\omega_l n \Delta t + \phi_l).$$

The amplitudes and phases of the eigenmodes as well as the eigenvector components are the fitting parameters. The variance of the fit is minimized using the SD algorithm, imposing orthogonality on the eigenvectors $\boldsymbol{\xi}_l$ of the modes at every iterative step using the Gram-Schmidt algorithm. Then the velocity sequence is projected onto the eigenvectors

$$\mathbf{v}^l(t_n) = \boldsymbol{\xi}_l (\boldsymbol{\xi}_l^H \mathbf{v}(t_n))$$

to filter out a large amount of both other modes and the noise that usually bias the estimator (2.56). Depending on the quality of the first estimate, a further application of MUSIC to every projected sequence \mathbf{v}^l will either yield an improved estimate of the frequency ω_l , or it will show several peaks, none of them close to the original, indicating a spurious frequency. Applying in turns MUSIC and then the projection of the ionic velocities onto the eigenmodes, the scheme may be repeated until self-consistency in the

variance of the fit is reached. It is possible to improve the signal-to-noise ratio further by performing a symmetry decomposition of the MD trajectory by conventional group theoretical analysis using projection operators [MSB94] and applying the scheme to the symmetrized trajectories. The final accuracy of the procedure can be assessed from the residual deviation of the fit and a more extensive simulation should be performed, if it does not prove satisfactory. This approach has been successfully applied to the determination of the vibrational spectra of C_{60} [KAP92], C_{70} [OAKP94] and ferrocene $[Fe(C_5H_5)_2]$ [MSB94]. The results presented in section 3 have been obtained with a version of Kohanoff's program modified by Margl *et.al.* [MSB94].

2.3.4 Computational Cost

It is apparent that the CP method as described in the previous sections offers several advantages over approaches based on matrix diagonalization:

- It does not require the evaluation and storage of the full Hamiltonian ($\mathcal{O}(N_{PW}^2)$ words of memory, where N_{PW} denotes the number of PWs in the expansion of the wavefunctions).
- It avoids matrix diagonalization, which is computationally very expensive, as the number of operations indeed grows as $\mathcal{O}(N_{PW}^3)$.
- It offers the particular attractive feature of being an iterative scheme; once $E^{ps}[\{\phi_n^{ps}\}]$ has been minimized for a given ionic configuration, it is straightforward to use the solution as a starting point for another (not very) different geometry. Furthermore, the calculation can be started with a low E_{cut} and then be improved by adding more PWs.

However, the CP scheme requires only the storage of the wave functions, i.e., $\mathcal{O}(N_{val}N_{PW})$ words (N_{val} is the number of valence electrons), plus the storage of the local potential

$$V_{loc}(\mathbf{r}) := (V^H[\bar{n}] + V_\sigma^{xc}[n_+^{ps}, n_-^{ps}] + \tilde{v}_{ps}^{loc})(\mathbf{r}), \quad \tilde{v}_{ps}^{loc}(\mathbf{r}) := \sum_{\mathbf{n}, \nu} \tilde{v}_{ps}^{loc, \nu}(\mathbf{r} - \mathbf{R}_\nu^n),$$

which requires $\mathcal{O}(N_{rs})$ words. N_{rs} denotes the number of points of the FFT mesh (both real-space and reciprocal space), which is $N_{rs} \simeq x^{3/2}N_{PW}$ (x has been defined in section 2.3.1 as the ratio between E_{dcut} and E_{cut}). The basic steps in the computation of $E^{ps}[\{\phi_n^{ps}\}]$ and $\partial E/\partial c_n^{ps}(\mathbf{G})^*$ are illustrated in Fig. 2.2; this shows the most convenient space (real or Fourier space) chosen for the evaluation of different terms, and the order of operations needed for the calculation of the various contributions. It is common practice [EMR93] to consider only multiplications and/or divisions as contributions to the operation count, since they are the most expensive elementary operations on a computer. As indicated in the diagram, direct (\rightarrow) or inverse (\leftarrow) FFTs are used to transform between real and reciprocal space. The transforms are handled by a standard fast Fourier routine and need not to be discussed here. From results of computational analysis (see, for instance [PTVF92]) it is

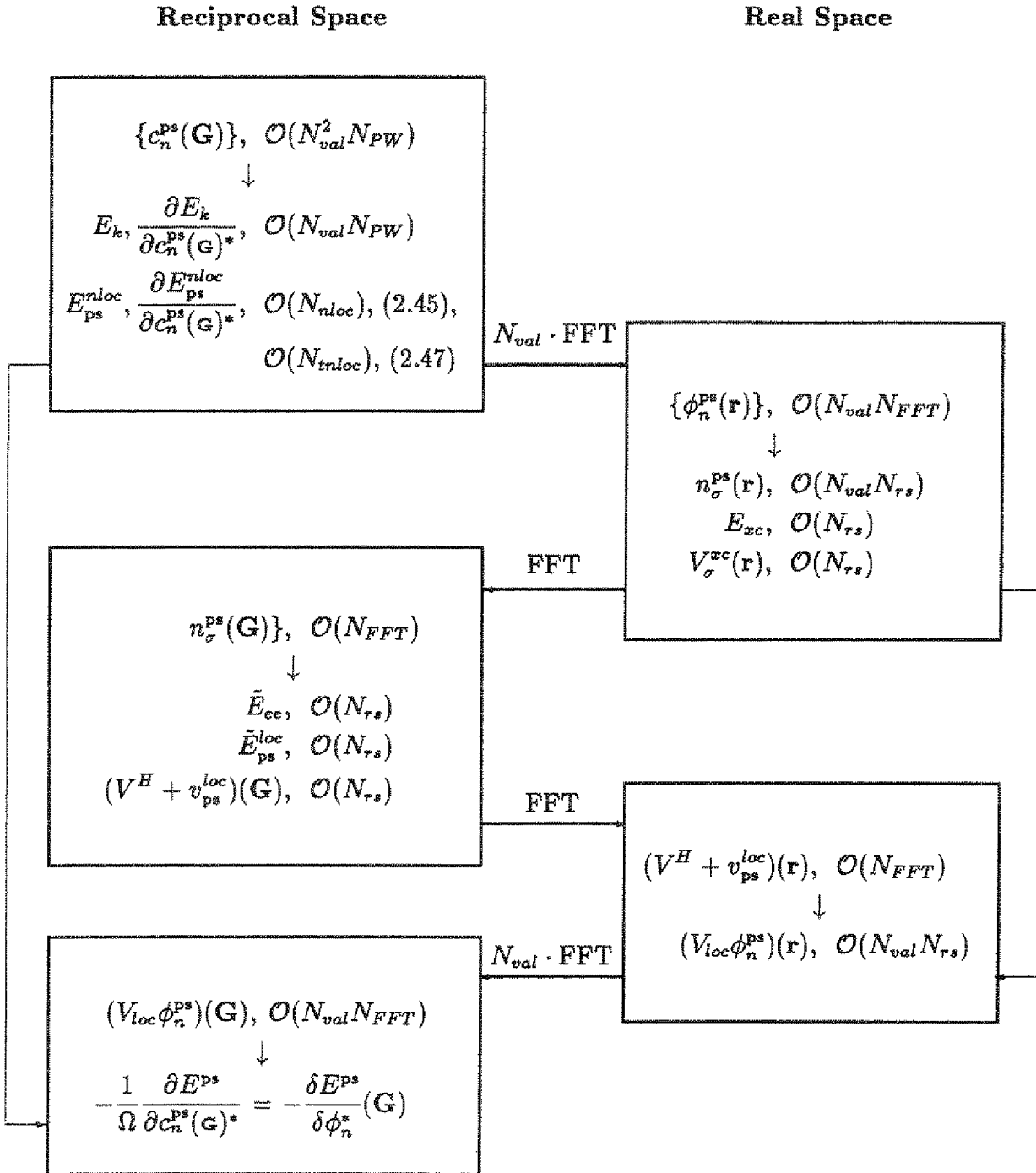


Figure 2.2: Block diagram illustrating the basic steps making up one iteration in the computation of the energy and the forces on the electrons, together with the number of operations needed in their calculation. See text for the definition of the various quantities.

known to require $N_{FFT} \simeq N_{rs} \log_2 N_{rs}$ operations. Depending on the form of the nonlocal PP used (eqs. 2.45 or 2.47), $N_{nloc} \simeq N_{GH} N_L N_I N_{val} N_{PW}$ and $N_{tnloc} \simeq N_L N_I N_{val} N_{PW}$

operations are required respectively for its contribution to the energy and the forces, where N_I is the total number of atoms, $N_L = \sum_{l=0}^{l_{max}} (2l+1)$ and N_{GH} is the number of integration points of the Gauss-Hermite integration formula. For systems where N_{val} is much smaller than N_{PW} , the most time-consuming steps are then the $2N_{val}$ FFTs needed to set up the density in real space and the contribution of V_{loc} to the forces on the electrons in reciprocal space. For sufficiently large systems the orthogonalization of the wavefunctions (first line of the uppermost block in Fig. 2.2) which grows as $N_{val}^2 N_{PW}$, dominates and the numerical cost of the algorithm still grows with the third power of the system size. The search for algorithms that scale quadratically or even linearly with system size (see, for instance, [ODMG95, MG94, HTP94]) is the subject of continuing research interest.

The various terms shown in Fig. 2.2 are updated once during an SD or MD step. On the other hand, in a single CG step, $E^{ps}[\{\phi_n^{ps}\}]$ and n_σ^{ps} are evaluated three times to minimize E^{ps} along the conjugate direction \mathbf{d}_n (see section 2.1.3). This leads to an increase of the absolute computational cost of a CG step by about a factor of 2 – 3 with respect to an SD and/or MD step, but the difference in cost is greatly reduced and is more than counterbalanced by the better efficiency of the former method. It is well known [ŠCPB89, BG90], and has been verified in the present calculations, that the CG algorithm reduces the number of iterations by a factor of 5 – 10, depending on the system in study. Some absolute figures to assess the demand of the programs for computing time for the class of systems studied here may be found in section 3.

Chapter 3

Results

Up to now, there is little structural information about microclusters (i.e., clusters with up to ~ 13 atoms) available from experiments [MPC95]. One reason for this situation is simply given by the size of these particles, which are too small for traditional solid state methods as nuclear magnetic resonance (NMR) or x-ray diffraction to be directly applicable. The formation of single crystals of microclusters is, however, severely hampered by the often high reactivity of these molecules already present at room temperature, which results from “dangling bonds”. Exceptions are rare, consisting of clusters with saturated bonds, such as small clusters of sulfur and selenium [Don74] and several carbon clusters such as C_{60} [FSM⁺91]. On the other hand, photoelectron detachment spectroscopy (PE) is now a well-established experimental tool for the study of structural and electronic properties of size-selected clusters. These experiments usually investigate charged clusters, which allow for highly selective mass-separation in mass spectrometers by simply applying electric and/or magnetic fields. The spectra convey a wealth of information on electronic excitation properties that have the potential to provide a valuable source of structural information, where opportunities for direct comparison with experiments are rare. The interpretation of these spectra still remains a prominent task in the field of cluster physics. To clarify the origin of the various features contained in these spectra a close collaboration between theoretical and experimental physicists would be desirable, as these spectra depend usually on (and can be modified by) many experimental parameters. An experimental group at the Forschungszentrum Jülich led by Gerd Ganteför has been able to check our theoretical predictions by highly resolved photoelectron detachment measurements [GPS96]. Therefore, after presenting some computational details of our method in section 3.1, a short summary of the experimental setup will be given in section 3.2 to provide the reader with some information that will be needed for the discussion of our results in sections 3.3-3.5.

3.1 Computational Details

As already mentioned in section 2.3, we use a repeated-cell scheme and consider only Bloch waves at the $k = 0$ point of the BZ. In the calculations for clusters of sulfur and phosphorus a large face-centered cubic unit cell with lattice constant 30 a.u., was used, while a simple cubic unit cell with lattice constant 20 a.u. was used for the Si_nC_m^- molecules. No further symmetry restrictions have been applied to the MD simulations. The calculations for the larger clusters were repeated using a larger cell (lattice constant 36 a.u. for S_n^- clusters, 30 a.u. for Si_nC_m^- clusters), which resulted in negligible changes (less than $\sim 1\%$) in bond lengths, bond angles and dihedral angles. As already mentioned in section 2.3.1, for clusters of sulfur and phosphorus we use the PP parameters of Bachelet *et al.* [BHS82] with *sp* nonlocality ($l_{\text{max}} = 2$) and energy cutoff $E_{\text{cut}} = 14$ Ry for the orbital functions. For the density, we chose $E_{\text{dcut}} = 28$ Ry, which results in ~ 3200 and ~ 9000 plane waves in the expansion of the wave functions and the density, respectively. As has been shown in previous calculations on neutral sulfur [HJCP88, JH90b] and phosphorus [JH90c] clusters carried out at our institute, this provides a reliable description of structural parameters and binding energies less than 1% from the convergence limit. Test calculations on C_2 indicated,

PP	E_{cut} (Ry)	D_e (eV)	r_e (a.u.)	ω (cm $^{-1}$)
BHS	18	-5.96	2.54	1569
BHS	27	-6.76	2.41	1853
BHS	39	-6.95	2.37	1868
BHS	54	-7.05	2.36	1871
BHS	70	-7.11	2.35	1883
TM	18	-6.12	2.47	1537
TM	27	-6.91	2.37	1847
TM	33	-7.06	2.35	1878
TM	39	-7.15	2.34	1899
TM	53	-7.18	2.34	1897
TM	70	-7.19	2.34	1896
AE-LSD ^a		-7.19	2.35	1869
CI ^b		-5.8	2.35	1940
exp. ^c		-6.21	2.34	1855

^aRef. [PA82].

^bRef. [RB87].

^cRef. [HH79].

Table 3.1: Spectroscopic parameters (see text) of C_2 , $^1\Sigma_g^+$. The frequencies have been determined from the second derivatives of the potential energy curve.

however, that an application of the same kind of PP to compounds of this element is not desirable, as its use would require a comparatively high cutoff of more than 50 Ry to obtain a comparable level of accuracy. The results for the well-depth D_e , the bond length

r_e and the vibration frequency (ω) for the $^1\Sigma_g^+$ GS of C_2 are given in table 3.1 (see the values labeled “BHS”). This led us to test *sp* nonlocal PPs of Troullier and Martins [TM91] on the mixed C-Si clusters. As can be deduced from table 3.1 (values labeled “TM”), this PP shows more favourable convergence properties. Full convergence, however, cannot be claimed with our choice for E_{cut} , i.e., 30 Ry, although all parameters shown deviate by less than 2% from their values at $E_{cut} = 54$ Ry (which may serve as a reference point). Further tests included several other states of C_2 , Si_2 and SiC, which all showed a less critical behaviour. Our choice for the parameters leads to ~ 11000 and ~ 31000 PWs in the expansion of the wave functions and the density, respectively. For clusters of S_n^- and P_n^- , the factorized form (2.36) of the nonlocal part of the PP was adopted to speed up calculations, whereas, in the case of $Si_nC_m^-$ clusters, a Gauss-Hermite integration with $N_{GH} = 13$ integration points was used to evaluate contributions from the nonlocal parts (2.35) of the PP to the energy and the forces.

With appropriate values of the artificial mass for the electronic degrees of freedom $\mu = 300$ a.u. and the integration time step $\Delta t = (2-7) \times 2.419 \cdot 10^{-17}$ seconds, the deviations from the BO energy surface during the MD runs have always been less than 0.005 eV per atom for times of the order of ~ 2000 time steps.

Before applying our extrapolation scheme to calculate the total energy of charged clusters, we ensured that the density was always small near the cell boundaries by translating and/or rotating the clusters within the cell. We tested the energy extrapolation mainly on several sulfur clusters. The change in the energy of S^- using an extrapolation parameter of 16 instead of 8 (see section 2.3.2) was only $\sim 3 \times 10^{-5}$ eV, so that our choice of this parameter should be very reliable. Further tests involved increasing the FFT mesh from 32^3 to 48^3 points and the energy cutoff from 14 to 37.8 Ry, with an increase in the number of plane waves in the expansion of the density to over 39000. The change in the electron affinity of S^- (2.42 eV to 2.37 eV) indicates that further expansion of the basis set will change little. We have also tested the effect of increasing the dimensions of the unit cell on our extrapolation scheme. For the C_1 isomer of S_7^- discussed below [Fig. 3.12(a)], we increased the lattice constant from 30 to 36 a.u., enlarged the FFT-mesh to 36^3 points and the number of plane waves in the expansion of the density to ~ 16000 . The calculated vertical detachment energy (VDE) decreased by only 0.02 eV.

For the exchange-correlation functional of the electron gas, we have used the Vosko *et al.* [VWN80] (for S_n^- , P_n^-) and Perdew-Zunger [PZ80] (for $Si_nC_m^-$) parametrizations of the Monte Carlo numerical results of Ceperley and Alder [CA80], respectively.

GS and local minima are found by selecting initial geometries of sulfur, phosphorus and silicon-carbon clusters from those suggested in the literature ([HJCP88, JH90b] for S_n , [JH90c, JS92] for P_n) and/or found upon MD simulations on isomeric structures of the neutral clusters (all Si_nC_m clusters). Taking the neutral local minimum shapes as trial initial states, we perform an extensive MD search for the anionic clusters finding several close local minima by means of a dynamical simulated annealing strategy. First we relax the electronic degrees of freedom to their GS and then run repeated cycles of CG (less than ~ 100 time steps), combined SD (electrons and ions, ~ 10 time steps) and CP-MD (~ 1000 time steps). As described in section 2.2.1, we keep the instantaneous temperature

of the simulations during the MD runs at constant values in the range of 400-1000 K to within a certain tolerance (± 10 K). The temperature is then reduced to 100-300 K in the vicinity of local minima. Depending on the size of the system and the quality of the initial geometry, about 5000-20000 MD steps are needed to find the most prominent low-lying local minima nearby. The CPU time required for each time step was in the range of 1-9 seconds on a Cray YMP8/864 computer, depending on the number of occupied electronic states and the energy cutoff used.

For the comparison with experimental PE spectra, we focus on vertical excitation processes; i.e., we keep the atomic geometry unchanged. For every anionic cluster in its GS, we consider all the final states corresponding to the removal of a single electron that are covered by the DF formalism, i.e., the lowest states of every symmetry only. These are not GSs and sometimes require calculations for determinantal states that have holes below the Fermi energy, which cannot be obtained by straightforward total energy minimization. Therefore, in order to compute the total energy of the final states, we have adopted a constrained minimization procedure, in which we relate the occupation numbers and the order or symmetry of the orbitals.

3.2 Experimental Setup

The present section is devoted to a brief description of those aspects of the experiments accompanying our calculations that concern the discussion of our results in the following sections. A more detailed description of the apparatus may be found in [CGE92]. The experimental setup as depicted in Fig. 3.1 consists of a pulsed arc cluster ion source (PACIS) [GSLMB90, SLJ⁺91], a time-of-flight (ToF) mass spectrometer, an excimer laser for electron detachment, and a time-of-flight electron spectrometer. The sulfur clusters are generated by pulsed ignition of an electric arc, the lower electrode of which has the shape of a crucible containing the material under investigation. About 10% of the emitted material is charged. Reactive materials such as phosphorus require special treatment to avoid direct contact with air. In this case, the source chamber is designed as a glove box that is flooded with an inert gas (N_2) during manipulation and evacuated during the measurements. For the same reason, phosphorus must be stored under water outside the chamber, which is a source of oxide and hydride impurities in spite of the efforts to minimize contamination (see section 3.4 for a discussion of the implications on the measurements). During ignition, a pulse of He gas is flushed through the gap between the electrodes and carries the vaporized material into an extender, where clusters grow on cooling. After leaving the extender, the gas containing the neutral and ionic clusters passes through a conical nozzle into vacuum and forms a supersonic jet. After passing a skimmer, the anions in the beam are accelerated in a pulsed electric field (time-of-flight (ToF) mass spectrometer), where the clusters are accelerated to the same kinetic energy $E_{kin} = eU$ and thereby separated according to their time-of-flight or their masses, respectively. A typical mass spectrum [see, e.g., Fig. 3.3(II)] contains lines corresponding to every size of clusters present in the beam. The overall shape of the spectrum depends on the following parameters of the source:

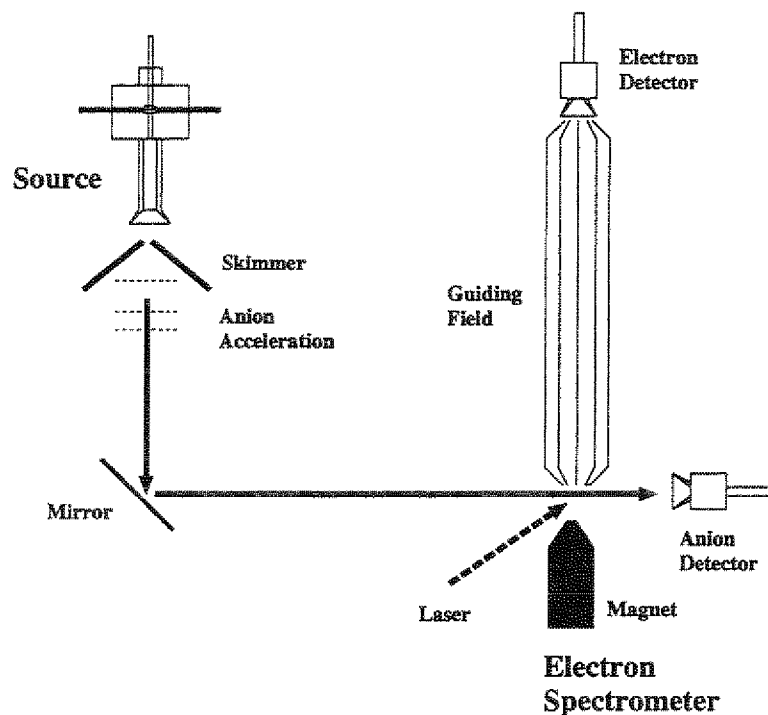


Figure 3.1: Schematic experimental setup.

- the intensity of the He gas pulse (stagnation pressure),
- the time-delay (Δt_{HA}) between the opening of the He valve and the ignition of the arc,
- the time-delay (Δt_{AE}) between ignition and the switching on of the electric field,
- the voltage of the arc, and
- the duration of the arc.

It is important to discuss the effect of changing these parameters, since this can result in the preferential generation of different isomers. A lower intensity of the He pulse results in a slower transport of the clusters through the extender and favours the formation of larger clusters. The time delay Δt_{HA} has a similar influence, because at the beginning and the end of the He pulse its intensity and therefore its flow velocity is low. The parameter Δt_{AE} determines whether clusters leaving the source first or later are detected in the mass spectrum. Clusters leaving the source immediately after ignition have spent a short time in the extender and are smaller. The voltage of the arc determines the rate of vaporization and the partial pressure of the material, a large value of which results in more collisions and larger clusters. The duration of the arc has only a minor influence on the mass spectrum.

Finally, the anion beam is directed into the interaction region of a “magnetic bottle” ToF electron spectrometer. A selected bunch of phosphorus clusters of a particular size

is irradiated by a UV-laser pulse of energy 100 μJ –1 mJ (second, third, and fourth harmonics of a Nd-Yag laser, corresponding to $h\nu=2.33$, 3.49, and 4.66 eV, respectively). The detached electrons are guided towards the electron detector by magnetic fields, and their kinetic energies E_{kin} are determined from the measured time-of-flight. Their binding energy E_b in the cluster is then determined by the equation of the photoelectric effect

$$E_b = h\nu - E_{kin}.$$

The energy resolution, which is limited by the Doppler effect due to the velocity of the anions, increases with decreasing electron kinetic energy and increasing mass of the anions. In the measurements presented in sections 3.3-3.5 it varies between 0.02-0.1 eV. There is also an uncertainty in the absolute value of the BE of ± 0.05 eV.

3.3 Sulphur Cluster Anions

S_n^- clusters constitute an ideal starting point for the determination of cluster structures from PE data, since the structures of their neutral counterparts are among the best characterized of all atomic clusters. One reason for this is the fact that sulfur is exceptional in that many S_n microclusters either occur as or may be prepared as molecular crystals ($n=6-8, 10-13, 18, 20$) [Don74, Ste84], which allows for the application of x-ray structural analysis.

In recent years there have been studies of the neutral clusters using a range of experimental techniques. Raman spectroscopy of sulfur vapor up to 700°C [Ref. [LPC⁺88]] indicates the presence of chainlike species of S_3 , two isomers of S_4 , chainlike helical conformers with $n > 4$, and cyclic species with $n=6, 7, 8$. Infrared studies of matrix isolated sulfur clusters [BMA91] have also been interpreted to imply the presence of two S_4 isomers.

The characterization of the structures of the cluster ions (S_n^\pm) is more difficult, although there has been much evidence for their existence. The cations S_n^+ were detected up to $n=56$ several years ago [Mar84]. The sulfur anions S_n^- have also been the subjects of many studies. S^- , S_2^- , and S_3^- have been identified in single crystals [LJ73] and their electron affinities in the gas phase have been determined by photoelectron spectroscopy to be 2.077 eV [HL85a], 1.66 eV [CBH74], and 2.09 eV [NE86], respectively. The reactivities of S_n^- ions up to $n=6$ with several molecular species have been measured by Fourier transform ion cyclotron resonance (FT-ICR) [SBNSB92], and reactions with NO_2 were observed in all cases. For $n=2-5$ there is a direct transfer of an electron to nitric oxide, indicating that the affinities of these ions are less than that of NO_2 (2.28 eV, Ref. [WHMP81]). The reaction of S_5^- with NO_2 led to a considerable yield of S_3^- , which was viewed as evidence for a chainlike rather than a cyclic structure [SBNSB92]. The reactivity of the cations S_n^+ with NO_2 showed a drop at $n=5$, suggesting that there may be a structural transition from chains to rings [SBNSB92]. The wide range of measurements on sulfur clusters documents both the interest in their properties and their structural flexibility. There have also been numerous theoretical studies. Hohl *et al.* [HJCP88] – using a combination of density functional (DF) calculations with molecular dynamics (MD) – and Raghavachari *et al.*

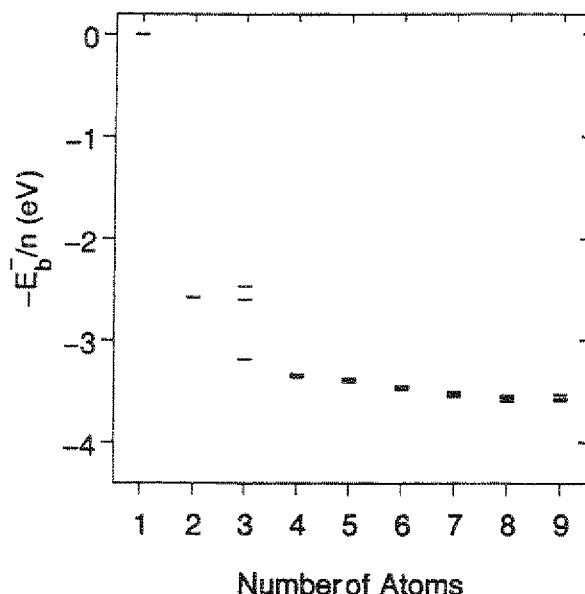


Figure 3.2: Binding energies per atom E_b^-/n for S_n^- clusters as a function of n .

[RRB90] – using Hartree-Fock calculations with fourth order Møller-Plesset corrections – studied neutral clusters up to $n=13$. In the case of S_4 there are several isomers with comparable energies. The two most stable are singlet states with *cis*-planar (C_{2v}) and rectangular (D_{2h}) symmetries, with most calculations showing the former to be slightly more stable [QSM90, vN91] (see Sec. 3.3.1). There have been fewer studies of charged sulfur clusters. Zakrzewski and von Niessen [ZvN94] have recently considered S_3 , S_4 , and S_5 and their positive and negative ions. Their results for the vertical attachment energies of the neutral clusters at their optimum geometries complement our own.

3.3.1 Optimal Geometries, Vibration Frequencies, and Vertical Excitation Energies

We present the structures of energetically low-lying isomers of sulfur cluster anions in Figs. 3.5-3.15 and Tables 3.6-3.11. Distances and bond angles not given explicitly are related by symmetry to values in the tables. Angles are given to the nearest degree, and the sign of the dihedral angle γ has been chosen in accordance with the convention of Ref. [KP60]. Apart from the distances between the end atoms in the “broken ring” structures, we include in the figures and tables only interatomic distances shorter than 5.3 a.u., the minimum in the pair correlation function of liquid sulfur between the first peak for covalently bonded pairs and the second peak for non-bonded pairs [SWL86]. “Bonds” are shown black for distances <4.8 a.u. and white from 4.8 to 5.3 a.u.

We have estimated the relative stabilities of equally charged clusters using self-consistent energies without extrapolation. The calculated binding energies per atom

$$E_b^-/n = [(n-1)E_1 + E_1^- - E_n^-]$$

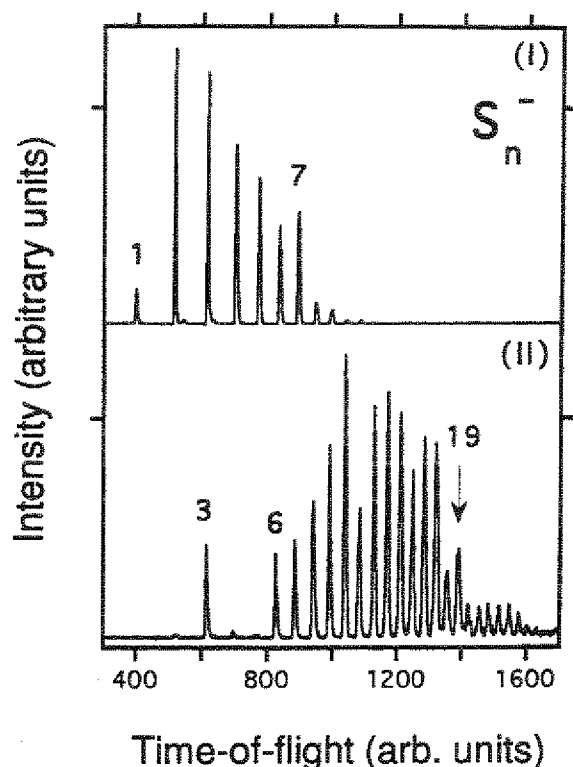
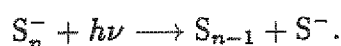


Figure 3.3: Mass spectra of S_n^- clusters generated by the PACIS. I: slow cooling of the sulfur plasma, II: more rapid cooling.

are plotted in Fig. 3.2 for all anionic structures considered here. The stability increases with increasing cluster size n , so that S_n^- clusters should be observable for all n in the range studied here. With the exceptions of the upper C_{2v} and $D_{\infty h}$ isomers of S_3^- , there are numerous minima in the potential energy surface of the anion clusters with similar energies. Most features contained in the PE spectra 3.7-3.13 provided by [GPS96] can be interpreted approximatively according to the Franck-Condon principle. This is the approximation that the transition is vertical, i.e., the transition takes place from the minimum of the BO energy surface of the anion to vibrationally excited states on the BO energy surface of the neutral species without change of the geometrical structure. As the BO-approximation, this is based on the view that the nuclei move much more slowly than electrons. The nuclei respond only after the transition by breaking into vigorous vibration. Some of the spectra (see, e.g., Fig. 3.7) also contain features that do not originate in electronic transitions, such as a feature at very low kinetic energy (4.4-4.5 eV BE, denoted BG) that corresponds to background electrons. These are generated by scattered light striking surfaces within the spectrometer. The laser flux is also high enough to allow fragmentation to take place via multi-photon processes, and features of the spectrum of S^- were found in the spectra of several S_n^- clusters. These result from the process



A second photon can detach the electron from the monomer, resulting in a superposition

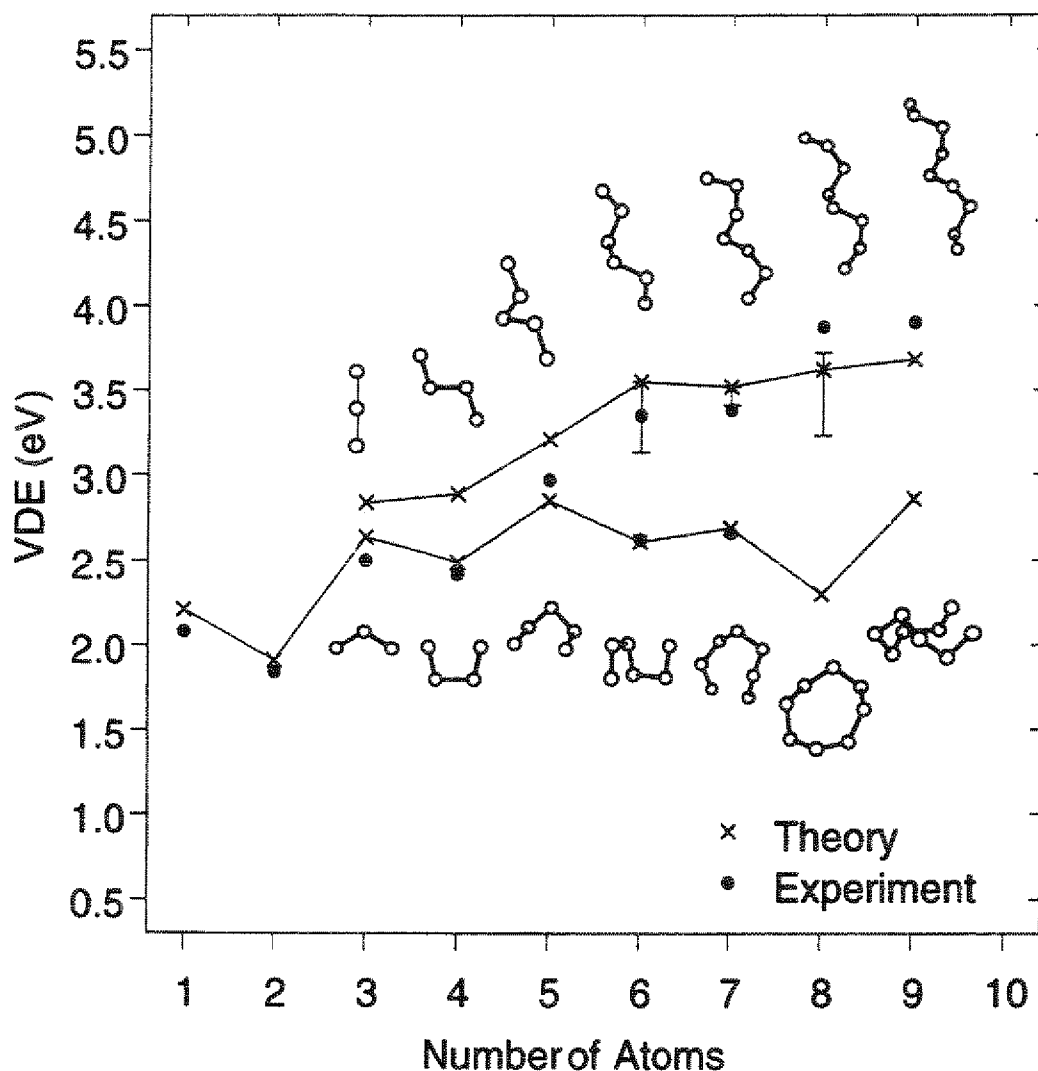


Figure 3.4: Vertical detachment energies of sulfur anions S_n^- , $n=1-9$. Circles: experiment, crosses: calculations, including values for helical chains. The bars cover the values for other chain structures.

of the spectra of the monomer and the cluster. These peaks (~ 2.1 eV, denoted A) are relatively small and easy to identify. The spectra for S_n , $n=1-3$ are also in good agreement with earlier experimental results [HL85a, CBH74, NE86].

The two photoelectron spectra for S_6^- and S_7^- displayed in Fig. 3.13 have been obtained at two different adjustments [(I), (II)] of the cluster source and are of special interest, because they differ completely. As we will show in the following, this indicates the generation of different isomers with different source adjustments. The effect of the corresponding adjustments on the mass spectra is shown in Fig. 3.3.2. In case (I) the source is adjusted to favor small clusters with $n=2-7$. With the exception of the trimer, clusters with $n < 6$ have a very low intensity in spectrum (II). The progression starts at S_6^- and reaches a maximum

n	A	B	C	D	E					
2	1.84(0.05)	1.91	2.3(0.1)	2.45	2.73(0.1)	2.98	4.4(0.15)			
3	Frag		2.50(0.05)	2.64	3.7(0.1)	3.73 3.77	3.9(0.1)	3.95		
4	Frag		2.42(0.05)	2.49	2.7(0.1)		2.96(0.05)	3.19	3.87(0.1)	3.96
5	Frag		2.97(0.03)	2.85 3.28	3.9(0.1)	3.81 3.92				
6(I)	2.62(0.1)	2.61	3.3(0.15)	3.17	4.1(0.1)	3.80				
6(II)	3.35(0.05)	3.55								
7(I)	2.66(0.05)	2.69	3.47(0.07)	3.88	4.14(0.07)	4.15	4.4(0.1)	4.51		
7(II)	3.38(0.05)	3.52	3.6(0.2)	3.62						

Table 3.2: Binding energies (at the maxima) of transitions in the photoelectron spectra of S_n^- , $n=1-7$ (eV). Assignments A-D correspond to those in the spectra [Fig. 3.7], experimental numbers are given in the left column with uncertainties in brackets, calculated values in the right column. “Frag” denotes features assigned to photoemission from S_1^- ions generated by photofragmentation.

at S_{10}^- . Only S_3^- , S_6^- and S_7^- have relatively high intensities in both spectra. Since all the adjustment parameters differ in the two cases and each spectrum can be obtained using more than one set of parameters, it is difficult to analyze the growth processes responsible. However, spectrum (I) is probably the result of a slower process similar to an annealing of the clusters, and spectrum (II) the result of a more rapid cooling process. In spectrum (II), the He pulse is more intense, which increases the jet velocity, so the clusters have shorter times-of-flight than in (I) and spend less time in the extender. If all other parameters were the same, the average cluster size would be smaller in (II) than in (I). However, using a higher arc voltage increases the rate of vaporization and the partial pressure of sulfur, and larger clusters can result. We will provide evidence for this assumption in the following, when we discuss the photoelectron spectra of the individual clusters.

It should be noted that the DF formalism applies to the lowest state of a given symmetry and not just to the ground state of a given molecule, and we use the fitting procedure of von Barth [vB79] to obtain the corresponding physical multiplet energies. The resulting spin multiplets of the atom and the neutral clusters with the optimal geometries of the atom and all ions from S_2^- to S_9^- shown in the figures are given in appendix C. Fig. 3.4 shows a comparison of the calculated VDE with values extracted from the photoelectron spectra, including values for S_6^- and S_7^- found in both spectra. In the case of ions with $n > 5$, there are a variety of chain structures that are local minima on the BO energy surface and we show both the range of VDE values and the result for the helical chain. The curves show that the VDEs depend strongly on the geometry. The overall agreement is remarkably good, indicating a high probability, although no guarantee that the most stable structures were found. Moreover, transitions into excited states of S_n can be identified and provide valuable additional information. Details are given in Table 3.2, where we list the VDE and the binding energies corresponding to different transitions for the spectra shown in Figs. 3.7, 3.8 and 3.13.

Furthermore, vibrational fine structure is resolved in the spectra of S_n^- with $n=2,3,4,6$.

Molecule	Symmetry	Method	Frequency ω_e		
S ₂	$D_{\infty h}({}^3\Sigma_g^-)$	Expt ^a	725.65 (σ_g)		
		Expt ^b	725 \pm 12		
		here	691 (σ_g)		
		CI ^c	778 (σ_g)		
S ₃ 3.9(a)	$C_{2v}({}^1A_1)$	Expt ^d	256 (a_1), 575 (a_1), 656 (b_2)		
		here	247 (a_1), 583 (a_1), 660 (b_2)		
		DF ^e	257 (a_1), 602 (a_1), 690 (b_2)		
		MP2 ^f	263 (a_1), 577 (a_1), 758 (b_2)		
S ₃ 3.9(b)	D_{3h}	here	478 (e'), 625 (a'_1)		
		DF ^g	478 (e'), 619 (a'_1)		
S ₄ 3.9(c)	$C_{2v}({}^1A_1)$	here	111 (a_1), 238 (a_2), 334 (b_2), 336 (a_1), 652 (b_2), 689 (a_1)		
			CI ^h	141 (a_1), 222 (a_2), 353 (b_2), 421 (a_1), 693 (b_2), 701 (a_1)	
		S ₄ 3.9(d)	$D_{2h}({}^1A_g)$	here	67 (b_{3u}), 249 (a_u), 322 (a_g), 335 (b_{1g}), 668 (b_{2u}), 697 (a_g)
				CI ^h	120i (b_{2u}), 262 (a_u), 334 (a_g), 355 (b_{3g}), 782 (b_{1u}), 877 (a_g)
S ₄ 3.10(a)	$C_{2h}({}^1A_g)$	here	98 (a_u), 107 (b_u), 216 (a_g), 462 (a_g), 638 (b_u), 648 (a_g)		
		CI ^h	101 (a_u), 140 (b_u), 252 (a_g), 528 (a_g), 678 (a_g), 681 (b_u)		

^aRef. [HH79].

^bPresent work, photoelectron detachment

^cRef. [QSM90], CISD(TZ2P+f).

^dRef. [LPLC86].

^eRef. [MHA93], TZ2P+f, LSD.

^fRef. [RAH⁺86], quoted by Ref. [MHA93], MP2, 6-31G*.

^gRef. [MHA93], TZ2P+f, LSD

^hRef. [QSM90], CISD(DZP).

Table 3.3: Calculated vibration frequencies ω_e (cm⁻¹) of selected isomers of neutral S_n, n=2-4. Additional labels refer to the figures.

As already mentioned in section 2.3.3, we have used the self-consistent multiple-signal classification (MUSIC) procedure described by Kohanoff [Koh94] to calculate the vibration frequencies of local minima on the BO energy surface of the neutral clusters closest to the geometry of the most stable isomer of the anion. The calculations require non-thermally equilibrated MD trajectories for the system in question. We remove an electron from the anion and allow the systems to evolve in MD runs (at \sim 300 - 500 K) to find the closest minimum on the energy surface of the neutral cluster. The resulting structural parameters are given in Table 3.12. The cluster atoms are then displaced by small amounts, either randomly or according to the eigenvectors of the expected normal modes,

Molecule	Symmetry	Method	Frequency ω_e
S ₆ 3.10(b)	D _{3h}	here	108(e''), 161 (a'' ₂), 207 (e'), 249 (a'' ₁), 271(a' ₁), 301 (e''), 672 (e'), 710 (a' ₁)
S ₆ 3.10(c)	D _{3d}	Expt ⁱ	180 (e _u), 203 (e _g), 265 (a _{1g}), 312 (a _{2u}), 390 (a _{1u}), 451 (e _u), 462 (e _g), 477 (a _{1g})
		here	160 (e _u), 187 (e _g), 255 (a _{1g}), 303 (a _{2u}), 347 (a _{1u}), 458 (e _u), 474 (e _g), 476 (a _{1g})
S ₉ 3.10(d)	C ₂	Expt ^j	100, 104, 111, 117, 151, 155, 161, 181, 188, 215, 222, 245, 256, 297, 416, 436, 442, 454, 455, 463, 477
		here	89(a), 119(b), 135(b), 148 (a), 170(a), 201(b), 219(b), 230(a), 230(b), 242(b), 295(a), 393(a), 419(a), 429(a), 435(b), 454(a), 465(a), 483(a)

ⁱRef. [Ste75a].

^j α -S₉ from Reference [SSS85].

Table 3.4: Calculated vibration frequencies ω_e (cm⁻¹) of selected isomers of neutral S_n, n=6,9. Additional labels refer to the figures.

and the trajectories are followed for 2000 to 8000 time steps at 300 K. The results for selected clusters are given in Tables 3.3 (2-4 atoms) and 3.4 (6 and 9 atoms), together with experimental frequencies. For the clusters with n=2-4 atoms, the agreement is generally better than found with other methods of calculation.

Adiabatic energy differences, i.e., the energy differences between the optimized structures of anion and neutral cluster, will be discussed where appropriate.

S₁⁻

In the case of sulfur, or for any atom with the valence configuration p^2 or p^4 , the energies for the multiplet ³P, ¹D and ¹S can be obtained by von Barth [vB79] fits to the corresponding equations and their energies together with energies of higher excited states with respect to the GS of the anion are given in appendix C. The limits on the reliability of the procedure are shown by the results for the (single determinant) state ³P, where a direct calculation gives a VDE of 2.42 eV. A fit using all three determinants gives 2.21 eV, while the measured value is 2.08 eV [HL85a]. The photoelectron spectra of S₁⁻ [Figs. 3.7(a), 3.8(a)] show a feature assigned to this transition as well as a further feature assigned to the transition into the ¹D state of neutral S at 3.223 eV BE, which is also overestimated by our calculated value (3.63 eV).

Molecule	Symmetry	ω_e
S_2^-	$D_{\infty h}, {}^2\Pi_g$	Expt ^a 589.4 (σ_g) here 577
S_3^- 3.5(a)	$C_{2v}, {}^2B_1$	Expt ^b 235.5 (a_1), 535 (a_1), 571 (b_1) here 216 (a_1), 529 (a_1), 557 (b_1)

^aRef. [CC78] (S_2^- in ultramarine green).

^bRef. [CC78] (from blue and red sulphur solutions in dimethylformamide and hexamethylphosphoramide).

Table 3.5: Calculated vibration frequencies (ω_e , cm^{-1}) of S_2^- and S_3^- .

S_2^-

The attachment of an additional electron to the neutral sulfur isomers generally leads to an appreciable increase in the bond lengths. The calculated value for S_2^- (see Table 3.6) is $\sim 6\%$ larger than that in the neutral dimer (3.61 a.u.) and slightly larger than that reported below for S_3^- . In S_2^- the added electron occupies an antibonding $\pi_g^*(3p)$ orbital and the strength of the double bond in S_2 is reduced accordingly.

As explained in section 2.1.2 and appendix B, the transition energies into some multiplet states, such as the ${}^1\Sigma_u^-, {}^1\Sigma_u^+, {}^3\Sigma_u^-, {}^3\Sigma_u^+, {}^1\Delta_u$ and ${}^3\Delta_u$ of the $\dots 5\sigma_g^2 2\pi_u^3 2\pi_g^3$ configurations of S_2^- , cannot be computed with the von Barth fitting procedure, since the orbitals in the determinants required differ only by phase factors. However, the remaining calculated excitation energies to the ${}^3\Sigma_g^-, {}^1\Delta_g$, and ${}^1\Sigma_g^+$ states of S_2 (1.91, 2.45, 2.98 eV) are in satisfactory agreement with the the first three peaks (1.84, 2.45, 2.73 eV) observed in Fig. 3.7(b).

A single vibrational progression with a frequency of $725 \pm 12 \text{ cm}^{-1}$ is assigned to feature A in the spectrum, in accordance with earlier measurements (725.65 cm^{-1} [HH79]). Although the calculated value [691 cm^{-1} (σ_g)] deviates noticeably from these results, the agreement is better than that achieved by CI calculations (778 cm^{-1} , [QSM90]). The measured frequency of S_2^- (Table 3.5) is for solutions. The dependence on the host is shown, for example, by the Raman frequencies of S_2^- in NaI, KI, and RbI (599.8, 600.0, and 605.7 cm^{-1} , respectively) [SF76]. Data for S_2^- in ultramarine green [CC78] is given in Table 3.5.

S_3^-

We have found three local minima in the energy surface for this ion (Table 3.6). The open ground state [${}^2B_1, C_{2v}$, Fig. 3.5(a)] with valence electron configuration $1a_1^2 1b_2^2 2a_1^2 2b_2^2 3a_1^2 1b_1^2 1a_2^2 4a_1^2 3b_2^2 2b_1^1$ differs from the C_{2v} singlet ground state of S_3 by having a ($\sim 3.6\%$) longer bond and a ($\sim 20\%$) smaller bond angle. The present values (see Tables 3.6 and 3.12) agree well with recent CI calculations (3.58 a.u., 117° for S_3 ; 3.76 a.u., 115° for S_3^-) [ZvN94]. The bond length in the matrix isolated anion has been estimated by electron paramagnetic resonance (EPR) to be 3.97 a.u. [LL78] The calculated dissociation energy (into S_2^- and

Molecule	Symmetry	State	ΔE
S_2^- $d_{12}=3.81$	$D_{\infty h}$	${}^2\Pi_g$	0.0
S_3^- 3.5(a) $d_{12,13}=3.79; \alpha_1=115^\circ$	C_{2v}	2B_1	0.0
S_3^- 3.5(b) $d_{12,13}=4.17; d_{23}=4.20; \alpha_1=61^\circ; \alpha_{2,3}=60^\circ$	C_{2v}	2B_2	1.73
S_3^- 3.5(c) $d_{12,13}=4.06$	$D_{\infty h}$	${}^2\Pi_u$	2.22
S_4^- 3.5(d) $d_{12,34}=3.71; d_{14}=5.83; d_{23}=4.28; \alpha_{1,4}=78^\circ; \alpha_{2,3}=102^\circ$	C_{2v}	2A_2	0.0
S_4^- 3.5(e) $d_{12,34}=3.69; d_{14,23}=4.92$	D_{2h}	2A_u	0.05
S_4^- 3.5(f) $d_{12,34}=3.76; d_{23}=4.03; \alpha_{2,3}=108^\circ$	C_{2h}	2B_g	0.13

Table 3.6: Structure parameters for isomers of S_n^- , $n=2-4$, with energies ΔE relative to the ground state (eV). Bond lengths d_{ij} in a.u., bond angles α_i and dihedral angles γ_{ij} in degrees. Additional labels refer to the figures.

S) is 4.4 eV/molecule (experimentally 3.3 eV/molecule) [NE86], somewhat larger than the estimate found for the dissociation of S_3 [HJCP88]. The second C_{2v} structure [Fig. 3.5(b) and Table 3.6] is a Jahn-Teller distorted version of the D_{3h} structure (equilateral triangle) of S_3 and has an energy much (1.73 eV) higher than the first and much longer bonds (4.20 a.u.). The structure of a high-lying linear [$D_{\infty h}$, Fig. 3.5(c)] isomer is also given in Table 3.6.

The measured excitation energies (2.50, 3.7, 3.9 eV) are consistent with transitions for the open structure [Fig. 3.5(a)] to the 1A_1 , ${}^3A_2/{}^3B_1$ and 3B_2 state of the neutral cluster (2.64, 3.73/3.77, 3.95 eV), but not with excitations for the ring structure [Fig. 3.5(b)] (1.34, 2.93, 2.94 eV for the 1A_1 , 3A_2 , 3B_1 states, respectively). The calculated adiabatic electron affinity (2.50 eV) for the C_{2v} ground state of S_3^- is in acceptable agreement with the experimental value (2.396 ± 0.02 eV). Minor deviations between the VDE (2.50 ± 0.05 eV) and the adiabatic electron affinity (EA, 2.396 ± 0.02 eV) obtained from spectrum 3.7(c) and the values found in an earlier work ([CBH74], VDE= 2.41 ± 0.03 , EA= 2.106 ± 0.014 eV) are attributed to different vibrational temperatures of the anions.

As explained above, the interpretation of the vibrational structure contained in the spectrum requires the calculation of the fundamental modes of the local minimum structures on the BO energy surface of the neutral trimer at the GS geometry of the anion. Meyer *et al.* [MSHO72] assigned a band in the gas phase absorption spectrum at 590 cm^{-1} to the a_1 stretching frequency of S_3 . Raman bands at 651 and 585 cm^{-1} for S_3 in an SO_2 matrix and at 662 and 583 cm^{-1} in solid argon [TB75] were assigned to the b_2 and a_1 stretching modes [HTB73]. A Raman study of sulfur vapor [LPLC86] identified three fundamental modes at 656 , 575 and 256 cm^{-1} , and a more detailed investigation by the same group assigned the a_1 bending and stretching modes to wave numbers of 281 and 581 cm^{-1} ,

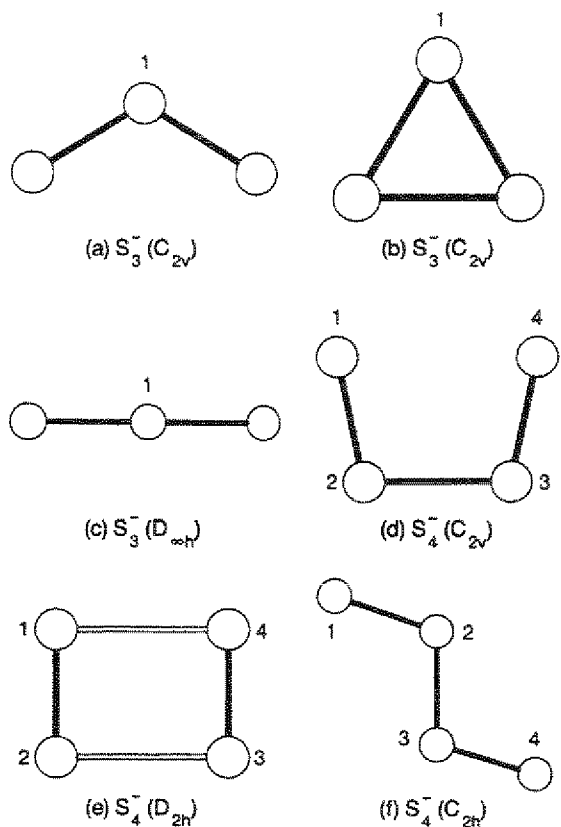


Figure 3.5: Structures of (a-c) S_3^- and (d-f) S_4^- .

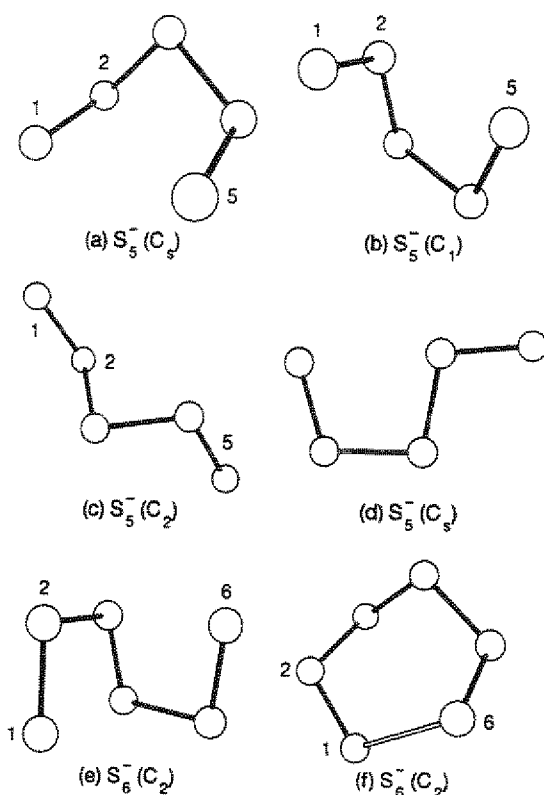


Figure 3.6: Structures of (a-d) S_5^- and (e-f) S_6^- .

respectively [PEC93]. In the infrared spectra of S_3 in solid argon, the b_2 stretching mode has been identified [BMA91], although the wave numbers reported (674.5 , 676.2 and 680 cm^{-1}) depend on the trapping site. While there is some scatter in the measured frequencies, our calculated values of the harmonic vibration frequencies are in overall agreement and deviate least (less than 4 %) from the results in Ref. [LPLC86]. The reoptimization after ionization of the C_{2v} structure [3.5(b)] of S_3^- gave the D_{3h} isomer of S_3 [Fig. 3.9(b), Table 3.12], to which no measured spectral features have been attributed. Vibration frequencies calculated for these two isomers of S_3 using other methods [RAH⁺86, MHA93] are also given in Table 3.12. The vibration frequency ($570 \pm 24 \text{ cm}^{-1}$) encountered in the photoelectron spectrum is larger than that in Ref. [NE86] ($500 \pm 48 \text{ cm}^{-1}$), which might be due to the difference between hot and cold bands. It agrees well with the calculated value $583 (a_1)$ of the C_{2v} isomer, but falls in a pronounced gap of the spectrum for the D_{3h} isomer. There is no evidence that the latter is generated by the PACIS. The measured frequencies of S_3^- are for solutions [CC78] and agree well with the values calculated here (Table 3.5). The structures of both S_3^- isomers [3.5(a) and 3.5(c)] relax on ionization to the C_{2v} isomer of S_3 [Fig. 3.9(a)], whose structural parameters are given in Table 3.12.

S_4^-

Three structures of the anion [Fig. 3.5(d-f)] have very similar energies [Table 3.6]. The most stable – a *cis*-planar structure with C_{2v} symmetry [Fig. 3.5(d)] – was also found in a recent theoretical study [ZvN94], with bond angles $\sim 12\%$ larger and the “long” bond distance $\sim 9\%$ smaller than ours.

We have noted that recent theoretical [QSM90] and experimental work [BMA91] on neutral S_4 indicate that the most stable isomer has *cis*-planar (C_{2v}) symmetry. This is supported by calculations using the present method, where we find that this isomer is 0.05 eV more stable than the planar rectangular ring structure [Fig. 3.5(e), D_{2h}] discussed previously. [HJCP88] The energy extrapolation scheme lifts the near-degeneracy between these two forms, the final separation being ~ 0.11 eV. The D_{2h} form of the anion is not stable, as the additional electron causes one of the longer bonds to open. A third structure 0.13 eV above the C_{2v} isomer is a planar *trans* isomer with C_{2h} symmetry [Fig. 3.5(f)]. A preference for the *cis* form is also evident in the larger anions. Other structures considered here – planar and nonplanar – had higher energies and were unstable on annealing at 300–500 K.

The measured binding energies in the spectrum of S_4^- (Table 3.2) are consistent with the calculated multiplet structures of the C_{2v} [3.5(d)] and D_{2h} [3.5(e)] geometries, but incompatible with the sole presence of the C_{2h} form [3.5(f)] (with multiplet energies 2.89, 3.36, 4.07 eV for 1A_g , 3B_u , 1B_u , respectively). On the other hand, neither the C_{2v} nor the D_{2h} isomer can account for feature C in the spectrum at 2.7 eV BE (see Table 3.2), which in turn compares best with the VDE of the C_{2h} form [2.89 eV (1A_g)]. Therefore, we cannot rule out a contribution of the C_{2v} isomer to the photoelectron spectrum on the base of the present data.

This ambiguity is not removed by the analysis of the vibrational fine structure in the spectrum, although the lower frequency (250 ± 16 cm^{-1}) at feature B assigned to the ground state transition lies closer to the calculated values for the C_{2v} [238 cm^{-1} (a_2)] and D_{2h} [249 cm^{-1} (a_u)] isomers than to any obtained for the C_{2h} form. On the other hand, the second feature termed C in Figure 3.7(d) and Table 3.2 shows a more pronounced vibrational progression corresponding to a vibration frequency of 630 ± 24 cm^{-1} . This value agrees better with the calculated frequencies for the C_{2h} isomer [638 cm^{-1} , (b_u)] than with frequencies calculated for the C_{2v} [652 cm^{-1} (b_2)] and D_{2h} [668 cm^{-1} (b_{2u})] isomers, although the C_{2v} value is still within the error bars. The comparatively large vibrational progression observed at this feature is also more compatible with the C_{2h} structure than with the others, since this structure differs most between the anion and the neutral species (the deviations in the bond angles and the bond lengths are $\sim 4\%$ and $\sim 5\%$ respectively for the C_{2h} isomer compared to less than 2% and 3% respectively for the C_{2v} and D_{2h} isomers). This is consistent with the observation that feature C (at binding energy 2.7 ± 0.1 eV) cannot be assigned to any of the electronic transitions of the C_{2v} and D_{2h} isomers, but fits better to the calculated VDE of the C_{2h} isomer (2.89 eV). As the calculations predict that the C_{2h} isomer is only 0.13 eV less stable than the GS, it is likely that both C_{2v} and C_{2h} geometries or all three isomers of S_4^- considered here contribute to the spectrum.

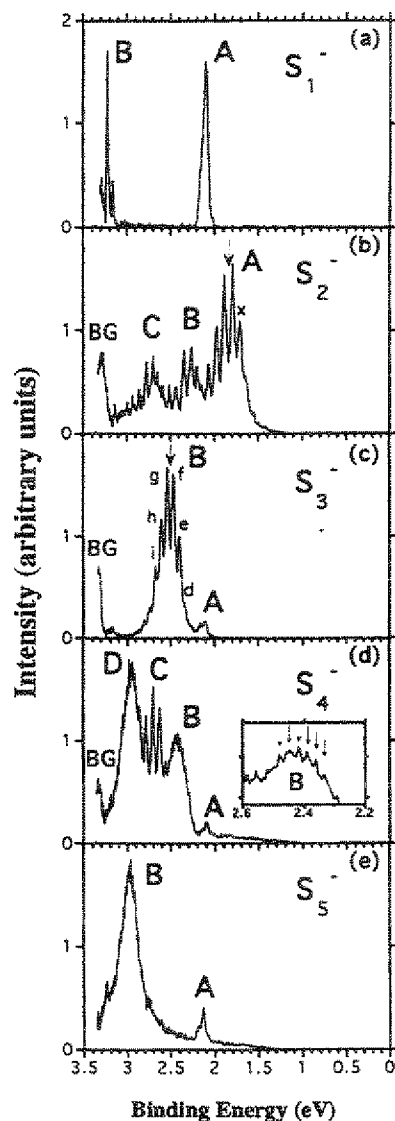


Figure 3.7: Photoelectron spectra of S_n^- -clusters ($n=1-5$) recorded at $h\nu=3.49$ eV photon energy. See text for a discussion of the features marked.

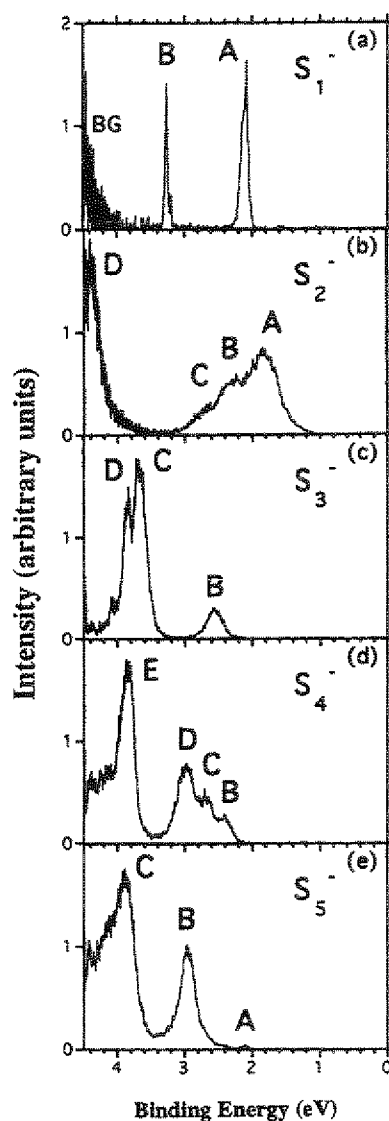


Figure 3.8: Photoelectron spectra of S_n^- -clusters ($n=1-5$) recorded at $h\nu=4.66$ eV photon energy. See text for a discussion of the features marked.

The fundamental vibration modes of S_4 have been studied in both Raman and infrared spectroscopy. Clark and Cobbold [CC78] reported Raman bands at 352 cm^{-1} and 674 cm^{-1} , and Brabson *et al.* [BMA91] measured infrared spectra of sulfur in an argon matrix. Absorptions at 661.6 and 642.4 cm^{-1} behaved differently on annealing and photolysis, and were identified with the C_{2v} open-chain [Fig. 3.9(c)] and the branched ring nonplanar isomers of S_4 , respectively. We compare the vibration frequencies found in the present investigation also with these values and with those of Quench *et al.* [QSM90] in Table 3.3. While it is not possible to make a definite assignment on the basis of these results,

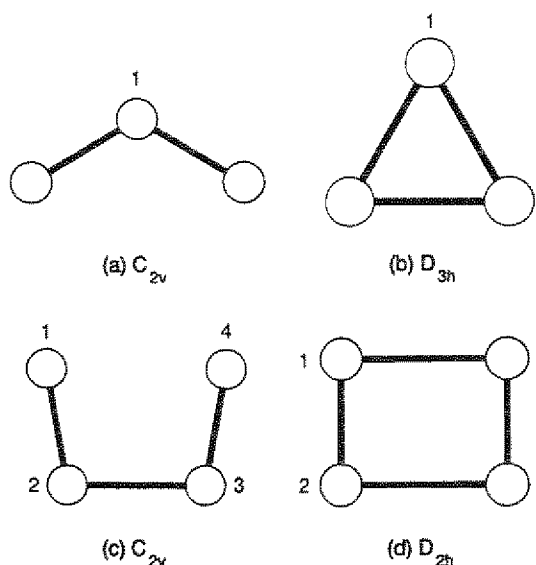


Figure 3.9: Structures of selected isomers of neutral S_3 and S_4 .

particularly as the measured values are in a matrix, our calculations show modes at 652 and 689 cm^{-1} for the C_{2v} isomer [Fig. 3.9(c)].

We note that the calculated value for the adiabatic electron affinity of the C_{2v} isomer of S_4^- (2.38 eV) agrees very well with the results of a CI calculation with Davidson correction, 2.46 eV [ZvN94].

S_5^-

The most stable isomer in S_5^- (Table 3.7) is a broken ring with C_s symmetry [Fig. 3.6(a)], reminiscent of the C_s “envelope” predicted for S_5 [HJCP88], with one bond broken by the additional electron. This has also been found in CI calculations of S_5^- [ZvN94], where the large interatomic separation (5.70 a.u.) is 10% shorter than ours (6.35 a.u.). The extra electron occupies an antibonding orbital with a large amplitude in this region. We show below that the same is true for S_6^- and S_7^- , where the addition of an electron to neutral rings also leads to bond breaking. The next local minimum in the energy surface (0.04 eV higher) is a *cis-trans* (C_1) form [Fig. 3.6(b)] that can also be derived from the C_s isomer of S_5 by breaking another bond. The comparatively small dihedral angle in this cluster can be viewed as a remnant of the pattern already encountered in the *cis-planar* (C_{2v}) structure of S_4^- . Another isomer (0.09 eV above the most stable) is a helical chain [Fig. 3.6(c)] with C_2 symmetry. The terminal bonds in this structure have a similar length to the bonds in S_3^- , indicating a bond order between one and two. The central bonds are longer, approaching the value in catenapolysulfur S_∞ (3.90 a.u.) [Don74]. A similar pattern is observed in the bond lengths of longer helical chains. A gap of 0.18 eV separates these structures from a *cis-trans* planar (C_s) form [Fig. 3.6(d)]. This also contains the motif of the *cis-planar* (C_{2v}) isomer of S_4^- and was found by annealing the C_s isomer of neutral S_5 considered previously

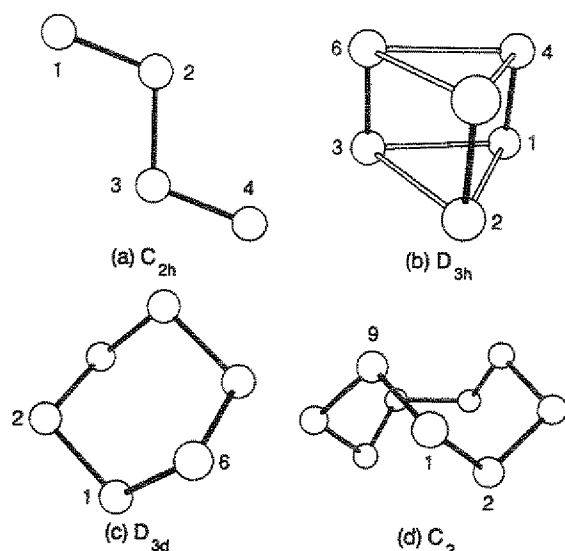


Figure 3.10: Structures of selected isomers of neutral S_4 , S_6 , and S_9 .

Molecule	Symmetry	State	ΔE
S_5^- 3.6(a) $d_{12,45}=3.76$; $d_{15}=6.35$; $d_{23,34}=3.98$; $\alpha_{1,5}=87^\circ$; $\alpha_{2,4}=108^\circ$; $\alpha_3=95^\circ$; γ_{12} , $-\gamma_{45}=40^\circ$; $\gamma_{15}=0^\circ$; γ_{23} , $-\gamma_{34}=-76^\circ$	C_s	$^2A''$	0.0
S_5^- 3.6(b) $d_{12}=3.79$; $d_{23}=3.85$; $d_{34}=4.23$; $d_{45}=3.71$; $\alpha_2=111^\circ$; $\alpha_3=100^\circ$; $\alpha_4=105^\circ$; $\gamma_{23}=-62^\circ$; $\gamma_{34}=-11^\circ$	C_1	2A	0.04
S_5^- 3.6(c) $d_{12,45}=3.75$; $d_{23,34}=3.98$; $\alpha_{2,4}=112^\circ$; $\alpha_3=98^\circ$; $\gamma_{23,34}=-112^\circ$	C_2	2B	0.09

Table 3.7: Structure parameters for the isomers of S_5^- , with energies relative to the ground state (eV). Bond lengths d_{ij} in a.u., bond angles α_i and dihedral angles γ_{ij} in degrees. Additional labels refer to the figures.

[RRB90].

The pronounced peak B in the spectra [Figs. 3.7(e), 3.8(e)] of S_5^- (2.97 ± 0.03 eV) (feature A is assigned to fragmentation into S_4^-) is closest to the value calculated for the 3.6(a) structure (2.85 eV), but two other structures [Fig. 3.6(b), Fig. 3.6(c)] have excitation energies only 0.04 and 0.09 eV higher. While the VDE of structure [Fig. 3.6(b), 2.80 eV] is also close to the experimental result, the VDE (3.21 eV) and especially the lowest-lying triplet state (3B , 3.34 eV) of structure [Fig. 3.6(c)] fall in a gap in the photoelectron spectrum of S_5^- , and there is no evidence that the latter isomer is generated by the PACIS. A tentative assignment of the features in the spectrum to either 3.6(a) or 3.6(b) would require that peak B stems both from the GS transition and the transition into the corresponding lowest excited states at 3.28 eV [$^3A''$, 3.6(a)] and 3.30 eV [3A , 3.6(b)], respectively. This slightly favors structure 3.6(a), whose transition energy is 0.3 eV higher than the observed peak position, but still lies within the first intense band. While no higher excited states of 3.6(b) can be obtained within LSDA, the broad unstructured feature around peak C at 3.9 eV is compatible with transitions into excited states of 3.6(a) at 3.81 eV ($^1A''$) and 3.92 eV ($^3A'$). Since the calculations predict that 3.6(a) and (b) are almost degenerate ($\Delta E = 0.04$ eV) and no vibrational fine structure could be resolved, the interpretation of the measured spectra is not altogether conclusive, and in view of the uncertainties in both experiment and theory, either (or both) of these structures could be present.

S_6^-

The structure of S_6^- [C_2 , Fig. 3.6(e), Table 3.8] was found by annealing a chainlike geometry and can be seen as two overlapping C_{2v} *cis*-planar sections. The dihedral angle (see Sec. 3.3.2) between the bisecting planes is $\sim 80^\circ$. A puckered chairlike S_6^- ring with C_2 symmetry [Fig. 3.6(f)] is only 0.02 eV higher in energy. The increase in the bond length (to 5.09 a.u.) caused by the additional electron is less than in the S_5^- ground state ring. The remaining structural parameters deviate little from the experimental values in S_6 [Don74], the bond lengths by at most 2%, the bond angles by less than 5%, and the dihedral angles by $\sim 2\%$. Another C_2 boat structure [Fig. 3.11(a)], consisting of two weakly bound sulfur

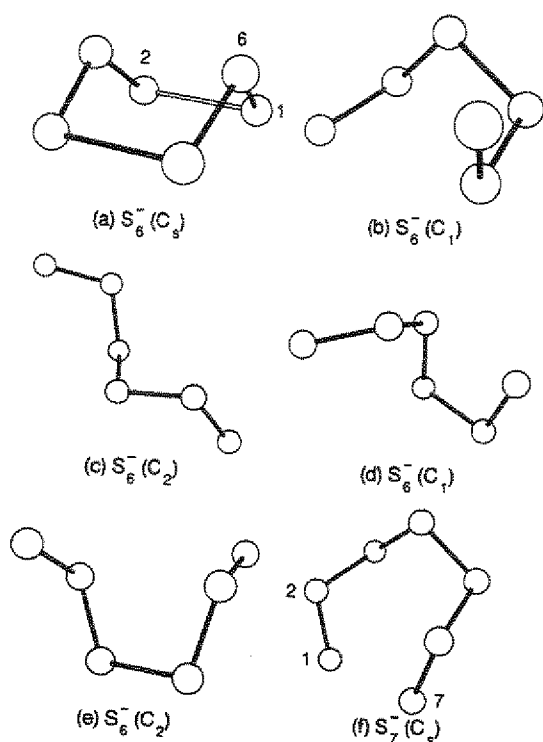


Figure 3.11: Structures of (a-e) S_6^- and (f) $S_7^-(C_s)$.

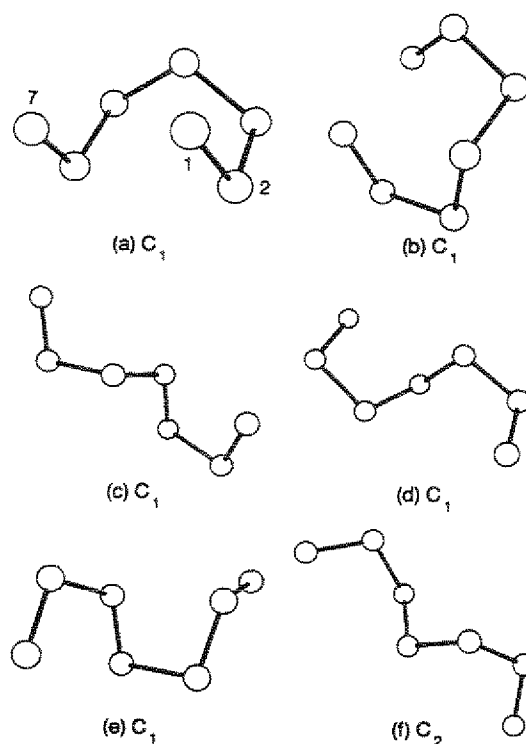


Figure 3.12: Structures of S_7^- .

trimers, lies 0.10 eV above the isomer in Fig. 3.6(e). The energy minimum is shallow and the structure distorts readily to lower (C_1) symmetry on annealing. We also found a C_1 isomer [Fig. 3.11(b)], a helical (C_2) chain [Fig. 3.11(c)], and two structures containing the *cis*-planar motif of S_4^- [Fig. 3.11(d),(e)], with energies 0.12, 0.17, 0.20 and 0.25 eV above the most stable isomer. The all-*trans* chain [3.11(c)] is slightly less stable (by 0.05 eV) than the *cis-trans* chain [3.11(b)]. Annealing of an all-*cis* chain also led to the puckered ring [Fig. 3.6(f)].

The calculated VDE (2.61 eV) of the most stable isomer of S_6^- [Fig 3.6(e)] is in excellent agreement with the measured value for ground state transition in Fig. 3.13(a) (2.62 ± 0.1 eV). Apart from the virtually degenerate structure Fig 3.6(f), whose VDE is 2.70 eV, the other structures have VDEs in the range (2.87-3.55 eV) and their appearance in the spectrum can therefore be ruled out. Although the structures 3.6(e) and 3.6(f) have almost equal energies, the VDE (see above) and higher vertical excitations of the former isomer [3.17 eV (3B), 3.80 eV (1B)] agree better with the peak positions in Fig. 3.13(a) (3.3 ± 0.15 eV, 4.1 ± 0.1 eV) than those of the latter isomer [3.51 eV (3B), 3.89 eV (1B)]. This view is also supported by the comparatively small theoretical AEA for S_6^- (1.86 eV), which is compatible with the large difference between the structures of the ground states of the anion (C_2) and the corresponding neutral prismane cluster [Fig 3.10(c)](D_{3d}). This is an example, which illustrates that neutral and charged clusters might have substantially

Molecule	Symmetry	State	ΔE
S_6^- 3.6(e) $d_{12,56}=3.69$; $d_{23,45}=4.53$; $d_{34}=3.65$; $\alpha_{2,5}=99^\circ$; $\alpha_{3,4}=97^\circ$; $\gamma_{23,45}=-5^\circ$; $\gamma_{34}=-73^\circ$	C_2	2A	0.0
S_6^- 3.6(f) $d_{12,56}=3.80$; $d_{16}=5.09$; $d_{23,45}=3.96$; $d_{34}=3.98$; $\alpha_{1,6}=102^\circ$; $\alpha_{2,5}=107^\circ$; $\alpha_{3,4}=106^\circ$; $\gamma_{12,56}=64^\circ$; $\gamma_{16}=-62^\circ$; $\gamma_{23,45}=-76^\circ$; $\gamma_{34}=75^\circ$	C_2	2B	0.02
S_6^- 3.11(a) $d_{12}=4.97$; $d_{16,23}=3.80$; $d_{34,56}=3.81$; $d_{45}=4.71$; $\alpha_{1,2}=95^\circ$; $\alpha_{3,6}=112^\circ$; $\alpha_{4,5}=97^\circ$; $\gamma_{12,45}=0^\circ$; γ_{16} , $-\gamma_{23}=81^\circ$; γ_{34} , $-\gamma_{56}=82^\circ$	C_s	$^2A''$	0.10

Table 3.8: Structure parameters for isomers of S_6^- , with energies relative to the ground state (eV). Bond lengths d_{ij} in a.u., bond angles α_i and dihedral angles γ_{ij} in degrees. Additional labels refer to the figures.

different geometries. The photoelectron spectrum Fig. 3.13(b) of S_6^- is the first of a series of spectra of larger S_n^- clusters up to $n=6-9$ that have been generated with source adjustment (II). These clusters have relatively high VDE and show at most two clearly resolved transitions at relatively high BE. The only observable peak in Fig. 3.13(b) at 3.35 ± 0.05 eV lies in the range of calculated vertical excitation energies of the chainlike isomers, Figs. 3.11(b-e) (i.e., 3.13-3.55 eV). It may in general be assumed that a comparatively sharp envelope in the spectrum as in Fig. 3.13(b) indicates a similarity in the structures of the anion and the neutral, although this individually depends on the local shapes of both energy surfaces. We therefore searched for the minima on the energy surfaces of the neutral S_6 closest to the chain isomers in Figs. 3.11(b-d). While the chain isomers Figs. 3.11(b,d) readily distort to the ring isomer Fig. 3.11(a), the helical chain Fig. 3.11(c) is the only isomer that preserves both its chain topology and the all-*trans* pattern of its dihedral angles in the neutral species. Relaxation of the neutral chain from the anionic C_2 structure to a rather close C_1 form (not included in the figures) results in an energy lowering of only 0.37 eV. We observed also the reverse transition from the neutral C_1 isomer into the anionic C_2 chain upon charging. The C_1 isomer is stable against MD runs up to 300 K, and its all-*trans* pattern might be stabilized by a rotational energy barrier against distortion to *cis-trans* or all-*cis* patterns that are encountered in the ring isomers (a detailed discussion about rotational barriers in sulphur compounds may be found in [Ste75b, Ste83] the latter also estimates the barrier to be ~ 0.9 eV high). Although the helical chain matches best the features contained in the spectrum, we do not attempt any definite assignment here, since we assume that the clusters generated by the PACIS with source adjustment (II) are the result of a rapid quenching process and do not necessarily represent energetically favourable structures (see the discussion in section 3.3.2).

The S_6^- structure [Fig 3.6(e)] relaxes to the prismane (D_{3h}) form [Fig 3.10(b)] of the neutral cluster after electron removal, which is a local minimum on the energy surface of the neutral cluster. If the structure [Fig 3.6(f)] is taken as the starting geometry for S_6 ,

it relaxes to the (D_{3d}) ground state [Fig 3.10(c)]. The vibration frequencies calculated for both S_6 structures are given in Table 3.4 together with measured values of the latter. The only frequency measured for the S_6 structure ($570 \pm 32 \text{ cm}^{-1}$) is significantly higher than both the calculated and Raman frequencies of the D_{3d} isomer and falls in a pronounced gap of the spectrum for the D_{3h} isomer. Since the vibrational structure was only observed in spectrum $S_6^-(\text{II})$, where the anions are supposed to be chainlike, this is evidence that the neutral cluster does not have time to relax to one of the more stable isomers during the measurement. It is also consistent with the observation [LPC⁺88] that *all* unbranched sulfur rings regardless of the size have no fundamental frequencies above 530 cm^{-1} . To examine this point further, we have studied the vibrations of S_6 by performing thermally non-equilibrated MD-runs starting from the helical (C_2) geometry found for the S_6^- anion. The existence of a totally symmetric (a) vibration with frequency 619 cm^{-1} provides further support for the above picture.

S_7^-

As in the case of S_6^- , there are no structures consisting entirely of planar sections, and the most stable isomer is a distortion of the neutral S_7 ground state, a chairlike ring with C_s symmetry [SRS77a, SRS77b, SSP⁺80]. The “long” bond in S_7 (experimentally 4.12 a.u.) opens to give a distorted chairlike C_s form [Fig. 3.11(f) and Table 3.9] with a broken “bond” of length 5.47 a.u.. This structure was found by annealing an all-*cis* chain. The other changes in the structure of S_7 are also small, with bond lengths changing by less than $\sim 1\%$, and angles by less than $\sim 5\%$. The second longest bond of the S_7 chair [experimentally 3.97 a.u.] can also open in the anion, leading to another C_1 isomer [Fig. 3.12(b)] only 0.02 eV less stable than the first. The additional charge is localized on a “bond” of length 5.59 a.u. Another isomer that is virtually degenerate ($\Delta E \sim 0.005 \text{ eV}$) with Fig. 3.11(f) is a distorted boat (C_1) structure [Fig. 3.12(a)] derived from a C_s isomer in neutral S_7 [HJCP88] by breaking its longest bond. Other isomers [Figs 3.12(c)-(e)] show the planar sections familiar from the *cis*-planar (C_{2v}) structure of S_4^- and have energies in a

Molecule	Symmetry	State	ΔE
S_7^- 3.11(f) $d_{12,67}=3.76$; $d_{17}=5.47$; $d_{23,56}=4.00$; $d_{34,45}=3.91$; $\alpha_{1,3,5,7}=107^\circ$; $\alpha_{2,6}=110^\circ$; $\alpha_4=109^\circ$; $\gamma_{12}, -\gamma_{67}=74^\circ$; $\gamma_{23}, -\gamma_{56}=-104^\circ$; $\gamma_{34}, -\gamma_{45}=82^\circ$	C_s	$^2A''$	0.0
S_7^- 3.12(a) $d_{12}=3.71$; $d_{17}=5.75$; $d_{23}=4.13$; $d_{34}=3.83$; $d_{45}=3.94$; $d_{56}=3.99$; $d_{67}=3.74$; $\alpha_1=100^\circ$; $\alpha_2=108^\circ$; $\alpha_3=103^\circ$; $\alpha_4=109^\circ$; $\alpha_5=104^\circ$; $\alpha_6=110^\circ$; $\alpha_7=93^\circ$; $\gamma_{12}=86^\circ$; $\gamma_{17}=-10^\circ$; $\gamma_{23}=-37^\circ$; $\gamma_{34}=-80^\circ$; $\gamma_{45}=70^\circ$; $\gamma_{56}=58^\circ$; $\gamma_{67}=-84^\circ$	C_1	2A	0.0

Table 3.9: Structure parameters for isomers of S_7^- , with energies relative to the ground state (eV). Bond lengths d_{ij} in a.u., bond angles α_i and dihedral angles γ_{ij} in degrees. Additional labels refer to the figures.

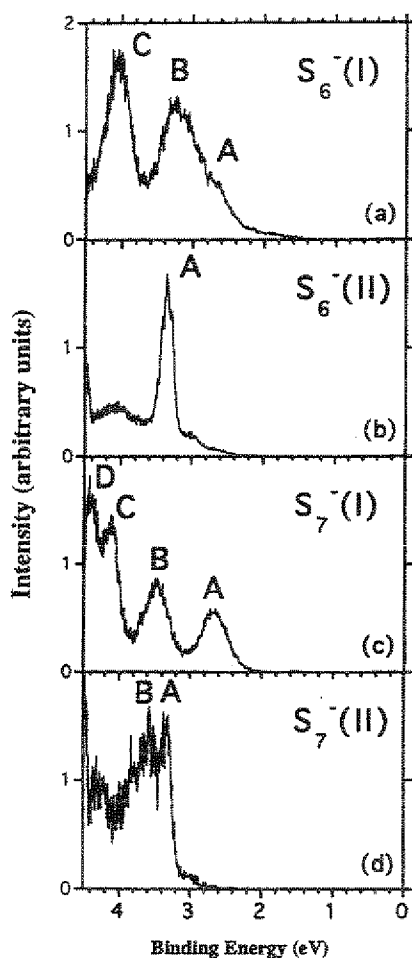


Figure 3.13: Photoelectron spectra of S_6^- and S_7^- recorded at $h\nu=4.66$ eV photon energy. Spectra are shown for each cluster for two source adjustments corresponding to the mass spectra shown in Fig. 3.3. Adjustment I: S_6^- (a) and S_7^- (c), adjustment II: S_6^- (b) and S_7^- (d).

narrow range (0.02 eV wide) starting 0.28 eV above the ground state. A helical (C_2) chain [Fig. 3.12(f)] lies 0.36 eV above the most stable isomer. Hybrids of planar and chainlike sections tend to become more stable than helices as the cluster size increases.

The photoelectron spectrum of S_7^- with source adjustment (I) [Fig. 3.13(c)] shows rather broad peaks with unresolved vibrational fine structure at 2.66 ± 0.05 (VDE), 3.47 ± 0.07 , 4.14 ± 0.07 and 4.4 ± 0.1 eV. The overall agreement with the corresponding values for the most stable isomer [Fig. 3.11(f)] (see Table 3.2) is rather good, especially for the VDE (2.69 eV). While the results (2.52 and 3.81 eV) for the isomer [Fig. 3.12(a)] are less compatible with the peak positions, the vertical excitation energies of isomer [Fig. 3.12(b)] correspond well with the experimental values. The remaining isomers have all VDEs above 3.4 eV and can therefore be ruled out from consideration. As might be expected from the preceding discussion, the peak positions (3.38 ± 0.05 and 3.6 ± 0.2 eV) in the spectrum Fig. 3.13(d) generated with source adjustment (II) lie in the range of the calculated vertical excitation energies of the chainlike isomers Figs. 3.12(c-f) and agree best with the values for the helical chain Fig. 3.12(f) [3.52 eV (3B), 3.62 (1A)]. As for the helical chain isomer of S_6^- , we found also a close local minimum on the energy surface of S_7^- , just 0.29 eV more stable

Molecule	Symmetry	State	ΔE
S_8^- 3.14(a) $d_{12,56}=3.86$; $d_{18,45}=3.97$; $d_{23,67}=4.00$; $d_{34,78}=4.07$; $\alpha_{1,2,5,6}=109^\circ$; $\alpha_{3,4,7,8}=116^\circ$; $\gamma_{12,56}=-80^\circ$; $\gamma_{23,67}=94^\circ$; $\gamma_{18,45}=92^\circ$; $\gamma_{34,78}=-107^\circ$	D_2	2B_1	0.0
S_8^- 3.14(b) $d_{23,67}=4.40$; $d_{12,34,56,78}=3.66$; $d_{18,45}=5.25$; $\alpha_{2,3,6,7}=101^\circ$; $\alpha_{1,4,5,8}=95^\circ$; $\gamma_{18,23,45,67}=0^\circ$; $\gamma_{12,56}$, $-\gamma_{34,78}=89^\circ$	C_{2v}	2B_1	0.06

Table 3.10: Structure parameters for isomers of S_8^- , with energies relative to the ground state (eV). Bond lengths d_{ij} in a.u., bond angles α_i and dihedral angles γ_{ij} in degrees. Additional labels refer to the figures.

than the geometry in Fig. 3.12(f). It is a (with respect to its long axis) contracted C_2 helical chain.

S_8^-

The best known of the neutral sulfur clusters is the D_{4d} crown shaped ring [Ste84, Ste85], and our calculations indicate that the most stable S_8^- isomer is a distortion of this structure to D_2 symmetry [Fig. 3.14(a)]. Compared with the experimental data for (neutral) orthorhombic (α -) S_8 at 100 K [CYB⁺77], the additional electron induces an approximately uniaxial stretch, with two bonds on opposite sides of the ring increasing in length by 5%. A C_{2v} isomer [Fig. 3.14(b)] is only 0.06 eV higher in energy than the ring. It may be viewed as two loosely bound *cis*-planar (C_{2v}) tetramers, such as found in S_4^- , since the bond lengths [Table 3.10] deviate by only $\sim 3\%$ from those in S_4^- , and the orbitals along the shortest distance (5.25 a.u.) between the tetramers are weakly bonding. Since the LSD approximation often overestimates the strengths of bonds between closed shell systems [JG89], the long, weak bond between the tetramers may be an artifact of this approximation. The *cis*-planar tetramer is found as a structural unit in other isomers. For example, a C_2 structure with slight distortions from C_{2h} symmetry [Fig. 3.14(c)] lies 0.34 eV above the ground state and differs from Fig. 3.14(b) only in the relative orientation of the planar segments. An isomer with C_1 symmetry and a planar section [Fig. 3.14(e)] lies 0.02 eV above the C_2 structure. Two others with terminal planar sections, including one with C_2 symmetry and planar units at each end, lie a further 0.07-0.08 eV higher. In addition to the most stable all-*cis* ring isomer [Fig. 3.14(a)], we considered a ring derived from it by inverting two dihedral angles. The energy of the resulting C_1 species [Fig. 3.14(d)] is 0.35 eV above that of the ground state ring. This structure is more compact than that in Fig. 3.14(a), and the increased strain caused by the additional electron results in one weak bond of length 5.19 a.u. There are numerous chain structures derived by the addition of a single atom to S_7^- chains. The lengths of the central bonds of the all-*trans* helical chain [0.56 eV] are close to the measured values in catenapolysulfur (S_∞ , 3.90 a.u.) [Don74], the bond and dihedral angles are $\sim 3\%$ larger and $\sim 10\%$ smaller, respectively. Several chainlike structures differ from the helix in the sign of one or more dihedral angles and have energies within 0.12

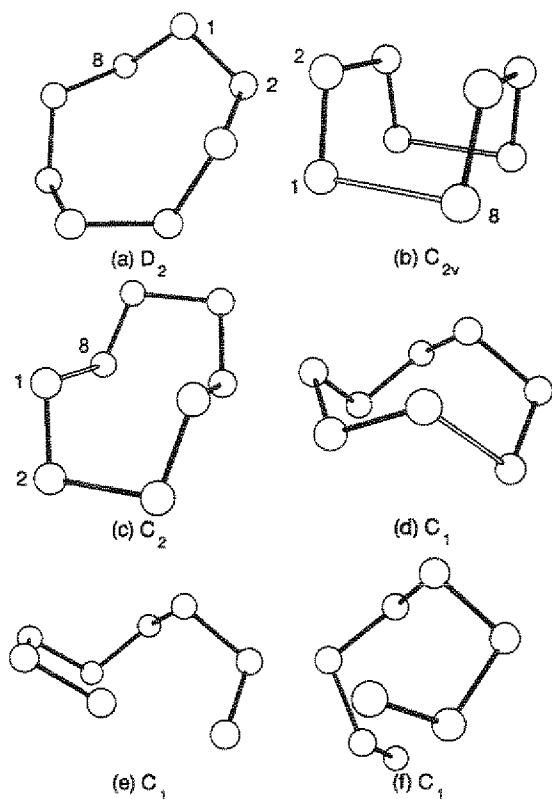


Figure 3.14: Structures of S_8^- . (a-d) "Closed", (e-f) "open".

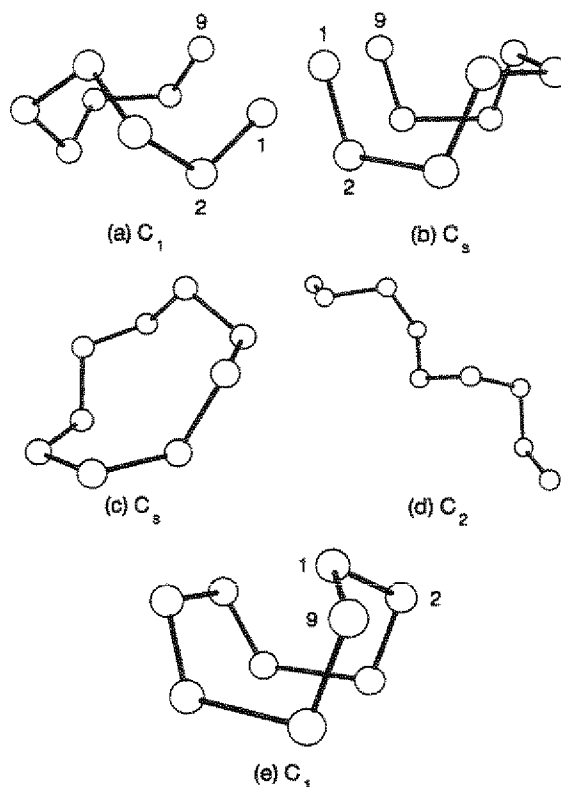


Figure 3.15: Structures of S_9^- .

eV below and above this isomer. Of particular interest are structures with one and two terminal planar tetramers (C_1 and C_2 symmetry, respectively) that are 0.12 eV more stable than the helical chain.

There are only two peaks A and B observable in the spectrum shown in Fig. 3.16 at 3.87 ± 0.07 and 4.3 ± 0.07 eV, respectively. These values are again in the same range as those for the chainlike isomers, but, as already pointed out, we do not attempt to make a definite assignment here. The excitation energies calculated for the helical chain isomer (not shown in the figures) are at 3.62, 3.89 and 4.12 eV and cannot account for the features contained in the spectrum. Nevertheless, we found, as for the helices of S_6^- and S_7^- that a C_2 all-*trans* chain (not shown in the figures) is the closest local minimum on the energy surface of the neutral isomer, just 0.82 eV more stable than the anion structure. The origin of a weak feature at ~ 3.2 eV BE is unclear, and it might due to the presence of a further isomer.

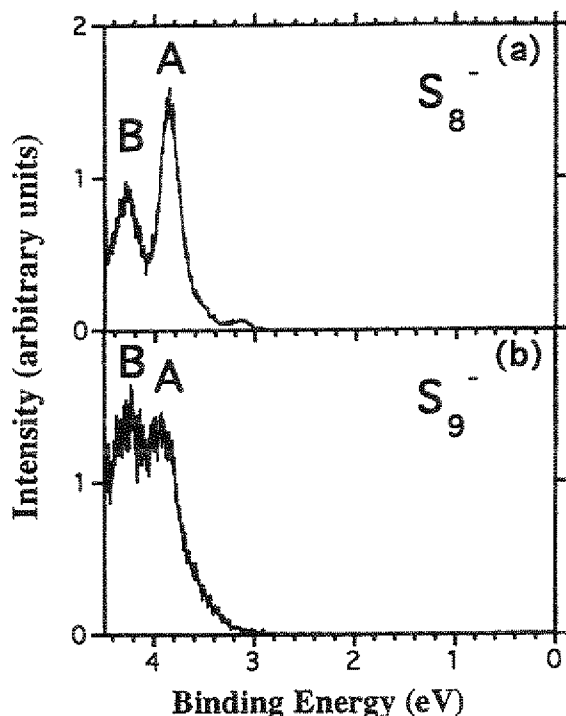


Figure 3.16: Photoelectron spectra of S_n^- -clusters ($n=8,9$) recorded at $h\nu=4.66$ eV photon energy. See text for a discussion of the features marked.

S_9^-

The rapidly increasing number of isomers with cluster size rules out any attempt at completeness for larger clusters, but we have studied several isomers of S_9^- to see whether trends in the smaller anions continue. The experimental geometries of S_9 and its ions are not known [SSS85], but the theoretical prediction [HJCP88, RRB90] of a C_2 ring as the most stable form of S_9 is consistent with the Raman spectra of microcrystalline samples [SSS85]. The corresponding structure obtained with the present basis set is given in Table 3.12. The most stable isomer of S_9^- encountered is a C_1 distortion of the neutral ground state [Fig. 3.15(a) and Table 3.11], where one interatomic separation increases from 3.94 to 5.38 a.u.. The anion structure related to the C_s boat isomer of S_9 [Fig. 3.15(b)] lies 0.06 eV higher. It also has C_s symmetry, and can be derived from the S_8^- isomer [Fig. 3.14(b)] by inserting a single atom in place of one of its longest bonds. The *cis*-planar (C_{2v}) tetramers are distorted, the dihedral angle being 35° . A C_s chair isomer [Fig. 3.15(c)] is 0.10 eV higher in energy, with structural parameters similar to those reported previously for an isomer of S_9 [HJCP88]. The all-*trans* helical chain [Fig. 3.15(d), C_2] lies 0.40 eV above the ground state and has a pattern of bond lengths and angles that is similar to that found in the helical isomer of S_8^- . As in the case of the smaller clusters, isomers with one (C_1) and two (C_2) terminal planar tetramers are more stable than the helix, in S_9^- by 0.02 eV and 0.12 eV, respectively. The energy of the last structure that we considered, a C_1 cage

Molecule	Symmetry	State	ΔE
S_9^- 3.15(a) $d_{12,89}=3.76$; $d_{19}=5.38$; $d_{23}=3.97$; $d_{34,56}=3.92$; $d_{45}=3.91$; $d_{67,78}=3.95$; $\alpha_{1,5,6,9}=109^\circ$; $\alpha_{2,4}=110^\circ$; $\alpha_3=105^\circ$; $\alpha_7=107^\circ$; $\alpha_8=112^\circ$; $\gamma_{12}=-77^\circ$; $\gamma_{19}=-55^\circ$; $\gamma_{23}=66^\circ$; $\gamma_{34}=84^\circ$; $\gamma_{45}=-78^\circ$; $\gamma_{56}=-75^\circ$; $\gamma_{67}=108^\circ$; $\gamma_{78}=-79^\circ$; $\gamma_{89}=105^\circ$	C_1	2A	0.0
S_9^- 3.15(b) $d_{12,89}=3.71$; $d_{19}=5.72$; $d_{23,78}=4.09$; $d_{34,67}=3.84$; $d_{45,56}=3.95$; $\alpha_{1,9}=95^\circ$; $\alpha_{2,8}=108^\circ$; $\alpha_{3,7}=105^\circ$; $\alpha_{4,6}=111^\circ$; $\alpha_5=110^\circ$; $\gamma_{12}, -\gamma_{89}=112^\circ$; $\gamma_{23}, -\gamma_{78}=-35^\circ$; $\gamma_{34}, -\gamma_{67}=-95^\circ$; $\gamma_{45}, -\gamma_{56}=101^\circ$	C_s	$^2A''$	0.06

Table 3.11: Structure parameters for isomers of S_9^- , with energies relative to the ground state (eV). Bond lengths d_{ij} in a.u., bond angles α_i and dihedral angles γ_{ij} in degrees. Additional labels refer to the figures.

[Fig. 3.15(e)] very similar to a C_s isomer of S_9 described in Ref. [HJCP88], was 0.14 eV above the helix. The additional electron causes the longer bonds between the atoms labeled 3,4 and 7,8 in Fig. 3.15(e) to increase to 4.61 and 4.74 a.u., respectively, significantly larger than the longest bond in the *cis*-planar (C_{2v}) tetramer unit (~ 4.28 a.u.).

The peak positions obtained from the analysis of the photoelectron spectrum in Fig. 3.16 (3.90 ± 0.1 and 4.3 ± 0.1 eV) are closer to the values of the C_2 chain (3.68, 3.94 and 4.24 eV) than to any of the values computed for the ringlike structures (2.63-2.86 eV), but no definite assignment is possible nor attempted in this case (see the discussion above and in section 3.3.2). Again, we found a close minimum (0.91 eV more stable than the anion structure) with C_1 symmetry and all-*trans* motif (not shown in the figures) on the energy surface of the neutral species.

Although the photoelectron spectrum of S_9^- exhibits no vibrational fine structure, we have calculated vibration frequencies of the most stable (C_2) isomer of S_9 shown in Fig. 3.10(d), since its vibration frequencies are of particular interest. Two different forms of S_9 have been identified, but it has not yet proved possible to prepare single crystal samples [SSS85]. The essential details of the structure could nevertheless be determined from the Raman spectra, since the distribution of the vibration frequencies was quite different from those of other sulfur rings. In particular, there were gaps in the frequency distributions between 310 and 410 cm^{-1} and 490 and 600 cm^{-1} . The frequency spectrum was only consistent with C_1 or C_2 symmetry, and with relatively narrow ranges of bond lengths (3.84 – 3.95 a.u.) and dihedral angles ($70 - 130^\circ$). We have performed a detailed study of the vibration frequencies of the most stable isomer found in the MD/DF calculations [HJCP88], and compare the results with the measured Raman frequencies [SSS85] in Table 3.4. The low symmetry of the molecule and the relatively large number of modes (21) complicate the calculations, and we include only modes whose symmetries can be identified unambiguously. The differences between the frequencies in the α - and β -forms of S_9 [SSS85] – the symmetric ring deformation, for example, leads to intense Raman lines at 188 and 181 cm^{-1} , respectively – indicate that we cannot expect detailed agreement between theory

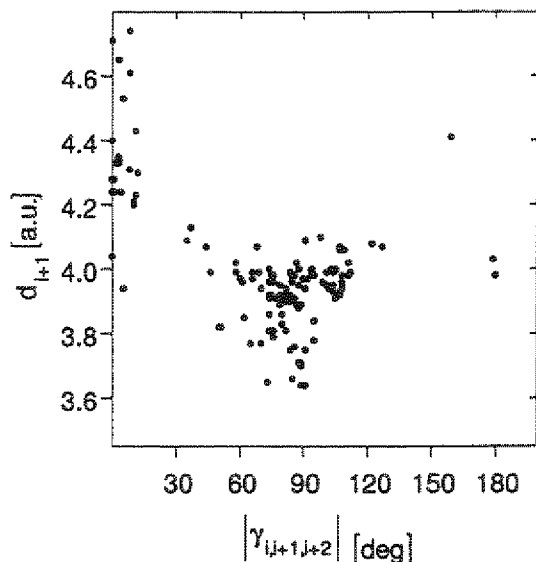


Figure 3.17: Variation of the length of the central bond d of three adjacent bonds with dihedral angle γ .

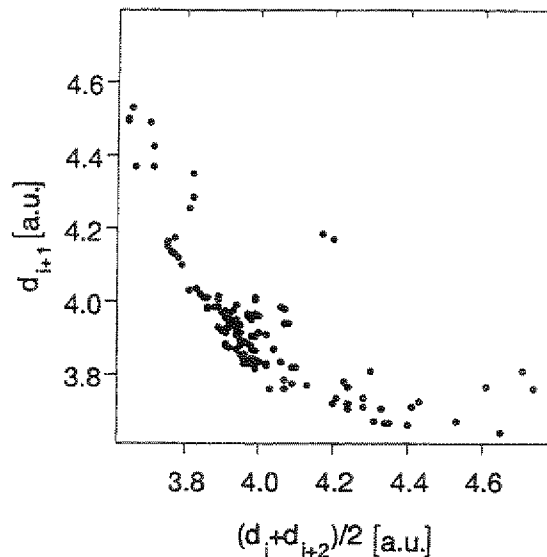


Figure 3.18: Variation of bond length d with the mean length of the two neighboring bonds.

and experiment. Nevertheless, the overall agreement is satisfactory, particularly concerning the frequency gaps mentioned above. We have little doubt that the most stable isomer in S_9 is the C_2 structure shown in Fig. 3.10(d).

3.3.2 Trends and Discussion

The planar C_{2v} motif first encountered in S_4^- also appears in planar sections of the larger anions. Structures consisting entirely of this pattern exist only for even values of n , in which case they are among the most stable isomers. Its presence is also apparent in Fig. 3.17, which plots bond length against dihedral angle γ for all anion structures shown in the tables. A similar relationship has been observed by Steudel and coworkers [Ste84, Ste85, Ste75b, Ste75c, Ste77a, Ste77b, Ste83] for neutral sulfur clusters. Apart from a cluster of points near 90° reminiscent of the “normal” dihedral angle distribution [Pau49] (this configuration minimizes the repulsion between the lone pair π orbitals at the S atoms), there is a second cluster of values near $\gamma = 0^\circ$. The elongation of the central bond as γ decreases from 90° to 0° is favorable for a negatively charged molecule. A second trend noted by Steudel and coworkers for the neutral clusters is the inverse relationship between bond length and the mean of the lengths of the neighboring bonds. This trend is also found in the anionic structures (Fig. 3.18, for all anion structures shown in the tables). Another family of anion geometries of low energy consists of the opened or puckered rings of the neutral clusters, where at least one of the bonds is strained or broken due to the presence of the additional electron. The ground states of S_5^- , S_7^- , S_8^- and S_9^- belong to this family. Open chainlike structures without planar sections also occur, and their stability relative to

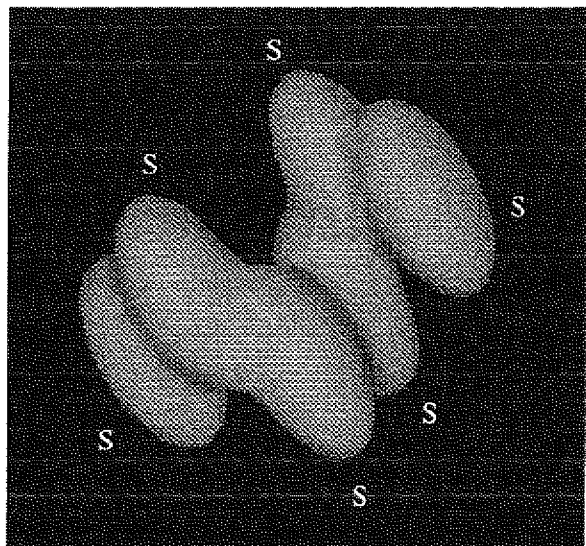


Figure 3.19: Isosurface plot of the electron density of the chain isomer of S_6^- shown in Fig. 3.11(c). The density on the surface is 0.007 a.u..

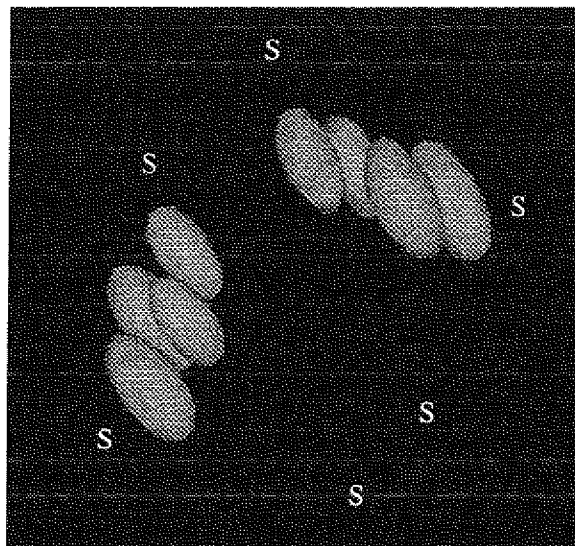


Figure 3.20: Isosurface plot of the magnetization density of the chain isomer of S_6^- shown in Fig. 3.11(c). The magnetization density on the surface is 0.0008 a.u..

the most stable isomers decreases with increasing cluster size. Hybrids of all-*trans* chains with the C_{2v} *cis*-planar unit of S_4^- occur in S_6^- – S_8^- and are on average ~ 0.1 eV more stable than their all-*trans* counterparts.

The comparison between theory and experiment [Fig. 3.4 and Table 3.2] indicates that clusters generated by the source are ringlike up to S_5^- and chainlike for S_8^- and S_9^- . S_6^- and S_7^- can occur in both forms, with source adjustments *I* and *II* favoring rings (low VDE) and chains (higher VDE), respectively. In Fig. 3.4 we plot the VDE values for the cage- and ringlike structures found for the anions. For $n > 5$ there is a variety of chain structures, and the ranges of VDE values are shown by bars for $n=6$ –8. The difference between the VDE of the two classes of structures is striking. Apart from a small peak at S_5^- , the broken ring structures show almost constant or even decreasing VDE with increasing cluster size, while the values for the chains increase at first and then saturate near S_6^- . The outermost electron is more tightly bound in the chains, an effect that has also been observed in carbon clusters [YTC⁺88]. The eigenvalue spectra support this view, since there is a relatively small gap between the uppermost two occupied orbitals in the chain isomers. Since the sum of the eigenvalues is one contribution to the total energy, a small gap leads to a high VDE. The gap decreases continuously with increasing cluster size from 0.83 eV in the C_{2h} chain isomer of S_4^- to 0.06 eV in the C_2 helical chain isomer of S_9^- . The charged broken rings and planar structures are more compact, and both the energy of the highest occupied electron state remains high and its separation from the next occupied orbital remains large as the cluster size increases. Consequently, the VDEs are considerably lower than in the chain isomers. Apart from S_1^- , S_2^- and the D_{3h} and D_{2h} rings of S_3^- and S_4^- , the largest eigenvalue gap (2.23 eV) and the lowest VDE was found in the first genuine ring in S_8^- . The

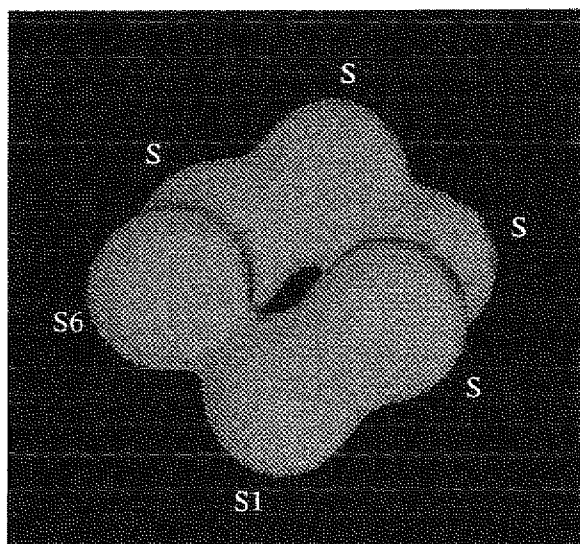


Figure 3.21: Isosurface plot of the electron density of the isomer of S_6^- shown in Fig. 3.6(f). The density on the surface is 0.001 a.u..

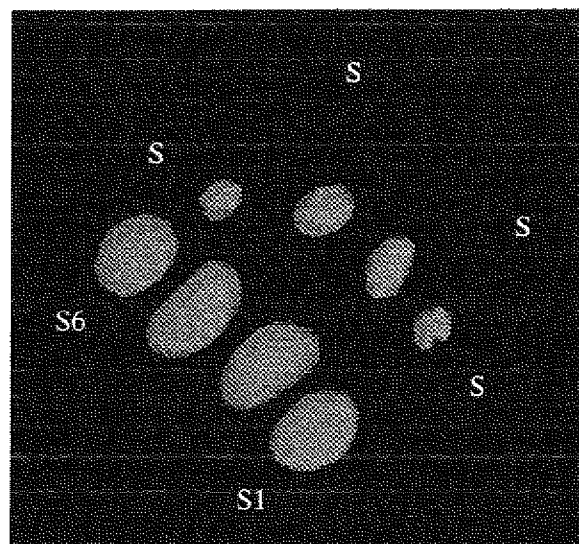


Figure 3.22: Isosurface plot of the magnetization density of the isomer of S_6^- shown in Fig. 3.6(f). The magnetization density on the surface is 0.0008 a.u..

exceptionally low VDE of S_2^- is not surprising, since the additional electron must occupy an antibonding orbital with a relatively large amplitude.

These differences in the KS eigenvalues and the VDEs can be related to differences in the electronic structure. Representative for all (helical) chains, we show in Figures 3.19 and 3.20 isosurface plots of the electronic and magnetization density, respectively, of the chain isomer of S_6^- shown in Fig. 3.11(c). Both pictures are taken from the same perspective. As inspection shows, the magnetization density $m_z(\mathbf{r}) = (n_+ - n_-)(\mathbf{r})/2$ (a.u.) of all anion clusters is, within the numerical accuracy, identical (apart from a factor ± 2) to the single-particle density of the excess KS-electron. As in this case, a detailed study of the densities of all chain isomers shows that the additional electron occupies an antibonding orbital localized mainly on the terminal bonds of the chain. The potential energy is then lower in longer chains with larger distances between the ends. This picture is consistent with the saturation of the VDE found in longer chains. As a typical example for the electronic structure of the ring isomers, we reproduce in Figures 3.21 and 3.22 isosurface plots of the electronic and magnetization density, respectively, of the ring isomer of S_6^- shown in Fig. 3.6(f). Again, both pictures are taken from the same perspective. The surplus electron (whose density is proportional to the magnetization density in Fig. 3.22) occupies an antibonding orbital with comparatively high amplitude in the region of a strained bond between atoms labeled 1 and 6. A high degree of localization of the excess electron can also be observed in the remaining ring isomers that leads to the presence of strained and/or broken bonds in all ring isomers considered. For simple electrostatic reasons, this is energetically less convenient for the excess electron than the situation encountered in the chain isomers.

Molecule	Symmetry	ΔE
S ₂ $d_{12}=3.61$	$D_{\infty h}$	0.0
S ₃ 3.9(a) $d_{12,23}=3.66$; $\alpha_2=118^\circ$	C_{2v}	0.0
S ₃ 3.9(b) $d_{12,23,13}=3.94$; $\alpha_{1,2,3}=60^\circ$	D_{3h}	0.27
S ₄ 3.9(c) $d_{12,34}=3.61$; $d_{23}=4.21$; $\alpha_{2,3}=100^\circ$	C_{2v}	0.0
S ₄ 3.9(d) $d_{12,34}=3.60$; $d_{14,23}=4.71$; $\alpha_{1,2,3,4}=90^\circ$	D_{2h}	0.03
S ₄ 3.10(a) $d_{12}=3.97$; $d_{13,24}=3.65$; $\alpha_{1,2}=111^\circ$	C_{2h}	0.44
S ₆ 3.10(c) $d_{12}, \dots=3.92$; $\alpha_1, \dots=103^\circ$; $\gamma_{23,16,45} = -\gamma_{12,34,56}=74^\circ$	D_{3d}	0.0
S ₆ 3.10(b) $d_{14,25,36}=3.59$; $d_{12}, \dots=5.07$; $\alpha_{123}, \dots=60^\circ$; $\alpha_{125}, \dots=90^\circ$	D_{3h}	0.21
S ₉ 3.10(d) $d_{12,45}=3.88$; $d_{19,56}=3.94$; $d_{23,34}=3.92$; $d_{67,89}=3.90$; $d_{78}=3.91$; $\alpha_{1,5}=107^\circ$; $\alpha_{2,4}=110^\circ$; $\alpha_3=103^\circ$; $\alpha_{9,6}=106^\circ$; $\alpha_{7,8}=109^\circ$; $\gamma_{23}, -\gamma_{45}=75^\circ$; $\gamma_{12}, -\gamma_{34}=-76^\circ$; $\gamma_{19,56}=-63^\circ$; $\gamma_{89,67}=113^\circ$; $\gamma_{78}=-85^\circ$	C_2	0.0

Table 3.12: Structure parameters for isomers of S_n , $n = 2, 3, 4, 6, 9$ with energies relative to the ground state (eV). Bond lengths d_i ; in a.u., bond angles α_i and dihedral angles γ_i ; in degrees. Additional labels refer to the figures.

The transition from closed to open structures as n increases through 6-7 is interesting, since the calculations predict that the most stable isomer is closed for all cluster sizes. Although an unambiguous analysis of the growth processes of the clusters would require careful measurements of the partial pressures, temperatures and flow velocities at various points in the source, we now show that energetic stability is not the only criterion for the occurrence of particular structures in a cluster beam. The higher conformational freedom and/or the greater number of low-energy vibrational modes of the chains means that they are favored by entropy, or, likewise, by the (Helmholtz) free energy at higher temperatures, an effect also found in carbon clusters [BMB88, ASG90]. Correspondingly, we also observed in our simulations that the number of local minima on the BO energy surface of the larger anions (i.e., at $T = 0$) with chainlike geometries is much greater than the number of isomers with closed structures. The statistical weight of the chain isomers in the ensemble of S_n^- clusters in the source will be raised by the fact that their comparatively high VDE immunizes them against discharge processes. If charge transfer processes occur, all-*trans* chains could be further stabilized compared to other chain isomers, as our results indicate that these geometries are local minima in the anion and the neutral cluster. Furthermore, if the S_n^- clusters grow as chains (i.e., through the addition of terminal atoms), ring formation

by bonding between the terminal atoms will be hampered by the negative charge localized on these atoms. Accordingly, the (hot) cluster beam leaving the source should be imagined as an ensemble of different isomers with predominantly chainlike structures, at least for the larger anions S_n^- , $n \geq 6$. A more rapid cooling process or "quenching" would then freeze the structures of the isomers into geometries of close local minima on the BO energy surface, whereas a slower process, including many subsequent heating and cooling cycles induced by collisions similar to an annealing of the clusters, would result in a distribution of geometries that is dominated by the absolute minimum structure. We note that similar [GHB⁺95] observations have been made in beams of carbon clusters, where rapid cooling can result in the production of several isomers that are not necessarily the most stable. For example, most C_{60} clusters have ring and double ring structures, and the cage-like fullerene isomer dominates only if slow annealing is allowed. Accordingly, for S_6^- and S_7^- , rings are observed when conditions allow a slower cooling of the plasma and more time for the nuclei to rearrange. There are fewer isomers in the smaller clusters, the time required for structural relaxation is shorter, and only the most stable ringlike structures are observed. It is possible that ringlike structures could also be generated for S_n^- , $n \geq 8$, if the cluster beam is annealed suitably, as found in C_n clusters [GHB⁺95]. Together with our results, the photoelectron spectra [Fig. 3.13(a-d)] provide direct spectroscopic evidence for the existence of different cluster isomers in the gas phase. The existence of multiple isomers can also be inferred from measurements of reaction kinetics (see [MDO87, CJ90] and references therein).

3.4 Phosphorus Cluster Anions

The cluster structures of phosphorus, the neighboring element of sulfur in the periodic table, have been particularly difficult to characterize. Although experimental data on the dimer and the tetramer have been available for over sixty years [JH90a], it is less than ten years since P_n^+ ions were identified mass spectrometrically up to $n = 24$ [Mar86]. The dominant components in the vapor phase of the group Va (group 15) elements (P, As, Sb, Bi) are tetramers, and clusters with multiples of four atoms dominate in the mass spectra obtained, for example, in photoionization measurements of Sb_n with n up to 300 [BCC⁺95]. Phosphorus clusters have often been studied as components of organometallic and other molecules [Sch90, BG93]. However, although there have been several theoretical studies of charged and neutral phosphorus clusters, and systematic trends in the structural patterns have been discussed by several authors [BG93, vSH88, Häs94], there has been an almost complete lack of experimental studies that provide structural information about the isolated clusters. Here, we try to provide further information by comparing our CP-MD results on phosphorus cluster anions P_n^- up to $n=9$ with photoelectron spectra obtained from [GPS96].

We perform calculations for neutral clusters at the anionic and other geometries, and we have identified new P_n isomers, including one for the heptamer that could be the most stable.

Earlier calculations on neutral and charged clusters with up to 11 atoms [JH90c, SJ92, JS92] predicted that the most stable isomers found for P_5 , P_6 , and P_7 were derived from the “roof” or “butterfly” structure of P_4 (C_{2v}) by the addition of one, two, and three atoms, respectively, and for P_8 a wedge-shaped (C_{2v}) structure related to the cuneane isomer of $(CH)_8$ [JH90c].

Phosphorus cluster anions up to $n=9$ have been detected previously by Snodgrass *et al.* [SCF⁺85], who also performed photoelectron spectroscopy on P_2^- . Photoelectron spectroscopy on cluster anions of other group Va (group 15) elements has been carried out by Polak *et al.* [PHGL91] (antimony Sb_n and bismuth clusters Bi_n to $n = 4$) and by Gausa *et al.* [GKS⁺] (Sb_n^- and Bi_n^- to $n=9$, comparison with density functional calculations to $n=5$). These and other works will be discussed below. As in the section 3.3, the comparison of the measurements and calculations focus on the vertical detachment energies and the vibration frequencies.

3.4.1 Optimal Geometries, Vibration Frequencies, and Vertical Excitation Energies

In this section we discuss the structures of phosphorus anions and the excitation energies to states of the neutral clusters. We focus on the vertical detachment energies (VDE), where the geometrical structure is unchanged, but adiabatic energy differences will be discussed where appropriate. Structural parameters of the anions are given in Tables 3.13-3.16, and vibration frequencies in Table 3.14.

P_1^-

The energy differences between the ground state of the phosphorus anion and the low-lying states of the atom are calculated to be 0.85 eV (4S), 2.39 eV (2D) and 2.90 eV (2P) using the scheme described in sec. 2.1.2. This is in acceptable agreement with the measured electron affinity of phosphorus (0.7465 eV) [HL85a] (one of the lowest of any element, reflecting the half-full shell in the atom) and the lowest excited states of the atom at 2.16 eV (2D_0) and 3.07 eV (2P_0) [MZM85] above the GS of the anion. The photoelectron spectrum (not included in the figures) shows these three peaks clearly, although the spin-orbit splitting is not resolved in the present experiment.

 P_2^-

The calculated VDE of P_2^- (0.86 eV) corresponds to the excitation to the ground state of P_2 , measured to be 0.68 ± 0.05 eV in the spectra. The energies of states derived from the ground state configuration of P_2 ($\sigma_g^2 \pi_u^4, ^1\Sigma_g^+$) by the excitation $\sigma_g \rightarrow \pi_g$ ($\sigma_g \pi_u^4 \pi_g$; $^3\Pi_g, ^1\Pi_g$) are accessible to LSD calculations using the approach of von Barth (2.1.2), and we discuss these energies below. However, states arising from the excitations $\pi_u \rightarrow \pi_g$ ($\sigma_g^2 \pi_u^3 \pi_g$; $^3\Sigma_u^+, ^3\Sigma_u^-, ^3\Delta_u$, and related singlets) [Her50] are indistinguishable in an LSD calculation, as is explained in section 2.1.2 and in appendix B. The only "mixed-symmetry" determinantal KS state of this configuration has an excitation energy of 3.98 eV. Information about these states can nevertheless be found from experimental measurements on other group Va (group 15) dimers or could be gained by CI calculations, where it is possible to distinguish between states with "+" and "-" symmetry, i.e., the symmetry according to reflection in a plane containing the molecular axis. Observed intensity maxima in the PE spectra lie at 3.03, 3.65, and 4.10 eV binding energy and the measured energy differences (T_e) for the (shorter) equilibrium separation of the ground state of P_2 are 2.33, 3.53, and 3.50 eV for $^3\Sigma_u^+, ^3\Sigma_u^-,$ and $^3\Pi_g$ states, respectively [HH79]. The calculated vertical excitation energy (MD/DF) for the $^3\Pi_g$ state is 4.22 eV, with an energy 3.30 eV above P_2 ($^1\Sigma_g^+$) at the energy minimum for P_2^- . The narrow range of energies of the $^3\Sigma_u^-, ^3\Delta_u,$ and $^3\Pi_g$ states makes an assignment difficult. Nevertheless, while the $^3\Delta_u$ state has not yet been observed in P_2 , there is evidence that it lies between the $^3\Sigma_u^+$ and $^3\Sigma_u^-$ states in the other group Va (group 15) dimers N_2 [HH79, LG91], As_2 [HCR⁺85], and Bi_2 and Sb_2 [PHGL91, BL89]. Vibration frequencies of P_2 (730 ± 80 cm^{-1}) and P_2^- (560 ± 120 cm^{-1}) can be observed in the spectra. These vibration frequencies differ somewhat from those determined by Snodgrass *et al.* ($\omega_e(P_2)$ 774 ± 48 cm^{-1} , $\omega_e(P_2^-)$ 630 ± 50 cm^{-1} [SCF⁺85]). The calculated values (MD/DF) in Table 3.14 (781 and 659 cm^{-1}), however, are in good agreement with all available experimental data for P_2 and P_2^- .

 P_3^-

The trimer anion P_3^- has been investigated previously by Burdett and Marsden [BMC88] and Hamilton and Schaefer [HS90]. Both sets of workers found three low-lying minima: an equilateral triangle ($D_{3h}, ^3A_2'$), a linear closed-shell singlet ($D_{\infty h}, ^1\Sigma_g^+$), and a bent (C_{2v})

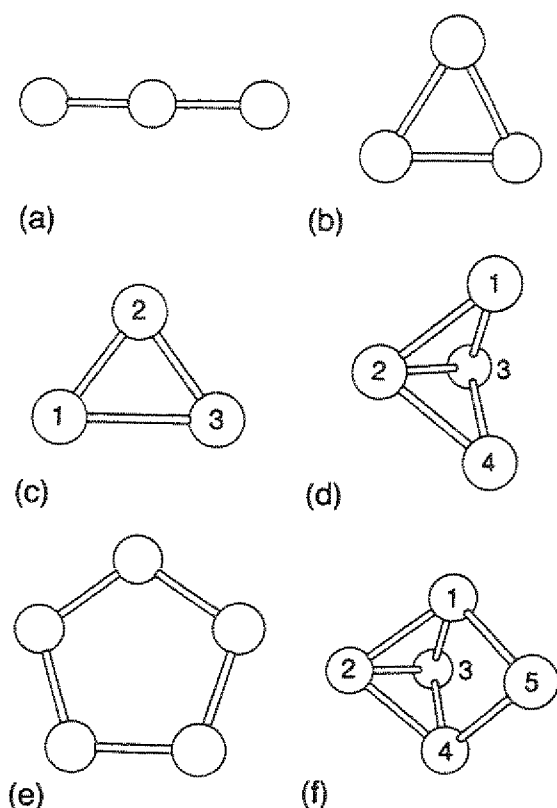


Figure 3.23: Structures of (a-c) P_3^- , (d) P_4^- , and (e-f) P_5^- .

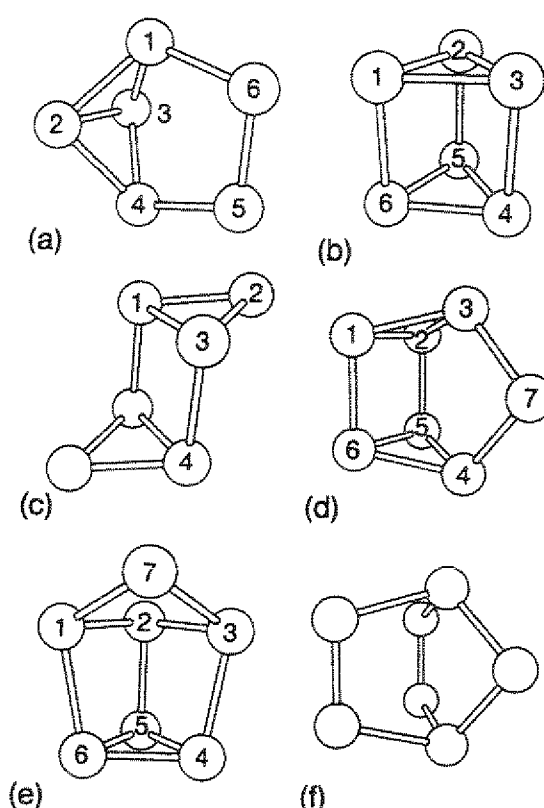


Figure 3.24: Structures of (a-c) P_6^- and (d-f) P_7^- . Labels in (f) are as in (d).

triplet. The first two were found to be so close in energy that a definite prediction of the ground state was not possible. In the present MD/DF calculations the linear structure has the lowest energy, but the D_{3h} and C_{2v} structures are only 0.06 and 0.27 eV less stable. The vertical detachment energies of the three structures (Fig. 3.23(a-c)) show striking differences, however, being 3.00 eV, 1.88 eV, and 1.73 eV, respectively. There are, of course, higher-lying states of P_3 corresponding to each of the three structures found for P_3^- . They will contribute to the measured intensity near peaks (D,E) in Fig. 3.26, but all occur at binding energies well above 3.0 eV. The lowest quartet state for the D_{3h} structure, for example, has a vertical excitation energy of 4.08 eV. All calculations performed to date on P_3^- give a consistent picture: The linear and equilateral triangular structure are virtually degenerate, and the bent (C_{2v}) form is only ~ 0.2 eV higher in energy. It is very likely that more than one isomer can be generated, depending on the experimental conditions. The spectra (Figs. 3.25 and 3.26) show five peaks at 1.68, 1.96, 2.89, 3.91 and 4.32 eV binding energy. The calculated vertical excitation energies to the first two states in P_3 are (1.73 eV, 3.70 eV for C_{2v}) and (1.88 eV, 4.08 eV for D_{3h}). In view of the uncertainties in both experiment and theory, either (or both) of these structures could be present. We note, however, the large gap in the excitation spectrum for both

Molecule	Symmetry	ΔE
P_2^-	$D_{\infty h}, {}^2\Pi_g$	0.0
$d_{12}=3.72$		
P_3^- 3.23(a)	$D_{\infty h}, {}^1\Sigma_g^+$	0.0
$d=3.68$		
P_3^- 3.23(b)	$D_{3h}, {}^3A_2'$	0.06
$d=4.08, \alpha=60^\circ$		
P_3^- 3.23(c)	$C_{2v}, {}^1A_1$	0.27
$d_{12,23}=3.90, \alpha_{123}=72.6^\circ$		
P_4^- 3.23(d)	C_{2v}	0.0
$d_{12}=4.18, d_{23}=4.09, \alpha_{213}=58.6^\circ, \alpha_{124}=77.1^\circ$		
P_5^- 3.23(e)	D_{5h}	0.0
$d=3.96, \alpha=108^\circ$		
P_5^- 3.23(f)	C_{2v}	1.44
$d_{12}=4.28, d_{23}=4.18, d_{15}=4.16, \alpha_{213}=58.5^\circ, \alpha_{124}=75.2^\circ, \alpha_{154}=77.5^\circ$		
P_6^- 3.24(a)	C_{2v}	0.0
$d_{12}=4.24, d_{23}=4.18, d_{16}=4.08, d_{56}=3.96, \alpha_{213}=59.1, \alpha_{124}=90.1^\circ, \alpha_{216}=108.2^\circ, \alpha_{165}=104.5^\circ$		
P_6^- 3.24(b)	D_{3h}	0.30
$d_{12}=4.14, d_{16}=4.60$		
P_6^- 3.24(c)	C_{2h}	0.35
$d_{12}=4.06, d_{13}=4.18, d_{34}=4.45, \alpha_{123}=62.3^\circ, \alpha_{234}=99.8^\circ$		

Table 3.13: Structure parameters for isomers of P_n^- , $n=2-6$ with energies ΔE relative to the ground state (eV). Bond lengths d_{ij} in a.u., bond angles α_i in degrees. Additional labels refer to the figures.

isomers, which means that the strong peak at 2.89 eV must come from another structure. Since the linear isomer gives a vertical excitation at 3.00 eV, the measured binding energy curves are consistent with the existence of at least *two* isomers, one of which is linear. The photoelectron spectrum of P_5^- at $h\nu=3.49$ eV shows evidence for photofragmentation into P_3^- and P_2 , with different relative intensities of the features corresponding to peaks (A-C) observed here. This indicates that peak C might be arising from a different isomer than from peaks A and B. This is consistent with the results of the calculations. According to the above assignment, peak C in the spectrum of P_3^- should exhibit vibrational fine structure corresponding to the vibrational modes of linear P_3 . The calculations indicate that the neutral and negatively charged trimers have the same bond lengths, so that a narrow peak should occur in the photoelectron spectrum. No fine structure is observed, and the peak is broader than expected. Both features are consistent with the thermal excitation of hot bands, since thermal excitation would result in the preferential excitation of low energy modes that are beyond the energy resolution of the apparatus.

Vibration frequencies for P_3^- have been calculated by Hamilton and Schaefer [HS90] using the Hartree-Fock approach, and the results are compared with the present work in Table 3.14. Apart from the C_{2v} isomer, the results show the expected tendency of the HF method to overestimate vibration frequencies. Feature A is assigned to the ground

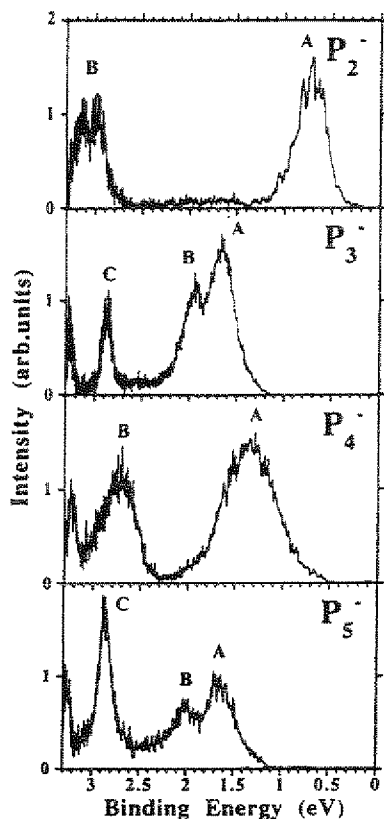


Figure 3.25: Photoelectron spectra of P_n^- clusters ($n=2-5$) recorded at $h\nu=3.49$ eV photon energy. See text for a discussion of the features marked.

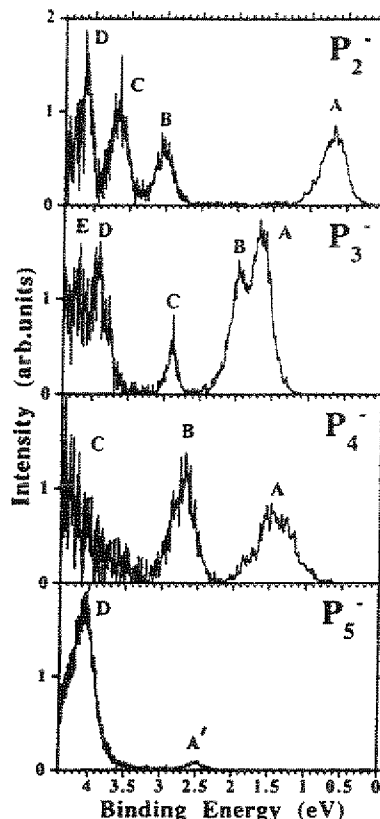


Figure 3.26: Photoelectron spectra of P_n^- clusters ($n=2-5$) recorded at $h\nu=4.66$ eV photon energy. See text for a discussion of the features marked.

state transition and exhibits vibrational fine structure when recorded with $h\nu=2.33$ eV. The spectrum is consistent with the excitation of either two vibrational modes of P_3^- (frequencies $340/435\pm 40$ cm^{-1}) or a single mode (frequency 390 ± 50 cm^{-1}). While the former values would be compatible with the C_{2v} isomer, the latter would favour the D_{3h} isomer.

All features observed in the spectrum of Sb_3^- have been assigned to emission from the D_{3h} isomer [PHGL91]. In the absence of spin-orbit coupling, the present calculations, as well as those of Balasubramanian *et al.*, [BSD91] predict a single vertical excitation energy to a $^2E''$ state. This state, which undergoes a Jahn-Teller distortion to two nearby minima, would be split by spin-orbit coupling.

P_4^-

The phosphorus tetramer has the familiar tetrahedral (T_d) structure. The additional electron in the anion, however, results in a Jahn-Teller distortion that is so large that it is not meaningful to analyze the equilibrium structure (Fig. 3.23(d)) in terms of tetrahedral

Molecule	Symmetry		ω_e
P_2	$D_{\infty h}, {}^1\Sigma_g^+$	Expt ^a	780.77
		Expt (here)	730±80
		MD/DF	781
P_2^-	$D_{\infty h}, {}^2\Pi_u$	Expt. ^b	630±50
		Expt (here)	560±120
		MD/DF	659
P_3		Expt (here)	460±65, 645±60
P_3	$D_{\infty h}$	MD/DF	140 (π_u), 484 (σ_g), 723 (σ_u)
P_3	C_{2v}	MD/DF	334 (b_2), 409 (a_1), 623 (a_1)
P_3^-		Expt (here)	390±50 or 340/435±40
P_3^- 3.23(a)	$D_{\infty h}$	MD/DF	176 (π_u), 482 (σ_g), 809 (σ_u)
		HF(DZP) ^c	188 (π_u), 552 (σ_g), 886 (σ_u)
P_3^- 3.23(b)	D_{3h}	MD/DF	427 (e'), 572 (a'_1)
		HF(DZP) ^c	457 (e'), 641 (a'_1)
P_3^- 3.23(c)	C_{2v}	MD/DF	313 (b_2), 449 (a_1), 607 (a_1)
		HF(DZP) ^c	158, 337, 686
P_5^- 3.23(e)	D_{5h}	MD/DF	207 (e''_2), 294 (e'_2), 487 (a'_1), 493 (e'_2), 453 (e'_1)
		HF ^d	224 (e''_2), 336 (e'_2), 509 (a'_1), 532 (e'_2), 564 (e'_1)
		HF ^e	233 (e''_2), 348 (e'_2), 514 (a'_1), 531 (e'_2), 563 (e'_1)

^aRef. [HH79]

^bRef. [SCF⁺85]

^cRef. [HS90]

^dRef. [HS89]

^eRef. [Jan89], unscaled values

Table 3.14: Vibration frequencies (ω_e , cm^{-1}) of selected phosphorus clusters.

symmetry. The vertical detachment energies calculated for transitions to the lowest-lying singlet and triplet structures are 1.35 and 2.91 eV, respectively. There are two pronounced peaks in the measured spectra of P_4^- , at 1.35 eV and 2.69 eV, both of which can be interpreted in terms of transitions from the “roof”-shaped isomer.

The very broad first peak indicates a large difference between the geometries of the most stable isomers of the anion and neutral clusters. The calculated adiabatic electron affinity, the difference between the lowest energies of P_4^- and P_4 is only 0.19 eV, in satisfactory agreement with the onset in the measured spectra. Relaxation of the neutral tetramer from the anionic structure to the tetrahedral form results in an energy lowering of 1.16 eV.

The “roof” structure is also found to be the most stable in calculations for Sb_4^- and Bi_4^- [GKS⁺].

P_5^-

The pentamer is an interesting case. The planar (cyclo- P_5) anion has been stabilized as a ligand [SB87] and prepared by reacting white phosphorus in solution with tetrahydrofuran [BO89]. It has been calculated to be the most stable isomer in Sb_5^- and Bi_5^- [GKS⁺]. Hartree-Fock calculations [HS89, Jan89] give a consistent picture of both geometry (P-P bond lengths of 3.955 and 3.959 a.u, respectively) and vibration frequencies (Table 3.14). Scherer and Brück [SB87] noted that *cyclo- P_5^-* could possibly be formed from P_3^- and P_2 , and Hamilton and Schaefer [HS89] observed that the high frequency vibration observed by Baudler and coworkers [BO89] could be due to the presence of P_3^- . Calculations by Glukhotsev *et al.* [GS93] indicate that the D_{5h} isomer of P_5^- is stable with respect to both dissociation ($P_5^- \rightarrow P_3^- + P_2$; $\Delta E=71.6$ kcal/mol) and disproportionation ($2P_5^- \rightarrow 2P_3^- + P_4(T_d)$; $\Delta E=116.4$ kcal/mol.)

The present calculations lead to two low-lying isomers. The planar ring (D_{5h} , Fig. 3.23(e)) has bonds of length 3.96 a.u. and is 1.44 eV more stable than the structure (3.23(f)) related to the most stable form found for the neutral pentamer. The planar ring is isovalent with the cyclopentadienyl anion $(CH)_5^-$ and is an "aromatic" 6π -system [GS93].

There is a striking difference between the vertical detachment energies of the two isomers of the anion (D_{5h} : 4.04 eV, C_{2v} : 2.08 eV). A single peak at 4.04 eV dominates the spectrum of P_5^- measured at $h\nu=4.66$ eV. This is in excellent agreement with the calculated value for the planar pentagonal form (3.23(e)). The C_{2v} isomer (3.23(f)) related to the structure predicted to be the most stable in the neutral heptamer is much less stable and has a much lower excitation energy. There is no evidence that this isomer is generated by the PACIS.

The calculated vibration frequencies (Table 3.14) are about 10% below the Hartree-Fock values, which are generally higher than experimental frequencies by approximately this amount [Jan89].

 P_6^-

The most stable isomer in all the present calculations was the C_{2v} form (Fig. 3.24(a)), which is 0.3-0.5 eV more stable than the other isomers (3.24(b,c)). While the measured photoelectron spectra (peak positions given in Table 3.17) are in reasonable agreement with the calculated values for the lowest-lying states of P_6 (2.29, 3.33 eV), the other stable structures found give similar values [2.44, 3.70 eV for 3.24(b); 2.65, 3.43 eV for 3.24(c)]. It is certainly possible that the source produces more than one isomer.

 P_7^-

Simulated annealing led in the heptamer P_7 not only to low-lying isomers of the anions, but to a stable isomer of the neutral cluster – the C_{2v} structure shown in Fig. 3.24(d) – that had not been found in earlier work [JH90c]. The MD/DF calculations indicate that this structure is slightly (0.11 eV) more stable than the C_s ("roof plus trimer") isomer. The anionic structure (Fig. 3.24(d)) is the most stable in all the present calculations, with a second isomer (3.24(e)) 0.40-0.45 eV higher. The open form (3.24(f)) related to structure

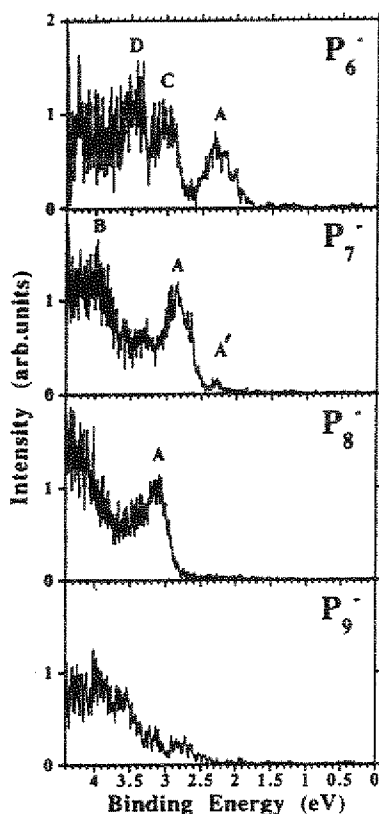


Figure 3.27: Photoelectron spectra of P_n^- -clusters ($n=6-9$) recorded at $h\nu=4.66$ eV photon energy. See text for a discussion of the features marked.

(3.24(d)) is a further 0.6 eV higher. Structures 3.24(d,e) are related to the prism structure of P_6 by bridging bonds in and between the triangular faces, respectively. Comparison of 3.24(e) with the “roof plus trimer” structure of P_7 (Fig. 5(b) of Ref. [JH90c]) shows that the effect of the additional charge in the anion is very large. The energy change in P_7 between these two structures is correspondingly large (0.68 eV).

The measured intensities fall for clusters with more than six atoms, and relatively unstructured backgrounds become more apparent. The pronounced peak A in the spectrum (Fig. 3.27) of P_7^- (VDE 2.79 eV) is closest to the value calculated for the 3.24(d) structure (3.11 eV), but the other two structures have excitation energies only 0.2 eV higher. Another feature A' is weak, and its location close to the BE of peak A in the spectrum of P_6^- suggests that it may originate from a photofragmentation process. The structural relaxations on removal of an electron from structures 3.24(d) and 3.24(e) are quite different. In the former, the anionic and neutral structures are very similar, the change in energy on relaxation is only ~ 0.1 eV, and we expect a sharp rise in intensity to the maximum at the VDE. In the latter, the calculations predict a relaxation of ~ 0.6 eV and a much broader peak. Although the calculations predict that 3.24(d) is more than 0.4 eV more stable than 3.24(e), the interpretation of the measured spectra is ambiguous, and it is possible that both isomers are present.

Molecule	Symmetry	ΔE
P_7^- 3.24(d)	C_{2v}	0.0
$d_{16}=4.28, d_{12}=4.24, d_{13}=4.20, d_{37}=4.01, \alpha_{612}=102.9^\circ, \alpha_{132}=60.8^\circ, \alpha_{137}=111.4^\circ, \alpha_{374}=100.0^\circ$		
P_7^- 3.24(e)	C_s	0.41
$d_{12}=4.15, d_{17}=4.08, d_{16}=4.49, d_{56}=4.18, d_{46}=4.08, \alpha_{217}=83.9^\circ, \alpha_{216}=88.8^\circ, \alpha_{165}=89.0^\circ, \alpha_{164}=100.8^\circ, \alpha_{654}=58.5^\circ$		
P_7^- 3.24(f)	C_{2v}	1.47
$d_{16}=3.80, d_{13}=4.33, d_{37}=4.00, \alpha_{613}=104.8^\circ, \alpha_{132}=92.5^\circ, \alpha_{137}=104.4^\circ$		
P_8^- 3.28(a)	C_s	0.0
$d_{13}=4.26, d_{37}=4.02, d_{34}=4.33, d_{27}=4.08, d_{25}=4.32, d_{45}=4.15, d_{46}=4.23, \alpha_{134}=90.3^\circ, \alpha_{137}=104.6^\circ, \alpha_{273}=100.1^\circ, \alpha_{725}=100.2^\circ, \alpha_{734}=96.7^\circ, \alpha_{346}=89.8^\circ, \alpha_{456}=61.4^\circ$		
P_8^- 3.28(b)	C_{2v}	0.23
$d_{13}=4.33, d_{78}=4.77, d_{27}=4.13, d_{25}=4.20, \alpha_{456}=71.1^\circ, \alpha_{643}=86.6^\circ, \alpha_{273}=102.7^\circ$		
P_8^- 3.28(c)	C_{2v}	1.28
$d_{14}=4.07, d_{34}=4.92, d_{45}=4.61, d_{36}=4.20, \alpha_{345}=88.4^\circ, \alpha_{341}=88.6^\circ, \alpha_{145}=103.9^\circ, \alpha_{412}=91.6^\circ, \alpha_{436}=91.2^\circ, \alpha_{432}=88.5^\circ, \alpha_{632}=91.8^\circ$		
P_8^- 3.28(d)	D_{4h}	1.43
$d_{45}=4.10, d_{34}=4.86$		

Table 3.15: Structure parameters for isomers of P_7^- and P_8^- , with energies ΔE relative to the ground state (eV). Bond lengths d_{ij} in a.u., bond angles α_i in degrees. Additional labels refer to the figures.

P_8^-

The predicted structures of the P_8 -isomers gave perhaps the most unexpected results in the earlier study of neutral clusters [JH90a]. The cubic structure that had been favoured by several authors proved to be much (1.7 eV) less stable than the wedgelike (C_{2v}) analog of the cuneane form of $(CH)_8$. A third isomer (D_{2h}) had an energy between these two. Apart from the occurrence of P_8 -cages in crystalline phosphorus [TK69], we are unaware of any experimental information on the structure of the isolated clusters.

The MD/DF calculations predict several local minima in the energy surface of the anion. The two with the lowest energies are derived from the cuneane structure, with 3.28(a) being more stable by 0.22 eV. In the latter, there is a large expansion in two of the parallel bonds. This configuration is unstable to annealing at 300K, with one of the long bonds breaking and the other contracting to give a structure with lower symmetry (not shown here). A similar situation occurs in the structures related to a cube, where the more symmetrical structure (3.28(d)) has four expanded bonds. The more stable of the pair (3.28(c)) – with energy 1.3 eV above that of the most stable isomer – has one broken bond and seven bonds of length comparable with those in the cubic form of P_8 . Annealing from the D_{2h} structure of P_8 [JH90c] also results in structure 3.28(c). The structure 3.28(b) does presumably not correspond to an energy minimum, as annealing leads directly to the most stable form 3.28(a).

Our calculations lead to VDE values that are significantly higher for the most stable isomer (3.28(a)) than for all others. For example, we found 3.0 eV for 3.28(a) and 2.5 eV for

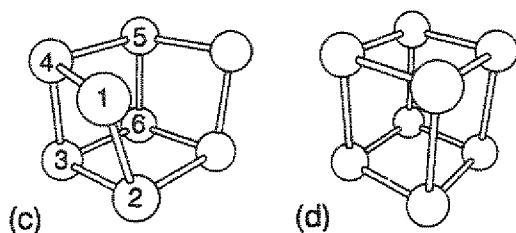
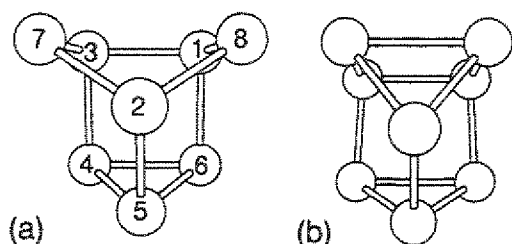


Figure 3.28: Structures of P_8^- . Labels in (b) and (d) are as in (a), (b), respectively.

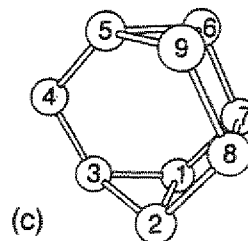
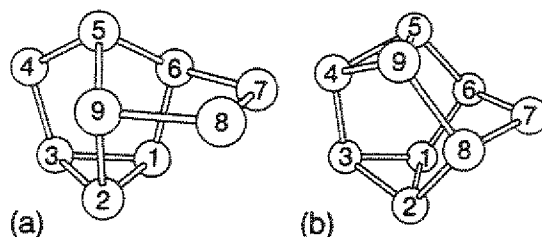


Figure 3.29: Structures of P_9^- .

3.28(c). The vertical excitation energies are consistent with these results. The agreement between the measured VDE (3.05 eV) and the calculated value (3.02 eV) is very good, while the values for the other three isomers are much lower (2.34-2.55 eV).

P_9^-

Our calculations predict that the most stable isomer of P_9^- is the C_s form shown in Fig. 3.29(a), which may be viewed as a dimer attached to the most stable form of P_7^- . The C_{2v} unit 3.29(b) found in crystalline Hittorf's phosphorus [TK69], is only ~ 0.2 eV higher, and structure 3.29(c) is more than 1 eV less stable.

The most stable isomers in P_9^- have VDE values that are 3.60 eV (3.29(a)) and 3.28 eV (3.29(b)). The VDE for the latter, less stable structure is then in better agreement with the measured value (3.11 eV). But structure 3.29(c) has a VDE of 3.1 eV, and the experimental information is not sufficient to make a definite assignment in this case.

3.4.2 Trends and Discussion

The trends in the structures of the phosphorus cluster anions are reminiscent of the neutral clusters. The structures are "three-dimensional" from $n = 4$, and from $n = 7$ they show distributions in bond lengths, bond angles, and dihedral angles that are similar to those found in bulk phases of the element. Phosphorus atoms prefer three-fold coordination, although two-fold coordinated atoms generally have shorter bonds. The shortest bonds found were the multiple bonds occurring in the dimer and trimer. Bonds in rectangular structural units (bond angles $\sim 90^\circ$) are generally longer than those in triangular units, and the presence of rectangular units is energetically unfavourable. An example is the case

Molecule	Symmetry	ΔE
P_9^- 3.29(a)	C_s	0.0
$d_{34}=4.05, d_{45}=4.04, d_{56}=4.18, d_{67}=4.14, d_{78}=3.91, d_{16}=4.12, d_{12}=4.17, d_{13}=4.31, \alpha_{345}=101.6^\circ$ $\alpha_{456}=99.5^\circ, \alpha_{567}=102.6^\circ, \alpha_{561}=102.6^\circ, \alpha_{678}=106.6^\circ, \alpha_{613}=101.2^\circ, \alpha_{612}=104.9^\circ, \alpha_{132}=57.8^\circ$		
P_9^- 3.29(b)	C_{2v}	0.27
$d_{45}=4.14, d_{56}=4.31, d_{59}=3.91, d_{67}=4.32, \alpha_{945}=60.6^\circ, \alpha_{456}=109.6^\circ, \alpha_{567}=103.1^\circ,$ $\alpha_{678}=95.8^\circ, \alpha_{687}=104.8^\circ$		
P_9^- 3.29(c)	C_{2v}	1.49
$d_{45}=4.03, d_{56}=4.15, d_{69}=4.37, d_{67}=4.30, d_{78}=4.12, \alpha_{345}=110.0^\circ, \alpha_{456}=123.3^\circ, \alpha_{569}=58.2^\circ,$ $\alpha_{567}=95.8^\circ, \alpha_{678}=91.6^\circ, \alpha_{659}=63.6^\circ$		

Table 3.16: Structure parameters for isomers of P_9^- , with energies ΔE relative to the ground state (eV). Bond lengths d_{ij} in a.u., bond angles α_i in degrees. Additional labels refer to the figures.

of P_9^- , where 3.29(c) is less stable than the otherwise similar structure 3.29(b). Rings with approximately pentagonal projections are found, and the most stable form of P_8^- can be viewed as a "pentagon plus trimer" structure.

The anionic structures are generally more open than the corresponding neutral systems, and there are other differences arising from the different number of electrons. In P_4 , for example, the tetrahedral structure is stable, while P_4^- undergoes a Jahn-Teller distortion. For $n = 3, 5$, on the other hand, the anion structures have higher symmetries (D_{3h}, D_{5h}) than the Jahn-Teller distorted structures of P_3 and P_5 . As in the case of the sulfur clusters, the presence of the additional electron in the anion can stabilize structures that are unstable in the neutral clusters. In S_n^- these were chain structures that revert otherwise to the more stable rings. The vertical detachment in the former were larger than in the latter, where the most weakly bound electron occupied an orbital localized to one bond or atom. The differences in VDE are smaller in the phosphorus anions, but we note that P_8^- has two local minima (3.28(b),(d)) – corresponding to structures with two and four expanded bonds, respectively – that are less stable than the related structures (3.28(a),(c)), where the additional charge is located in the region of one (broken) bond.

In those cases, such as P_4^- , P_5^- , and P_8^- , where the energy calculations give an unambiguous prediction of the form of the most stable isomer, the calculated detachment energies are in satisfactory agreement with experiment. The measurements indicate that the most stable form of P_8^- (with high probability P_8 as well) has a "wedge" (cuneane) rather than a cubic structure. In P_3^- , where the present and earlier calculations predict the existence of three isomers with different structures but very similar energies, we show that the source generates at least two isomers, one of them linear. Spectra for P_5^- taken with $h\nu=3.49$ eV (below the electron affinity 4.04 eV) show fragmentation into P_3^- and P_2 . We have noted above (Sec. 3.4.1) that there is evidence that the same process occurs in solutions containing the pentamer anion. The situation in P_7^- and P_9^- is less definite. The energies of the most stable isomers in these cases are only ~ 0.2 eV lower than the next most stable, and the vertical excitation energies in the P_7^- isomers are similar. The VDE of the second most stable isomer of P_9^- is in better agreement with the measured value

n	A'	A	B	C	D	E
1		0.75	2.16	3.07		
2		0.68	3.03	3.65	4.10	
3		1.68	1.96	2.89	3.91	4.32
4		1.35	2.69	>4.40		
5	2.49	4.04				
6		2.22	2.59	3.00	3.47	
7	2.19	2.79	4.00			
8	2.20	3.05				
9	2.70	3.11				

Table 3.17: The BE's in eV of the electronic transitions observed in the photoelectron spectra of P_n^- . The uncertainty in the measurements is ± 0.05 eV except for $n = 1$. The BE's of features A correspond to the VDE's.

than the value of the most stable isomer.

3.5 Mixed Silicon-Carbon Cluster Anions Si_nC_m^-

Elements belonging to the same group of the periodic table have properties in common, and carbon and silicon (group 14) are no exceptions. Nevertheless, their differences are very pronounced. The immense variety of organic chemistry, reflecting the ability of carbon to form single, double and triple bonds, is not shared by silicon, which favors multi-directional single bonds. It is perhaps not surprising that the structures of the elemental clusters show striking differences.

For pure carbon clusters with up to 10 atoms, *ab initio* calculations [PC59, RB87, MFG90] have predicted odd-membered clusters to have linear optimal structures, whereas cyclic forms have been ascribed to even-membered C_n clusters, although at least linear C_4 might be favoured by entropy at room temperature [ASG90, BMB88]. And indeed, experimental results show evidence for the presence of both linear and cyclic geometries: linear C_4 has been observed in matrix Fourier transform infrared measurements [SG89, WSG91] and by photoelectron spectroscopy [ABKN91], while the rhombic form has been observed only indirectly in a Coulomb explosion experiment [VFK⁺91], which is difficult to interpret unambiguously. The larger clusters have been observed [HGK⁺95] to form monocyclic rings and there is evidence for the existence of bicyclic rings for C_n , $n \gtrsim 20$. Finally, many clusters with even numbers $n \gtrsim 28$ have lowest-energy isomers that belong to the famous fullerenes [GDC⁺92].

By contrast, Si_n clusters are predicted to be cage-like for $5 \leq n \leq 11$ [RR88, RR90, AP90, LVWR95] and the peaks in the abundance spectra corresponding to fullerene structures in C_n are absent in Si_n [AMS91]. CP-MD calculations [RAP94] have predicted that for Si_n with $n \gtrsim 25$, the atoms are organized into two shells: an outer one reminiscent of a fullerene topology and an inner one of highly coordinated atoms.

While the combination of theory and experiment has led to a rather detailed picture of the elemental clusters, this is not so for mixed clusters Si_nC_m . It is natural to expect that such clusters exhibit structural features of C_n and Si_n , and this has been confirmed by a number of studies in the past years. The experimental work includes absorption spectra in matrices [PMG92, PMG94] and in the gas phase [RBRR94, OGP⁺94], and the recent PE studies [NTN⁺95] of Si_nC_m^- anions. These data provide a challenge to theoreticians, as does the large number of topologically distinct isomers that can occur in mixed clusters. While there have been numerous theoretical ([GS84], [GS85, Rit91, BDF⁺92], [DC94], [AGS90], [LG88], [MAZ89], [Rit94], [FMZ95], [MFZP93, MFZ⁺94], [FZM⁺94]) and experimental ([PMGS90, BR92, MGLSS84], [PMG91], [Rit92, PMG92], [PMGRG95], [WG92], [PMG94]) publications on individual Si_nC_m clusters, a systematic investigation is still missing. We note that the *bulk* phases of SiC also have remarkable properties. There are more than 100 crystalline forms ("polytypes") [Yeo88], characterized by different stacking sequences of close-packed layers that can have long periods. The amorphous phase (α -SiC) is a high-temperature semiconductor whose structure has been the subject of some debate. A recent study using a combination of MD and DF calculations [FGPB93] showed that the structure has many (40-45%) homonuclear bonds, with the C atoms tending to form chainlike structures.

Photoelectron spectra of pure C_n^- anions [YTC⁺88, ABKN91] consist of sharp features for $n=3-9$ and of relatively broad features for $n \geq 10$. Furthermore, the VDEs of odd numbered clusters display much lower values than those of the even numbered ones for $n < 10$ and, starting at $n=10$, the even/odd pattern inverts. Both observations can be explained qualitatively by a transition from linear optimal structures to ring topologies at $n=10$. The peaks in the transition between anion and the neutral species of three dimensional structures are broader than those between the species of linear isomers, because the freedom of bending or rocking vibrations having low frequencies is higher in the former and the peaks of these low frequency vibrations cannot be observed separately. The even-odd alternation of the VDEs can also be understood, since even numbered linear anions have a $\pi^2\pi^1$ configuration, i.e., an attached electron occupies the HOMO, whereas odd numbered chains have a π^1 configuration, i.e., the electron occupies the higher lying LUMO. The pattern inverts for ring isomers, since two more electrons of the former lone pairs of the chain enter the π system after closure of the ring. This is consistent with recent numerical results [WB92, LS90, PA92] and has been affirmed by ion chromatography measurements on clusters with up to 10 atoms [vHKGB93].

Photoelectron spectra of Si_n^- for $n \leq 12$ [CYP⁺87] and Raman spectra of Si_n^- for $n=4,6,7$ [HOM⁺93] have been interpreted successfully by theoretical investigations [RR91a, RR91b, RR92, GM95], assigning, e.g., a rhombus to Si_4^- , a trigonal bipyramid to Si_5^- , a tetragonal bipyramid to Si_6^- and a "triplet tetracapped tetrahedron" to Si_7^- . As these investigations have shown, in some cases (e.g., C_6^- , C_8^- , Si_6^- , Si_8^- , Si_9^- [RB87, RR91a]), the geometries of both carbon and silicon cluster anions can differ substantially from those of their neutral counterparts.

While the structures of pure C_n^- and Si_n^- anions are thus relatively well understood through a combination of theory and experiment, the structures of anionic $Si_nC_m^-$ clusters, which are essential for interpreting PE data, have not yet been studied systematically. We describe here the results of an extended series of DF calculations on $Si_nC_m^-$ anions ($n+m \leq 8$) and their neutral counterparts and focus on the comparison of our results to available PE spectra of these clusters [GPS96, NTN⁺95].

3.5.1 Optimal Geometries, Vibration Frequencies, and Vertical Excitation Energies

The interatomic distances included in Tables 3.18-3.22 are shorter than 3.82 a.u. between C atoms and 5.35 a.u. between Si atoms, which corresponds to the minima of the respective pair correlation functions of liquid C [GMCP90] and Si [ŠCP91] between the first peak for covalently bonded pairs and the second peak for nonbonded pairs. For C-Si distances, we have chosen the arithmetic mean of both values, i.e., 4.57 a.u. as a cutoff distance. "Bonds" are shown in Figures 3.30-3.39 for interatomic distances < 5.3 a.u., irrespective of the atomic species. The photoelectron spectra have been recorded at $h\nu=3.49$ eV [NTN⁺95] and $h\nu=3.8$ eV photon energy [GPS96], respectively.

Molecule	Symmetry	State	ΔE
SiC ⁻	$C_{\infty v}$	$^2\Sigma^+$	0.00
$d_{12}=3.17$;			
SiC ₂ ⁻ 3.30(a)	C_{2v}	2B_2	0.00
$d_{12}=2.49$; $d_{13,23}=3.56$; $\alpha_{123,213}=70^\circ$; $\alpha_{132}=41^\circ$;			
SiC ₂ ⁻ 3.30(b)	$C_{\infty v}$	$^2\Pi$	0.03
$d_{12}=2.43$; $d_{23}=3.32$;			
Si ₂ C ⁻ 3.30(c)	$D_{\infty h}$	$^2\Pi_g$	0.00
$d_{12,13}=3.25$;			
SiC ₃ ⁻ 3.30(e)	$C_{\infty v}$	$^2\Pi$	0.00
$d_{12}=2.45$; $d_{23}=2.52$; $d_{34}=3.22$;			
SiC ₃ ⁻ 3.30(f)	C_{2v}	2A_2	0.49
$d_{12,23}=2.58$; $d_{14,34}=3.78$; $d_{24}=3.45$; $\alpha_{123}=152^\circ$; $\alpha_{214,234}=62^\circ$;			
SiC ₃ ⁻ 3.31(a)	C_{2v}	2B_1	0.67
$d_{12,23}=2.70$; $d_{13}=2.76$; $d_{14,34}=3.54$; $\alpha_{123}=61^\circ$; $\alpha_{214,234}=126^\circ$; $\alpha_{143}=46^\circ$;			
Si ₂ C ₂ ⁻ 3.31(b)	C_s	$^2A''$	0.00
$d_{12}=2.49$; $d_{13}=3.56$; $d_{14}=3.49$; $d_{23}=3.77$; $d_{34}=4.56$; $\alpha_{123}=66^\circ$;			
$\alpha_{214}=155^\circ$; $\alpha_{143}=50^\circ$; $\alpha_{234}=89^\circ$;			
Si ₂ C ₂ ⁻ 3.31(c)	$D_{\infty h}$	$^2\Pi_g$	0.10
$d_{12}=2.48$; $d_{14,23}=3.26$;			
Si ₃ C ⁻ 3.31(e)	C_{2v}	2A_2	0.00
$d_{12,14}=3.38$; $d_{13}=3.58$; $d_{23,24}=4.49$; $\alpha_{214}=161^\circ$; $\alpha_{234}=96^\circ$;			

Table 3.18: Structure parameters for isomers of Si_nC_m^- , $n+m=2-4$, with energies ΔE relative to the ground state (eV). Bond lengths d_{ij} in a.u. and bond angles α_{ijk} in degrees. Bond angles are given where appropriate. Additional labels refer to the figures, where also the atom numberings are defined.

SiC⁻

Our calculations for neutral SiC yield a $^3\Pi$ GS [$\dots(\pi)^3(\sigma)^1$] with a $^3\Sigma^-$ excited state [$\dots(\pi)^2(\sigma)^2$] 0.42 eV above it, in agreement with CI results [BR92, 0.44 eV, MR-SOCI]. The lowest singlet $^1\Sigma^-$ state [$\dots(\pi)^4$] was found at 0.76 eV [BR92, 0.65 eV, MR-SOCI]. Although C₂ and Si₂ are well-known species [HH79], it was not until 1988 that SiC was identified spectrometrically by Bernath *et al.* [BRO⁺88]. The authors were able to resolve the 0-0 band of the $d^1\Sigma^+ - b^1\Pi$ electronic transition in the vibration-rotation spectrum of SiC. It has subsequently been detected [CGG⁺89] at millimeter wavelengths in the envelope of a carbon star. In combination with theoretical results, the $^3\Pi$ GS bond length has been estimated to $r_e = 3.248$ a.u., with an estimated accuracy of 0.002 a.u.. Our value $r_e = 3.24$ a.u. compares well with this result as well as with other theoretical predictions [BL87, 3.28 a.u., MRCI].

Addition of an electron to the abovementioned SiC triplet states yields a $^2\Sigma^+$ GS [$\dots(\pi)^4(\sigma)^1$] with a $^2\Pi$ state [$\dots(\pi)^3(\sigma)^2$] 0.47 eV above it. The shorter bond length in

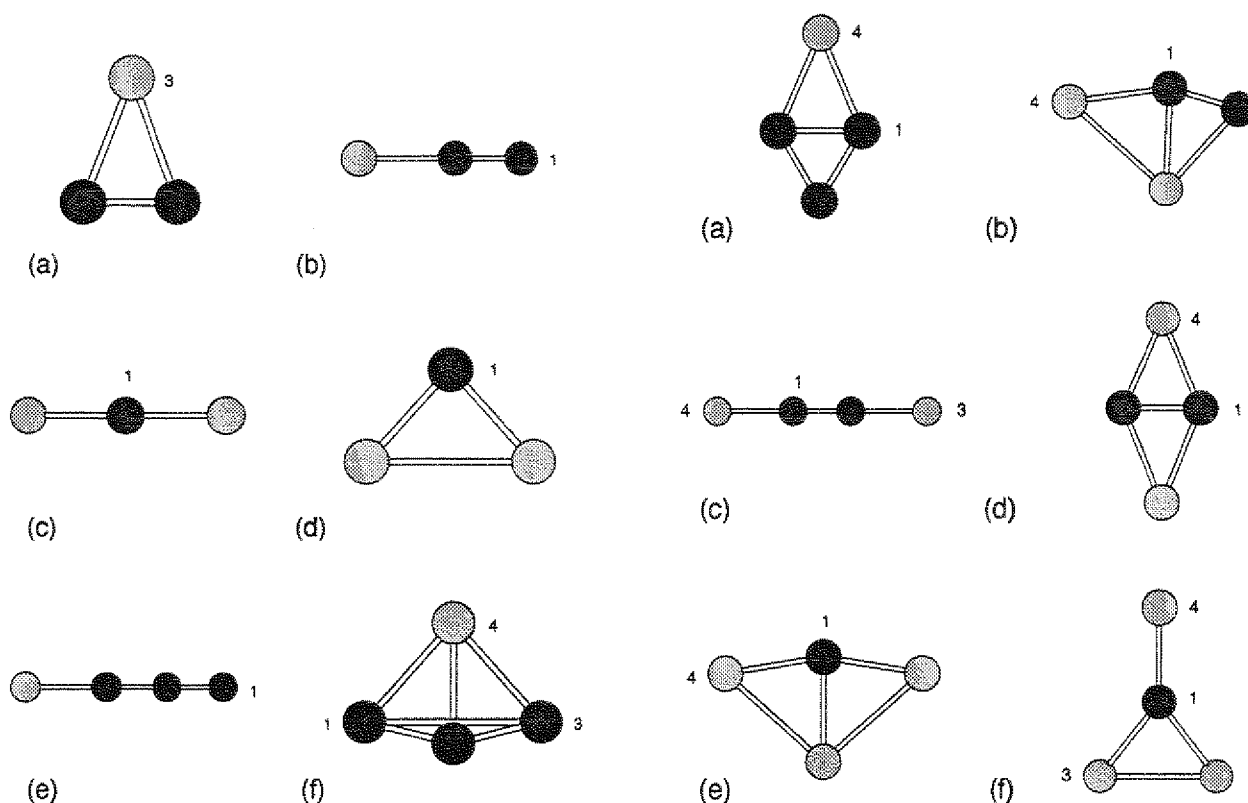


Figure 3.30: Structures of (a,b) SiC_2^- (c,d) Si_2C^- and (e,f) SiC_3^- . Light spheres are Si atoms, dark spheres are C atoms.

Figure 3.31: Structures of (a) SiC_3^- , (b-d) Si_2C_2^- and (e,f) Si_3C^- . Light spheres are Si atoms, dark spheres are C atoms.

the anion [3.17 a.u. ($^2\Sigma^+$)] than in the neutral GS is consistent with the presence of more π electrons in the former and is also observed with $\text{Si}_2/\text{Si}_2^-$ clusters [NHE87]. No other experimental results were found in the literature nor could a photoelectron spectrum be recorded by Ganteför *et al.* [GPS96] for this very elusive molecule, but we nevertheless list our results for the anion in Tables 3.18 and C.2.

SiC_2^-

According to our results, neutral SiC_2 has a C_{2v} 1A_1 GS with a C-Si-C angle of 41° . A linear Si-C-C structure is 0.19 eV less stable. The corresponding triplet states are 1.55 and 2.27 eV higher in energy. This is in agreement with the experimentally determined [SG85] bond angle of $40\text{-}41^\circ$ and theoretical values for the energy difference between the isomers of 0.22 eV [GS84, TCSCF] and 0.16 eV [DC94, QCISD(T)/6-311+G(3df,2p)]. Our calculated bond lengths [$r(\text{Si-C})=3.48$ a.u., $r(\text{C-C})=2.41$ a.u.] are in reasonable agreement with those extracted from spectroscopic data [$r(\text{Si-C})=3.42$ a.u., $r(\text{C-C})=2.36$ a.u., [MGLSS84]].

Adding an electron stabilizes the linear isomer [$^2\Pi$ state, Fig. 3.30(b)] with respect to the other, which is now virtually degenerate (0.02 eV higher) with a 2B_2 state of the C_{2v} anion shown in Fig. 3.30(a). The bond lengths in the C_{2v} isomer are larger in the

Total atoms	Composition		Figure	VDE		
	n	m		N	G	Calc
3 atoms	1	2	3.30(b)	1.54(0.06)	1.72(0.05)	1.69
	2	1	3.30(c)	-	1.17(0.05)	1.18
4 atoms	1	3	3.30(e)	2.76(0.04)	2.90(0.10)	2.86
	1	3	3.31(a)	1.93(0.10)	2.00(0.10)	2.08
	2	2	3.31(b)	1.93(0.08)	2.10(0.15)	2.07
5 atoms	3	1	3.31(e)	1.54(0.08)	1.60(0.05)	1.69
	1	4	3.34(a)	2.34(0.04)	2.33(0.05)	2.27
	2	3	3.34(d)	1.71(0.10)	1.77(0.05)	1.82
	3	2	3.35(a)	-	1.90(0.15)	1.88
6 atoms	4	1	3.35(d)	3.12(0.10)	-	3.21
	1	5	3.35(f)	3.14(0.03)	3.29(0.05)	3.22
	2	4	3.36(c)	2.49(0.08)	2.70(0.15)	2.59
	3	3	3.37(a)	2.16(0.08)	2.42(0.05)	2.51
	4	2	3.37(e)	2.10(0.08)	-	2.18
7 atoms	5	1	3.38(b)	1.74(0.08)	-	1.81
	2	5	3.38(e)	2.16(0.06)	2.22(0.05)	2.18
	6	1	3.39(c)	1.74(0.08)	-	[1.79]
8 atoms	7	1	3.39(e)	2.92(0.08)	-	[3.32]

Table 3.19: Si_nC_m^- clusters: vertical detachment energies (VDE, eV), with uncertainties in brackets, obtained from photoelectron spectra of Nakajima and coworkers [NTN⁺95] (denoted “N”) and Ganteför and coworkers (denoted “G”). Calculated VDEs (denoted “Calc”) are also given. Values in square brackets belong to isomers that are not the most stable.

anion by about 3%, while the bond angles remain the same. The photoelectron spectra of Fig. 3.32(a) [GPS96] and of Nakajima *et al.* [NTN⁺95] show relatively broad peaks around 1.72 ± 0.05 eV [GPS96] and 1.54 ± 0.06 eV [NTN⁺95], respectively, which would be compatible with the presence of both isomers with calculated VDEs 1.50 eV (C_{2v}) and 1.69 eV ($C_{\infty v}$). Fig. 3.32 also indicates the presence of an excited state at 3.62 ± 0.05 eV BE, which favours the linear isomer, whose first excited state ($^3\Pi$) lies at 3.69 eV BE, and excludes the C_{2v} isomer that has a 3B_2 state at 2.99 eV BE, since the spectrum shows only a very low signal at this value. The spectrum of Nakajima *et al.* [NTN⁺95] as well shows no significantly increased intensity near 3.0 eV, which should be observable, if the assignment to the C_{2v} isomer would be correct, so that the presence of this isomer in either of the experiments is unlikely.

Si_2C^-

The neutral Si_2C dimer has C_{2v} and $D_{\infty h}$ structures that are again close in energy, the 1A_1 state of the C_{2v} isomer being 0.11 eV more stable than the $^1\Sigma_g^+$ state of the linear isomer. The energy ordering and difference is similar to that reported in other studies ([Rit91, 0.08 eV, MBPT2/6-311G(2d)], [GS85, 0.09 eV, CISD]). Two triplet states were found at ~ 2.5 eV above the C_{2v} ground state. The C_{2v} structure has a SiC bond length of 3.21 a.u.

and a SiCSi angle of 116° , in accordance with other theoretical results ([Rit91, $r(\text{SiC})=3.22$ a.u., $\alpha(\text{SiCSi})=119.5^\circ$], [BDF⁺92, $r(\text{SiC})=3.18$ a.u., $\alpha(\text{SiCSi})=117.6^\circ$, TZ+2P+f CISD]). The length of the SiC bond is unusually short, as has already been noted by Grev and Schaefer [GS85], and this has been attributed to the strong polar character of this bond.

The addition of an electron causes the SiCSi angle of the C_{2v} isomer to increase in our simulations and we obtain the same linear isomer [Fig. 3.30(c)] with a $^2\Pi$ GS for both neutral species. Such a behaviour may already be expected from simple electrostatic considerations. Starting from an equilateral triangle, we found another local minimum with C_{2v} geometry [Fig. 3.30(d)] and 2A_1 GS only 0.01 eV higher in energy on the BO energy surface of the anion. As can be seen from Table C.2, the excitation spectra of the neutral species at the geometries of the anions show marked differences which should facilitate their distinction in the photoelectron spectra. The photoelectron spectrum of Ganteför *et al.* [GPS96] depicted in Figure 3.32 is indeed incompatible with the presence of the C_{2v} isomer. On the other hand, the calculated VDE (1.18 eV) of the linear species is in excellent agreement with the spectroscopic result (1.17 ± 0.05 eV) and the presence of a second peak with a broad, unresolved Franck-Condon profile at 3.66 eV BE is in reasonable agreement with our value for a transition into the lowest excited state [3.49 eV ($^3\Pi_g$)] of this isomer.

SiC₃⁻

As we have seen in the previous sections, there is a strong competition between cyclic and linear isomers in the series of neutral three-atomic silicon-carbon clusters: Si₃ has a cyclic GS structure¹, Si₂C has a weakly bent C_{2v} geometry, SiC₂ is cyclic (C_{2v}) and C₃ is linear (here and Ref. [RB87]). On the other hand, as our results indicate, three-atomic silicon-carbon anions are more inclined towards linear geometries: while Si₃⁻ is still cyclic [RR91a], Si₂C⁻ and SiC₂⁻ are linear, and photoelectron spectra of C₃⁻ [YTC⁺88] indicate that this isomer is linear, too. A similar behavior may now be expected for tetra-atomic clusters. Both Si₃ (here and Ref. [Rag86]) and Si₄⁻ are rhombic and C₄ might also prefer a rhombic form [ASG90]. Neutral SiC₃ indeed has a rhombic C_{2v} minimum structure with a 1A_1 GS (here and Ref. [AGS90]) and a transannular (cross ring) CC bond [$r(\text{CC})=2.72$ a.u. (here), $r(\text{CC})=2.78$ [AGS90]]. Another rhombic C_{2v} isomer with a transannular SiC bond [$r(\text{SiC})=3.58$ a.u. (here), $r(\text{SiC})=3.55$ [AGS90]] just 0.08 eV [AGS90, 0.19 eV] above the GS. A further, linear isomer with a $^3\Sigma^-$ GS isomer has an intermediate energy of 0.01 eV above the GS [AGS90, 0.18 eV]. Other structures and electronic states considered are appreciably higher (≥ 0.75 eV) above the GS.

In the anion, the near degeneracy of the isomers is lifted and their relative order reverses completely. The linear isomer [Figure 3.30(e)] is now more stable than the C_{2v} isomer with the transannular SiC bond [Figure 3.30(f), 0.49 eV higher] and the former GS, the C_{2v} isomer with a transannular CC bond [Figure 3.31(a)] is another 0.18 eV higher in energy.

¹Our LSDA calculations favour a $^3A'_2 D_{3h}$ isomer slightly (by 0.08 eV) over a $^1A_1 C_{2v}$ isomer, while Hartree-Fock calculations [Rag85, CCD+ST(4)] report an inverse ordering with the C_{2v} isomer being 0.02 eV more stable.

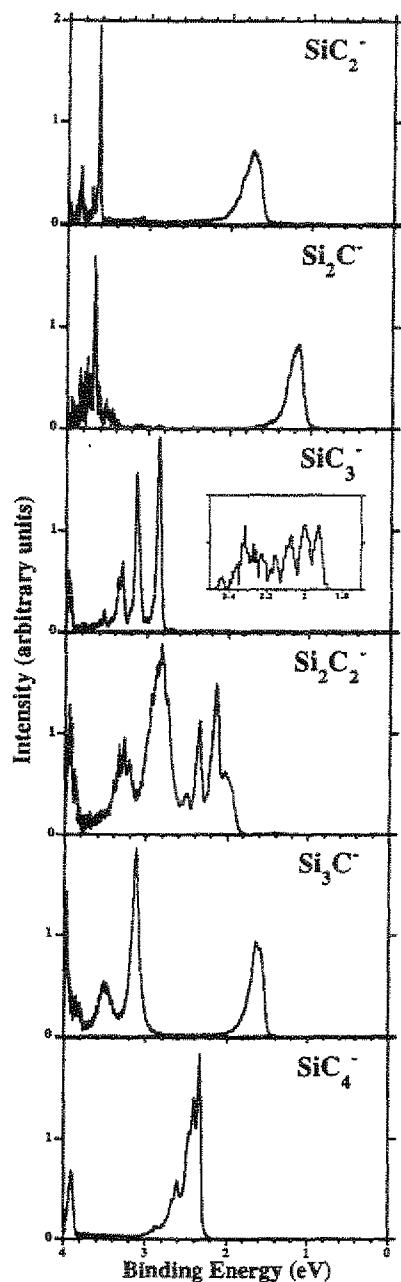


Figure 3.32: Photoelectron spectra of Si_nC_m^- -clusters ($n+m=3-5$) recorded at $h\nu=3.8$ eV photon energy.

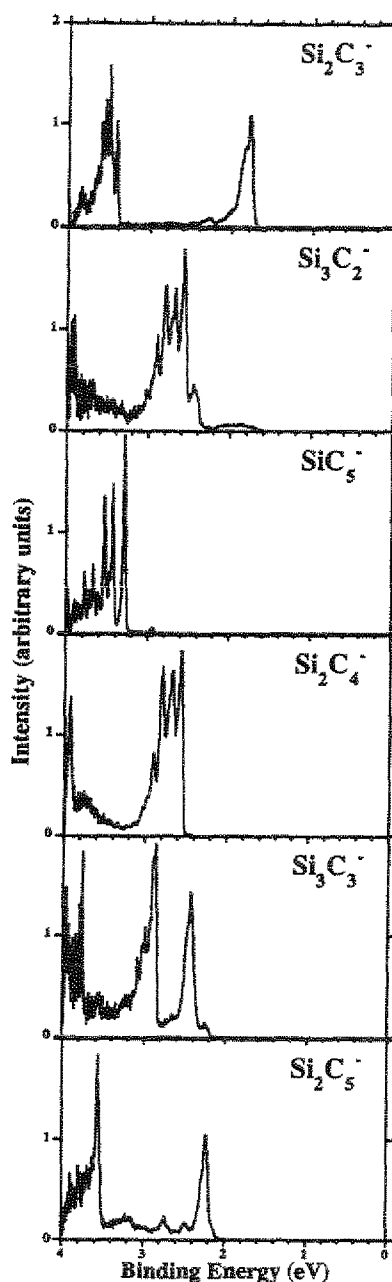


Figure 3.33: Photoelectron spectra of Si_nC_m^- -clusters ($n+m=5-7$) recorded at $h\nu=3.8$ eV photon energy.

Again, as already observed at the S_n^- (helical) chain isomers, the additional electron has a high amplitude at the terminal bonds of the linear isomer, which are contracted by $\sim 2\%$ compared to the neutral species.

The photoelectron spectra recorded by Ganteför *et al.* [GPS96] (Fig. 3.32) and Nakajima *et al.* [NTN⁺95] both reveal an interesting detail: apart from the main peaks (VDE:

Molecule	Symmetry	Method	Frequency ω_e
SiC ₃	$C_{\infty v}(^3\Sigma^-)$	Expt ^a	2178±250
		here	168 (π), 442 (π), 588 (σ), 1283 (σ), 1959 (σ)
Si ₂ C ₂	$C_s(^1A')$	SCF ^b	164 (π), 456 (π), 659 (σ) 1275 (σ), 2037 (σ)
		Expt ^a	1490±120
		here	172 (a''), 269 (a'), 424 (a'), 585 (a'), 673 (a'), 1530 (a')
Si ₂ C ₂	$D_{\infty h}(^3\Sigma_g^-)$	SCF ^c	245 (a''), 306 (a'), 537 (a') 668 (a'), 754 (a'), 1560 (a')
		here	123 (π_u), 425 (π_g), 455 (σ_g), 863 (σ_u), 1845 (σ_g)
Si ₂ C ₂	$D_{2h}(^1A_g)$	SCF ^c	117 (π_u), 278 (π_g), 493 (σ_g), 933 (σ_u), 1801 (σ_g)
Si ₂ C ₂	$D_{2h}(^1A_g)$	here	152 (b_{3u}), 288 (b_{2u}), 440 (a_g), 865 (b_{3g}), 907 (b_{1u}), 1011 (a_g)
		SCF ^c	213 (b_{3u}), 397 (b_{2u}), 522 (a_g), 978 (b_{3g}), 1011 (b_{1u}), 1067 (a_g)
		here	411±50
Si ₂ C ₃	$D_{\infty h}(^1\Sigma_g^+)$	Expt ^a	411±50
		here	97 (π_u), 236 (π_g), 450 (σ_g), 586 (π_u), 875 (σ_u), 1558 (σ_g), 2053 (σ_u)
		SCF ^d	85 (π_u), 210 (π_g), 442 (σ_g) 519 (π_u), 869 (σ_u), 1527 (σ_g), 2082 (σ_u)

^aPresent work [GPS96], photoelectron detachment

^bRef. [AGS90], TZ2P

^cRef. [PMGRG95], TZ2P

^dRef. [Rit94], MBPT(2)/DZP

Table 3.20: Calculated vibration frequencies ω_e (cm^{-1}) of selected isomers of neutral Si_nC_m^- , $n+m \leq 5$.

3.0±0.1 eV [GPS96], 2.76±0.4 eV [NTN+95]; first excited state at 3.13±0.1 eV [GPS96]) that are only compatible with the calculated excitation spectrum of the linear isomer (VDE: 2.86 eV, first excited state ($^1\Sigma^+$): 3.27 eV), there is another very weak signal at 1.93±0.1 eV [NTN+95] and 2.0±0.1 eV BE. Both experimental groups assign this feature to the presence of a second isomer, and Nakajima *et al.* [NTN+95] see indications that it might be produced by a ring isomer. In fact, the position of this feature agrees well with the calculated VDE of the C_{2v} isomer with the transannular CC bond, i.e. 2.08 eV, as can be seen from consulting Table C.2. The spectrum of Ganteför *et al.* [GPS96] shows also another, even slightly weaker peak at 2.31 eV BE, which agrees well with the VDE of the C_{2v} isomer with the transannular SiC bond, i.e., 2.35 eV. The peak at 3.0 eV BE exhibits also vibrational fine structure with frequency 2178±250 cm^{-1} (see Table 3.20), which is consistent with our assignment of this feature to the linear isomer. To conclude, the spectra show signs for the presence of all three isomers, while the dominant contributions stem from the linear GS of the anion.

Si_2C_2^-

There have been several studies of the structure of Si_2C_2 . Rhombic and linear states were studied by Trucks and Bartlett [TB86], who calculated energies up to fourth order in perturbation theory. Another more extensive study by Lammertsma and Güner [LG88] predicted a new low-lying isomeric state of C_s symmetry and Sudhakar *et al.* [SGL89] compared two rhombic D_{2h} structures in terms of a bond stretch isomerism. A higher level comparison of a number of isomers was provided by Fitzgerald and Bartlett [FB90]. We have reconsidered six different isomers and their triplet states, the lowest three of them being: a rhombic D_{2h} isomer with 1A_g GS is 0.18 eV below a distorted trapezoidal C_s structure ($^1A'$ state), which in turn is another 0.18 eV more stable than a linear isomeric state ($^3\Sigma_g^-$) of $D_{\infty h}$ symmetry. The energetic ordering is in accord with Ref. [LG88], who found for the corresponding energy differences 0.36 eV and 0.13 eV at the MBPT(4)/6-31G* level.

As might be suspected from the previous results, the linear isomer [Fig.3.31(c)] is favoured in the anion, but it is still 0.1 eV less stable than the true GS of the anion, which we found to be the distorted trapezoidal C_s structure [Fig.3.31(b)] ($^2A''$ state). The rhombic D_{2h} isomer [Fig.3.31(d)] is 0.25 eV less stable than the C_s structure of the anion. Furthermore, we observed several² isomers of the neutral species undergo considerable structural rearrangement upon charging, all transforming into the C_s isomer, which indicates that the "catchment region" of this isomer is comparatively large. On the other hand, the remaining structures did not change their shapes significantly upon charging.

The photoelectron spectra of Ganteför *et al.* [GPS96], Fig. 3.32, and Nakajima *et al.* [NTN⁺95] agree well with the calculated excitation spectrum of the C_s isomer, Table C.2. Our calculated VDE, 2.07 eV agrees particularly well with the position of the first peak in Fig. 3.32 at 2.1 ± 0.15 eV BE, whereas Nakajima *et al.* [NTN⁺95] give 1.93 ± 0.08 eV for the same quantity. Other peak positions at 2.73 ± 0.05 eV and 3.28 ± 0.05 eV BE agree well with the calculated transition energies into the $^3A''$ and the $^1A''$ excited states of the neutral species at 2.83 eV and 3.21 eV BE, respectively. The peak at 2.1 eV BE seems to be the first of a pronounced vibrational progression with frequency $\omega_e = 1492 \pm 120 \text{ cm}^{-1}$, which is compatible with the theoretical frequency spectrum of the C_s isomer (see Table 3.20). Theoretical results for the vibrational spectra of the remaining two isomers are, however, not compatible with the experimental value, which falls into a pronounced gap in their frequency spectra (between $\sim 1100 \text{ cm}^{-1}$ and $\sim 1800 \text{ cm}^{-1}$, as can be seen in Table 3.20). Although we found no definite sign for the presence of the linear isomer in the spectrum, it cannot be excluded, since our calculated peak positions [2.14 eV ($^3\Sigma_g^-$, VDE), 2.49 eV ($^1\Sigma_g^+$)] partially coincide with peaks of the most stable isomer and/or fall in ranges of comparatively high intensity. On the other hand, the rhombic isomer is, for example, incompatible with the spectrum, as its calculated VDE at 1.56 eV BE falls in an interval of almost zero intensity.

²Among them a trapezoidal C_{2v} structure (3B_1 state) 0.81 eV and a C_2 isomer (1A_1 state) 1.04 eV above the rhombic isomer.

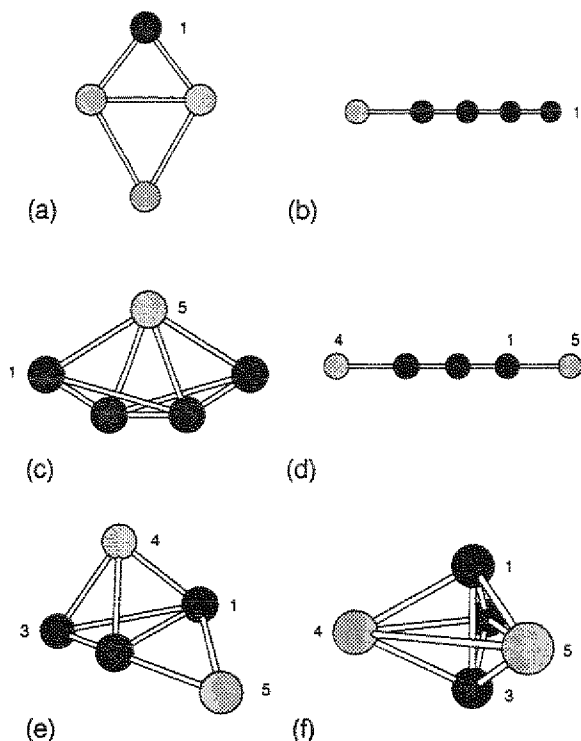


Figure 3.34: Structures of (a) Si_3C^- , (b,c) SiC_4^- and (d-f) Si_2C_3^- . Light spheres are Si atoms, dark spheres are C atoms.

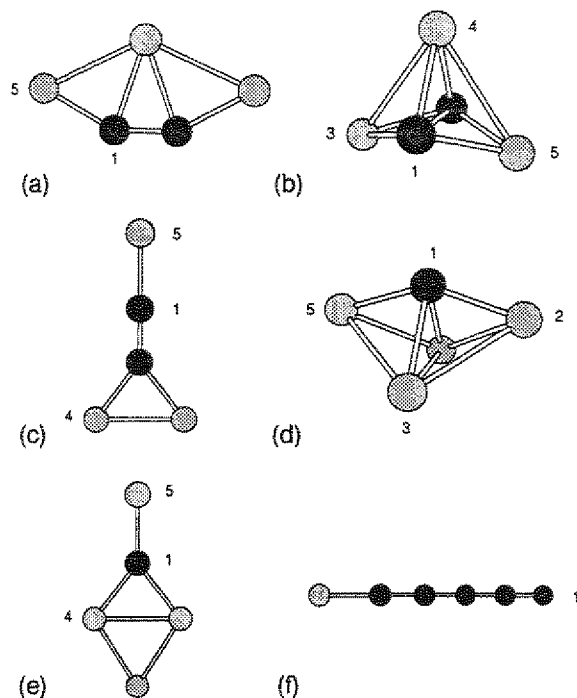


Figure 3.35: Structures of (a-c) Si_3C_2^- , (d,e) Si_3C^- , and (f) SiC_5^- . Light spheres are Si atoms, dark spheres are C atoms.

Si_3C^-

Experimentally, Si_3C has been identified in the products of vaporization of carbon/silicon mixtures trapped in Ar at 13 K by Presilla-Márquez and Graham [PMG92], who also identified fundamental vibrations. In Hartree-Fock calculations, Rittby [Rit92] investigated six different isomeric structures of the neutral species. We have reconsidered these structures, both in their singlet and triplet states, and found, in agreement with Ref. [Rit92] that a rhomboidal C_{2v} structure (1A_1 state) with two equivalent silicon atoms and a transannular SiC bond is the energetically most favourable isomer. The next C_{2v} structure, similar to the anion shown in Figure 3.31(f) with 3B_1 GS is 1.44 eV less stable than the rhombus and another rhomboidal C_{2v} structure with transannular SiSi bond is 0.40 eV higher in energy.

The energetic ordering of the structures is preserved in the anion, the rhomboidal isomer Fig. 3.31(e) now being only 0.80 eV more stable than structure Fig. 3.31(f) and 1.20 eV below the rhomboidal isomer Fig. 3.34(a). As might be expected, the experimental values for the VDE agree well with the calculated value for isomer Fig. 3.31(e), as may be seen from Table 3.19. The agreement is not only good for the VDE, it remains so even for peaks of excited states at 3.12 eV, 3.5 eV and 3.8 eV BE in the spectrum of Ganteför *et al.* [GPS96] (3.16 eV and 3.51 eV are the calculated values; a fourth state with a vertical excitation energy of 3.88 eV is not the lowest state of a given symmetry (3B_1) and therefore

Molecule	Symmetry	State	ΔE
SiC ₄ ⁻ 3.34(b)	C _{∞v}	² Π	0.00
$d_{12}=2.43$; $d_{23}=2.50$; $d_{34}=2.42$; $d_{45}=3.27$;			
Si ₂ C ₃ ⁻ 3.34(d)	D _{∞h}	² Π _u	0.00
$d_{12,23}=2.46$; $d_{15,34}=3.22$;			
Si ₃ C ₂ ⁻ 3.35(a)	C _{2v}	² B ₁	0.00
$d_{12}=2.51$; $d_{14,24}=3.82$; $d_{15,23}=3.33$; $d_{34,45}=4.56$; $\alpha_{123}=150^\circ$; $\alpha_{143}=84^\circ$;			
$\alpha_{345}=130^\circ$;			
Si ₄ C ⁻ 3.35(d)	C _{2v}	² A ₁	0.00
$d_{12,15}=3.47$; $d_{13,14}=3.84$; $d_{23,24,35,45}=4.54$; $d_{34}=4.67$; $\alpha_{215}=146^\circ$; $\alpha_{314}=75^\circ$;			

Table 3.21: Structure parameters for isomers of Si_nC_m⁻, $n + m = 5$, with energies ΔE relative to the ground state (eV). Bond lengths d_{ij} in a.u. and bond angles α_{ijk} in degrees. Bond angles are given where appropriate. Additional labels refer to the figures, where also the atom numberings are defined.

not covered by theory). On the other hand, the spectra do not show any increased intensity near 2.06 eV and 2.47 eV BE, which are the VDEs of isomers Fig. 3.31(f) and Fig. 3.34(a), respectively. These isomers may then be excluded from further consideration.

SiC₄⁻

SiC₄⁻ has been investigated experimentally by Withey and Graham [WG92], who identified a fundamental vibration. Moazzzen-Ahmadi nad Zerbetto [MAZ89] investigated the GS of linear SiC₄ by MBPT (2)/6-311G(d) calculations. Apart from this structure, which turned out to be the most stable in our calculations as well, we considered also a C_{2v} ring (¹A₁ state) 0.62 eV above the chain as well as several others, planar and nonplanar ones, all with considerably higher energies (>1.0 eV) than the chain.

As for SiC₂⁻ and SiC₃⁻, the relative stability of the linear chain Fig. 3.34(b) increases further (to 1.08 eV) in the anion, and the remaining structures become even less important. Indeed, there is no sign for the presence of the ring isomer [Fig. 3.34(c)] in Fig. 3.33, whose VDE (1.95 eV), e.g., falls into an energy interval of low intensity. On the other hand, VDE (2.27 eV) and the other calculated transition energies (> 4 eV) into excited states of the chain isomer are in accordance with the presence and position of only one peak (and the accompanying vibrational progression) at 2.33 and 2.34 eV BE in the spectra of Ganteför *et al.* [GPS96] and Ref. [NTN⁺95], respectively. The origin of another weak feature in the spectrum of Ref. [GPS96] at ~2.60 eV BE is unclear. It might either belong to the vibrational progression of the first peak or belong to a transition into an excited state. Unfortunately, the discussion of further peaks is not possible within LSDA, since it would require the calculation of multiplets arising from two unpaired π electrons (see the discussion in appendix B).

Si_2C_3^-

Si_2C_3 has been investigated experimentally in the vapor of Si/C mixtures by Presilla-Márquez and Graham [PMG94], who also reported the observation of two fundamental vibrations by Fourier transform infrared measurements. One of the vibrations was again observed by van Orden *et al.* [OGP⁺94] using infrared laser spectroscopy. Extensive calculations at the MBPT(2) level Rittby [Rit94] investigated nine different isomers of Si_2C_3 both in their singlet and triplet states. We also found that most stable isomer is a linear $D_{\infty h}$ chain ($^1\Sigma_g^+$ state), and the energetic ordering is the same as reported by Ref. [Rit94], apart from minor deviations. The second most stable structure encountered here, a planar C_s ring with a C_3 submolecule (not included in the figures) that is 0.68 eV less stable than the chain, has not been considered previously. We found, however, that it is not stable under simulated annealing at temperatures up to 600 K, where it transforms into the chain, and it might be that it is not a true minimum. We also considered nine other isomers, which turned out to be more than 1 eV less stable than the chain, among them a C_1 structure, similar to that of the anion shown in Fig. 3.34(e) at 1.38 eV, and a distorted C_{2v} bipyramid [see Fig. 3.34(f) for the corresponding structure of the anion] 1.55 eV above the minimum.

Again, charging stabilizes the linear chain [Fig. 3.34(d)] slightly, with respect to the other isomers, but also the C_1 isomer [Fig. 3.34(e)] becomes more stable than another C_{2v} structure (not included in the figures), which contains an triangular C_3 submolecule in a more equilateral form, and ends 1.45 eV above the minimum. The bipyramid [Fig. 3.34(f)] distorts to C_s symmetry and reaches a local minimum 1.46 eV above the most stable isomer. Inspection of Table C.2 shows that the presence of the second and third lowest energy isomers is not compatible with the observed peak positions in the spectra. Nakajima *et al.* [NTN⁺95] found a peak at 1.71 ± 0.1 eV, while Ganteför *et al.* [GPS96] report peak positions at 1.77 ± 0.05 eV and 3.5 eV, see also Fig. 3.33. Only the vertical excitation energies of the chain (VDE: 1.82 eV, $^3\Sigma_u$ state: 3.66 eV) can explain consistently the peak positions in the spectrum. The assignment to the chain is further supported by the observation of a vibrational progression at the second peak with frequency 411 ± 50 cm^{-1} , which is close to a fundamental vibration (at 450 cm^{-1}) of this isomer (see Table 3.20).

 Si_3C_2^-

Neutral Si_3C_2 has recently been investigated by Froudakis *et al.* [FMZ95], who considered five different isomers. We have considered these and other structures and found, in accordance with Ref. [FMZ95], that the structure of lowest energy is a planar C_{2v} pentagon with a C_2 submolecule, 0.52 eV below the most stable three-dimensional structure, a distorted D_{3h} bipyramid. Other structures (three-dimensional, planar and linear), with higher in energies will not be discussed here.

Charging affects little the relative stability of the two most stable isomers shown in Figure 3.35(a,b), which also turn out to be the most stable in the anion. Furthermore, we

observed that several isomers that were stable in the neutral species transformed readily into the pentagon upon charging in MD runs between 300 and 600 K. The third most stable neutral isomer (not considered by Ref. [FMZ95]), a planar C_s pentagonal ring with transannular CC bond transforms upon charging into the structure in Figure 3.35(c), which is virtually degenerate with the bipyramid (only 0.04 eV less stable). The photoelectron spectrum recorded by Ref. [GPS96] shown in Fig. 3.33 reveals several unusual features: apart from a sequence of sharp peaks that are almost identical in shape and position to those in the spectrum of Si_2C_4^- , there are other features of much lower intensity added. Re-estimation of the data revealed that the mass spectrometer was not able to resolve the small mass difference ($3m_{\text{Si}} + 2m_{\text{C}} = 108$ a.m.u., $2m_{\text{Si}} + 4m_{\text{C}} = 104$ a.m.u.) between Si_3C_2 and Si_2C_4 , yielding two overlapping peaks in the mass spectrum. Since the PACIS generates the more stable Si_2C_4^- in much higher abundance, the second, smaller maximum in the common intensity distribution corresponds to a mixture of both anions, by far dominated by Si_2C_4^- . This allows us to identify features arising from Si_3C_2^- as those that are missing in the spectrum of "pure" Si_2C_4^- . This yields peak positions at 1.9 and ≥ 2.43 eV, in agreement with those obtained for the VDE (1.88 eV) and the energy for excitation into the neutral 3B_2 state (2.59 eV) of the pentagonal structure. Of course, the experimental information is not sufficient to exclude the remaining isomers, although their presence in the beam is unlikely, given the comparatively large energy differences from the minimum structure.

Si_4C^-

Si_4C has been studied by Nakajima *et al.* [NTN⁺95] with MP2/6-31G* calculations. The authors report a distorted trigonal (C_{3v}) bipyramid with the C atom in an apical position to be the most stable isomer. This agrees with our findings, but an almost isoenergetic distorted pentagonal (C_{2v}) ring was found only 0.1 eV above. Another distorted trigonal (C_{2v}) bipyramid similar to the corresponding anion shown in Figure 3.35(d) is another 0.19 eV less stable.

The energetic ordering and the stability of the structures changes appreciably in the anion, the trigonal (C_{2v}) bipyramid [Fig. 3.35(d)] now being the most stable. This was also the result of MP2/6-31G* calculations of Ref. [NTN⁺95]. The second lowest-lying planar C_{2v} structure depicted in 3.35(e) is 0.38 eV higher in energy. All the remaining isomers considered underwent major topological changes in the anion and transformed into the bipyramidal minimum. The only observed peak at 3.12 ± 10 eV in the photoelectron spectrum of Ref. [NTN⁺95] agrees well with the VDE of the minimum structure (3.21 eV), while the second isomers VDE (2.01 eV) does not fit the spectrum. The exceptional high VDE [it is the highest among all our five-membered clusters and is even higher than the experimental value for C_5^- (2.27 eV)] can be explained by the additional bond between atoms 3 and 4 in Figure 3.35(d) that is created upon charging of the cluster. The substitution of a Si atom for C introduces considerable strain in the underlying D_{3h} trigonal bipyramid of Si_5 , causing a bond between atoms (3,4) to open in neutral Si_4C (equilibrium distance 5.55 a.u.). Furthermore, the more compact C atom attracts electron density from

Molecule	Symmetry	State	ΔE
SiC ₅ ⁻ 3.35(f)	$C_{\infty v}$	$^2\Pi$	0.00
$d_{12}=2.44; d_{23}=2.50; d_{34}=2.42; d_{45}=2.49; d_{56}=3.25;$			
SiC ₅ ⁻ 3.36(a)	C_{2v}	2A_1	0.81
$d_{12,45}=2.56; d_{13,35}=3.55; d_{16,56}=3.42; d_{23,34}=2.55; \alpha_{165}=68^\circ; \alpha_{123}=88^\circ;$ $\alpha_{234}=157^\circ; \alpha_{216}=159^\circ;$			
Si ₂ C ₄ ⁻ 3.36(c)	$D_{\infty h}$	$^2\Pi_u$	0.00
$d_{12,34}=2.47; d_{16,45}=3.19; d_{23}=2.43;$			
Si ₃ C ₃ ⁻ 3.37(a)	C_1	2A	0.00
$d_{12}=2.45; d_{16}=3.24; d_{23}=2.49; d_{34,35}=3.55; d_{45}=4.24; \alpha_{435}=73^\circ;$			
Si ₄ C ₂ ⁻ 3.37(e)	C_1	2A	0.00
$d_{12}=2.97; d_{14,23}=3.46; d_{15}=3.89; d_{16}=3.53; d_{25}=3.90; d_{26}=3.52;$ $d_{34}=4.69; d_{35}=4.62; d_{45}=4.63; d_{56}=4.64;$			
Si ₅ C ⁻ 3.38(b)	C_s	$^2A'$	0.00
$d_{12}=3.42; d_{13}=3.83; d_{14}=3.59; d_{15}=3.83; d_{23}=4.78; d_{25}=4.79; d_{26}=4.65;$ $d_{34,45}=4.43; d_{35}=4.59; d_{36}=4.46; d_{56}=4.45;$			
Si ₅ C ⁻ 3.38(c)	C_{2v}	2B_2	0.00
$d_{12,13,14,15}=3.61; d_{16}=4.08; d_{23,45}=4.50; d_{25,34}=5.24; d_{26,36,46,56}=4.60;$			
Si ₂ C ₅ ⁻ 3.38(e)	$D_{\infty h}$	$^2\Pi_g$	0.00
$d_{12,45}=2.45; d_{17,56}=3.22; d_{23,34}=2.43;$			

Table 3.22: Structure parameters for isomers of Si_nC_m⁻, $n + m = 6, 7$, with energies ΔE relative to the ground state (eV). Bond lengths d_{ij} in a.u. and bond angles α_{ijk} in degrees. Additional labels refer to the figures, where also the atom numberings are defined.

the Si sites in the cluster, which can be seen in Figures 3.44 and 3.45, where we reproduce isosurface plots of the electronic density of the Si₄C⁻ isomer in Figure 3.35(d). The region of high density (>0.023 a.u.) enclosed by the surface shown in Figure 3.45 is localized around the C atom. After ionization, the attached electron will be repelled by the partial charge around the C atom and will be pushed into the Si₄ substructure, as we can see in Figure 3.46, where an isosurface of the magnetization density of the same cluster is shown. This quantity, which is proportional to the single-particle density of the additional electron, attains a large amplitude between the Si atoms (3,4) opposite to the C atom in the cluster, where it contributes to the formation of a bond (equilibrium distance 4.67 a.u.), which explains why this level is so tightly bound. Pure Si₅⁻ has also an exceptional high VDE, as has already been noted previously [CYP⁺87, RR91a]. Contrary to our observations at Si₄C⁻, Raghavachari and Rohlfing [RR91a] have found that the additional electron of Si₅⁻ goes into an orbital that is antibonding between the two apex atoms, causing them to move apart. They argue that the strain hereby introduced in the Si₅ structure is compensated by a contraction of the equatorial Si₃ substructure, which results in an increased bonding that stabilizes the uppermost electronic state.

SiC_5^-

Neutral and anionic SiC_5 have been studied by Nakajima *et al.* [NTN⁺95] at the MP2/6-31G* level of theory, who also calculated adiabatic electron affinities at the PMP4(SDTQ) level. As in the previous cases, we investigated several isomeric structures of the neutral species, among them a linear ($C_{\infty v}$) chain, a planar pentagonal (C_{2v}) ring and a planar (C_{2v}) structure of rhombus SiC_3+C_2 [see Fig. 3.36(b) for the (similar) structure of the corresponding anion]. The latter is a very flexible molecule: the transannular C_2 fragment in the ringlike SiC_3 submolecule undergoes hindered internal rotation with only a very shallow minimum at C_{2v} symmetry. The chain was found to be the absolute minimum, the other two isomers are 0.24 eV and 0.39 eV less stable, respectively. Several other isomeric states that have been considered have even higher energies and will not be discussed here.

The energetic ordering is not reversed in the anion, and the energy differences of the less stable isomers [Figs. 3.36(a) and 3.36(b)] to the linear chain [Fig. 3.35(f)] rather increase to 0.81 and 1.18 eV, respectively. The dominant features in the photoelectron spectrum of SiC_5^- agree reasonably with calculated values for the linear chain. The experimental VDE is 3.14 ± 0.03 eV, our theoretical value is 3.22 eV. The next higher predicted peak position [3.51 eV, corresponding to a transition into the $^1\Sigma^+$ state of the neutral species], is outside the sampling interval of Ref. [NTN⁺95] (0-3.49 eV BE). The topological changes between the anionic and neutral chain are minor (bond lengths changed by less than 2%), and this also visible in the better resolved spectrum of Ganteför *et al.* [GPS96], Fig. 3.33, where the 0-0 peak of the first progression has also maximal intensity, i.e., the nuclear vibrational ground states of the anion has greatest overlap with the vibrational ground state of the neutral species. Usually, the VDE is assigned to the maximum of the envelope of the peaks accompanying a transition, which is in this case restricted to lie between the peaks of the 0-0 and the $1 \leftarrow 0$ transition. Apart from this, its position is largely arbitrary, and the position of the highest peak seems to be a reasonable choice. This gives 3.28 ± 0.1 eV for this value, in good agreement with the calculated 3.22 eV. A second peak appears at 3.53 ± 0.1 eV BE in this spectrum, in good agreement with our value of 3.51 eV for the BE of the first excited state. No other features are visible in the sampling interval of the measurement, in accordance with our calculated excitation energies for this isomer (see Table C.2).

Nakajima *et al.* [NTN⁺95] see evidence for the presence of a second ringlike isomer in their spectrum and give reasons for their assignment of a feature of low intensity near 1.7 eV by comparison with the EA they calculated for the planar structure [Fig. 3.36(b)]. Starting with their structure, we basically confirmed their results, but found on the other hand that the VDE of this isomer (3.14 eV) is not compatible with the experimental VDE they give (1.65 ± 0.1 eV). Since the VDE corresponds in general to a peak of high intensity and they identify the EA with the threshold energy (onset), the VDE can be determined much more reliably, so that their assignment must be questioned. On the other hand, the anion structure [Fig. 3.36(b)] is much less stable than the linear chain (1.19 eV) and also less stable (0.38 eV) than the second lowest-energy structure, the C_{2v} pentagonal ring shown in Figure 3.36(a), even in the neutral species. However, the VDE of this isomer is

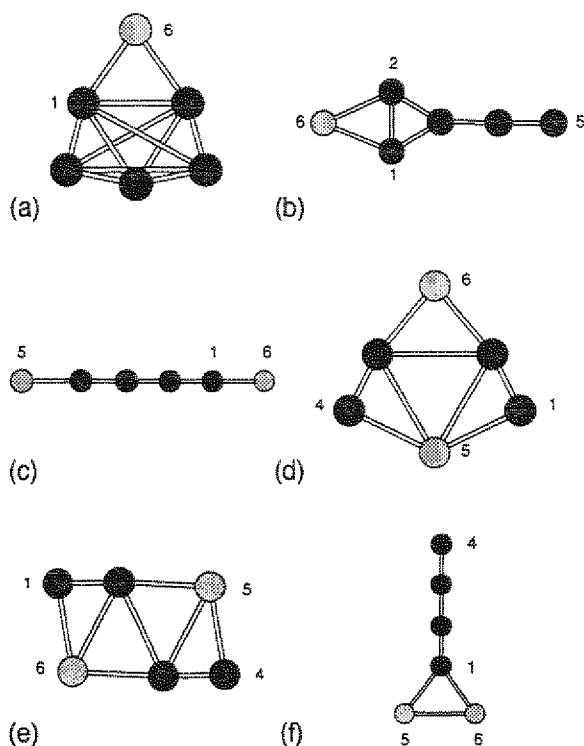


Figure 3.36: Structures of (a,b) SiC_5^- and (c-f) Si_2C_4^- . Light spheres are Si atoms, dark spheres are C atoms.

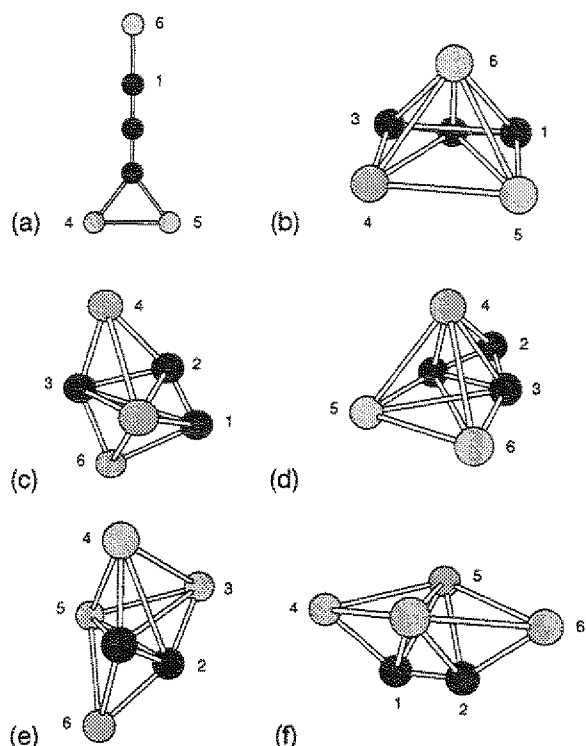


Figure 3.37: Structures of (a-d) Si_3C_3^- and (e,f) Si_4C_2^- . Light spheres are Si atoms, dark spheres are C atoms.

also too large (2.86 eV) to explain the feature near 1.7 eV so that the origin of this feature remains unclear. Moreover, the spectrum of Ref. [GPS96] shows almost zero intensity in the same energy range, but a small feature at 2.9 eV BE, which might stem from the pentagonal ring. The comparatively high VDE of the linear isomer compared to its ring analogue is in line with our expectations for the even-odd alternation of VDEs in linear and ringlike C_n clusters, since even-membered rings should have low VDEs, unlike odd-membered chains.

Si_2C_4^-

Five different structures of Si_2C_4 have recently been investigated by Froudakis *et al.* [FZM⁺94] at the SCF, MP2 and CASTP2 levels. We reconsidered their structures as well as several others. In accordance with Ref. [FZM⁺94], we found the linear $D_{\infty h}$ nuclear arrangement with Si atoms in terminal positions and a ${}^3\Sigma_u^-$ state the most stable isomer, followed by a hexagonal C_s ring (“chair structure”) [similar to the anion 3.36(d)] 0.79 eV higher in energy. Our next structure in the energetic ordering, a version of this ring distorted to planar C_{2h} symmetry [similar to the anion 3.36(e)] has not been considered before and was found to lie only 0.08 eV above the C_s ring. Considerably higher in energy than the last isomer (0.64 eV), we found a planar C_{2v} structure with two Si atoms attached to the

same end of a C_4 chain submolecule [see Fig. 3.36(f) for the structure of the corresponding anion]. Other structures also considered by Ref. [FZM⁺94] were found at 1.08, 2.69 and 1.93 eV above the linear isomer (in the energetic ordering given by Ref. [FZM⁺94]).

In the anion, the chain [Fig. 3.36(c)] is again stabilized with respect to the other structures and is now 0.48 eV more stable than the chair [Fig. 3.36(d)], 0.62 eV more stable than the ring [Fig. 3.36(e)] and 0.71 eV more stable than the structure in Fig. 3.36(f). All other isomers of the anion are even higher in energy. For the VDE, Nakajima *et al.* [NTN⁺95] have determined the value 2.49 ± 0.08 eV and Ref. [GPS96] 2.57 ± 0.05 eV, which agrees particularly well with the value for linear chain, i.e., 2.59 eV. Another transition might occur at 2.79 ± 0.05 eV, but this assignment is not definite, since this peak almost coincides with the peaks of the first vibrational progression. The energy, however, agrees well with our theoretical energy of the transition into the $^1\Sigma_u^+$ state, 2.85 eV. There are no definite signs of other electronic excitations in the remainder of the spectrum. Inspection of Table C.2 in appendix C shows that none of the other isomers matches the pattern of the peak positions. The fact that the VDE (3.15 eV) of isomer [Fig. 3.36(f)] is higher than the corresponding value of isomer [Fig. 3.36(c)] may be explained by the tendency of the surplus electron to have high amplitude at the ends of the chain, which is energetical more favourable, if C atoms are present there (see the discussion in section 3.5.2).

$Si_3C_3^-$

In extensive theoretical calculations, Mühlhäuser and coworkers investigated as many as 17 different isomers of this molecule [MFZP93, MFZ⁺94] by reoptimizing the most stable HF geometries at the MP2(TZP) and MP2(TZ2P) levels. We re-examined 8 of their most stable structures as well as other geometries. While the lowest-energy isomer was found, in accordance with Ref. [MFZ⁺94], to be a distorted C_s pentagonal pyramid, with a strongly bent (apical angle 44°) C_3 submolecule, the energetic ordering we obtained sometimes differed from that reported before. We found also several low-energy isomers not considered previously, among them as our second most stable a distorted C_s hexagonal ring with a weakly (135°) bent C_3 submolecule (not included in the figures) 0.51 eV above the minimum structure, and a planar C_{2v} isomer with a linear C_3 submolecule, similar to the anion structure in Fig. 3.37(a), 0.85 eV above the minimum.

Charging seems to favor structures energetically that contain an almost linear C_3 submolecule, such as the planar C_{2v} isomer [Fig. 3.37(a)] which is the most stable in the anion. 0.31 eV higher in energy, we found a C_s structure shown in Fig. 3.37(b), which was no low-energy structure (1.43 eV above the minimum) in the neutral species. As already mentioned, strongly bent C_3 submolecules seem to be energetically unfavorable in the anion, and indeed, the C_s ground state of the neutral species distorts to C_1 symmetry yielding the structure shown in Fig. 3.37(c) with a less bent C_3 subunit 0.08 eV higher in energy. The next isomer in the energetic ordering, another 0.33 eV less stable, is a distorted C_s prism depicted in Fig. 3.37(d). This structure was derived from the fourth isomer in energetical ordering (0.71 eV less stable than the absolute minimum) of the neutral species. Several other isomers had energies more than 0.8 eV above the minimum.

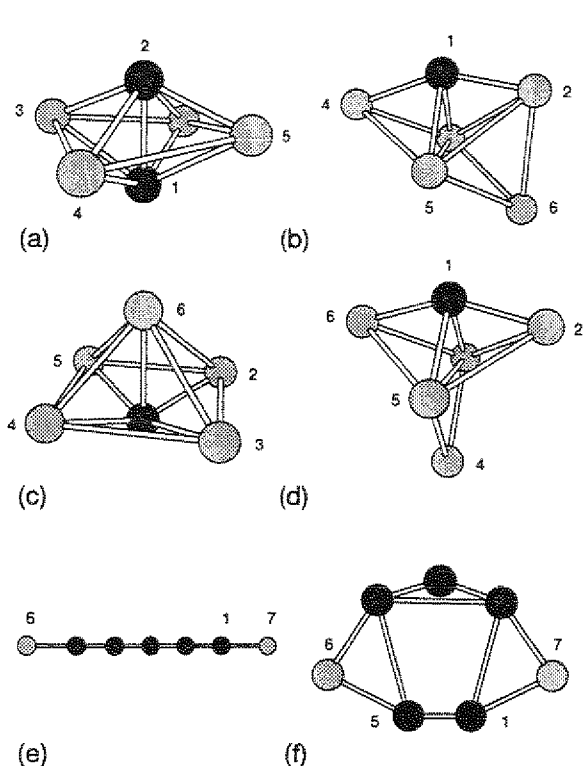


Figure 3.38: Structures of (a) Si_4C_2^- , (b-d) Si_5C^- , and (e-f) Si_2C_5^- . Light spheres are Si atoms, dark spheres are C atoms.

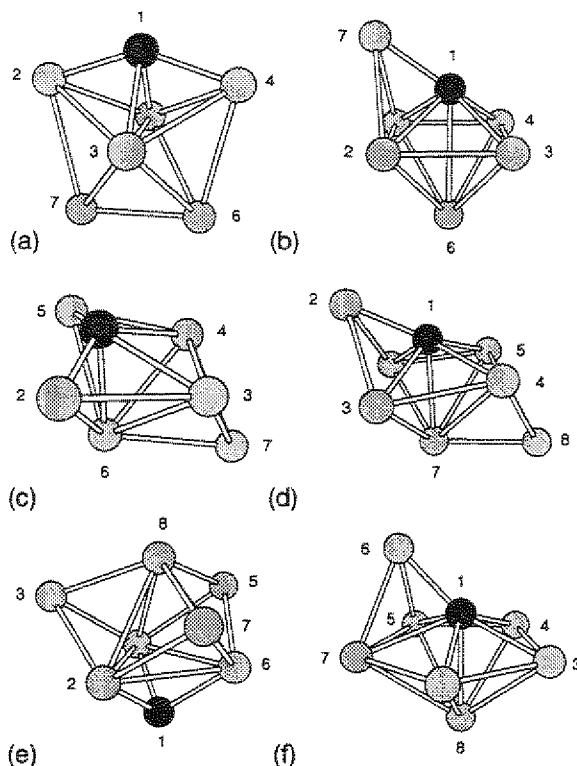


Figure 3.39: Structures of (a-c) Si_6C^- and (d-e) Si_7C^- . Light spheres are Si atoms, dark spheres are C atoms.

The experimental VDEs for this molecule are 2.16 ± 0.08 eV [NTN⁺95] and 2.42 ± 0.05 eV. Our value for the most stable isomer (2.51 eV) agrees well with the latter result, and also the higher excitation energies at 2.93 eV (3A_1), 3.07 (1A_1) and 3.73 (3A_1)³ match the pattern of the peak positions in the spectrum (at 2.88 eV, 3.25 eV, and 3.75 eV). The remaining isomers are less compatible with the features in the spectrum, as can be seen from their VDEs (see Table C.2).

Si_4C_2^-

Four different structures of Si_4C_2 have been investigated by Froudakis *et al.* [FZM⁺94] and only one of them has been found to be a true minimum. It is a C_{2v} isomer close to the anion structure shown in Figure 3.37(f). Another distorted D_2 octahedron [see Fig. 3.38(a) for the corresponding anion] is virtually degenerate ($\Delta E=0.06$ eV) with the first isomer. There were several less stable structures, among them a C_1 structure close to the anion shown in Figure 3.37(e) 0.6 eV above the minimum.

The energetical ordering of the corresponding anions is again different from that of the neutral species, and the most stable anion is now structure [Fig. 3.37(e)], which is 0.20 eV

³The last two values belong to states that are not the most stable of a given symmetry and are therefore not covered by theory.

more stable than isomer 3.37(f) and 0.46 eV more stable than structure 3.38(a). The only isomer that can account for the features in the spectra, is the minimum structure 3.37(e). Nakajima *et al.* [NTN⁺95] report a VDE of 2.10 ± 0.08 and our value for structure 3.37(e) is 2.18 eV, while all other low-energy isomers (less than 0.5 eV above the minimum) considered in this work have VDEs below 1.2 eV. The appearance of a second peak at ≥ 3.30 eV is in reasonable agreement with our first excitation energy [3.48 eV (3A state)] for this isomer. An interesting phenomenon encountered here is the remarkable difference between the VDEs of the individual isomers. While isomer 3.37(f) and 3.38(a) have roughly the same value, that of 3.37(e) is more than twice as large. This can be related to structural differences of the isomers. The C atoms of structure 3.37(e) are rather embedded into the Si substructure, resulting in a high coordination of the C atoms in this isomer. This inhibits the formation of a double bond between them. The bond is strained considerably in the neutral species, resulting in an interatomic distance of 3.12 a.u.. In isomer 3.37(f) of the anion, on the other hand, which looks more like a C_2 dimer loosely bound to a planar Si_4 cluster, they are linked by a double bond (bond distance: 2.49 a.u.). The closer CC distance in 3.37(f) lowers the potential between them, which induces a higher partial charge at the C atoms than in 3.37(e). An attached electron will consequently be pushed away farther into the Si substructure, resulting in a higher amplitude of the excess electron in regions of high potential energy (i.e., beyond atoms 4 and 6, here) than in 3.37(e). In 3.37(e) however, the partial charge at the C atoms is weaker than in (f), so that an attached electron is even able to enter the (low-potential) region between them and to strengthen the CC bond (resulting in the typical single bond distance of 2.97 a.u.), which stabilizes the corresponding electronic level and increases the VDE. The neutral D_2 octahedron [Fig. 3.38(a)] underlying the anion in Figure 3.38(a) exhibits already maximal coordination and no strained bonds so that an attached electron cannot compensate for its repulsion from the partial charges on the C atoms into the Si_4 ring by participating in the stabilization of a bond. On the contrary, it is even forced to occupy antibonding orbitals near the Si atoms, causing the bonds between atoms (3,4) and (5,6) to open in the anion (to ~ 4.95 a.u.).

Si_5C^-

Nakajima *et al.* [NTN⁺95] not only determined the VDE from their photoelectron spectrum to be 1.74 ± 0.08 eV, but also performed MP2/6-31G* calculations in order to determine the most stable isomer of the anion. They found a C_{2v} structure with 2A_1 electronic state which is similar to our structure shown in Fig. 3.38(d). This isomer is, however, only the third lowest-energy structure encountered in our calculations, and we found two virtually degenerate isomers, a distorted octahedron [Fig. 3.38(c)] and a slightly more stable ($\Delta E = 0.01$ eV) C_s variant [Fig. 3.38(b)] of the structure in Fig. 3.38(d) to be about 0.28 eV more stable than the C_{2v} structure. The C_s isomer [Fig. 3.38(b)] could also be conceived as consisting of a SiC dimer [consisting of atoms labeled 1 and 2 in Fig. 3.38(b)] attached to a slightly bent Si_4 cluster. The bond lengths in the Si_4 subunit between 4.43 and 4.45 a.u. support this view, indicating a rather strong bond order between one and

two. The closely related isomer [Fig. 3.38(d)] is, on the other hand, less tightly bound and has double bonds only between atoms (3,4) and (4,5).

From the calculated VDEs of these isomers (1.81 eV, 1.54 eV, 2.07 eV), only the first of the most stable isomer fits the experimental value. In particular the last value of the minimum structure proposed by Ref. [NTN⁺95] is not compatible with their own experimental result. There are no further peaks of sizeable intensity in their spectrum, apart from a steep increase in intensity at the upper border of their sampling interval (3.49 eV), indicating the presence of a second peak around ≥ 3.4 eV, which would again agree with the first excitation energy of our minimum structure [3.38 eV, (³A') state]. To conclude, no definite indication for the presence of any of the remaining isomers can be seen in the spectrum, although our calculations indicate that the two lowest-energy isomers are almost degenerate. Unfortunately, the resolution in the experiment is not high enough to decide about the presence of smaller peaks at the corresponding energies (isomer 3.38(c) should lead to peaks around 1.54, 3.39 and 3.61 eV in the energy range of interest, according to our calculations). The different VDEs of isomers 3.38(b) and 3.38(d) can be understood as a consequence of the different bond strengths of these clusters already observed above. The *C_s* structure has two additional single bonds between atoms (2,6) and (3,5) compared to the *C_{2v}* structure and in total twice as much double bonds than this isomer. This both stabilizes the former isomer with respect to the latter, and is an energetical less favourable situation for the attached electron, which, repelled from the partial charge around the C atom into the Si substructure, has now fewer empty orbitals with bonding character at its disposal. This leads to a somewhat higher VDE for isomer [Fig. 3.38(d)].

Si₂C₅⁻

The results of Ref. [NTN⁺95] and of Ref. [GPS96, see Fig. 3.33] indicate a VDE of 2.16 ± 0.06 eV and 2.22 ± 0.05 eV, respectively. No other peaks are discernible in the spectrum of Ref. [NTN⁺95], and the next definite peak in the spectrum of Ref. [GPS96] appears at 3.56 eV BE.

Our calculations indicate the existence of two low-energy isomers of the anion, a *D_{∞h}* chain [Fig. 3.38(e)] and a *C_s* pentagonal ring [Fig. 3.38(f)] that is 0.72 eV less stable. About the same energy differences and ordering were also found for the neutral species. As might be expected from the distinct energy difference, only the most stable isomer can account for the spectral features, with VDE at 2.18 eV and an excitation energy of 3.73 eV for a transition into the ³Σ_u state of the neutral chain, in contrast to the ring, which has excitation energies well above 3.0 eV. The comparatively high VDE of this isomer compared to its linear analogue is in line with our considerations on the even-odd alternation of VDEs in linear and ringlike C_n clusters, since odd-membered rings should have high VDEs, unlike odd-membered chains.

Si_6C^-

The spectrum of Ref. [NTN⁺95] shows a distinct peak at 1.74 ± 0.08 eV, their value for the VDE. Another, much broader feature with unresolved vibrational fine structure attains its maximum around 2.7-3.1 eV. We found a C_{2v} structure [Fig. 3.39(a)] to be the most stable both for the anion and for the neutral species. It can be derived from the minimum structure of Si_5C^- [Fig. 3.38(b)] either by capping the face between atoms (3,5,6) with an additional Si atom, or, likewise, by replacing a Si atom of the optimal structure of Si_7 (which we found, in accordance with Raghavachari and Rohlfiing [RR88], to be a pentagonal D_{5h} bipyramid) by a C atom. The large interatomic separation between the Si atoms (2,7) and (4,6) of 5.11 a.u. is much larger than standard values for elemental Si clusters (4.3-4.8 eV [LPKJ⁺93]), and the molecule is in fact rather floppy in our simulations, undergoing low-energy bending vibrations at $T=300$ K. A C_s structure [Fig. 3.39(b)] lies 0.30 eV higher in energy, followed by another C_s isomer [Fig. 3.39(c)] at 0.36 eV. The latter isomer can as well be derived from the optimal structure of Si_5C^- by capping a face containing a C atom. Other structures considered were both less stable and/or not true minima on the BO energy surface. However, at most the C_s isomer shown in [Fig. 3.39(b)] would be compatible with the spectral features. The calculated VDE is 1.79 eV, and further calculated excitation energies are 3.17 eV ($^3A''$) and 3.36 eV ($^1A''$), but this assignment is admittedly not very conclusive, regarding the energy difference to our most stable isomer and the broad vibrational progression observed around the second feature that suggests a major geometrical change between anion and the neutral species, which has not been observed for this isomer.

Motivated by the observation of Nakajima *et al.* [NTN⁺95] of a similarity between this spectrum and the photoelectron spectrum of pure Si_7 , we experimented with replacing Si atoms with C atoms in the lowest-energy isomers of Si_7 . Replacing a Si atom in axial position in the D_{5h} pentagonal bipyramid GS of Si_7 leads to a low-energy structure (0.07 eV less stable than the "most stable" minimum), which is, however, not stable against MD runs at about 300 K and is probably not a true minimum (not included in the figures). Replacing Si atoms in several positions in the second most stable Si_7 structure, a C_{3v} tricapped tetrahedron 0.79 eV less stable than the D_{5h} GS (see Ref. [RR88]), lead upon annealing to less stable local minimum geometries or to any of the structures already known. So, despite all our efforts, it is possible that we have not found the true minimum, although we have little doubt that the structure in Figure 3.39(a) is the most stable. On the other hand, the energy difference between the lowest-energy isomer and the isomer in Fig 3.39(c) (0.36 eV) should not be overstressed, as recent publications on C_{20} [RSO⁺93] and C_{24} [RZP⁺94] have shown that the inclusion of gradient corrections to the potentials (see sec. 2.1.2) can have dramatic effects on the energy ordering of the isomers, changing relative energy differences by up to 8 eV. Another possible explanation for our failure to explain the spectrum of Ref. [NTN⁺95] conclusively might be that Si_6C^- clusters cannot be distinguished from Si_3C_8^- by the mass spectrometer, since both clusters have the same mass. Since Ref. [NTN⁺95] vaporize a silicon-carbon rod using a laser, they cannot control the Si:C ratio in the vaporized material, and it is possible that Si_3C_8^- is produced in signif-

icant amounts, which would lead to a superposition of the corresponding spectra. In fact, the observation of a broad vibrational progression with obviously large vibrational quanta is more consistent with a C_8 submolecule with strong CC bonds than with a structure containing relatively weak SiSi or SiC bonds. However, this should not be overstressed, since the same argument also applies to other $Si_nC_m^-$ cluster pairs in clusters already discussed here: Si_4C^- and SiC_8^- , $Si_4C_2^-$ and SiC_9^- , Si_5C^- and $Si_2C_8^-$, and Si_7C^- has the same mass as both $Si_4C_8^-$ and SiC_{15}^- . This raises the question of why no signs for the presence of other isomers were found in the spectra of Si_4C^- , $Si_4C_2^-$ and Si_5C^- . A possible reason is that intensities of the clusters in the beam generally decrease with increasing number of atoms, so that larger clusters might be less significant in the spectrum. Alternatively, the other clusters in these cases (SiC_8^- , SiC_9^- and $Si_2C_8^-$) are all carbon-rich and can be expected to have properties more similar to those of pure carbon clusters. The experimental VDEs of C_8^- and C_9^- are 4.42 and 3.70 eV [YTC⁺88], respectively. This is beyond the scope of the instrument (0 - 3.49 eV), and it may also apply to the corresponding silicon-containing clusters. The properties of Si_3C_8 in the present case might already be affected by the higher percentage of Si in its structure. As we discuss in section 3.5.2, its VDE might be lowered, resulting in an observable signal in the spectrum.

The marked difference of the VDEs of isomers [Fig. 3.39(a)] and [Fig. 3.39(c)] stems from the fact that in (a) the surplus electron contributes to strengthening of the bond between atoms (6,7). If cluster [Fig. 3.39(a)] is derived from the underlying pentagonal bipyramid of Si_7 by replacing a Si atom by C, considerable strain is introduced into the Si substructure *opposite* to the C site, causing the bond between atoms (6,7) to open (to a bond length in the neutral isomer of 4.71 a.u.). An attached electron will move away from the partial negative charge accumulated around the C site and consequently attain a large amplitude opposite the apical C atom as well. Its contribution to local bonding results in a double bond in the anion (bond length 4.44 a.u) between atoms (6,7) and a considerable stabilization of the state the excess electron occupies. On the other hand, the replacement of a Si by a C atom in the Si_7 cluster yielding [Fig. 3.39(c)] introduces strain *near* the C atom in the structure, not opposite to it. An attached electron, however, cannot bind strongly to this site, since it will be repelled by the partial charge centered around the C site and will be shifted to the opposite end of the Si substructure. But in this case, the structure of the Si_7 cluster has remained almost intact here, with high coordination numbers of the Si atoms, and a high occupancy of the bonding orbitals and the excess charge is forced into regions of high potential energy.

Si_7C^-

The spectrum of Si_7C^- of Ref. [NTN⁺95] resembles closely that of pure Si_8^- of the same authors, apart from a weaker resolution. This suggests that SiC_7^- might be related to Si_8^- just by replacing one Si atom by C. Two relevant low-energy structures for Si_8 have been reported by Raghavachari and Rohlfing [RR88]: a bicapped C_{2h} octahedron and a tetracapped C_{2v} tetrahedron. In agreement with Ref. [RR88], we have found that the former isomer is 0.41 eV more stable than the latter. Replacing one Si atom by C atoms in

different positions we generated six different structures for the anion that we investigated by simulated annealing, as well as five structures not related to these isomers of Si_8 . The lowest (C_s) isomer [Fig. 3.39(d)] is in fact derived from the most stable structure of Si_8 . It can also be derived by face-capping either of the low-energy isomers in Figure 3.39(b) and Figure 3.39(c) of Si_6C^- . This isomer is almost degenerate (only 0.10 eV more stable) with the C_{3v} structure depicted in Fig. 3.39(e) and 0.44 eV more stable than the C_s isomer in Fig. 3.39(f).

However, the first and the last structure cannot account for the features contained in the spectrum, since their VDEs (2.05 eV and 2.45 eV, respectively) are much lower than experimental VDE which Nakajima *et al.* [NTN⁺95] report to be 2.92 ± 0.08 eV. This favors the C_{3v} isomer, whose VDE is 3.32 eV. Lowest excitation energies of this structure at 3.47 and 3.55⁴ eV BE are, however, outside the range of the instrument and it is not possible to make the assignment more definite. In line with the discussion in the preceding section, we should note that the spectrum might be affected by the presence of isomers of Si_4C_8^- and SiC_{15}^- , which have the same mass as Si_7C^- and cannot be distinguished by the mass spectrometer.

3.5.2 Trends and Discussion

While it is generally known (see, e.g., Ref. [CW88]) that C prefers double bonds and Si favors single bonds, only few attempts have been made to relate this observation to atomic properties. Within LSD, Harris and Jones [HJ79] explained experimentally known trends in the bond strengths of group 14 dimers by the radial extent of the atomic orbitals of the bonding partners. In this picture, the relative strength of the CC bond compared with the SiSi bond (e.g., C_2 and Si_2 have binding energies of 6.2 and 3.2 eV [HH79]), is related to the fact that carbon atoms are more compact than Si atoms. The preference for double bonds of carbon can be understood from the relative compactness of the atomic s and p orbitals. In Si, the p orbital has its antinode considerably displaced outward from that of the s orbital and falls off considerably more slowly. In C, the two orbitals peak at practically the same distance from the nucleus and fall off on almost the same length scale. This induces comparatively short bond distances, increases the contribution of p orbitals to bonding and favors double bonds over single bonds. Compact $2p$ orbitals can be found in all first-row atoms, because there are no underlying p -states in the core to which valence p states must be orthogonal. For elements higher in the periodic table, in particular Si, there is a p -core, and this is considerably more extended than the s -core. Accordingly, the valence p orbitals are displaced outwards with respect to their s counterparts. This weakens the contribution of p orbitals to bonding and consequently favors single bonds over double bonds, resulting in reduced bond strengths compared to C. For example, while it is known that CC and SiC σ bonds have nearly identical strengths (~ 3.8 and ~ 3.7 eV [GS84]), SiC π bonds have only about 60 % of the analogous CC bond strength [Wal93, STG87]. We can conclude

⁴The corresponding 1A_1 state is again not the lowest of a given symmetry and is therefore not covered by theory.

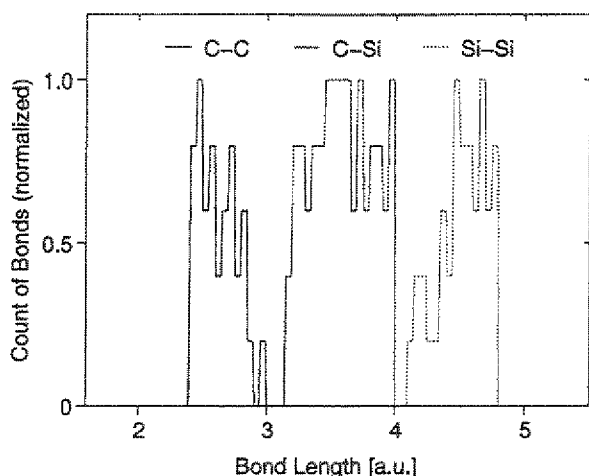


Figure 3.40: Bond length distribution (CC, C-Si and Si-Si bonds) of low-energy Si_nC_m^- -clusters ($n + m = 2-8$, with energies less than 1.6 eV above the most stable isomer). The number of bonds is sampled over intervals of 0.05 a.u..

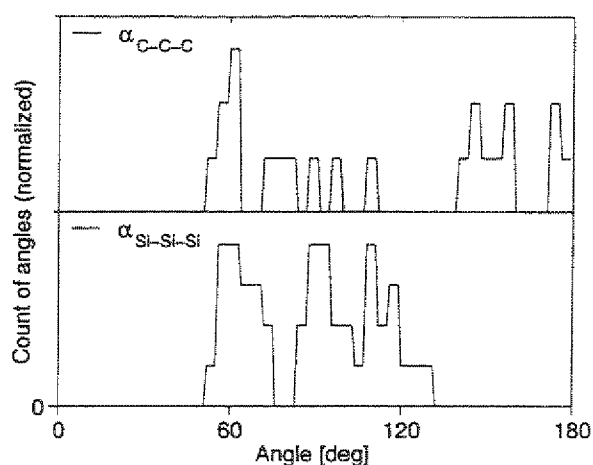


Figure 3.41: Bond angle distribution (CCC and SiSiSi angles) of low-energy Si_nC_m^- -clusters ($n + m = 3-8$, with energies less than 1.6 eV above the most stable isomer). The number of angles is sampled over intervals of 4° .

that it should be energetical favorable for mixed silicon-carbon clusters that the carbon atoms should form connected submolecules within the cluster, as may indeed be verified by consulting the Figures 3.30-3.39. These qualitative arguments may be illustrated in Figure 3.40, where we compare the bond length distribution of CC, C-Si and Si-Si bonds, sampled over the 65 most stable (with energy difference less than 1.6 eV to the most stable isomer) mixed silicon carbon clusters included in our calculations. For CC bonds, the curve shows a distinct preference for smaller bond lengths close to ~ 2.4 a.u. and decreases towards ~ 2.9 a.u., which are standard values for CC double and single bonds [MFZ⁺94], respectively. The curve for Si-Si bonds, on the other hand, shows the opposite trend, favoring long bonds (~ 4.5 a.u.) over short ones (~ 4.3 a.u.), which are close to the typical values for Si-Si single and double bonds [LPKJ⁺93], respectively, but we encountered also substantially strained Si-Si bonds (~ 4.9 a.u.), which are not shown in the Figure 3.40. The distribution of Si-C bond lengths is more balanced between the typical length of a double bond, ~ 3.2 a.u. [MFG90], and the standard value for a single bond ~ 3.6 a.u. [TB86]. These values are close to the nearest-neighbor distances in the bulk (2.62 a.u. for C, 3.98 a.u. for Si, both in the diamant crystal phase).

Increased bond length and strength are not the only consequences of the small spatial extent of the atomic p orbitals of C. Probably of equal importance for structural properties is (if we think in LCAO terms) the remarkable ease of sp hybridization in carbon [GJ85], due to the comparative closeness of the atomic $2s$ and $2p$ levels. While small C_n clusters have low-lying linear and ring isomers, in which the C atoms are sp hybridized, no such isomers are known for Si clusters, nor have we found Si-Si-Si bond angles close to 180° in our simulations. This can also be seen in Figure 3.41, where we plot the distribution of CCC (upper curve) and Si-Si-Si (lower curve) bond angles of our 65 most stable isomers

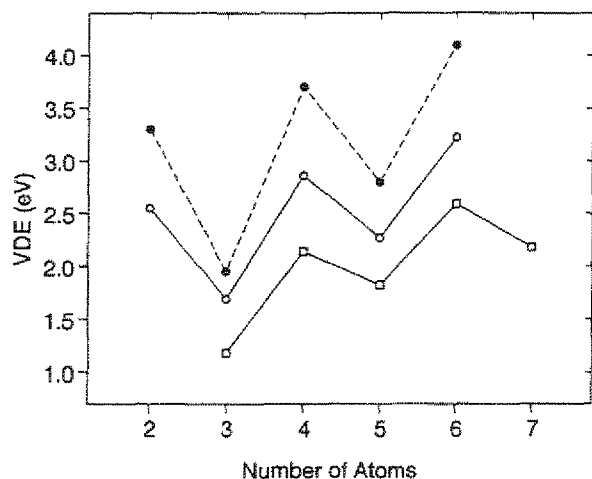


Figure 3.42: VDEs of linear Si_nC_m^- -clusters, \bullet : $n=0$ [YTC⁺88], \circ : $n=1$, \square : $n=2$.

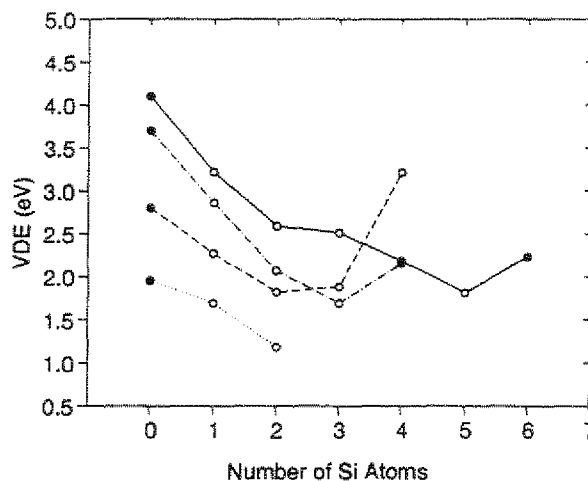


Figure 3.43: VDEs of Si_nC_m^- -clusters, $n+m$ = full line: 6, dashed: 5, dash-dotted: 4, dotted: 3. Experimental values (\bullet) are from [YTC⁺88, C_n^-], and [NTN⁺95, Si_n^-].

of Si_nC_m^- , although the statistics are less definite than in our previous example (before, we accepted every bond, but now we accept only the occurrence of 2 C (Si) bonds in succession).

While the former considerations focus exclusively on the properties of the single atoms to discuss the differences between CC, CSI and SiSi bonds, it is worth examining the corresponding dimers more closely to understand the topology of silicon-carbon compounds better. In C_2 , the GS⁵ ($^1\Sigma_g^+$) is $\pi_u^2\pi_u^2$ bonded whereas in SiC, we found a $\pi^3\sigma$ bonded ($^3\Pi$) GS, and we have a $\sigma_g^2\pi_u^2$ bond in Si_2 ($^3\Sigma_g^-$ state). This is in line with our previous discussion: in C_2 , the $\sigma_g 2p$ is closer in energy to the $\sigma_u 2s$ than in Si, a property that is inherited from the underlying atomic $2s$ and $2p$ levels. Consequently, the energy splitting upon hybridization between these molecular orbitals is more pronounced in C_2 than in Si_2 , shifting the $\sigma_u 2s$ eigenvalue to lower and the $\sigma_g 2p$ eigenvalue to higher energies. As a result, the $\sigma_g 2p$ level lies above the $\pi_u 2p$ level in C_2 , while the opposite holds true for Si_2 . SiC takes an intermediate position between these cases. Consider now an atom or radical approaching the C_2 molecule. As the $\pi_u 2p$ orbitals are both completely filled and the $\sigma_g 2p$ level is empty, it is the most probable position for a successful bonding and the molecule will preferentially grow along the molecular axis. This also explains the extraordinary stability of catenated compounds involving chains or rings of carbon atoms, which distinguishes carbon from other elements. The opposite holds true for an attempted bonding to the Si_2 molecule, where an attack of the $\sigma_g 2p$ level, which is completely filled, would hardly be successful, and it is much more likely that bonding to the empty $\pi_u 2p$ orbital of the molecules will take place, suggesting an off-line growth. Indeed, the final, stable geometry of, e.g., Si_4 is a (D_{2h}) rhombus and not a chain. The resulting bonds can be expected

⁵LSDA gives the wrong order here, reporting the $^3\Pi_u$ state to be ~ 0.5 eV more stable than the $^1\Sigma_g^+$, while the experimental results indicate that it is 0.08 eV less stable than the latter.

to be less directional, as the Si $\pi_u 2p$ orbitals are rather extended. This explains also the observed tendency of silicon-rich clusters for three-dimensional structures.

In contrast to the situation encountered in S_n^- and P_n^- clusters, $Si_n C_m^-$ clusters have several features that complicate the discussion of their VDEs. First of all, there are more highly symmetric compounds ($C_{\infty v}$, $D_{\infty h}$, etc.), where there are not enough valence electrons to fill the bonding orbitals completely. An example we encountered are linear C_n chains, where the even-numbered chains have a $^3\Sigma_g^-$ GS [PC59] with two unpaired π electrons. An electron attached to an even-numbered chain will therefore enter a HOMO and is much stronger bound (i.e., has much higher VDE) than in odd-numbered chains [$^1\Sigma_g^+$ (π^4) GS], where it must enter the LUMO (see the uppermost curve in Figure 3.42, where we reproduce experimental VDEs of [YTC+88]). In the remaining curves, we plot the VDEs of linear chain isomers of $Si_n C_m^-$ with (from top to bottom) one and two C atoms replaced by Si atoms. Obviously, the even-odd alternation prevails even if Si is mixed in, although somewhat weakened in amplitude. Furthermore, since the partially empty π levels are bonding, electron attachment to even-numbered chains will in general increase the bond strength and reduce the bond distance in these chains, as we already observed in the preceding section. Another trend can be expected from our previous discussion: attached electrons should bind more strongly to carbon sites, since in carbon submolecules the occupied orbitals are more compact and closer to the nuclei than their silicon counterparts, which can also be concluded from Figures 3.42. Identifying the VDEs with the binding energies of the attached electrons, we can see that the binding is strongest in pure C_n chains, and decreases monotonically as more and more C atoms are replaced by Si. This is not the whole story, as we can see from Figure 3.43, where we plot the calculated VDEs of some of our most stable isomers (together with some experimental results [YTC+88, NTN+95]). The curves interpolate values for $n+m=3,4,5,6$. The entries in the first three columns are mostly linear isomers, whose even-odd alternation accounts for the fact that the onset of $n+m=5$ curve is shifted to smaller values with respect to the $n+m=4$ curve. Apart from such shell-closure effects, which are most important in the carbon-rich linear chains and monocyclic rings, the VDEs should be higher in the larger clusters for simple electrostatic reasons, a feature shown by the curves. The expected trend that the excess electron is more tightly bound to carbon-rich than to silicon-rich clusters is also clearly visible, although there is considerable additional structure. This results from the second complication we encounter in going from elementary clusters such as S_n^- or P_n^- to mixed clusters such as $Si_n C_m^-$ clusters. C and Si sites in the structures are no longer equivalent, as shown by the smaller spatial extension of C compared to that of Si. This will induce considerable strain in Si_n structures, if Si atoms are replaced by C atoms. Another feature we already discussed in the example of $Si_2 C^-$, is that the smaller spatial extent of the C atomic orbitals will result in a polar character of SiC bonds, which tends to deplete Si_n submolecules in the clusters from electrons to the advantage of C_m fragments. As in the example of the high-density region of the $Si_4 C^-$ isomer in Figure 3.45, which is localized at the C atom, inspection of our charge densities shows that this leads in all cases to a partial negative charge at the carbon atoms, which tends to push attached electrons away from carbon sites into the silicon subunit. This can also be seen at the

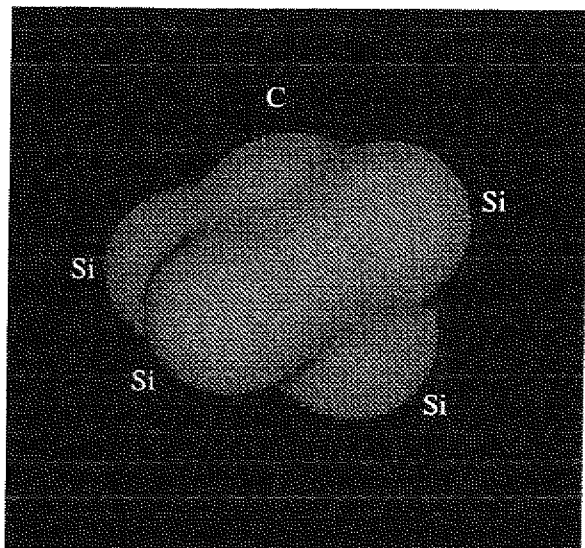


Figure 3.44: Isosurface plot of the electron density of the isomer shown in Fig. 3.35(d) of Si_4C^- . The density on the surface is 0.008 a.u..

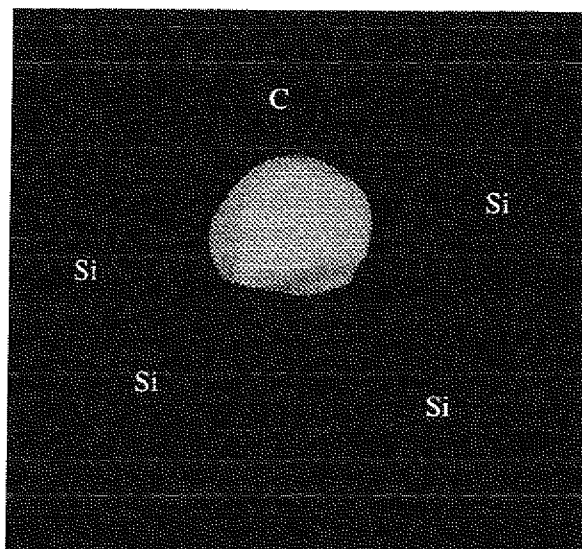


Figure 3.45: Isosurface plot of the electron density of the isomer shown in Fig. 3.35(d) of Si_4C^- . The density on the surface is 0.0023 a.u..

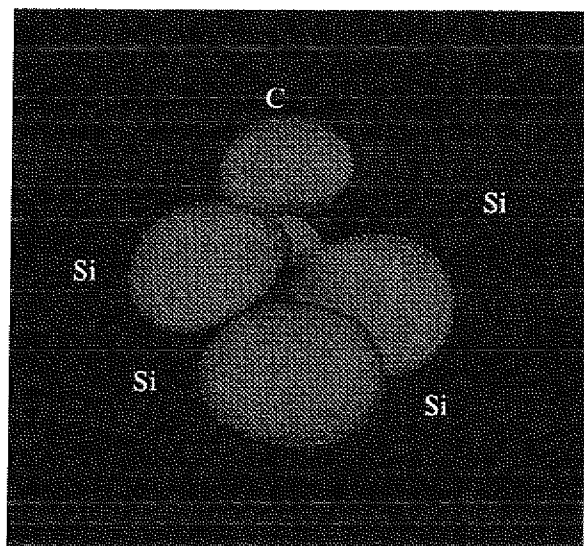


Figure 3.46: Isosurface plot of the magnetization density of the isomer shown in Fig. 3.35(d) of Si_4C^- . The magnetization density on the surface is 0.00006 a.u..

example of the magnetization density of the Si_4C^- isomer in Figure 3.46, where the most prominent accumulation of density is situated between the Si atoms opposite to the C site. If all bonds in the Si submolecule are saturated, the excess electron becomes localized in regions of high potential energy, which would result in a low VDE, but it may also stabilize SiSi bonds, that might have been strained by the presence of C atoms in the cluster, and a higher VDE will result. The density in Figure 3.46 is an example for the latter case,

since the accumulation of electronic density between the two Si atoms at the bottom of the picture stabilizes a bond strained in the neutral isomer (the contraction of the bond length upon charging is $\sim 16\%$). As we have already seen in the preceding section, the interplay of these two factors can account for the irregular behavior of VDEs of silicon-rich clusters, including the exceptionally high VDE of Si_4C^- in Figure 3.43 (see last section for a discussion) and the tendency of the (experimental [NTN⁺95]) VDEs of Si_n^- clusters to be larger than those of the Si_nC^- clusters of the same size (since the absence of C atoms in a silicon-rich cluster is in general energetically more favourable for an attached electron), which is also observable in Figure 3.43. To conclude, we can discern two regimes of Si_nC_m^- clusters with different behavior of the VDEs:

- Carbon-rich clusters with linear C_n submolecules. They show even-odd alternation of the VDEs due to shell-closure effects. Since there are only few Si atoms in the cluster, partial charges at the carbon sites are both small and insignificant for the VDEs.
- Silicon-rich clusters, where the behavior of the VDEs is dominated by the presence of negative partial charges around the carbon sites. Due to electrostatic repulsion, the additional electron will be shifted to Si sites in the cluster, where it is comparatively weak bound unless it happens to contribute to increased bonding in the Si_n substructure, as we argued above.

The discussion above demonstrated that a reliable description of the geometry and both the electron density and magnetization densities⁶ of the anion clusters, as provided by density functional theory, is crucial for a qualitative understanding and an accurate quantitative description of the various features contained in the photoelectron spectra. Exceptional cases are Si_6C^- and Si_7C^- , where the VDEs of isomers that are not the most stable (less than ~ 0.4 eV above the GS) are in better agreement with the measured values than the values of the most stable isomers. It might be interesting to study the effect of gradient corrections to the exchange-correlation potential (see section 2.1.2), as recent publications [RSO⁺93, RZP⁺94] report dramatic consequences for the energy ordering of isomers of carbon clusters, changing relative energy differences by up to 8 eV. This could be a possible objective for future investigations.

⁶The magnetization density $m_z(\mathbf{r}) = (n_+ - n_-)(\mathbf{r})/2$ (a.u.) of all anion clusters inspected appears to be identical (apart from a factor ± 2) to the single-particle density of the excess KS-electron within the numerical accuracy.

Chapter 4

Conclusion

We have presented a scheme based on density functional theory that is able to describe accurately photoelectron spectra of complex nanosystems, such as anionic S_n^- , P_n^- and $Si_nC_m^-$ clusters. The success of our approach rests on two factors: the accurate determination of the ground state structures within the local spin-density approximation with the simulated annealing approach of Car and Parrinello, and the application of the Δ SCF scheme without further approximations to obtain excitation energies that include final state effects. Although this approach is confined to the lowest states of a given symmetry, we obtain in most cases sufficient excitation energies to make a definite assignment. As we have shown in various examples, differences in the geometries of the clusters may have major implications for the electronic excitation energies and the vertical detachment energy (VDE), a prominent example being the striking difference of the VDEs of ring and chainlike isomers of S_n^- . This has enabled us to explain a corresponding transition in the features observed experimentally in the photoelectron spectra upon readjustment of the source parameters as resulting from a generation of different classes of isomers.

Other examples of the effects of structural differences on the VDEs are found in our results. In P_5^- the VDEs of the two most stable isomers, a D_{5h} ring and a C_{2v} structure differed by more than 2 eV, and in Si_5C^- two isomers with related structures [shown in Figures 3.38(b) and 3.38(c)] have appreciably different VDEs (1.81 and 2.07 eV, respectively). To differentiate between such cases makes severe demands on both the accuracy and the efficiency of the computational methods, particularly if the ground state structure is not known. Our results show that the the local spin-density approximation within density functional theory addresses both requirements. The observable (and in many cases understandable) sensitivity of VDEs and excitation energies to structural differences makes us confident that the comparison of vibrationally resolved photoelectron spectra with computer simulations can enable us to gain information about cluster structures that is otherwise inaccessible.

Appendix A

FFT Coefficients and Isolated Systems

For further use in section 2.3.2, we shall derive here exact relations between the FFT components and the Fourier components and the Fourier transform of the density. The Fourier series of a density that is periodic over a direct lattice with lattice constant la_{lat} may be written

$$\tilde{n}_l(\mathbf{r}) = \sum_{\{\mathbf{G}\}_l} \tilde{n}(\mathbf{G}) e^{i\mathbf{G}\mathbf{r}}; \quad \tilde{n}_l(\mathbf{G}) = \frac{1}{l^3\Omega} \int_{l^3\Omega} d^3r \tilde{n}(\mathbf{r}) e^{-i\mathbf{G}\mathbf{r}}, \quad \mathbf{G} \in \{\mathbf{G}\}_l \quad (\text{A.1})$$

where $\{\mathbf{G}\}_l$ denotes the vectors of the reciprocal lattice corresponding to a lattice spacing la_{lat} . Under the condition that

$$\tilde{n}_l(\mathbf{G}) = 0 \quad \text{for } \mathbf{G} \notin \Delta V := \left\{ \mathbf{G} \mid \mathbf{G} = \sum_{i=1}^3 \lambda_i \frac{\mathbf{b}_i}{l}, \quad -\frac{N_i}{2} < \lambda_i \leq \frac{N_i}{2} \right\},$$

the FFT components and the Fourier components of the density are related by:

$$\tilde{n}^{fft}(\mathbf{G}) = l^3 N \tilde{n}_l(\mathbf{G}), \quad \mathbf{G} \in \{\mathbf{G}\}_l \quad (\text{A.2})$$

where $\{\mathbf{G}\}_l$ denotes the reciprocal-space FFT mesh defined by (2.50). This may be seen by inserting (A.1) into the defining equation of the FFT coefficients¹

$$\begin{aligned} \tilde{n}^{fft}(\mathbf{G}) &= \sum_{\{\mathbf{r}\}_l} \tilde{n}(\mathbf{r}) \exp -i\mathbf{G}\mathbf{r} \\ &= \sum_{\{\mathbf{r}\}_l} \sum_{\{\mathbf{G}'\}_l} \tilde{n}_l(\mathbf{G}') \exp i\mathbf{G}'\mathbf{r} \exp -i\mathbf{G}\mathbf{r} \end{aligned}$$

¹It should be noted that no difficulties arise in interchanging orders of summation, since all sums are finite in the case, where the relation is valid.

$$\begin{aligned}
&= \sum_{\{\mathbf{G}'\}_l} \tilde{n}_l(\mathbf{G}') \underbrace{\sum_{\{\mathbf{r}\}_l} \exp i(\mathbf{G}' - \mathbf{G})\mathbf{r}}_{=l^3 N \sum_{\mathbf{n} \in \mathbb{Z}^3} \delta(\mathbf{G}' - \mathbf{G}, \sum_{i=1}^3 n_i N_i \mathbf{b}_i), \mathbf{n} \in \mathbb{Z}^3} \\
&= \sum_{\mathbf{n} \in \mathbb{Z}^3} \tilde{n}_l(\mathbf{G} + \sum_{i=1}^3 n_i N_i \mathbf{b}_i) l^3 N \\
&= l^3 N \tilde{n}_l(\mathbf{G}), \text{ if } \tilde{n}_l(\mathbf{G}) = 0 \text{ for } \mathbf{G} \notin \Delta V
\end{aligned}$$

This last condition can always be fulfilled for the original periodic density (i.e., $l = 1$) by adjusting the size N of the FFT mesh, due to the finite cutoff in the expansion of the density. In the case of increased lattice spacings $l > 1$, this condition implies further that the periodic density must be negligibly small at the cell boundary, so no high-frequency oscillations are introduced by cutting it there. If this can be fulfilled for all l , then the above relation implies for the Fourier transform of the isolated density of a single unit cell

$$\tilde{n}^{fft}(\mathbf{G}) = \frac{N}{\Omega} \hat{n}(\mathbf{G}), \quad \mathbf{G} \in \{\mathbf{G}\}_l, \quad l \geq 1, \quad (\text{A.3})$$

since, due to the finite support² of \hat{n} in \mathbf{k} -space, we have $\hat{n}(\mathbf{G}) = l^3 \Omega \tilde{n}_l(\mathbf{G})$.

In the remainder of this section, a sketch of the proof that the series (2.51) converges to the \mathbf{k} -space integral (2.52) shall be given. Let us first define the following volume elements ΔV_l in \mathbf{k} -space of volume $(2\pi)^3 / (l^3 \Omega)$ surrounding all $\mathbf{G} \in \{\mathbf{G}\}_l$:

$$\Delta V_l(\mathbf{G}) := \left\{ \mathbf{k} \mid \mathbf{k} = \mathbf{G} + \sum_{i=1}^3 \lambda_i \frac{\mathbf{b}_i}{l}, \quad -\frac{1}{2} < \lambda_i \leq \frac{1}{2} \right\}.$$

As may be readily verified, the series (2.51) may be written as an integral over \mathbf{k} -space of the following step function

$$\phi_l(\mathbf{k}) = \sum_{\{\mathbf{G}\}_l} a_{\mathbf{G}} \chi_{\Delta V_l(\mathbf{G})}(\mathbf{k}), \quad a_{\mathbf{G}} = \begin{cases} \frac{1}{(2\pi)^3} |\hat{n}(\mathbf{G})|^2 \frac{4\pi}{\Omega^2} & \text{if } \mathbf{G} \in \{\mathbf{G}\}_l \setminus \{0\} \\ 0 & \text{if } \mathbf{G} = 0 \end{cases}$$

where the characteristic functions

$$\chi_{\Delta V_l(\mathbf{G})}(\mathbf{k}) = \begin{cases} 1 & \text{if } \mathbf{k} \in \Delta V_l(\mathbf{G}) \\ 0 & \text{otherwise} \end{cases}$$

have been used. Obviously, we have

$$\lim_{l \rightarrow \infty} \phi_l(\mathbf{k}) = \frac{1}{(2\pi)^3} |\hat{n}(\mathbf{k})|^2 \frac{4\pi}{k^2} \text{ almost everywhere.}$$

²The support of a function $f(\mathbf{x})$ is the closure of the set $\{\mathbf{x} \mid f(\mathbf{x}) \neq 0\}$.

³As it stands, the definition for ΔV_l holds only for lN_i odd. For lN_i even, the ranges for λ_i should be modified to $-1 < \lambda_i \leq 0$. This is just a technicality that does not defeat the argument and has been omitted for simplicity's sake.

Since the region ΔV where $\hat{n}(\mathbf{k})$ is nonzero is finite, there exists an integrable function $G(\mathbf{k})$ with $|\phi_l(\mathbf{k})| \leq G(\mathbf{k})$ a.e. (take, e.g., $G(\mathbf{k}) = 9/(2\pi)^3 m^2/k^2$, where $m := \max_{\Delta V} |\hat{n}(\mathbf{k})|$), so that the dominated convergence theorem (see, e.g. [RS72, §I, (I.16)]) is applicable. This implies that

$$\begin{aligned} \lim_{l \rightarrow \infty} \frac{1}{2} \int d\mathbf{k} \phi_l(\mathbf{k}) &= \lim_{l \rightarrow \infty} \frac{1}{2} \frac{(2\pi)^3}{l^3 \Omega} \sum_{\{\mathbf{G}\}_l \setminus \{0\}} \frac{1}{(2\pi)^3} |\hat{n}(\mathbf{G})|^2 \frac{4\pi}{G^2} \\ &= \frac{1}{2} \int d\mathbf{k} \lim_{l \rightarrow \infty} \phi_l(\mathbf{k}) \\ &= \frac{1}{2} \int \frac{d\mathbf{k}}{(2\pi)^3} |\hat{n}(\mathbf{k})|^2 \frac{4\pi}{k^2}. \end{aligned}$$

Convergence can also be ensured, if the contribution of the central volume $\Delta V(0)$ to the series (2.51), or to the approximation of the integral (2.52) respectively, is replaced by

$$\frac{1}{2} \int_{\Delta V_l(0)} \frac{d\mathbf{k}}{(2\pi)^3} |\hat{n}(\mathbf{k})|^2 \frac{4\pi}{k^2} \approx \frac{1}{2} |\hat{n}(\mathbf{0})|^2 \int_{\Delta V_l(0)} \frac{d\mathbf{k}}{(2\pi)^3} \frac{4\pi}{k^2} = \frac{4\pi \Omega}{l^3 N^2} |n^{fft}(\mathbf{0})|^2 \int_{[-\frac{1}{2}, \frac{1}{2}]^3} dx \frac{1}{|\sum_{i=1}^3 x_i \mathbf{b}_i|^2},$$

where the last integral may be calculated numerically to high precision using, e.g., spherical coordinates. This is done in our program.

Appendix B

Excited States within the von Barth Scheme

As already mentioned in section 2.1.2, excited states that cannot be represented by a single Slater determinant in the noninteracting case can be obtained by the procedure of von Barth [vB79], whose application may be illustrated by two examples. Consider, the p^4 configuration of the sulfur atom that gives rise to the three terms 3P , 1D and 1S . Solving for the determinantal states that enter the corresponding excited states, we find the following relations¹

$$\begin{aligned} |1 \uparrow, 1 \downarrow, 0 \uparrow, -1 \uparrow\rangle &= |^3P, 1, 1\rangle \\ |1 \uparrow, 0 \uparrow, 0 \downarrow, -1 \uparrow\rangle &= |^3P, 0, 1\rangle \\ |0 \uparrow, 0 \downarrow, -1 \uparrow, -1 \downarrow\rangle &= |^1D, 2, 0\rangle \\ |1 \uparrow, 1 \downarrow, 0 \downarrow, -1 \uparrow\rangle &= \frac{1}{\sqrt{2}}(|^3P, 1, 0\rangle + |^1D, 1, 0\rangle) \\ |1 \uparrow, 1 \downarrow, 0 \uparrow, -1 \downarrow\rangle &= \frac{1}{\sqrt{2}}(|^3P, 1, 0\rangle - |^1D, 1, 0\rangle) \\ |1 \downarrow, 0 \uparrow, 0 \downarrow, -1 \uparrow\rangle &= \frac{1}{\sqrt{2}}|^3P, 0, 0\rangle + \frac{1}{\sqrt{6}}|^1D, 0, 0\rangle + \frac{1}{\sqrt{3}}|^1S, 0, 0\rangle \\ |1 \uparrow, 0 \uparrow, 0 \downarrow, -1 \downarrow\rangle &= \frac{1}{\sqrt{2}}|^3P, 0, 0\rangle - \frac{1}{\sqrt{6}}|^1D, 0, 0\rangle - \frac{1}{\sqrt{3}}|^1S, 0, 0\rangle \\ |1 \uparrow, 1 \downarrow, -1 \uparrow, -1 \downarrow\rangle &= \frac{2}{\sqrt{6}}|^1D, 0, 0\rangle - \frac{1}{\sqrt{3}}|^1S, 0, 0\rangle. \end{aligned}$$

Since the states of different total angular momentum J that belong to each term are degenerate in the absence of spin-orbit interaction and the energies are invariant under an overall change of sign of all m_{li} and/or m_{si} , we are left with six different equations for the

¹The MS determinantal states are characterized by the one-particle numbers $m_{11}, m_{s1}, \dots, m_{14}, m_{s4}$ (only quantum numbers of the one-particle orbitals in the 3s-shell are given), the multiplet states are characterized by symmetry labels $^{2S+1}X, M_L, M_S$, where $X = S, P, D, \dots$ correspond to $L = 0, 1, 2, 3, \dots$. Here, out of the 15 possible states only those corresponding to $M_L, M_S \geq 0$ are shown, since the local-density energies are invariant under a change of sign in M_L, M_S .

three unknown quantities

$$\begin{aligned}
 E(1 \uparrow, 1 \downarrow, 0 \uparrow, -1 \uparrow) &= E(^3\text{P}) \\
 E(1 \uparrow, 0 \uparrow, 0 \downarrow, -1 \uparrow) &= E(^3\text{P}) \\
 E(0 \uparrow, 0 \downarrow, -1 \uparrow, -1 \downarrow) &= E(^1\text{D}) \\
 E(1 \uparrow, 1 \downarrow, 0 \downarrow, -1 \uparrow) &= \frac{1}{2}(E(^3\text{P}) + E(^1\text{D})) \\
 E(1 \downarrow, 0 \uparrow, 0 \downarrow, -1 \downarrow) &= \frac{1}{2}E(^3\text{P}) + \frac{1}{6}E(^1\text{D}) + \frac{1}{3}E(^1\text{S}) \\
 E(1 \uparrow, 1 \downarrow, -1 \uparrow, -1 \downarrow) &= \frac{2}{3}E(^1\text{D}) + \frac{1}{3}E(^1\text{S}).
 \end{aligned}$$

Although there are in general more determinants than pure-state energies, in certain cases, the number of determinants of different energy may be smaller than the number of multiplets with different energy and the von Barth procedure is not applicable. Examples we encountered are linear molecules with two inequivalent unpaired π electrons, as for example the excited state configuration $\sigma_g^2\pi_u^3\pi_g$ of the phosphorus dimer, which gives rise to the terms² $^3\Sigma_u^+$, $^3\Sigma_u^-$, $^3\Delta_u$, and related singlets [Her50]. To illustrate the difficulties encountered, let us consider the more general problem of two inequivalent electrons in the cylinder symmetric potential of a diatomic molecule. In Russell-Saunders coupling, symmetry species of a diatomic molecule are characterized by the total electronic spin and by the magnitude of the axial component of orbital angular momentum. For a homonuclear dimer, the symmetry property even (g) or odd (u) with respect to reflection of the coordinates of all electrons in the plane bisecting the nuclear axis in the center of mass (σ_h) is also defined. In addition, for Σ states with zero axial angular momentum, the property + or - is precisely defined for the operation of reflection in any plane passing through the internuclear axis ($\infty\sigma_v$). "+" states remain unchanged under this operation, while "-" states change signs. Let us see how this is accomplished in our two-electron example by constructing states of the requested symmetries from two-particle Slater determinants. If we use, e.g., cylindrical coordinates (ρ, z, φ) ³, the spatial parts of the single-particle solutions that enter the Slater determinants have the general form [Sla63]

$$\phi_{i,m}(\rho_j, z_j, \varphi_j) = f_i(\rho_j, z_j)e^{im\varphi_j} =: \phi_{i,m}(j), i, j = 1, 2.$$

Here, m denotes the angular momentum about the intermolecular axis, and the f_i may be (in the homonuclear case) either symmetric or antisymmetric under the operation σ_h . Spatial parts of Slater determinants that would be compatible with a Σ state (all m must add up to zero) would then be

$$\Phi_m^\pm = \frac{1}{\sqrt{2}}(\phi_{1,m}(1)\phi_{2,-m}(2) \pm \phi_{1,m}(2)\phi_{2,-m}(1))$$

where the upper sign would be appropriate for a triplet state and the lower for a singlet state. As inspection shows, these determinants are still not symmetric with respect to

²The symmetrization postulate forbids the existence of $^1\Sigma_u^-$ and $^3\Sigma_u^+$ states only, if the π orbitals are equivalent (see also below).

³In elliptical coordinates (with $r_I := |\mathbf{r} - \mathbf{R}_I|$, $I = 1, 2$ and $R := |\mathbf{R}_1 - \mathbf{R}_2|$, these read $\mu := (r_1 + r_2)/R$, $\nu := (r_1 - r_2)/R$ and ψ) the μ and ν dependent parts of the orbitals separate as well (see, e.g. [SW93]).

σ_v ⁴, instead we have $(P_{\sigma_v} \Phi_m^\pm) = \Phi_{-m}^\pm$. But $+/-$ symmetry can be taken into account, if we use linear combinations of Slater determinants such as $(\Phi_m \pm \Phi_{-m})/\sqrt{2}$ for $+$ and $-$ states, respectively. For a Δ state, on the other hand, a possible spatial part of a Slater determinant would read

$$\Phi^\pm = \frac{1}{\sqrt{2}}(\phi_{1,m}(1)\phi_{2,m'}(2) \pm \phi_{1,m}(2)\phi_{2,m'}(1)), \quad m + m' = 2.$$

Since in this case the momenta m and m' about the intermolecular axis of every determinant are required to add up to 2, we cannot construct (anti)symmetric linear combinations of these determinants with respect to application of σ_v , and consequently, a Δ state does not exhibit $+/-$ symmetry. The single-particle wave functions that enter these determinants differ only by their phase factors $\exp(\pm im\phi_i)$, which a CI wavefunction, consisting of a sum of such determinants for several m , nevertheless sensitively depends on. Therefore, CI energy terms of, e.g., $^1\Sigma^+$, $^1\Sigma^-$ and $^1\Delta$ states will (in general) differ. This holds also true, if we evaluate the energy expectation values of the corresponding determinants within the Hartree-Fock (HF) approximation, since phase relations like $\exp im(\phi_1 \pm \phi_2)$ between the orbitals enter the energy expectation value via the exchange integral. The energy terms of the correctly symmetrized linear combinations of single determinantal HF states can be recovered by application of the analogues to the von Barth equations within HF theory [ZRB77]. The physical origin of the energy-difference is the so-called angular correlation [Sla63], which takes into account the relative angular position of the two electrons around the internuclear axis. Since the $+/-$ states considered above contain factors $\cos m(\phi_1 - \phi_2)$ and $\sin m(\phi_1 - \phi_2)$, respectively, a $+$ state will have largest amplitude if the electrons move in diametrically opposite directions, in contrast to the $-$ state, which has zero amplitude in this case (for $m \neq 0$). Therefore, a $+$ state should be energetically favored by correlation.

Within LSDA, however, the (spin-)densities are independent of phase factors of the orbitals like $\exp(\pm im\phi_i)$ and consequently, the potentials and KS eigenvalues are independent of m and m' . This means that we would obtain the same energies if we would set, e.g., $m=m'=0$ in the above equations, and we can see that in this case, LSDA can only distinguish paired and unpaired spin. For example, in the case of the $\sigma_g^2\pi_u^3\pi_g$ configuration of the phosphorus dimer, the above equations apply with $m=m'=1$, but since the KS energies are independent of m and m' , we obtain only two different KS energies (for paired and unpaired spin) for the six unknown energy terms. Unfortunately, it is not possible to determine the symmetry of the state by, e.g., the application of Hund's rules, since these fail for dimers (for example, all first-row dimers have a $^1\Sigma_g$ GS, apart from B_2 and O_2 , which are the only ones to obey at least the first rule [HH79]). This should not be confused with the Hund's distinction of the various coupling cases of the spins and angular momenta that applies well to a diatomic molecule [Atk83]. It is not possible to appeal to the Hohenberg-Kohn theorem for the lowest state of a *well-defined* mixture of symmetries proven by von Barth, since the mixture is in this case by no means definite, and we make

⁴Applying σ_v is equivalent to change simultaneously the signs of ϕ_1 and ϕ_2 , or likewise, to exchange m and $-m$).

no attempt to ascribe these KS states to any physical states. We note in passing that similar, but less severe difficulties are encountered for a $\pi_1\pi_2$ configuration, when the π orbitals are equivalent. Such a configuration gives rise to the three terms $^3\Sigma^-$, $^1\Sigma^+$ and $^1\Delta$, but LSDA can distinguish only a triplet and a singlet term. While the assignment of the triplet term is unambiguous, there is no formal justification to identify the singlet with the $^1\Sigma^+$ term, apart from the fact that a transition into a $^1\Delta$ state is dipole-forbidden [Atk83] and cannot be observed in most spectroscopic experiments (but see, for example, [KN93]). However, it is established tradition to do so (see [JG89] and references therein) and the reader should be aware of this.

Appendix C

Vertical Excitation Energies of Selected Clusters

In the first table, we list the calculated vertical excitation energies of the atom and all S_n^- isomers shown in Figs. 3.5-3.15, and in the second table the corresponding values for the $Si_n C_m^-$ clusters Figs. 3.30-3.39. Only values that correspond to transitions into the lowest excited state of a given symmetry of the neutral species are considered. In the case of S_2 , ... denotes the occupancies $1\sigma_g^2 1\sigma_u^2 2\sigma_g^2 2\sigma_u^2 3\sigma_g^2 1\pi_u^4 1\pi_g^4 4\sigma_g^2 4\sigma_u^2$ of the lower lying orbitals.

Table C.1: Calculated values (eV) for VDE and for vertical transition energies for S_n^- , $n=1,9$.

Species	Symmetry/ Electronic configuration	Excited state	Excitation Energy
S_1^-	[Ne]3s ² p ⁴	³ P	2.21
		¹ D	3.63
		¹ S	4.21
	[Ne]3s ² 3p ³ 4s ¹	⁵ S ^{oa}	8.82
		³ S ^{oa}	9.17
		³ D ^{oa}	10.67
		¹ D ^{oa}	10.85
		³ P ^{oa}	11.87
		¹ P ^{oa}	12.04
S_2^-	... 5σ _g ² 2π _u ⁴ 2π _g ²	³ Σ _g ⁻ , VDE	1.91
		¹ Δ _g ⁻	2.45
		¹ Σ _g ⁺	2.98
	... 5σ _g ¹ 2π _u ⁴ 2π _g ³	³ Π _g	6.25
		¹ Π _u	6.90
S_3^- 3.5(a)	C_{2v}	¹ A ₁ , VDE	2.64

Continued on next page.

^aDetachment from the S^- ²P ground state into these states is a two-electron transition.

Species	Symmetry	Excited state	Excitation Energy
S_3^- 3.5(b)	C_{2v}	3A_2	3.73
		3B_1	3.77
		3B_2	3.95
		1A_2	4.02
		1B_1	4.13
		1B_2	4.84
		1A_1 , VDE	1.34
		3A_2	2.93
		3B_1	2.94
		1A_2	3.29
S_3^- 3.5(c)	$D_{\infty h}$	1B_1	3.34
		3B_2	5.91
		1B_2	6.85
		$^3\Pi_u$, VDE	2.84
S_4^- 3.5(d)	C_{2v}	$^1\Sigma_g^+$	3.02
		$^1\Pi_u$	3.27
		1A_1 , VDE	2.49
S_4^- 3.5(e)	D_{2h}	3B_2	3.19
		1B_2	3.96
		3B_1	4.09
		1B_1	4.33
		1A_u , VDE	2.47
		$^3B_{3u}$	3.11
		$^1B_{3u}$	3.90
		$^3B_{3g}$	3.94
		$^1B_{3g}$	4.19
		$^3B_{2g}$	4.45
S_4^- 3.5(f)	C_{2h}	$^1B_{2g}$	4.73
		1A_g , VDE	2.89
		3B_u	3.36
		1B_u	4.07
		3B_g	3.87
		1B_g	4.11
S_5^- 3.6(a)	C_s	$^1A'$, VDE	2.85
		$^3A''$	3.28
		$^1A''$	3.81
		$^3A'$	3.92
S_5^- 3.6(b)	C_1	1A , VDE	2.80
		3A	3.30
S_5^- 3.6(c)	C_2	1A , VDE	3.21
		3B	3.34
		1B	3.96
		3A	4.25

Continued on next page.

Species	Symmetry	Excited state	Excitation Energy
S_5^- 3.6(d)	C_s	$^1A'$, VDE	2.77
S_6^- 3.6(e)	C_2	1A , VDE	2.61
		3B	3.17
		1B	3.80
		3A	4.53
S_6^- 3.6(f)	C_2	1A , VDE	2.70
		3B	3.51
		1B	3.89
		3A	4.09
S_6^- 3.11(a)	C_s	$^1A'$, VDE	2.87
		$^3A'$	3.89
S_6^- 3.11(b)	C_1	1A , VDE	3.43
		3A	3.53
S_6^- 3.11(c)	C_2	1A , VDE	3.55
		3B	3.56
		1B	4.23
		3A	4.28
S_6^- 3.11(d)	C_1	1A , VDE	3.13
		3A	3.15
S_6^- 3.11(e)	C_2	1A , VDE	3.46
		3B	3.73
		1B	4.34
S_7^- 3.11(f)	C_s	$^1A'$, VDE	2.69
		$^3A''$	3.88
		$^3A'$	4.15
		$^1A''$	4.51
S_7^- 3.12(a)	C_1	1A , VDE	2.52
		3A	3.81
S_7^- 3.12(b)	C_1	1A , VDE	2.69
		3A	3.68
S_7^- 3.12(c)	C_1	1A , VDE	3.46
		3A	3.46
S_7^- 3.12(d)	C_1	3A , VDE	3.44
		1A	3.46
S_7^- 3.12(e)	C_1	1A , VDE	3.41
		3A	3.53
S_7^- 3.12(f)	C_2	3B , VDE	3.52
		1A	3.62
		1B	4.17
S_8^- 3.14(a)	D_2	1A , VDE	2.30
		3B_1	4.33
		1B_1	4.49

Continued on next page.

Species	Symmetry	Excited state	Excitation Energy
S_8^- 3.14(b)	C_{2v}	3A	4.68
		1A_1 , VDE	2.54
		3A_2	3.81
		1A_2	4.17
S_8^- 3.14(c)	C_2	3A_1	4.34
		1A , VDE	2.68
		3B	3.57
		1B	3.88
S_8^- 3.14(e)	C_1	1A , VDE	2.86
S_8^- 3.14(d)	C_1	3A	3.60
		1A , VDE	3.35
S_8^- 3.14(f)	C_1	3A	3.45
		1A , VDE	3.25
S_9^- 3.15(a)	C_1	3A	3.56
		1A , VDE	2.86
S_9^- 3.15(b)	C_s	3A	3.82
		$^1A'$, VDE	2.83
		$^3A''$	3.86
		$^1A''$	4.34
S_9^- 3.15(c)	C_s	$^1A'$, VDE	2.64
		$^3A''$	4.06
		$^1A''$	4.24
		3B , VDE	3.68
S_9^- 3.15(d)	C_2	1A	3.94
		1B	4.24
		1A , VDE	2.63
S_9^- 3.15(e)	C_1	3A	3.64

Table C.2: Calculated values (eV) for VDE and for vertical transition energies for $Si_n C_m^-$, $2 \leq n + m \leq 8$.

Species	Symmetry	Excited state	Excitation Energy
SiC	$C_{\infty v}$	$^3\Pi$, VDE	2.55
		$^3\Sigma^-$	3.25
		$^1\Pi$	3.27
		$^1\Sigma^+$	3.30
SiC ₂ 3.30(a)	C_{2v}	1A_1 , VDE	1.50
		3B_2	2.99
		1B_2	3.55
SiC ₂ 3.30(b)	$C_{\infty v}$	$^1\Sigma^+$, VDE	1.69
		$^3\Pi$	3.69

Continued on next page.

Species	Symmetry	Excited state	Excitation Energy
		$^1\Pi$	4.19
Si ₂ C 3.30(c)	$D_{\infty h}$	$^1\Sigma^+$, VDE	1.18
		$^3\Pi_g$	3.49
		$^1\Pi_g$	3.94
Si ₂ C 3.30(d)	C_{2v}	1A_1 , VDE	1.56
		3B_2	2.90
		1B_2	3.37
SiC ₃ 3.30(e)	$C_{\infty v}$	$^3\Sigma^-$, VDE	2.86
		$^1\Sigma^+$	3.27
		$^3\Pi$	4.36
		$^1\Pi$	4.96
SiC ₃ 3.30(f)	C_{2v}	1A_1 , VDE	2.35
		3B_1	2.83
		1B_1	3.55
SiC ₃ 3.31(a)	C_{2v}	1A_1 , VDE	2.08
		3B_1	3.00
		1B_1	3.38
Si ₂ C ₂ 3.31(b)	C_s	$^1A'$, VDE	2.07
		$^3A''$	2.83
		$^1A''$	3.21
Si ₂ C ₂ 3.31(c)	$D_{\infty h}$	$^3\Sigma_g^-$, VDE	2.14
		$^1\Sigma_g^+$	2.49
		$^3\Pi_g$	4.55
		$^1\Pi_g$	4.92
Si ₂ C ₂ 3.31(d)	D_{2h}	1A_g , VDE	1.56
		$^3B_{3g}$	3.62
		$^1B_{3g}$	3.76
Si ₃ C 3.31(e)	C_{2v}	1A , VDE	1.69
		3B_1	3.16
		1B_1	3.51
Si ₃ C 3.31(f)	C_{2v}	1A_1 , VDE	2.06
		3B_1	2.33
		1B_1	2.45
Si ₃ C 3.34(a)	C_{2v}	1A_1 , VDE	2.47
		3B_1	2.59
		1B_1	3.02
SiC ₄ 3.34(b)	$C_{\infty v}$	$^1\Sigma^+$, VDE	2.27
		$^3\Pi$	4.62
		$^1\Pi$	5.08
SiC ₄ 3.34(c)	C_{2v}	1A_1 , VDE	1.95
		3B_1	4.13
		1B_1	4.55
Si ₂ C ₃ 3.34(d)	$D_{\infty h}$	$^1\Sigma_g^+$, VDE	1.82

Continued on next page.

Species	Symmetry	Excited state	Excitation Energy
		$^3\Sigma_u$	3.66
		$^1\Sigma_u$	3.92
Si ₂ C ₃ 3.34(e)	C ₁	1A , VDE	1.93
		3A	3.01
Si ₂ C ₃ 3.34(f)	C _s	$^1A'$, VDE	2.01
		$^3A'$	3.28
Si ₃ C ₂ 3.35(a)	C _{2v}	1A_1 , VDE	1.88
		3B_2	2.59
		1B_2	2.94
		3A_2	4.34
		1A_2	4.48
Si ₃ C ₂ 3.35(b)	C _{2v}	1A_1 , VDE	2.32
		3A_2	3.91
		1A_2	4.19
Si ₃ C ₂ 3.35(c)	C ₁	1A_1 , VDE	2.73
		3B_2	2.79
		1B_2	2.92
Si ₄ C 3.35(d)	C _{2v}	1A_1 , VDE	3.21
		3B_2	3.37
		1B_2	3.48
Si ₄ C 3.35(e)	C _{2v}	1A_1 , VDE	2.01
		3A_2	3.00
		1A_2	3.20
SiC ₅ 3.35(f)	C _{∞v}	$^3\Sigma^-$, VDE	3.22
		$^1\Sigma^+$	3.51
		$^3\Pi$	4.48
		$^1\Pi$	4.99
SiC ₅ 3.36(a)	C _{2v}	1A_1 , VDE	2.86
		3B_1	3.48
		1B_1	3.70
Si ₁ C ₅ 3.36(b)	C _{2v}	1A_1 , VDE	2.78
		3B_1	4.26
		1B_1	4.62
Si ₂ C ₄ 3.36(c)	D _{∞h}	$^3\Sigma_u^-$, VDE	2.59
		$^1\Sigma_u^+$	2.85
		$^3\Pi_u$	4.91
		$^1\Pi_u$	5.25
Si ₂ C ₄ 3.36(d)	C _s	$^1A'$, VDE	2.75
		$^3A'$	3.50
Si ₂ C ₄ 3.36(e)	C _{2h}	1A_g , VDE	2.61
		3B_g	3.68
		1B_g	3.86
Si ₂ C ₄ 3.36(f)	C _{2v}	1A_1 , VDE	3.15

Continued on next page.

Species	Symmetry	Excited state	Excitation Energy
		1B_1	3.38
		3B_1	3.39
Si ₃ C ₃ 3.37(a)	C_{2v}	1A_1 , VDE	2.51
		3A_1	2.93
Si ₃ C ₃ 3.37(b)	C_s	$^1A'$, VDE	2.76
		$^3A''$	3.41
		$^1A''$	3.57
Si ₃ C ₃ 3.37(c)	C_1	1A , VDE	1.99
		3A	3.50
Si ₃ C ₃ 3.37(d)	C_s	$^1A'$, VDE	2.00
		$^3A'$	3.69
Si ₄ C ₂ 3.37(e)	C_1	1A , VDE	2.18
		3A	3.48
Si ₄ C ₂ 3.37(f)	C_{2v}	1A_1 , VDE	1.02
		3B_1	3.30
		1B_1	3.58
Si ₄ C ₂ 3.38(a)	D_2	1A , VDE	1.07
		3B_1	3.84
		1B_1	4.16
Si ₅ C 3.38(b)	C_s	$^1A'$, VDE	1.81
		$^3A'$	3.38
Si ₅ C 3.38(c)	C_{2v}	1A_1 , VDE	1.54
		3A_2	3.39
		1A_2	3.61
Si ₅ C 3.38(d)	C_{2v}	1A_1 , VDE	2.07
		3B_1	3.01
		1B_1	3.34
Si ₂ C ₅ 3.38(e)	$D_{\infty h}$	$^1\Sigma_g^+$, VDE	2.18
		$^3\Sigma_u$	3.73
		$^1\Sigma_u$	3.95
Si ₂ C ₅ 3.38(f)	C_s	$^1A'$, VDE	3.17
		$^3A'$	3.75
Si ₆ C 3.39(a)	C_{2v}	1A_1 , VDE	2.47
		3B_1	3.00
		1B_1	3.17
Si ₆ C 3.39(b)	C_s	$^1A'$, VDE	2.27
		$^3A''$	2.79
		$^1A''$	3.00
Si ₆ C 3.39(c)	C_s	$^1A'$, VDE	1.79
		$^3A''$	3.17
		$^1A''$	3.36
Si ₇ C 3.39(d)	C_s	$^1A'$, VDE	2.05
		$^3A'$	3.01

Continued on next page.

APPENDIX C. CALCULATED VERTICAL EXCITATION ENERGIES

Species	Symmetry	Excited state	Excitation Energy
Si ₇ C 3.39(e)	<i>C</i> _{3v}	¹ A'	3.19
		³ A ₁ , VDE	3.32
		¹ A ₁	3.47
Si ₇ C 3.39(f)	<i>C</i> _s	¹ A', VDE	2.45
		³ A''	2.69
		¹ A''	2.91

Bibliography

- [ABKN91] Arnold, D.W., Bradforth, S.E., Kitsopoulos, T.N., and Neumark, D.M., *J. Chem. Phys.* **95** (1991) 8753.
- [AGL+94] Amar, F.G., Goyal, S., Levandier, D.J., Perera, L., and Scoles, G., IR spectroscopy of solvated molecules, in *Clusters of Atoms and Molecules II*, edited by Goldanskii, V.I., Schäfer, F.P., and Toennies, J.P., Springer Series in Chemical Physics, Springer-Verlag, 1994.
- [AGS90] Alberts, I. L., Grev, R.S., and Schaefer, H.F. III, *J. Chem. Phys.* **93** (1990) 5046.
- [AM76] Ashcroft, N. W. and Mermin, N. D., *Solid State Physics*, Holt Saunders, Philadelphia, 1976.
- [AMS91] Anderson, L.R., Maruyama, S., and Smalley, R.E., *Chem. Phys. Lett.* **176** (1991) 348.
- [AP90] Andreoni, W. and Pastore, G., *Phys. Rev. B* **41** (1990) 10243.
- [APJ92] Arias, T.A., Payne, M.C., and Joannopoulos, J.D., *Phys. Rev. B* **45** (1992) 1538.
- [AS72] Abramowitz, M. and Stegun, I. S., editors, *Handbook of Mathematical Functions*, Dover Publications, New York, 9th edition, 1972.
- [ASG90] Andreoni, W., Scharf, D., and Giannozzi, P., *Chem. Phys. Lett.* **173** (1990) 449.
- [AT87] Allen, M.P. and Tildesley, D.J., *Computer simulations of liquids*, Oxford Science Publications, Clarendon, 1987.
- [Atk83] Atkins, P.W., *Molecular Quantum Mechanics*, Oxford University Press, Oxford, 1983.
- [BCC+95] Bréchnac, C. et al., *J. Chem. Phys.* **102** (1995) 763.
- [BDF+92] Bolton, E.E., DeLeeuw, B.J., Fowler, J.E., Grev, R.S., and Schaefer, H.F. III, *J. Chem. Phys.* **97** (1992) 5586.

- [Bec88] Becke, A. D., *Phys. Rev. A* **38** (1988) 3098.
- [Bec92] Becke, A.D., *J. Chem. Phys.* **96** (1992) 2155.
- [BG90] Ballone, Pietro and Galli, Giulia, *Phys. Rev. B* **42** (1990) 1112.
- [BG93] Baudler, M. and Glinka, K., *Chem. Rev.* **93** (1993) 1623.
- [BH85] Biswas, M. I. and Hamann, D.R., *Phys. Rev. Lett.* **55** (1985) 2001.
- [BHS82] Bachelet, G. B., Hamann, D. R., and Schlüter, M., *Phys. Rev. B* **26** (1982) 4199.
- [BJ94] Ballone, P. and Jones, R. O., *J. Chem. Phys.* **100** (1994) 4941.
- [BKČ94] Bonačić-Koutecký, V. and Češpiva, L., *J. Chem. Phys.* **100** (1994) 490.
- [BL87] Bauschlicher, C.W., Jr. and Langhoff, S.R., *J. Chem. Phys.* **87** (1987) 2919.
- [BL89] Balasubramanian, K. and Li, J., *J. Mol. Spectroscop.* **135** (1989) 169.
- [BL93] Barnett, R.N. and Landman, U., *Phys. Rev. B* **48** (1993) 2081.
- [BMA91] Brabson, G.D., Mielke, Z., and Andrews, L., *J. Phys. Chem.* **95** (1991) 79.
- [BMB88] Bernholdt, D.E., Magers, D.H., and Bartlett, R.J., *J. Chem. Phys.* **89** (1988) 3612.
- [BMC88] Burdett, J.K., Marsden, C.J., and Chem., *New J.*, **12** (1988) 797.
- [BO27] Born, M. and Oppenheimer, R., *Ann. Phys.* **84** (1927) 457.
- [BO89] Baudler, M. and Ouzounis, D., *Z. Naturforsch. Teil B* **44** (1989) 381.
- [BP92] Blöchl, P.E. and Parrinello, M., *Phys. Rev. B* **45** (1992) 9413.
- [BR92] Butenhoff, T. J. and Rohlfing, E. A., *J. Chem. Phys.* **97** (1992) 1595.
- [BRO⁺88] Bernath, P.F., Rogers, S.A., O'Brien, L.C., Brazier, C.R., and McLean, A.D., *Phys. Rev. Lett.* **60** (1988) 197.
- [BSD91] Balasubramanian, K., Sumathi, K., and Dai, D., *J. Chem. Phys.* **92** (1991) 3494.
- [CA80] Ceperley, D. M. and Alder, B. J., *Phys. Rev. Lett.* **45** (1980) 566.
- [CBH74] Celotta, R.J., Bennett, R.A., and Hall, J.L., *J. Phys. Chem.* **60** (1974) 1740.
- [CC78] Clark, R.J.H. and Cobbold, D.G., *Inorg. Chem.* **17** (1978) 3169.

- [Cep78] Ceperley, D. M., *Phys. Rev. B* **18** (1978) 3126.
- [CGE92] Cha, C.Y., Ganteför, G., and Eberhardt, W., *Rev. Sci. Instrum.* **63** (1992) 5661.
- [CGG⁺89] Cernicharo, J., Gottlieb, C.A., Guélin, M., Thaddeus, P., and Vrtilek, J.M., *Astrophys. J.* **341** (1989) L25.
- [Che61] Chester, G. V., *Adv. Phys.* **10** (1961) 357.
- [CJ90] Creegan, K.M. and Jarrold, M.F., *J. Am. Chem. Soc.* **112** (1990) 3768.
- [CP85] Car, R. and Parrinello, M., *Phys. Rev. Lett.* **55** (1985) 2471.
- [Cri88] Crick, F., *What Mad Pursuit*, page 150, Penguin, London, 1988.
- [CS94] Charlé, K.-P. and Schulze, W., Optical properties of silver clusters in dielectric matrices, in *Clusters of Atoms and Molecules II*, edited by Goldanskii, V.I., Schäfer, F.P., and Toennies, J.P., Springer Series in Chemical Physics, Springer-Verlag, 1994.
- [CW88] Cotton, F.A. and Wilkinson, G., *Advanced inorganic chemistry*, Wiley, New York, 1988.
- [CYB⁺77] Coppens, P., Yang, Y.W., Blessing, R.H., Cooper, W.F., and Larsen, F.K., *J. Am. Chem. Soc.* **99** (1977) 760.
- [CYP⁺87] Cheshnovsky, O. et al., *Chem. Phys. Lett.* **138** (1987) 119.
- [DBB92] Delaly, P., Ballone, P., and Buttet, J., *Phys. Rev. B* **45** (1992) 3838.
- [dC89] deHeer, W.A. and Châtelain, A., *Phys. Rev. Lett.* **63** (1989) 2834.
- [DC94] Deutsch, P.W. and Curtiss, L.A., *Chem. Phys. Lett.* **226** (1994) 387.
- [DG90] Dreizler, R. M. and Gross, E. K. U., *Density Functional Theory: an approach to the quantum many body problem*, Springer-Verlag, Berlin, 1990.
- [dHKCC87] de Heer, W.A., Knight, W.D., Chou, M.Y., and Cohen, M.L., *Solid State Physics* **40** (1987) 93.
- [Don74] Donohue, J., *The Structure of the Elements*, chapter 9, Wiley, New York, 1974.
- [DW94] DiCenzo, S.B. and Wertheim, G.K., Supported clusters, in *Clusters of Atoms and Molecules II*, edited by Goldanskii, V.I., Schäfer, F.P., and Toennies, J.P., Springer Series in Chemical Physics, Springer-Verlag, 1994.
- [EE83] Englisch, H. and Englisch, R., *Physica* **121 A** (1983) 253.

- [EFC⁺90] Eberhardt, W. et al., *Phys. Rev. Lett.* **64** (1990) 780.
- [EMR93] Engeln-Müllges, G. and Reuter, F., *Numerik-Algorithmen mit Fortran 77-Programmen*, BI-Wissenschaftsverlag, Mannheim, Zürich, 1993.
- [FAPC91] Feuston, B.P., Andreoni, W., Parrinello, M., and Clementi, E., *Phys. Rev. B* **44** (1991) 4056.
- [FB90] Fitzgerald, G.B. and Bartlett, R.J., *Int. J. Quantum Chem.* **38** (1990) 121.
- [FGPB93] Finocchi, F., Galli, G., Parrinello, M., and Bertoni, C.M., *Physica B* **185** (1993) 379.
- [Fle87] Fletcher, R., *Practical Methods of Optimization*, John Wiley & Sons, Chichester, 1987.
- [FMZ95] Froudakis, G.E., Mühlhäuser, M., and Zdetsis, A.D., *Chem. Phys. Lett.* **233** (1995) 619.
- [FSM⁺91] Fleming, R.M. et al., in *Clusters and Cluster-Assembled Materials*, edited by Averback, R.S., Bernholc, J., and Nelson, D.L., volume 206 of *Mat. Res. Soc. Symp. Proc.*, page 691, 1991.
- [FZM⁺94] Froudakis, G. et al., *J. Chem. Phys.* **101** (1994) 6790.
- [GDC⁺92] Guo, T. et al., *Science* **257** (1992) 1660.
- [GEZ⁺92] García, A., Elsässer, C., Zhu, J., Louie, S.G., and Cohen, M.L., *Phys. Rev. B* **46** (1992) 9829.
- [GHB⁺95] Gunnarsson, O. et al., *Phys. Rev. Lett.* **74** (1995) 1875.
- [GHMC94] Grumbach, M. P., Hohl, D., Martin, R. M., and Car, R., *J. Phys.: Condens. Matter* **6** (1994) 1999.
- [GJ79] Garey, M.R. and Johnson, D.S., *Computers and Intractability: A Guide to the Theory of NP-Completeness*, Freeman, San Francisco, 1979.
- [GJ85] Gunnarsson, O. and Jones, R. O., *Phys. Rev. B* **31** (1985) 7588.
- [GKL⁺94] Gausa, M., Kaschner, R., Lutz, H.O., Seifert, G., and Meiwes-Broer, K.H., *Chem. Phys. Lett.* **230** (1994) 99.
- [GKS⁺] Gausa, M. et al., to be published.
- [GL76] Gunnarsson, O. and Lundqvist, B. I., *Phys. Rev. B* **13** (1976) 4274.
- [GM95] Grossman, J.C. and Mitáš, L., *Phys. Rev. Lett.* **1323** (1995) 74.

- [GMB57] Gell-Mann, M. and Brueckner, K. A., *Phys. Rev.* **106** (1957) 364.
- [GMCP90] Galli, G., Martin, R.P., Car, R., and Parrinello, M., *Phys. Rev. B* **42** (1990) 7470.
- [GN89] Godby, R.W. and Needs, R.J., *Phys. Rev. Lett.* **62** (1989) 1169.
- [GP91] Galli, G. and Parrinello, M., Ab-initio molecular dynamics: Principles and practical implementation, in *Computer Simulation in Materials Science*, edited by Meyer, M. and Pontikis, V., NATO ASI Series, Kluwer Academic Publishers, 1991.
- [GPS96] Ganteför, G., Pieperhoff, P., and Schulze Icking-Konert, G., 1996, private communication.
- [GS84] Grev, R.S. and Schaefer, H.F. III, *J. Chem. Phys.* **80** (1984) 3552.
- [GS85] Grev, R.S. and Schaefer, H.F. III, *J. Chem. Phys.* **82** (1985) 4126.
- [GS93] Glukhovtsev, M.N. and Schleyer, P. v.R., *J. Phys. Chem.* **97** (1993) 8200.
- [GSLMB90] Ganteför, G., Siekmann, H.R., Lutz, H.O., and Meiwes-Broer, K.H., *Chem. Phys. Lett.* **165** (1990) 293.
- [Häs94] Häser, M., *J. Am. Chem. Soc.* **116** (1994) 6925.
- [HC92] Hartke, B. and Carter, E. A., *J. Chem. Phys.* **97** (1992) 6569.
- [HCR⁺85] Heimbrook, L.A., Chestnoy, N., Rasanen, M., Schwartz, G.P., and Bondybey, V.E., *J. Chem. Phys.* **83** (1985) 6091.
- [Hed65] Hedin, L., *Phys. Rev.* **139** (1965) 796.
- [Her50] Herzberg, G., *Molecular Spectra and Molecular Structure*, volume I. Spectra of Diatomic Molecules, Van Nostrand, Princeton, 1950.
- [HGK⁺95] Handschuh, H., Ganteför, G., Kessler, B., Bechthold, P.S., and Eberhardt, W., *Phys. Rev. Lett.* **74** (1995) 1095.
- [HH79] Huber, K.P. and Herzberg, G. *Molecular Spectra and Molecular Structure. IV. Constants of Diatomic Molecules*, Van Nostrand, Reinhold, 1979.
- [HH90] Harris, J. and Hohl, D., *J. Phys.: Condens. Matter* **2** (1990) 5161.
- [HJ74] Harris, J. and Jones, R. O., *J. Phys. F* **4** (1974) 1170.
- [HJ79] Harris, J. and Jones, R. O., *Phys. Rev. A* **19** (1979) 1813.

- [HJCP88] Hohl, D., Jones, R.O., Car, R., and Parrinello, M., *J. Chem. Phys.* **89** (1988) 6823.
- [HK64] Hohenberg, P. and Kohn, W., *Phys. Rev.* **136** (1964) B 864.
- [HL69] Hedin, L. and Lundqvist, S., *Solid State Physics* **223** (1969) 1.
- [HL85a] Hotop, H. and Lineberger, W.C., *J. Phys. Chem. Ref. Data* **14** (1985) 731.
- [HL85b] Hybertsen, M.S. and Louie, S.G., *Phys. Rev. Lett.* **55** (1985) 1418.
- [HM83] Hoare, M.R. and McInnes, J.A., *Adv. Phys.* **32** (1983) 791.
- [HOM⁺93] Honea, E.C. et al., *Nature* **366** (1993) 42.
- [HS89] Hamilton, T.P. and Schaefer, H.F. III, *Angew. Chem.* **101** (1989) 500.
- [HS90] Hamilton, T.P. and Schaefer, H.F. III, *Chem. Phys. Lett.* **166** (1990) 303.
- [HSC79] Hamann, D. R., Schlüter, M., and Chiang, C., *Phys. Rev. Lett.* **43** (1979) 1494.
- [HTB73] Hopkins, A.G., Tang, S.Y., and Brown, C.W., *J. Am. Chem. Soc.* **95** (1973) 3486.
- [HTP94] Hutter, J., Tuckerman, M., and Parrinello, M., *J. Chem. Phys.* **102** (1994) 859.
- [IZC79] Ihm, J., Zunger, A., and Cohen, M. L., *J. Phys.: Condens. Matter* **12** (1979) 4409.
- [Jac75] Jackson, J. D., *Classical Electrodynamics*, J. Wiley & Sons, New York, second edition, 1975.
- [Jan78] Janak, J. F., *Phys. Rev. B* **18** (1978) 7165.
- [Jan89] Janoschek, R., *Chem. Ber.* **122** (1989) 2121.
- [JG89] Jones, R. O. and Gunnarsson, O., *Rev. Mod. Physics* **61** (1989) 689.
- [JGP92] Johnson, B.G., Gill, P.M.W., and Pople, J.A., *J. Chem. Phys.* **97** (1992) 7846.
- [JH90a] Jones, R.O. and Hohl, D., *J. Chem. Phys.* **92** (1990) 6710.
- [JH90b] Jones, R.O. and Hohl, D., *Int. J. Quantum Chem.: Quantum Chem. Symposium* **24** (1990) 141.
- [JH90c] Jones, R.O. and Hohl, D., *J. Chem. Phys.* **92** (1990) 6710.

- [Jon93] Jones, R.O., J. Chem. Phys. **99** (1993) 1194.
- [JS92] Jones, R.O. and Seifert, G., J. Chem. Phys. **96** (1992) 7564.
- [KAP92] Kohanoff, J., Andreoni, W., and Parrinello, M., Phys. Rev. B **46** (1992) 4371.
- [KB82] Kleinman, L. and Bylander, D.M., Phys. Rev. Lett. **48** (1982) 1425.
- [Kcd⁺84] Knight, W.D. et al., Phys. Rev. Lett. **52** (1984) 2141.
- [KCWN90] Kitsopoulos, T.N., Chick, C.J., Weaver, A., and Neumark, D.M., J. Chem. Phys. **93** (1990) 6108.
- [Ker80] Kerker, G. P., J. Phys.: Condens. Matter **13** (1980) L189.
- [KGV83] Kirkpatrick, S., Gelatt, C.D., and Vecchi, M.P., Science **220** (1983) 671.
- [KLFH90] Krätchmer, W., Lamb, L.D., Fostiropoulos, K., and Huffman, D.R., Nature **347** (1990) 354.
- [KM90] Kohlenbrander, K.D. and Mandich, M.L., J. Chem. Phys. **92** (1990) 4759.
- [KN93] Kitsopoulos, T.N. and Neumark, D.M., Negative-ion photodetachment studies of small silicon and carbon clusters, in *On Clusters and Clustering*, edited by Stanley, H.E. and Guyon, E., Random Materials and Processes, North-Holland, 1993.
- [Koh94] Kohanoff, J., Comp. Mat. Sci. **2** (1994) 221.
- [Koh95] Kohn, W., Overview of density functional theory, in *Density Functional Theory*, edited by Gross, E.K.U. and Dreizler, R.M., NATO ASI Series, Plenum Press, 1995.
- [KP60] Klyne, W. and Prelog, V., Experientia **16** (1960) 521.
- [KQ94] Kreibig, U. and Quinten, M., Electromagnetic excitations of large clusters, in *Clusters of Atoms and Molecules II*, edited by Goldanskii, V.I., Schäfer, F.P., and Toennies, J.P., Springer Series in Chemical Physics, Springer-Verlag, 1994.
- [KTMS87] Kang, M. H., Tatar, R. C., Mele, E. J., and Soven, P., Phys. Rev. B **35** (1987) 5457.
- [LCP92] Laasonen, K., Csajka, F., and Parrinello, M., Chem. Phys. Lett. **194** (1992) 172.
- [Lev82] Levy, M., Phys. Rev. A **26** (1982) 1200.

- [Lew16] Lewis, G.N., J. Amer. chem. Soc. **38** (1916) 762.
- [LG88] Lammertsma, K. and Güner, O.F., J. Am. Chem. Soc. **110** (1988) 5239.
- [LG91] Laher, R.R. and Gilmore, F.R., J. Phys. Chem. Ref. Data **20** (1991) 685.
- [Lie83] Lieb, E. H., Int. J. Quant. Chem. **24** (1983) 243.
- [LJ73] Lunsford, J.H. and Johnson, D.P., J. Chem. Phys. **58** (1973) 2079.
- [LL78] Lin, M. and Lunsford, J.H., J. Mag. Reson. **29** (1978) 151.
- [LM83] Langreth, D. C. and Mehl, M. J., Phys. Rev. B **28** (1983) 1809.
- [LPC+88] Lenain, P., Picquenard, E., Corset, J., Jensen, D., and Steudel, R., Ber. Bunsenges. Phys. Chem. **92** (1988) 859.
- [LPKJ+93] Luke, B.T. et al., J. Am. Chem. Soc. **214** (1993) 357.
- [LPLC86] Lenain, P., Picquenard, E., Lesne, J.L., and Corset, J., J. Mol. Struct. **142** (1986) 355.
- [LPS84] Levy, M., Perdew, J.P., and Sahni, V., Phys. Rev. A **30** (1984) 2745.
- [LS90] Liang, C. and Schaefer, H.F. III, J. Chem. Phys. **93** (1990) 8844.
- [LVWR95] Li, S., Van Zee, R.J., Weltner, W. Jr., and Raghavachari, K., Chem. Phys. Lett. **243** (1995) 275.
- [Mar84] Martin, T.P., J. Chem. Phys. **81** (1984) 4427.
- [Mar86] Martin, T.P., Z. Phys. D **3** (1986) 211.
- [Mar87] Marple, S.L., Jr., *Digital Spectral Analysis with Applications*, Prentice-Hall, Englewood Cliffs, 1987.
- [MAZ89] Moazzzen-Ahmadi, N. and Zerbetto, F., Chem. Phys. Lett. **164** (1989) 517.
- [MC88] Martins, J. L. and Cohen, M. L., Phys. Rev. B **37** (1988) 6134.
- [MDO87] McElvany, S.W., Dunlap, B.I., and O'Keefe, A., J. Chem. Phys. **86** (1987) 715.
- [Mes69] Messiah, A., *Mécanique Quantique*, volume 1, Dunod, Éditeur, Paris, 1969.
- [MFG90] Martin, J.M.L., François, J.P., and Gijbels, R., J. Chem. Phys. **93** (1990) 8850.
- [MFZ+94] Mühlhäuser, M. et al., Z. Phys. D **32** (1994) 113.

- [MFZP93] Mühlhäuser, M., Froudakis, G., Zdetsis, A., and Peyerimhoff, S.D., *Chem. Phys. Lett.* **204** (1993) 617.
- [MG94] Mauri, F. and Galli, G., *Phys. Rev. B* **50** (1994) 4316.
- [MGLSS84] Michalopoulos, D.L., Geusic, M.E., Langridge-Smith, P.R.R., and Smalley, R.E., *J. Chem. Phys.* **80** (1984) 3556.
- [MHA93] Murray, C.W., Handy, N.C., and Amos, R.D., *J. Chem. Phys.* **98** (1993) 7145.
- [MMWI71] Maraudin, A.A., Montroll, E. W., Weiss, G.H., and Ipatova, I.P., *Solid State Physics Supplement* **3** (1971).
- [MPC95] Massobrio, C., Pasquarello, A., and Car, R., *Phys. Rev. Lett.* **75** (1995) 2104.
- [MRB90] Mandich, M.L., Reents, W.D. Jr., and Bondbey, V.E., Main group clusters: A review, in *Atomic and Molecular Clusters*, edited by Bernstein, E.R., volume 68 of *Studies in Physical and Theoretical Chemistry*, Elsevier, 1990.
- [MRR⁺53] Metropolis, N., Rosenbluth, A., Rosenbluth, M., Teller, A., and Teller, E., *J. Chem. Phys.* **21** (1953) 1087.
- [MSB94] Margl, P., Schwarz, K., and Blöchl, P.E., *J. Chem. Phys.* **100** (1994) 8194.
- [MSHO72] Meyer, B., Stroyer-Hansen, T., and Oommen, T.V., *J. Mol. Spectrosc.* **42** (1972) 335.
- [MZM85] Martin, W.C., Zalubas, R., and Musgrove, A., *J. Phys. Chem. Ref. Data* **14** (1985) 751.
- [NE86] Nimlos, N.R. and Ellison, G.B., *J. Phys. Chem.* **90** (1986) 2574.
- [NHE87] Nimlos, M.R., Harding, L.B., and Ellison, G.B., *J. Chem. Phys.* **87** (1987) 5116.
- [Nos84] Nosé, S., *J. Chem. Phys.* **81** (1984) 511.
- [NTN⁺95] Nakajima, A., Taguwa, T., Nakao, K., Gomei, M., and Kishi, R., *J. Chem. Phys.* **103** (1995) 2050.
- [OAKP94] Onida, G., Andreoni, W., Kohanoff, J., and Parrinello, M., *Chem. Phys. Lett.* **219** (1994) 1.
- [OB91] Ortiz, G. and Ballone, P., *Phys. Rev. B* **43** (1991) 6376.
- [OB94] Ortiz, G. and Ballone, P., *Phys. Rev. B* **50** (1994) 1391.

- [ODMG95] Ordejón, P., Drabold, D. A., Martin, R. M., and Grumbach, M. P., *Phys. Rev. B* **51** (1995) 1456.
- [OGP⁺94] Orden, A. Van, Giesen, T.F., Provencal, R.A., Hwang, H.J., and Saykally, R.J., *J. Chem. Phys.* **101** (1994) 10237.
- [Oxf93] *New Shorter Oxford Dictionary*, Clarendon Press, Oxford, 1993.
- [PA82] Painter, G.S. and Averill, F.W., *Phys. Rev. B* **26** (1982) 1781.
- [PA92] Parasuk, V. and Almlöf, J., *Theor. Chim. Acta* **83** (1992) 227.
- [Pau49] Pauling, L., *Proc. Nat. Acad. Sci.* **34** (1949) 495.
- [Pau60] Pauling, L., *The Nature of the Chemical Bond and the Structure of Molecules and Crystals*, Cornell University Press, Ithaca, New York, 1960.
- [PC59] Pitzer, K.S. and Clementi, E., *J. Am. Chem. Soc.* **81** (1959) 4477.
- [PCV⁺92] Perdew, J. P. et al., *Phys. Rev. B* **46** (1992) 6671, Erratum: *Phys. Rev. B* **48** (1993) 4978.
- [PEC93] Picquenard, E., El Jaroudi, O., and Corset, J., *J. Raman Spectrosc.* **24** (1993) 11.
- [Per86] Perdew, J. P., *Phys. Rev. B* **33** (1986) 8822, Erratum: *Phys. Rev. B* **34** (1986) 7046.
- [Per91] Perdew, J. P., Unified theory of exchange and correlation beyond the local density approximation, in *Electronic Structure of Solids '91*, edited by Ziesche, P. and Eschrig, H., Akademie Verlag, 1991.
- [PGHL92] Polak, M.L., Gerber, G., Ho, J., and Lineberger, W.C., *J. Chem. Phys.* **97** (1992) 8990.
- [PHGL91] Polak, M.L., Ho, J., Gerber, G., and Lineberger, W.C., *J. Chem. Phys.* **95** (1991) 3053.
- [PMG91] Presilla-Márquez, J.D. and Graham, W.R.M., *J. Chem. Phys.* **95** (1991) 5612.
- [PMG92] Presilla-Márquez, J.D. and Graham, W.R.M., *J. Chem. Phys.* **96** (1992) 6509.
- [PMG94] Presilla-Márquez, J.D. and Graham, W.R.M., *J. Chem. Phys.* **100** (1994) 181.
- [PMGRG95] Presilla-Márquez, J.D., Gay, S.C., Rittby, C.M.L., and Graham, W.R.M., *J. Chem. Phys.* **102** (1995) 6354.

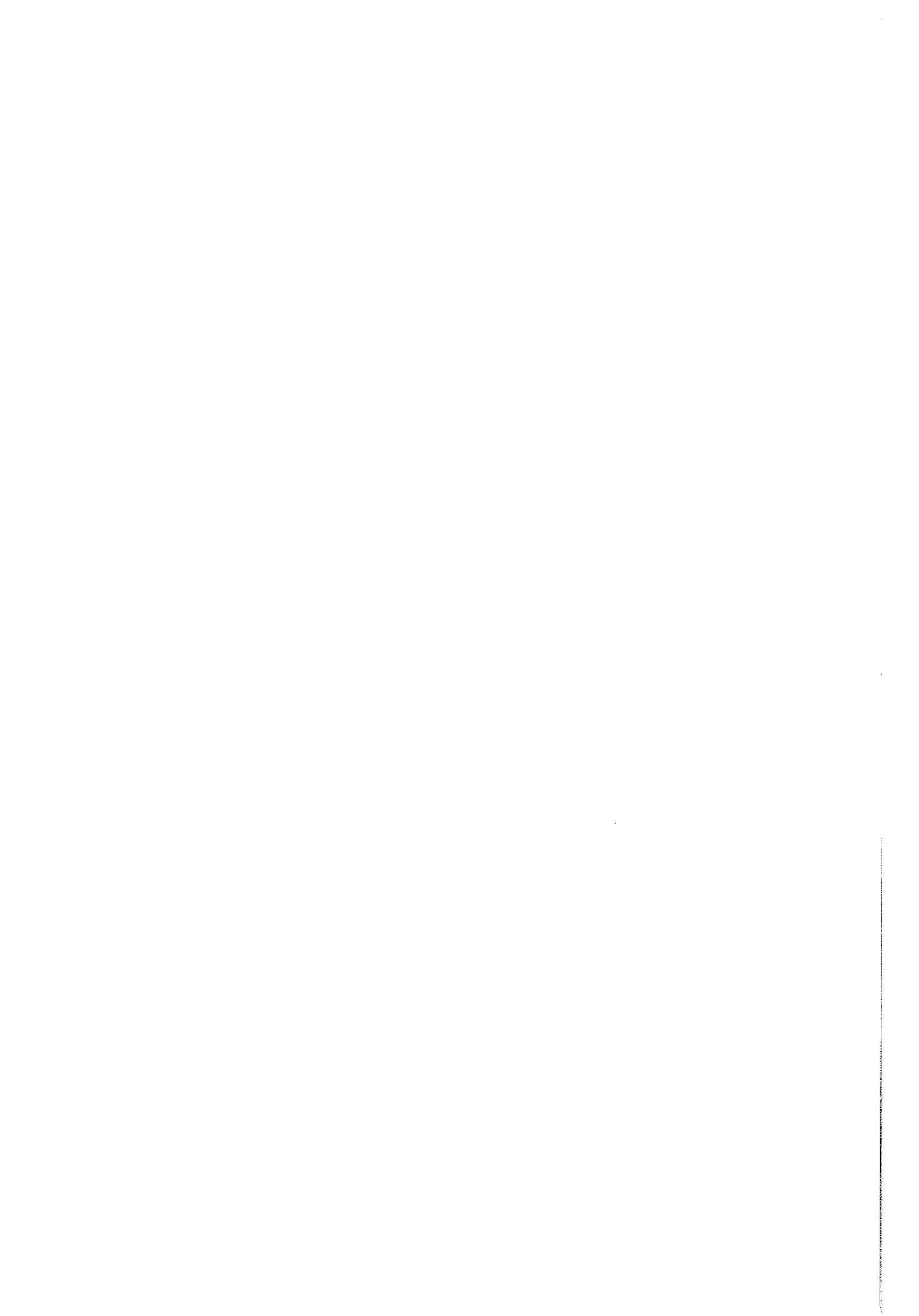
- [PMGS90] Presilla-Márquez, J.D., Graham, W.R.M., and Shepherd, R.A., *J. Chem. Phys.* **93** (1990) 5424.
- [PSB91] Pastore, G., Smargiassi, E., and Buda, F., *Phys. Rev. A* **44** (1991) 6334.
- [PTA92] Payne, M. C., Teter, M. P., and Allan, D. C., *Rev. Mod. Physics* **64** (1992) 1045.
- [PTVF92] Press, W. H., Teukolsky, S. A., Vetterling, W. T., and Flannery, B. P., *Numerical Recipes in Fortran - The Art of Scientific Computing*, Cambridge University Press, Cambridge, second edition, 1992.
- [Pul69] Pulay, P., *Mol. Phys.* **17** (1969) 197.
- [PY86] Perdew, J. P. and Yue, Wang, *Phys. Rev. B* **33** (1986) 8800.
- [PZ80] Perdew, J. P. and Zunger, A., *Phys. Rev. B* **23** (1980) 5048.
- [QSM90] Quelch, A.E., Schaefer, H.F. III, and Marsden, C.J., *J. Am. Chem. Soc.* **112** (1990) 8719.
- [Rag85] Raghavachari, K., *J. Chem. Phys.* **83** (1985) 3520.
- [Rag86] Raghavachari, K., *J. Chem. Phys.* **84** (1986) 5672.
- [RAH⁺86] Rice, J.E., Amos, R.D., Handy, N.C., Lee, T.J., and Schaefer, H.F. III, *J. Chem. Phys.* **85** (1986) 963.
- [RAP94] Röthlisberger, U., Andreoni, W., and Parrinello, M., *Phys. Rev. Lett.* **72** (1994) 665.
- [RB87] Raghavachari, K. and Binkley, J.S., *J. Chem. Phys.* **87** (1987) 2191.
- [RBRR94] Ross, S.C., Butenhoff, T.J., Rohlfing, E.A., and Rohlfing, C.M., *J. Chem. Phys.* **100** (1994) 4110.
- [RC73] Rajagopal, A. K. and Callaway, J., *Phys. Rev. B* **7** (1973) 1912.
- [RCB77] Ryckaert, J.P., Ciccotti, G., and Berendsen, H. J., *J. Comp. Phys.* **23** (1977) 327.
- [Rit91] Rittby, C.M.L., *J. Chem. Phys.* **95** (1991) 5609.
- [Rit92] Rittby, C.M.L., *J. Chem. Phys.* **96** (1992) 6768.
- [Rit94] Rittby, C.M.L., *J. Chem. Phys.* **100** (1994) 175.
- [RJBK90] Ray, U., Jarrold, M.F., Bower, J.E., and Krauss, J.S., *J. Chem. Phys.* **91** (1990) 2912.

- [RM90] Remmler, D.K. and Madden, P.A., *Mol. Phys.* **70** (1990) 921.
- [RMT⁺89] Rayane, D.P. et al., *J. Chem. Phys.* **91** (1989) 3100.
- [RR88] Raghavachari, K. and Rohlfing, C.McM., *J. Chem. Phys.* **89** (1988) 2219.
- [RR90] Rohlfing, C.McM. and Raghavachari, K., *Chem. Phys. Lett.* **167** (1990) 559.
- [RR91a] Raghavachari, K. and Rohlfing, C.McM., *J. Chem. Phys.* **94** (1991) 3670.
- [RR91b] Rohlfing, C.McM. and Raghavachari, K., *Chem. Phys. Lett.* **185** (1991) 244.
- [RR92] Rohlfing, C.McM. and Raghavachari, K., *J. Chem. Phys.* **96** (1992) 2114.
- [RRB90] Raghavachari, K., Rohlfing, C.McM., and Binkley, J.S., *J. Chem. Phys.* **93** (1990) 5862.
- [RS72] Reed, M. and Simon, B., *Methods of Modern Mathematical Physics*, volume I: Functional Analysis, Academic Press, New York, 1972.
- [RSO⁺93] Raghavachari, K. et al., *Chem. Phys. Lett.* **214** (1993) 357.
- [RZP⁺94] Raghavachari, K., Zhang, B., Pople, J.A., Johnson, B.G., and Gill, P.M.W., *Chem. Phys. Lett.* **220** (1994) 385.
- [Sau90] Saunders, W. A., *Phys. Rev. Lett.* **64** (1990) 3046.
- [SB87] Scherer, O.J. and Brück, T., *Angew. Chem.* **99** (1987) 59.
- [SBNSB92] Schindler, T., Berg, C., Niedner-Schatteburg, G., and Bondybey, V.E., *Ber. Bunsenges. Phys. Chem.* **96** (1992) 1114.
- [SCF⁺85] Snodgrass, J.T., Coe, J.V., Freidhoff, C.B., McHugh, K.M., and Bowen, K.H., *Chem. Phys. Lett.* **122** (1985) 352.
- [Sch90] Scherer, O.J., *Angew. Chem.* **102** (1990) 1137.
- [ŠCP91] Štich, I., Car, R., and Parrinello, M., *Phys. Rev. B* **44** (1991) 4262.
- [ŠCPB89] Štich, I., Car, R., Parrinello, M., and Baroni, S., *Phys. Rev. B* **39** (1989) 4997.
- [SF76] Sawicki, C.A. and Fitchen, D.B., *J. Chem. Phys.* **65** (1976) 4497.
- [SG85] Shepard, R.A. and Graham, W.R.M., *J. Chem. Phys.* **85** (1985) 1701.
- [SG89] Shen, L.N. and Graham, W.R.M., *J. Chem. Phys.* **91** (1989) 5115.
- [SGL89] Sudharkar, P.V., Güner, O.F., and Lammertsma, K., *J. Phys. Chem.* **93** (1989) 7289.

- [SJ91] Seifert, G. and Jones, R. O., *Z. Phys. D* **20** (1991) 77.
- [SJ92] Seifert, G. and Jones, R.O., *J. Chem. Phys.* **96** (1992) 2951.
- [SK65] Sham, L. J. and Kohn, W., *Phys. Rev.* **140** (1965) A 1133.
- [SK89] Sprik, M. and Klein, M. L., *J. Chem. Phys.* **91** (1989) 5665.
- [SL93] Shirley, E.L. and Louie, S.G., *Phys. Rev. Lett.* **71** (1993) 133.
- [Sla63] Slater, J.C., *Quantum Theory of Molecules and Solids*, volume 1, McGraw-Hill, New York, 1963.
- [SLF⁺91] Siekmann, H.R., Luder, C., Faehrmann, J., Lutz, H.O., and Meiwes-Broer, K.H., *Z. Phys. D* **20** (1991) 417.
- [SLJ⁺91] Siekmann, H.R. et al., *Z. Phys. D* **20** (1991) 417.
- [Sma83] Smalley, R.E., *Laser Chem.* **2** (1983) 167.
- [SN89] Sankey, O.F. and Niklewski, D. J., *Phys. Rev. B* **40** (1989) 3979.
- [SRS77a] Steudel, R., Reinhardt, R., and Schuster, F., *Angew. Chem.* **89** (1977) 756.
- [SRS77b] Steudel, R., Reinhardt, R., and Schuster, F., *Angew. Chem. Int. Edit. Engl.* **16** (1977) 715.
- [SSP⁺80] Steudel, R., Steidel, J., Pickardt, J., Schuster, F., and Reinhardt, R., *Z. Naturforsch. Teil B* **35** (1980) 1378.
- [SSS85] Steudel, R., Sandow, T., and Steidel, J., *Z. Naturforsch. Teil B* **40** (1985) 594.
- [Ste75a] Steudel, R., *Spectrochim. Acta Part A* **31** (1975) 1065.
- [Ste75b] Steudel, R., *Angew. Chem.* **87** (1975) 683.
- [Ste75c] Steudel, R., *Angew. Chem. Int. Edit. Engl.* **14** (1975) 655.
- [Ste77a] Steudel, R., *Angew. Chem.* **89** (1977) 757.
- [Ste77b] Steudel, R., *Angew. Chem. Int. Edit. Engl.* **16** (1977) 716.
- [Ste83] Steudel, R., *Z. Naturforsch. B* **38** (1983) 543.
- [Ste84] Steudel, R., in *Studies in Inorganic Chemistry*, edited by Müller, A. and Krebs, B., volume 5, page 3, Amsterdam, 1984, Elsevier.
- [Ste85] Steudel, R., *Nova Acta Leopoldina* **59** (1985) 231.

- [STG87] Schmidt, M.W., Truong, P.N., and Gordon, M.S., *J. Am. Chem. Soc.* **5217** (1987) 109.
- [SVB85] Scheffler, M., Vigneron, J. P., and Bachelet, G. B., *Phys. Rev. B* **31** (1985) 6541.
- [SW85] Stillinger, F. H. and Weber, T. A., *Phys. Rev. B* **29** (1985) 5262.
- [SW90] Soler, J. M. and Williams, A.R., *Phys. Rev. B* **42** (1990) 9728.
- [SW93] Schubert, M. and Weber, G., *Quantentheorie*, Spectrum Akademischer Verlag, Heidelberg, 1993.
- [SWL86] Stillinger, F.H., Weber, T.A., and LaViolette, R.A., *J. Chem. Phys.* **85** (1986) 6460.
- [SZLC89] Saito, S., Zhang, S.B., Louie, S.G., and Cohen, M.L., *Phys. Rev. B* **40** (1989) 3643.
- [TB75] Tang, S.-Y. and Brown, C.W., *Inorg. Chem.* **14** (1975) 2856.
- [TB86] Trucks, G.W. and Bartlett, R.J., *J. Mol. Struct. (Theochem.)* **135** (1986) 423.
- [TES+91] Tanigaki, K. et al., *Nature* **352** (1991) 222.
- [TJC+90] Taylor, K.J. et al., *J. Chem. Phys.* **93** (1990) 7515.
- [TK69] Thurn, H. and Krebs, H., *Acta Crystallogr. B* **92** (1969) 125.
- [TM91] Troullier, N. and Martins, J. L., *Phys. Rev. B* **43** (1991) 1993.
- [Van85] Vanderbilt, D., *Phys. Rev. B* **32** (1985) 8412.
- [vB79] von Barth, U., *Phys. Rev. A* **20** (1979) 1693.
- [vBH72] von Barth, U. and Hedin, L., *J. Phys. C: Solid State Phys.* **5** (1972) 1629.
- [VFK+91] Vager, Z., Feldman, H., Kella, D., Malkin, E., and Miklazky, E., *Z. Phys. B* **19** (1991) 413.
- [vHKGB93] von Helden, G., Kemper, P.R., Gotts, N.G., and Bowers, M.T., *Science* **259** (1993) 1300.
- [vN91] von Niessen, W., *J. Chem. Phys.* **95** (1991) 8301.
- [vSH88] von Schnering, H.G. and Hönle, W., *Chem. Rev.* **88** (1988) 243.
- [VWN80] Vosko, S. H., Wilk, L., and Nusair, M., *Can. J. Phys.* **58** (1980) 1200.

- [Wal93] Walsh, R., *Acc. Chem. Res.* **214** (1993) 357.
- [WB92] Watts, J.D. and Bartlett, R.J., *J. Chem. Phys.* **97** (1992) 3445.
- [WB94] White, J.A. and Bird, D.M., *Phys. Rev. B* **50** (1994) 4954.
- [WCH90] Wang, C.Z., Chan, C.T., and Ho, K.M., *Phys. Rev. B* **42** (1990) 11276.
- [WG92] Withey, P.A. and Graham, W.R.M., *J. Chem. Phys.* **96** (1992) 4068.
- [WHMP81] Woo, S.B., Helmy, E.M., Mauk, P.M., and Paszek, A.P., *Phys. Rev. A* **24** (1981) 1380.
- [WSG91] Withey, P.A., Shen, L.N., and Graham, W.R.M., *J. Chem. Phys.* **95** (1991) 820.
- [WV85] Wille, L.T. and Vennik, J., *J. Phys. A* **18** (1985) L419, L1113.
- [Yeo88] Yeomans, Y., *Solid State Physics* **41** (1988) 151, and references therein.
- [YOBC90] Yi, J., Oh, D., Bernholc, J., and Car, R., *Chem. Phys. Lett.* **174** (1990) 461.
- [YSK91] Yu, R., Singh, D., and Krakauer, H., *Phys. Rev. B* **43** (1991) 6411.
- [YTC+88] Yang, S. et al., *Chem. Phys. Lett.* **144** (1988) 431.
- [ZM83] Zumbach, G. and Maschke, K., *Phys. Rev. A* **28** (1983) 544, Erratum: *Phys. Rev. A* **29** (1984) 1585.
- [ZRB77] Ziegler, T., Rauk, A., and Baerends, E.J., *Theor. Chim. Acta* **43** (1977) 261.
- [ZvN94] Zakrzewski, V.G. and von Niessen, W., *Theor. Chim. Acta* **88** (1994) 75.



Danksagung

An erster Stelle möchte ich Herrn Dr. R.O. Jones für die interessante Themenstellung und die unterhaltsame Zusammenarbeit danken. Er war stets ansprechbar und immer an den Ergebnissen interessiert.

Besonders danken möchte ich Herrn Prof. P.H. Dederichs für seine Betreuung dieser Arbeit und seine freundliche und kompetente Unterstützung bei allen auftretenden Schwierigkeiten.

Viel verdanke ich auch Herrn Dr. G. Ganteför und seinen Mitarbeitern, den Herren P. Pieperhoff und G. Schulze Icking-Konert. Sie haben begleitende Experimente zu dieser Arbeit durchgeführt und mir nicht nur bei deren Präsentation geholfen.

Herzlich danken möchte ich auch Herrn Dr. P. Ballone, der mir vor allem in der Anfangsphase dieser Arbeit mit Rat und Tat geholfen hat, die Dinge ins Rollen zu bringen. Auch stammt die Programmversion, die schließlich zu den Simulationsrechnungen für die Kohlenstoff-Silizium Cluster verwendet wurde, zu großen Teilen von ihm.

Auch bei Herrn Prof. G. Eilenberger und den übrigen Mitgliedern unserer Gruppe möchte ich mich bedanken, deren Humor und Kompetenz einen anregenden Rahmen für diese Arbeit bildeten.

Für erhellende sowie erleichternde Diskussionen danke ich insbesondere Herrn Dr. A. Körner und Herrn Dr. A. Lichtenstein, der mir auch (unter anderem) bei der Erstellung der AVS Graphiken geholfen hat.

Viele andere waren am Gelingen zahlreicher Details der Arbeit beteiligt. In erster Linie möchte ich nennen: Dr. A. Borrmann, Dr. A. Bringer, B. Engels, Dr. D. Hohl, Dr. B. Kessler, M. Krenzlin, M. Maus, O. Pfaffenzeller, C. Schlebusch und Dr. Ch. Schroer.

Abschließend möchte ich meiner lieben Freundin Margarete, meiner Familie und Freunden danken, die eigentlich mit an erster Stelle hätten genannt werden müssen.



Jül-3268
August 1996
ISSN 0944-2952